

Computational and Experimental Investigation of Supersonic Convection over a Laser Heated Target

Eric C. Marineau

Dissertation submitted to the Faculty of the
Virginia Polytechnic Institute and State University
in partial fulfillment of the requirements for the degree of

Doctor of Philosophy
in
Aerospace Engineering

Joseph A. Schetz, Chair
Richard Barnwell
William J. Devenport
Reece E. Neel
Brian Vick

May 10 2007
Blacksburg, Virginia

Keywords: computational fluid dynamics (CFD), experimental fluid dynamics, conjugate
heat transfer (CHT), supersonic convection, turbulence, laser
Copyright 2007, Eric C. Marineau

Computational and Experimental Investigation of Supersonic Convection over a Laser Heated Target

Eric C. Marineau

ABSTRACT

This research concerns the development and validation of simulation of the beam-target interaction to determine the target temperature distribution as a function of time for a given target geometry, surface radiation intensity and free stream flow condition. The effect of a turbulent supersonic flow was investigated both numerically and experimentally.

Experiments were in the Virginia Tech supersonic wind tunnel with a Mach 4 nozzle, ambient total temperature, total pressure of 160 psi and Reynolds number of $5 \times 10^7/m$. The target consisted of a 6.35 mm stainless steel plate painted flat black. The target was irradiated with a 300 Watt continuous beam Ytterbium fiber laser generating a 4 mm Gaussian beam at 1.08 micron 10 cm from the leading edge where a 4 mm turbulent boundary layer prevailed. An absorbed laser power of 65, 81, 101, 120 Watts was used leading to a maximum heat flux between 1035 to 1910 W/cm^2 . The target surface and backside temperature was measured using a mid-wave infrared camera. The backside temperature was also measured using eight type-K thermocouples.

Two tests are made, one with the flow-on and the other with the flow-off. For the flow-on case, the laser is turned on after the tunnel starts and the flow reaches a steady state. For the flow-off case, the plate is heated at the same power but without the supersonic flow. The cooling effect is seen by subtracting the flow-off temperature from the flow-on temperature. This temperature subtraction is useful in cancelling the bias errors such that the overall uncertainty is significantly reduced.

A new conjugate heat transfer algorithm was implemented in the GASP solver and validated by predicting the temperature distribution inside a cooled nozzle wall. The conjugate heat transfer algorithm was used to simulate the experiments at 81 and 65 Watts. Most computations were performed using the Spalart-Allmaras turbulence model on a 280, 320 cell grid. A grid convergence study was performed.

At 65 Watts, good agreement was found in the predicted surface and backside temperature. On the surface, cooling was underpredicted close to the center and better agreement was seen away from the center. On the backside, good agreement was found for the temperature and temperature difference. Compared to the 65 Watt case, the 81 Watt case displays more asymmetry and a region of increased cooling is found upstream. The increased asymmetry was also seen on the backside by both the thermocouple and infrared temperature measurements. The computation underpredicts the surface temperature by 7% for the flow-off case. Again, cooling is underpredicted at the surface near the center. For all power settings, convective cooling significantly increases the time required to reach a given temperature.

Acknowledgments

I wish to thank my Advisor Dr. Schetz for his many useful technical, professional and personal advises throughout this endeavor. His knowledge of experimental fluid dynamics greatly helped me get-up to speed and compensated for my inexperience in the field such that today, I am not strictly a "CFD guy" but also an experimentalist. I also thank him and his family for inviting me for their Thanksgiving dinner every year.

I wish to thank Aerosoft Inc. for their technical support. Particularly Dr. Reece Neel, for his help in learning how to use Gasp, his numerous advices on the numerical side of this research and his fair criticism which helped me improve the experiment. I also thank him for his enthusiasm and never attempting to make me feel stupid when I committed a mistake.

I also want to acknowledge my other committee members namely, Dr. Richard Barnwell, Dr. William Devenport and Dr. Brian Vick for their support and constructive comments. Special thanks to Dr. Devenport for providing me with his compressible aerodynamics class notes and homework which greatly helped my teaching as well as developing a new set of slides while writing my dissertation during the spring 2007 semester.

Many thanks to Steve Edwards for his help with the data acquisition and laser control program. I am grateful for his meticulous work in putting in the backside thermocouples. His technical knowledge and dexterity are only matched by his kindness. I also thank him for providing me a laptop computer when mine broke during my redaction and then fixing the one he provided me with. I am also thankful to him and his wife Carla for receiving my parents and I for dinner during their visit in Blacksburg as well as their yearly dinner on the 4th of July.

I wish to thank Bruce Stanger and James Lambert from the AOE machine shop for their good job in building the wind tunnel model and window inserts.

Thanks to my past professors from Ecole Polytechnique for their contribution to my academic training: Professor Reggio, Professor Trepanier and particularly Professor Pelletier who first recommended Virginia Tech and supported my decision to study abroad. Thanks to my longtime friend Nathalie for her moral support and continuous friendship.

I wish to thank all the friends I had the opportunity to make during my stay in Blacksburg. More particularly, thanks to Luca "Dott. Ing." Maddalena and his family for receiving

me in Italy and letting me visit Venice with his sister. Many thanks to Serhat "Professor Sir Hat" Hosder for the airport rides and to Ari "Calteach" Bonanos, Leifur "Doc" Thor Leifsson, Rafael "Business" Perez, Gilberto "Giba" Goglio, Alessandro "M&N lover" Toso and Major A.J. Rolling for the good memories in Blacksburg. Thanks to Konda Reddy for his hospitality in California and the good times drinking Trois-Pistoles beer at the Cellar. Thanks to all my roommates at the Castle who didn't complained about the smell of steak in the middle of the night and particularly to Tim for the many 3-set tennis epics. Thanks to everybody from the French Table for the enjoyable conversations.

Lastly, I wish to thank my family, particularly my brother Claude to provide me with free airplane tickets twice a year during my stay at Tech, and most importantly to my parents Lucien and Therese for their perpetual support and for always believing in me.

Contents

1	Introduction	1
2	Conduction Heat Transfer	5
2.1	Analytical Solutions to the Heat Equation	5
2.1.1	Method of images	8
2.1.2	Kirchhoff Transformation	10
2.1.3	Moving Laser Beam	11
2.1.4	Dimensional Analysis	12
2.2	Numerical Solutions to the Heat Equation	16
3	Boundary Layers and Convective Heat Transfer	18
3.1	Turbulent Boundary Layers	18
3.2	Film Coefficients	21
3.2.1	Reference Properties Approach	22
3.2.2	Temperature-Ratio Correction Approach	22
3.2.3	Van Driest II Correlation	23
3.2.4	Film Coefficient in the Virginia Tech Supersonic Wind Tunnel	23
3.2.5	Film Coefficient for an Arbitrary Wall Temperature Distribution	24
3.3	Overview of Transition to Turbulence	26
4	Numerical Convective Heat Transfer	28
4.1	Conservation Equations	28

4.1.1	Transport of the $\mathcal{TK}\mathcal{E}$ and of the Mean Dissipation Rate	30
4.2	Turbulence Modeling	34
4.2.1	Eddy Viscosity Formulation	34
4.2.2	Sparlart-Allmaras One-equation Turbulence Model	35
4.2.3	Two-equation Turbulence Models	36
4.2.4	Analysis of Turbulence Models in Compressible Boundary Layers	38
4.3	Finite Volume Discretization and GASP Solver	41
4.3.1	Finite Volume Discretization	41
4.3.2	Spatial Reconstruction and Flux Computation	42
4.3.3	Boundary Condition	44
4.3.4	Linearization and Time Integration	46
4.4	Validation Studies	47
4.4.1	Low Speed Validation Cases	48
4.4.2	Supersonic Validation Cases	52
5	Conjugate Heat Transfer	59
5.1	CHT Theory	59
5.1.1	Dimensional Analysis	60
5.1.2	Effect of Conjugate Peclet Number	61
5.2	Numerical Algorithm	64
5.3	Validation Study	66
6	Experimental Apparatus and Methods	71
6.1	Design Methodology	71
6.2	Overview of Previous Experiments	72
6.3	Design Overview and Selection of Components	73
6.3.1	Design Overview	73
6.3.2	Splitter Plate and Paint	73
6.3.3	Laser	77

6.3.4	Optical Table	78
6.3.5	Infrared Camera	78
6.3.6	Thermocouples	82
6.3.7	Windows	84
6.3.8	Safety Considerations	86
6.3.9	Virginia Tech Supersonic Wind tunnel	86
6.4	Uncertainty Analysis	87
6.4.1	Sources of Bias Error	87
6.4.2	Uncertainty on the Temperature Difference	89
7	Experimental Results	98
7.1	Static Testing Results	98
7.2	Flow Survey	102
7.3	Test Matrix and Problem Type	103
7.4	65 Watt Case	104
7.4.1	Thermocouple Results	104
7.4.2	Infrared Camera Results	106
7.5	81 Watt Case	112
7.5.1	Thermocouple Results	112
7.5.2	Infrared Camera Results	117
7.6	101 Watts Case	121
7.7	120 Watt Case	123
7.8	Type 2 Results	126
7.9	Experimental Results Summary	126
8	Computational Model and Results	129
8.1	Grid and Time Convergence Study	132
8.1.1	Methodology	132
8.1.2	Spatial Discretization Error	134

8.1.3	Time Discretization Error	136
8.1.4	Total Error for Flow-on and Flow-off Conditions	137
8.1.5	Uncertainty on the Temperature Difference	139
8.2	Effects of the Turbulence Model	141
8.3	Flow Results	141
9	Comparison of Computation and Experiment	155
9.1	65 Watt case	155
9.1.1	Contour Plots of the Surface Temperature Difference	155
9.1.2	Time variation plot	156
9.1.3	Streamwise Temperature Profiles	159
9.2	81 Watt case	167
9.2.1	Surface Temperature Contour Plots	167
9.2.2	Time variation plot	167
9.2.3	Streamwise Temperature Profiles	170
9.3	Discussion	174
10	Conclusions	179
10.1	Contributions	179
10.2	Recommendations and Extensions	180
A	Generation of Missing Information at the Boundary	188
B	Numerical and Experimental Investigation of Mach 4 Flow in the Virginia Tech Supersonic Wind Tunnel	194
B.1	Experimental Results	194
B.2	Computational Results	195
C	Infrared Camera Model and Dynamic Response	203
D	Window Structural Analysis	208

E	Streamwise Temperature Profiles for $P = 65W$	211
F	Streamwise Temperature Profiles for $P = 81W$	218

List of Figures

1.1	Wall painting from the Stanzino delle Matematiche in the Galleria degli Uffizi (Florence, Italy). Painted by Giulio Parigi (1571-1635) in the years 1599-1600. (taken from [30])	2
1.2	The Airborne Laser (taken from [5])	2
2.1	Geometry for the analytical solution to the heat equation for a laser heated target	6
2.2	Dimensionless intensity profile for a Gaussian and a constant intensity beam	7
2.3	Image sources used to get a slab of finite thickness L	9
2.4	Arrangement of image sources and resulting geometry for a cuboid of lengths $2a$ and thickness L	10
2.5	Coordinate transformation for a sliding beam with a constant velocity . . .	11
2.6	Coordinate transformation for a beam moving with an arbitrary velocity . .	13
2.7	Normalized temperature for a semi-infinite geometry	14
2.8	Effect of L^* on the normalized temperature at $t^* = 25$	15
2.9	Effect of the target thickness on the maximum surface temperature	16
3.1	Film coefficient for a flat plate inside the Virginia Tech supersonic wind tunnel at Mach 4	27
3.2	Transition Reynolds Number (from Chen et. al [13])	27
4.1	Comparison between original and modified turbulence models and experiment of Mabey et. al (figure adapted form Catris [9])	40
4.2	Finite volume discretization	42

4.3	Spatial reconstruction is needed to express the face values as a function of the cell-centered values. The computation of the inviscid flux requires a left and a right state at each faces.	43
4.4	Nomenclature for the boundary conditions. When the Full is used the ghost cells values are applied directly on the boundary	44
4.5	The inlet boundary condition permits upstream influence. Fixing the pressure at the outlet and on the top surface insure no pressure gradient.	48
4.6	Experimental Apparatus: The wall temperature distribution is obtained with heated strips [57]	49
4.7	Stanton number for low velocity boundary layer on a heated wall with constant $T_w - T_e = 12.8K$ compared with experiment from Reynolds et al. [57]	49
4.8	Effect of wall temperature interpolation on Stanton number wall temperature. Results are compared with experiment from Reynolds et al. [56]	50
4.9	Effect of grid clustering	51
4.10	Stanton number for a low velocity boundary layer subjected to wall temperature step compared with experiment from Reynolds et al. [56]	51
4.11	Computed wall temperature over the adiabatic portion of the wall compared with experiment from Reynolds et al. [56]	52
4.12	Stanton number for a low velocity boundary layer subjected to double pulse in wall temperature compared with experiment from Reynolds et al. [56]	53
4.13	The inlet boundary condition doesn't permit upstream influence. Extrapolation at the outlet insure no influence from the boundary on the inside domain	54
4.14	Experimental configuration taken from Debieve et al. [20].	54
4.15	Skin friction coefficient for a supersonic boundary layer with an adiabatic wall compared with results from Debieve et al. [20].	54
4.16	Velocity profiles for a supersonic boundary layer on an adiabatic wall compared with experiment from Debieve et al. [20]	55
4.17	Skin friction coefficient and Stanton number for a supersonic boundary layer with a step in wall temperature with $T_w/T_r = 1.5$ compared with results from Debieve .et al. [20]	55
4.18	Skin friction coefficient and Stanton number for a supersonic boundary layer with a step in wall temperature with $T_w/T_r = 2$ compared with results from Debieve et al. [20]	56

4.19	Velocity profiles for a supersonic boundary layer with a step in wall temperature at $x=0$ for ratios of $T_w/T_r = 1.5$ compared with experiment from Debieve et al. [20]	57
4.20	Velocity profiles for a supersonic boundary layer with a step in wall temperature at $x=0$ for ratios of $T_w/T_r = 2$ compared with experiment from Debieve et al. [20]	57
4.21	Temperature profiles for a supersonic boundary layer with a step in wall temperature at $x=0$ for ratios of $T_w/T_r = 1.5$ compared with experiment from Debieve et al. [20]	58
4.22	Temperature profiles for a supersonic boundary layer with a step in wall temperature at $x=0$ for ratios of $T_w/T_r = 2$ compared with experiment from Debieve et al. [20]	58
5.1	Geometry for the CHT problem of a laser irradiated flat plate	60
5.2	Spatially averaged modified Nusselt number based of the plate thickness L vs conjugate Peclet number based on the plate thickness L taken from Cole [16]	62
5.3	Heat balance at the surface	63
5.4	Correlation for the film coefficient as a function of $\Lambda_L w/L$	64
5.5	Schematic of the conjugate heat transfer problem	65
5.6	Conjugate heat transfer iterative algorithm	66
5.7	Temperature distribution ($^{\circ}F$) inside the nozzle from thermocouple measurements by Back et al. [3] reported by Delise and Naraghi [21]	67
5.8	Cooled nozzle grid containing 6800 cells	68
5.9	Ratio of eddy to laminar viscosity for a cooled axisymmetric nozzle	69
5.10	Inside wall temperature for a cooled axisymmetric nozzle compared with experiment from Back et al. [3]	70
5.11	Mach number and wall temperature contour for a cooled axisymmetric nozzle using Spalart-Allmaras turbulence model	70
6.1	Overall experimental layout	74
6.2	Splitter plate and strut mount assembly	75
6.3	Splitter plate fixed on the wind tunnel wall irradiated with the guide beam	76
6.4	Beam Quality: The Gaussian fit is found on the upper left as well as the beam diameter	77

6.5	Laser LabVIEW control program GUI	79
6.6	Optical table setup	79
6.7	Data reduction of infrared camera images	92
6.8	Medtherm thermocouple detail taken from [18]	93
6.9	Backside thermocouple position	93
6.10	Reflectivity for 1064 nm coating at 0° [19]	94
6.11	Window insert	94
6.12	Transmissivity of calcium fluoride [51]	95
6.13	Side-view sketch of the Virginia Tech Supersonic Wind tunnel	95
6.14	Total pressure and total temperature as a function of time for a typical run .	96
6.15	An uncertainty in the emissivity of 0.09 unit introduces a temperature error of 3% (of the temperature in K) whereas an uncertainty on the laser power of 5% (of the temperature in K) introduces temperature error of 3.75%	96
6.16	Uncertainty on the temperature difference measured by the infrared camera on the surface and backside as a function of distance for $t = 1s$ and $t = 10s$ for $P=81 W$	97
6.17	Uncertainty on the temperature difference measured by the thermocouples as a function of time.	97
7.1	Picture of the static setup where the laser beam (simulated) is aimed at the splitter-plate insert	99
7.2	Starting characteristic of laser for different values of power	99
7.3	Relation between diode current and laser power	100
7.4	Good repeatability of backside temperature seen for successive irradiation at a fixed location	101
7.5	Flow visualization in used in determining the free stream Mach number and boundary layer thickness	103
7.6	Thermocouple temperature measurements at $P=65W$	105
7.7	Temperature difference between flow-off and flow-on condition at $P=65$. . .	105
7.8	Surface temperature for $P=65 W$ with the flow going from left to right . . .	107
7.9	Backside temperature for $P=65 W$ with the flow going from left to right . .	108

7.10	Surface temperature difference for $P=65$ W with the flow going from left to right (Note: the temperature difference is set to zero for temperatures below 333 K)	110
7.11	Backside temperature difference for $P=65$ W with the flow going from left to right	111
7.12	Backside thermocouple temperature measurements for run 1 at $P=81$ W . .	113
7.13	Backside thermocouple temperature measurements for run 2 at $P=81$ W . .	113
7.14	Backside thermocouple temperature measurements for run 3 at $P=81$ W . .	114
7.15	Backside thermocouple temperature measurements for run 4 at $P=81$ W . .	114
7.16	Backside thermocouple temperature measurements for run 5 at $P=81$ W . .	115
7.17	Backside thermocouple temperature measurements for run 6 at $P=81$ W . .	115
7.18	Backside temperature difference between flow-off and flow-on condition at $P=81$ W	116
7.19	Backside temperature difference between flow-off and flow-on condition at $P=81$ W	116
7.20	Backside temperature difference between flow-off and flow-on condition at $P=81$ W	117
7.21	Surface temperature for $P=81$ W with the flow going from left to right . . .	118
7.22	Backside temperature for $P=81$ W with the flow going from left to right . .	119
7.23	Surface temperature difference for $P=81$ W with the flow going from left to right	120
7.24	Backside temperature difference for $P=81$ W with the flow going from left to right	121
7.25	Backside thermocouple temperature measurements at $P=101$ W	122
7.26	Backside thermocouple temperature measurements at $P= 101$ W	122
7.27	Thermocouple temperature difference at $P=101$ W	123
7.28	Temperature contours (K) at $t = 10s$ for $P=120$ W	124
7.29	Temperature difference contours (K) for $P=120$ W	124
7.30	Maximum surface temperature for flow-on and flow-off conditions at $P = 120W$	125
7.31	Difference in the maximum surface temperature between the flow-off and flow-on conditions at $P = 120W$	126

7.32	Temperature on the backside for a type 2 test for $P=50$ W. The plate is pre-heated for 70 seconds and the tunnel started while the irradiation is maintained	127
7.33	Temperature difference on the backside	127
8.1	Ramp in laser power specified as a pointwise boundary condition	130
8.2	Medium grid for the fluid domain composed of four blocks. Half of the geometry is modeled due to symmetry	131
8.3	Surface grid topology	132
8.4	Maximum surface temperature for a steady state computation at $P=81$ Watts	135
8.5	Maximum surface temperature used in the evaluation of the time discretization error	136
8.6	Comparison of the maximum surface temperature between the numerical and analytical solution for the medium grid at a time step of 1×10^{-4}	138
8.7	Comparison of the solutions used in the evaluation of the uncertainty on the computed difference between the flow-off and flow-on cases. In the legend, medium refers to the medium grid with a H-C-H topology (seen in Fig. 8.2) whereas the cartesian refers to a fine cartesian grid	140
8.8	Pressure contours in the x-y plane. Dimensions are in <i>mm</i>	142
8.9	Pressure iso-contours at $t = 10s$ for $P=65$ W. A high pressure region is created upstream of the heat spot and a low pressure region is created downstream .	143
8.10	Temperature contours in the x-y plane dimensions are in <i>mm</i>	144
8.11	Density contours in the x-y plane dimensions are in <i>mm</i>	145
8.12	Streamlines in the x-z plane at $t = 10s$ dimensions are in <i>mm</i> . The heat source acts like a "bump"	146
8.13	x -vorticity at $t = 10s$ for $P=65$ W dimensions are in <i>mm</i>	147
8.14	y -vorticity at $t = 10s$ for $P=65$ W dimensions are in <i>mm</i>	147
8.15	z -vorticity at $t = 10s$ for $P=65$ W dimensions are in <i>mm</i>	148
8.16	Effect of heating on flow variables for $P = 65W$ at target center	149
8.17	Effect of heating on flow variables for $P = 65W$ 0.1 inch upstream of target center	151
8.18	Effect of heating on flow variables for $P = 65W$ 0.1 inch downstream of target center	153

8.19	Effect of heating on the u-velocity profile. The velocity decreases close to the wall	154
8.20	Effect of heating on the Mach profile. The increase in temperature increases the local speed of sound and local Mach number. The sonic line is shifted up	154
9.1	Comparison of surface temperature difference between CFD and experiment for P=65 W. Computation on top and experiment on bottom (Note: the experimental temperature difference is set to zero for temperatures below 333 K)	157
9.2	Comparison of backside temperature difference between CFD and experiment for P=65 W. Computation on top and experiment on bottom	158
9.3	Comparison between infrared measurement and computed surface temperature difference as a function of time for P=65 W.	160
9.4	Comparison between thermocouples measurement and computed backside temperature difference as a function of time for P=65 W at the center	161
9.5	Comparison between infrared and thermocouples measurement and computed backside temperature difference as a function of time for P=65 W	162
9.6	Comparison between infrared measurement and computed surface temperature as a function of time for flow-off condition and P=65 W	163
9.7	Comparison between infrared measurement and computed surface temperature as a function of time for flow-on condition and P=65 W	163
9.8	Comparison between infrared measurement and computed backside temperature as a function of time for flow-off condition and P=65 W	164
9.9	Comparison between infrared measurement and computed backside temperature as a function of time for flow-on condition and P=65 W	164
9.10	Infrared image on the backside: The target is located in a cavity and reflection is seen on the upper and lower part of the image	165
9.11	Comparison of the surface temperature difference between CFD and experiment for P=65 W	166
9.12	Comparison of the backside temperature difference between CFD and experiment for P=65 W for $t = 8s$	166
9.13	Comparison of surface temperature between CFD and experiment for P=81 W. Computation on top and experiment on bottom	168
9.14	Comparison of backside temperature between CFD and experiment for P=81 W. Computation on top and experiment on bottom	169

9.15	Comparison between infrared and thermocouple measurements and computed surface temperature as a function of time for the flow-off condition at P=81 W.	170
9.16	Comparison between infrared measurement and computed surface temperature difference as a function of time for P=81 W	171
9.17	Comparison between infrared and thermocouples measurement and computed backside temperature difference as a function of time for P=81 W	172
9.18	Comparison between infrared measurement and computed surface temperature as a function of time for the flow-off condition at P=81 W	173
9.19	Comparison between infrared measurement and computed surface temperature as a function of time for the flow-on condition at P=81 W	174
9.20	Comparison between infrared measurement and computed backside temperature as a function of time for flow-off condition and P=81 W	175
9.21	Comparison between infrared measurement and computed backside temperature as a function of time for flow-on condition and P=81 W	175
9.22	Comparison of the surface temperature between CFD and experiment for P=81 W	176
9.23	Comparison of the backside temperature between CFD and experiment for P=81 W $t = 8s$	176
A.1	Generated turbulent kinetic energy compared with computation	190
A.2	Generated ω compared with computation	190
A.3	Generated v-velocity component compared with computation	193
B.1	Pitot, cone-static and total temperature probes mounted on a assembly inserted through the tunnel floor	195
B.2	Measured Mach profile number in VT SST at Mach 4	196
B.3	Measured u-velocity profile in VT SST at Mach 4	196
B.4	Measured temperature profile in VT SST at Mach 4	197
B.5	Schlieren picture showing the oblique shock and the boundary layer thickness	198
B.6	Shear measurements performed by Orr in VT SST (taken from Orr [52]) . . .	199
B.7	Skin friction coefficient for a numerical simulation on a flat plate for the conditions measured behind the oblique shock compared to Van Driest II correlation	199
B.8	Computed Mach number profiles for the VT SST Mach 4 nozzle	200

B.9	Computed skin friction coefficient on the floor plate of VT SST at Mach 4 for $k - \omega$ and Menter's SST turbulence models. The geometry of the nozzle is also shown	201
B.10	Computed skin friction coefficient on the floor plate of the VT SST with and without the floor-plate shock	201
B.11	Comparison of computed u-velocity profiles with measurements	202
B.12	Linear velocity in laminar sublayer: as expected the flat plate solution has a greater slope	202
C.1	Calibration curves for different filters	206
D.1	Window displacement	209
D.2	Window tangential stress	209
D.3	Window radial stress	210
E.1	Comparison of surface temperature between computation and experiment at $t = 0.5s$ for $P = 65W$	212
E.2	Comparison of surface temperature between computation and experiment at $t = 4s$ for $P = 65W$	213
E.3	Comparison of surface temperature between computation and experiment at $t = 10s$ for $P = 65W$	214
E.4	Comparison of backside temperature between computation and experiment at $t = 1s$ for $P = 65W$	215
E.5	Comparison of backside temperature between computation and experiment at $t = 4s$ for $P = 65W$	216
E.6	Comparison of backside temperature between computation and experiment at $t = 8s$ for $P = 65W$	217
F.1	Comparison of surface temperature between computation and experiment at $t = 0.5s$ for $P = 81W$	219
F.2	Comparison of surface temperature between computation and experiment at $t = 4s$ for $P = 81W$	220
F.3	Comparison of surface temperature between computation and experiment at $t = 10s$ for $P = 81W$	221

F.4	Comparison of backside temperature between computation and experiment at $t = 1s$ for $P = 81W$	222
F.5	Comparison of backside temperature between computation and experiment at $t = 4s$ for $P = 81W$	223
F.6	Comparison of backside temperature between computation and experiment at $t = 8s$ for $P = 81W$	224

List of Tables

3.1	Universal Scaling Laws for Turbulent Boundary Layers	19
4.1	Contribution from $d_1 - d_2 + d_3$ adapted from Catris [9]	40
5.1	Effect of plate thickness and material on heat transfer coefficient	63
6.1	Laser Specifications	77
6.2	Indigo Merlin Infrared Camera Specifications	81
6.3	Infrared Camera NUC	81
6.4	Laser Window Properties	85
6.5	IR-Camera Window Properties	85
6.6	Characteristics of the Virginia Tech Supersonic Wind Tunnel	87
7.1	Power Output	101
7.2	Flow Survey Results	103
7.3	Test Matrix	103
7.4	Results summary for temperature and temperature difference of Surface ($ _s$) and Backside ($ _b$)	128
8.1	Free stream conditions	129
8.2	Number of cells for the discretization error determination	134
8.3	Spatial discretization error	135
8.4	Time discretization error	137
8.5	Effect of turbulence modeling	141

C.1 Infrared Camera Specifications	204
C.2 Computed Infrared Camera Specifications	205

Nomenclature

α	Cebeci and Smith closure coefficient or material thermal diffusivity
α_t	Turbulent thermal diffusivity
β^*	Wilcox $k - \omega$ closure coefficient
δ	Boundary layer thickness
δ^*	Boundary layer displacement thickness
δ_t	Diffusion length
\dot{q}	Heat source
ϵ	Dissipation rate of turbulent kinetic energy
η	Normalized normal wall distance, $\eta = y/\delta$
γ	Specific heat ratio, $\gamma = c_p/c_v$
κ	Von Karman constant
μ	Viscosity
μ_t	Eddy viscosity
ν	Kinematic viscosity, $\nu = \mu/\rho$
ω	Specific dissipation rate of turbulent kinetic energy
ρ	Density
τ	Fictional time
τ_w	Wall shear stress
τ_{xy}	Principal Reynolds shear stress, $\tau_{xy} = \mu_t \frac{\partial u}{\partial y}$

Θ	Transformed temperature
θ	Boundary layer momentum thickness
$\boldsymbol{\omega}$	Vorticity vector
$\boldsymbol{\tau}$	Shear rate tensor
\boldsymbol{F}	Inviscid flux hypervector
\boldsymbol{F}_v	Viscous flux hypervector
\boldsymbol{Q}	Conserved variables hypervector
\boldsymbol{q}	Primitive variables vector or heat flux vector
\boldsymbol{R}	Residual
A	Face area
a	Structural parameter
A^+	Van Driest damping constant
C	Law of the wall constant
C_1	First asymptotic matching constant
C_2	Second asymptotic matching constant
C_f	Skin friction coefficient, $C_f = 2\tau_w/\rho_e U_e^2$
c_p	Specific heat at constant pressure
c_v	Specific heat at constant volume
F_{kleb}	Klebanoff intermittency function
G	Green's function
g	Heat source
h	Characteristic grid size or specific enthalpy
I_0	Maximum intensity
k	Turbulent kinetic energy
k_t	Thermal eddy conductivity

L	Plate thickness
l_{mix}	Mixing length
M	Mach number
P	Laser power
p	Pressure or observed convergence order
Pr	Prandtl number, $Pr = c_p \mu / k_f$
Pr_m	Mixed Prandtl number, $Pr_m = c_p (\mu + \mu_t) / (k_f + k_t)$
Pr_t	Turbulent Prandtl number, $Pr_t = c_p \mu_t / k_t$
q	Heat flux
r	Recovery factor
Re_θ	Reynolds's number based on momentum displacement thickness
s	Specific entropy
S_t	Stanton number, $S_t = q_w / \rho_e U_e c_p (T_w - T_r)$
t	Thermal conductivity
t	Time
T_r	Recovery temperature, $T_r = T_e + r U_e^2 / 2 c_p$
u, v, w	Cartesian velocity components
u^+	Scaled velocity, $u^+ = u / u_\tau$
u_c	Van Driest transformed velocity
u_τ	Friction velocity, $u_\tau = \sqrt{\tau_w / \rho_w}$
V	Cell volume or beam velocity
w	Beam width
y	Normal wall distance
y^+	Turbulent length, $y^+ = y u_\tau / \nu_w$
0	Stagnation or initial value

e	Boundary layer edge value
f	Fluid
s	Solid
w	Wall value

Chapter 1

Introduction

Directed energy weapons have been of interest ever since Antiquity. Archimedes is said to have repelled an attack by Roman forces by focusing sunlight on the approaching ships using an array of parabolic mirrors causing them to catch fire. The veracity of this feat, illustrated in a painting from the Renaissance in Fig. 1, is still debated today and was reproduced in 2005 by a group of MIT students using the technology available at that time. In recent decades, remarkable progress has been made since the first invention of the solid state laser in the 1960's through gas dynamic, chemical, free electron and advanced solid state lasers pushing today's state-of-the-art [32]. The following programs have led to the development of the laser technology [32]:

- Baseline Demonstration Laser (BDL - 1973)
- Navy-ARPA Chemical Laser (NACL - 1978)
- Airborne Laser Laboratory (ALL; 1972 - 1983)
- Mid-Infrared Chemical Laser (MIRACL) program (1980)
- Alpha Space Laser (SBL) program
- Ground based Tactical High Energy Laser (THEL) program

such that today, the use of directed energy as an effective weapon is a reality that is being implemented through programs like the Airborne Laser [5] shown in Fig. 1 used to destroy ballistic missiles in their boost phase close to their launch area.

Directed energy weapons have many advantages as reported by Dunn [36] namely:

- Highly agile speed-of-light delivery



Figure 1.1: Wall painting from the Stanzino delle Matematiche in the Galleria degli Uffizi (Florence, Italy). Painted by Giulio Parigi (1571-1635) in the years 1599-1600. (taken from [30])



Figure 1.2: The Airborne Laser (taken from [5])

-
- Multiple target engagements and rapid retargeting
 - Deep magazines
 - Low incremental cost per shot
 - Lower logistical support requirements

However, many disadvantages are also present among those are:

- Atmospheric attenuation and turbulence
- Target suitability

As the beam travels through the atmosphere, it gets distorted by the density fluctuations and scattered by particulate matter. This means that the intensity profile reaching the target differs from the one leaving the laser. Typically, the beam area is increased and the maximum intensity is decreased such that the effectiveness of the weapon goes down. Adaptive optics is an active area of research for which the intensity profile is originally deformed to compensate for the effect of the atmosphere and get a minimally distorted intensity profile on the target.

Contrary to conventional weapons such as explosives which inflict damage through massive heat release and pressure waves, directed energy weapons must rely on the absorption of thermal energy at the target surface. The kill mechanism is therefore fundamentally different. For missiles, Leonard [42] has identified two kill mechanisms namely the sublimation of the target skin and structural failure from the weakening of the skin through heating. The flux of energy required to destroy a North Korean Taepo Dong 2 missile with a 3 *mm* thick steel skin is estimated using a simple energetic analysis. For the structural failure, a fluence of $2.4kJ/cm^2$ is obtained which is an order of magnitude lower than the fluence of $22kJ/cm^2$ required to sublime the skin. In his analysis, Leonard assumes that 10% of the radiation is absorbed by the target. For a structural failure to occur within 4 seconds, an average surface heat flux of $600W/cm^2$ must be applied. The analysis performed by Leonard is simplified but nevertheless useful in getting an estimate of the required heat flux and time scales involved in the destruction of a ballistic missile. The heat flux considered is much too low to get a laser supported detonation (LSD) wave at the surface and/or the formation of a plasma which is known to shield the target from the incoming beam.

With the advent of the Airborne Laser and other directed energy programs, the development of high-energy laser lethality testing capability for supersonic and hypersonic targets becomes essential. The Arnold Engineering Development Center (AEDC) has recently shown the desire to develop such a capability and has identified the following challenges in implementing a high energy laser ground test facility [22]:

- Integrating the laser with an appropriate test facility

-
- Shielding test facility operators, equipment, and structures from harmful levels of laser radiation
 - Development and validation of modeling and simulation tools

This research is concerned with the development and validation of modeling and simulation of the beam-target interaction. To our knowledge and that of AEDC, no experimental study of the lethality mechanism has ever been performed. Moreover, the temperature measurements of a laser heated target subjected to a supersonic flow has never been performed. The problem at hand can be defined in the following way:

For a given target geometry, surface radiation intensity and free stream flow condition, what is the target temperature distribution as a function of time?

The main objective of the present research is to develop a computational model and obtain experimental data through small scale testing in order to validate our computation model. The analysis tool can then be used by AEDC to design large scale experiments. A validation approach based on an increase in the problem complexity is used throughout the development process.

This document is organized in the following way. First, the heat conduction inside the solid is investigated in Chapter 2. An analytical solution is obtained and dimensional analysis is used to understand the parameters influencing the temperature distribution inside a laser irradiated target. Then, the numerical model used for solving the heat equation is presented.

In Chapter 3, the semi-empirical theory of turbulent compressible boundary layers and of convective heat transfer is presented. Chapter 4 introduces the equations of motion and the numerical methods used to compute turbulent convective heat transfer with complex wall temperature variations. Our numerical model is validated for low speed flow and supersonic flow by comparing the numerical results with experimental results from the literature. Chapter 5 focuses on conjugate heat transfer. The matching condition between the fluid and the solid is made nondimensional introducing the conjugate Peclet number. This nondimensional number determines the energy balance at the interface. The algorithm used to couple the heat conduction and flow solver is described and validated. Chapter 6 presents the experimental setup used to investigate the effect of supersonic flow over a laser heated target. All the key components are described and a rigorous uncertainty analysis is performed. Chapter 7 presents the experimental results. In Chapter 8, the numerical model used to replicate the experiment is presented and the effect of the heated wall on the flow field discussed. Lastly, a comparison between the numerical and experimental results is performed in Chapter 9.

Chapter 2

Conduction Heat Transfer

The prediction of the temperature field inside a laser heated target requires solving the solid heat conduction equation. First, an analytic solution to the problem is developed using Green's function method. The obtained solution isn't as general as wished and doesn't easily allow addition of convection cooling, but it is nevertheless very useful in assessing the key parameters affecting the temperature distribution inside the target. To overcome these limitations the heat conduction equation has to be solved numerically. The numerical methods used to solve the equation are therefore presented.

2.1 Analytical Solutions to the Heat Equation

The temperature distribution inside the solid is obtained by solving the heat conduction equation for an orthotropic solid which is written as [8]:

$$\rho c \frac{\partial T}{\partial t} = \nabla \cdot (K \nabla T) + g \quad (2.1)$$

Generally speaking, this equation is a non-linear partial differential equation. Nonlinearities arise from the temperature dependence of the material properties (c , K and ρ). Assuming that the material properties are constant, we can rewrite Eq. 2.1 as a linear partial differential equation:

$$\frac{\partial T}{\partial t} = \alpha \nabla^2 T + \frac{g}{K} \quad (2.2)$$

The assumption of constant material properties will later be relaxed using the Kirchhoff transformation. For a laser heated target, two equivalent formulations can be used. The first one interprets the heating phenomena directly and considers the laser as an external heat flux $q(\mathbf{r}, t)$ impinging perpendicularly on the material surface. In the second approach, it is assumed that the heat is accumulated at the surface and liberated as a heat source

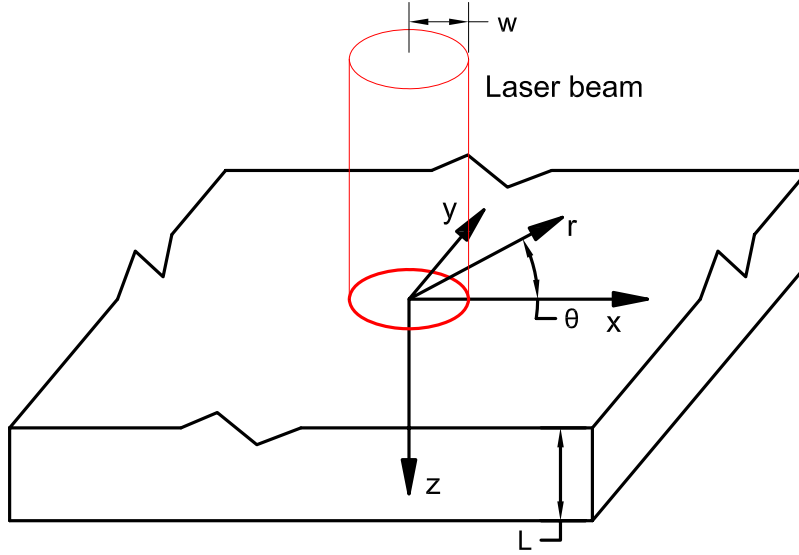


Figure 2.1: Geometry for the analytical solution to the heat equation for a laser heated target

$g(\mathbf{r}, t)$. Conde et al. [17] have demonstrated that the two approaches are mathematically equivalent when all the energy is absorbed at the surface. However, the second approach is more general as the penetration of radiation inside the target can be considered. It is therefore used here. The problem is formulated as:

$$\frac{\partial T(\mathbf{r}, t)}{\partial t} + \frac{g(\mathbf{r}, t)}{K} = \alpha \nabla^2 T(\mathbf{r}, t) \quad (2.3)$$

$$-\infty < x < \infty, \quad -\infty < y < \infty, \quad 0 \leq z \leq L, \quad t > 0$$

$$\frac{\partial T(\mathbf{r}, t)}{\partial x} \Big|_{x=0} = 0,$$

$$\frac{\partial T(\mathbf{r}, t)}{\partial y} \Big|_{y=0} = 0,$$

$$\frac{\partial T(\mathbf{r}, t)}{\partial z} \Big|_{z=0} = 0, \quad t > 0$$

$$T(\mathbf{r}, t) = 0, \quad t = 0; \quad (2.4)$$

Here, we have assumed that the target is a slab of thickness L , that the initial temperature is uniform and equal to zero such that the solution corresponds to the temperature increase due to the heat source. We neglect the effect of the edges since x and y are both unbounded. This approximation is valid if the temperature at the edges doesn't change. This will be the case if the beam diameter is small compared to the size of the target or if the irradiation time is sufficiently short. The problem geometry is depicted in Fig. 2.1

2.1. ANALYTICAL SOLUTIONS TO THE HEAT EQUATION

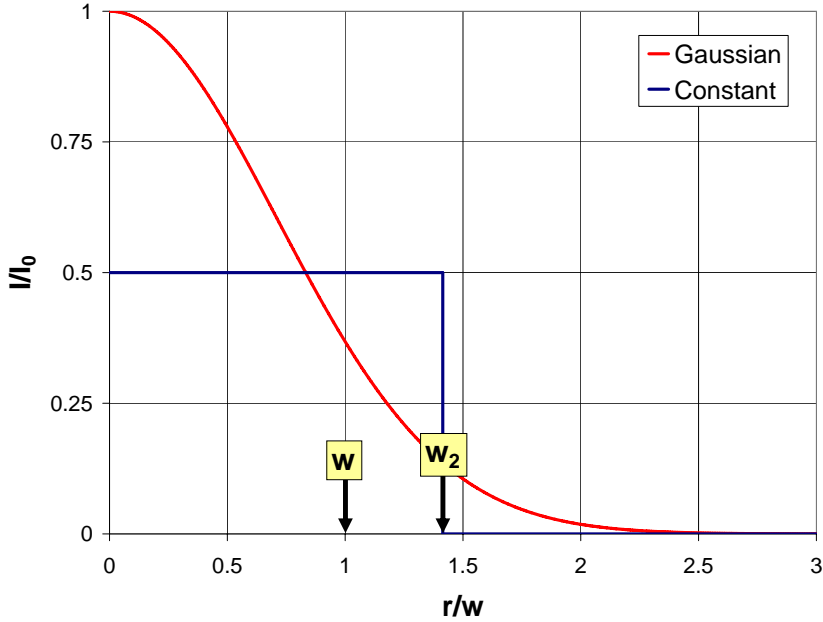


Figure 2.2: Dimensionless intensity profile for a Gaussian and a constant intensity beam

In order to solve the problem, the heat source must be specified. The general form for an instantaneous source applied at $t = 0$ expressed in cylindrical coordinates is [7]:

$$g(r, \theta, z) = I_0 f(r, \theta) \exp(-z/Z) \quad (2.5)$$

The z -exponential represents the decay of the source within the material thickness. For a laser delivering a Gaussian intensity profile and when the penetration depth Z is much smaller than the target thickness L , ($Z \ll L$), we can assume that the source is strictly located on the surface leading to:

$$g(r) = I_0 \exp(-r^2/w^2) = \frac{P}{\pi w^2} \exp(-r^2/w^2) \quad (2.6)$$

Here, w is the radius where the $g(r)$ decreases by a factor e^{-1} . A dimensionless plot of a Gaussian intensity distribution is shown in Fig. 2.1 and compared to a constant intensity profile with the same total power. Most laser manufacturers specify the value of w_2 as the beam waist which corresponds to the radius where the maximum intensity I_0 decreases by a factor e^{-2} . As seen in Fig. 2.1, a beam of constant intensity delivering the same power and having the same waist w_2 will have an intensity equal to half the maximum intensity of a gaussian beam. When computing the temperature distribution, assuming a Gaussian beam is not only closer to physical reality but also leads to a mathematical expression which is simpler and easier to evaluate numerically.

The temperature distribution is found using Green's function method [8]. The Green's function $G(x, y, z, t | x', y', z', t')$ is our building block and it can be seen as the impulsive

2.1. ANALYTICAL SOLUTIONS TO THE HEAT EQUATION

response of the system. It represents the temperature distribution $T(x, y, z, t)$ in an unbounded medium resulting from an instantaneous heat source of unit strength located at $\mathbf{r}' = (x', y', z')$ applied at time t' . In cartesian coordinates, it is given by [8]:

$$G(x, y, z, t | x', y', z', t') = \frac{1}{8(\pi\alpha(t-t'))^{\frac{3}{2}}} \exp \left[-\frac{(x-x')^2 + (y-y')^2 + (z-z')^2}{4\alpha(t-t')} \right] \quad (2.7)$$

or using cylindrical coordinates:

$$G(r, \theta, z, t | r', \theta', z', t') = \frac{1}{8(\pi\alpha(t-t'))^{\frac{3}{2}}} \exp \left[\frac{r^2 + r'^2 - 2rr' \cos(\theta - \theta') + (z-z')^2}{4\alpha(t-t')} \right] \quad (2.8)$$

The temperature distribution due to the instantaneous source is obtained by convolving $g(r)$ with $G(r, \theta, z, t | r', \theta', z', t')$. The temperature distribution for a continuous source is obtained by the superposition of instantaneous sources from $t' = 0$ to $t' = t$ which leads to:

$$T(r, z, t) = \int_{t'=0}^t \int_0^\infty \int_0^{2\pi} G(r, \theta, z, t | r', \theta', 0, t') \frac{g(r')}{\rho c} r' d\theta' dr' dt' \quad (2.9)$$

Performing the integration and using the following change of variables to simplify the final expression:

$$\beta = \sqrt{4\alpha(t-t')} \quad (2.10)$$

we get:

$$T(r, z, t) = \int_0^{\delta_t} \frac{P}{K\pi^{3/2}} \exp \left(\frac{-r^2}{\bar{w}^2 + \beta^2} \right) \exp \left(\frac{-z^2}{\beta^2} \right) \frac{1}{\bar{w}^2 + \beta^2} d\beta \quad (2.11)$$

where:

$$\delta_t = 2\sqrt{\alpha t} \quad (2.12)$$

is called the diffusion length and represents the heat penetration depth. This solution doesn't satisfy the insulated boundary condition at $z = L$. It is nevertheless valid when $\delta_t < L$ such that the temperature at $z = L$ has not start changing.

2.1.1 Method of images

The adiabatic wall boundary condition at $z = L$ can be enforced by using the method of images [7]. The temperature distribution within the slab of thickness L is obtained by computing the solution for an unbounded medium with source or sinks. For each source located at a point z' , the image points are located at

$$z'_n = 2nL \pm z' \quad \text{for } n = 0, \pm 1, \pm 2, \dots \quad (2.13)$$

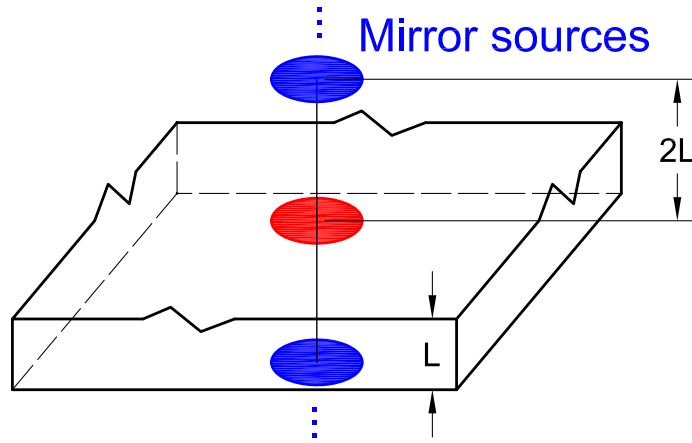


Figure 2.3: Image sources used to get a slab of finite thickness L

For an insulated boundary, all image points are sources, whereas for a boundary maintained at $T = 0$ both sources and sink are used. It follows that the exponential in z in Eq. 2.11 is replaced by:

$$\sum_{n=-\infty}^{\infty} \sigma_n \exp\left(-\frac{(z - 2nL \pm z')^2}{4\alpha t}\right) \quad (2.14)$$

where $\sigma_n = 1$ when both sides are insulated and $\sigma_n = (-1)^n$ for an insulated slab at $z = 0$ and at $T = 0$ at $z = L$. The \pm sign in the exponent implies that the sum of the terms is taken once with a + sign and once with a - sign. One can easily notice that when $L \Rightarrow \infty$, only the $n = 0$ term remains such that we get a consistent result with the semi-infinite case.

For a surface source $z' = 0$ and both sides insulated we get:

$$\sum_{n=-\infty}^{\infty} \exp\left(-\frac{(z - 2nL)^2}{4\alpha t}\right) \quad (2.15)$$

The image sources used to get a slab of thickness L are represented in Fig. 2.1.1. Replacing the z -exponential in Eq. 2.11 with Eq. 2.15, we get the temperature distribution for a slab of thickness L :

$$T(r, z, t) = \int_0^{\delta t} \frac{P}{K\pi^{3/2}} \exp\left(\frac{-r^2}{w^2 + \beta^2}\right) \sum_{n=-\infty}^{\infty} \exp\left(-\frac{(z - 2nL)^2}{\beta^2}\right) \frac{1}{w^2 + \beta^2} d\beta \quad (2.16)$$

The effect of insulated edges can also be taken into account using the method of images. The arrangement of image sources in the x - y plane resulting in a square cuboid of lengths $2a$ and thickness L are shown in Fig. 2.1.1. The temperature is obtained by the superposition of solutions for a single beam (Eq. 2.16). Let $T(x, y, z, t; x_c, y_c)$ be the temperature for a single

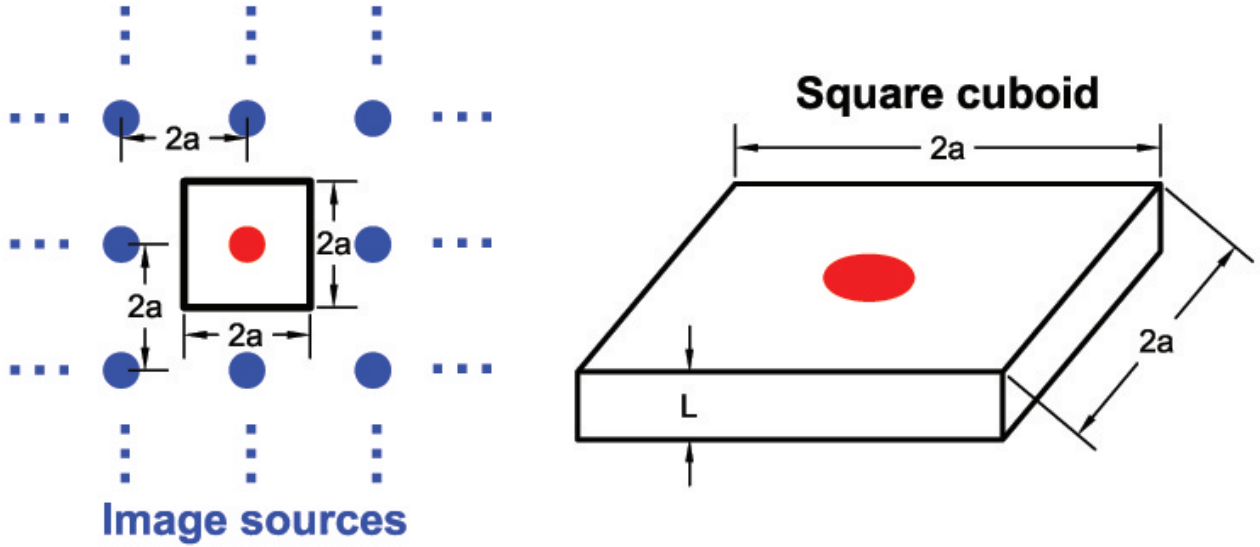


Figure 2.4: Arrangement of image sources and resulting geometry for a cuboid of lengths $2a$ and thickness L

beam centered at (x_c, y_c) which is obtained by substituting r^2 with $(x - x_c)^2 + (y - y_c)^2$ in Eq. 2.16. The temperature distribution in the cuboid is then:

$$T_{\text{cub}}(x, y, z, t) = \sum_{m,n=-\infty}^{\infty} T(x, y, z, t; 2na, 2ma) \quad (2.17)$$

and satisfies the insulated boundary condition on the edges.

2.1.2 Kirchhoff Transformation

The nonlinearities in the material properties can be addressed using the following change of variables:

$$\Theta = \frac{1}{K_0} \int_{T_0}^T K(T') dT' \quad (2.18)$$

which is called Kirchhoff Transformation. Substituting Eq. 2.18 into the heat equation 2.1 leads to:

$$\frac{\partial \Theta}{\partial T} = \alpha(T) \nabla^2 \Theta + \frac{g}{K_0} \quad (2.19)$$

This equation is still non-linear as generally α is a function of temperature. Assuming a constant thermal diffusivity is therefore the strong assumption of the method. For some

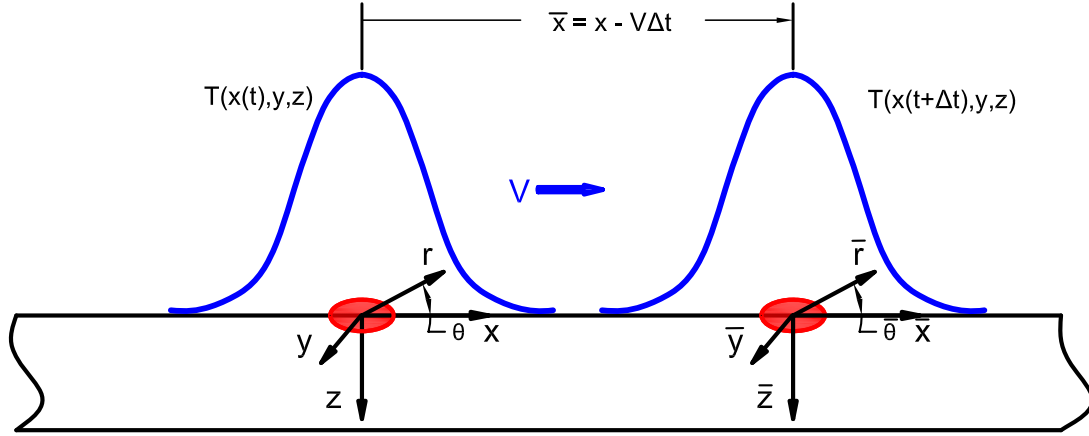


Figure 2.5: Coordinate transformation for a sliding beam with a constant velocity

materials such as Germanium this assumption is valid. Kirchhoff transformation was used by Conde et al. [17] to accurately compute the temperature distribution in a thick film of germanium induced by an excimer laser. For most metals, α is a function of temperature and can't be assumed constant. However, if one is interested in the steady state solution, the time derivative in Eq. 2.19 is equal to zero such that thermal diffusivity doesn't intervene. This means that the steady state temperature can be accurately computed using Kirchhoff transformation even when the thermal diffusivity is temperature dependant.

2.1.3 Moving Laser Beam

For the previous solution, the heat source g was assumed fixed. It is agreed that Cline and Anthony [15] were the first to model the temperature distribution for a moving beam. They have developed a steady state solution for a beam moving in the x direction with a constant scanning velocity V . The solution is obtained by using the following coordinate transformation:

$$\bar{x} = x - Vt \quad (2.20)$$

which describes a the temperature distribution in a reference frame moving with the beam. This leads to a steady state temperature distribution that moves with the beam such at that the cooling rate can be expressed as:

$$\frac{\partial T}{\partial t} = -V \frac{\partial T}{\partial x} \quad (2.21)$$

As seen in Fig. 2.5

2.1. ANALYTICAL SOLUTIONS TO THE HEAT EQUATION

Here, a more general approach is used as no steady state is assumed and the trajectory of the beam is arbitrary but known as a function of time see Fig. 2.6. We have:

$$\bar{x} = x - x_c(t) \quad (2.22)$$

$$\bar{y} = y - y_c(t) \quad (2.23)$$

where the x and y-velocity components of the beam are:

$$u_c(t) = \frac{dx_c}{dt} \quad (2.24)$$

$$v_c(t) = \frac{dy_c}{dt} \quad (2.25)$$

Temperature distribution in a slab of thickness L due to a moving Gaussian beam is obtained by substituting Eqs 2.22 and 2.23 into Eq. 2.16 using Eq. 2.10

$$T(x - x_c(t), y - y_c(t), z, t) = \quad (2.26)$$

$$\int_0^{\delta t} \frac{P}{K\pi^{3/2}} \exp \left[\frac{-\left(x - x_c\left(t - \frac{\beta^2}{4\alpha}\right)\right)^2 - \left(y - y_c\left(t - \frac{\beta^2}{4\alpha}\right)\right)^2}{w^2 + \beta^2} \right]$$

$$\sum_{n=-\infty}^{\infty} \exp \left(-\frac{(z - 2nL)^2}{\beta^2} \right) \frac{1}{w^2 + \beta^2} d\beta$$

Our approach is very general and can be used to compute the temperature distribution in a target irradiated by an oscillating beam. We can imagine that situation arising in an anti-missile system when the laser can't perfectly stay still on the target. The solution can also be used to compute the temperature distribution in a rotating missile if curvature effects are neglected.

2.1.4 Dimensional Analysis

Introducing the following non-dimensional variables:

$$r^* \equiv \frac{r}{w}, \quad z^* \equiv \frac{z}{w}, \quad t^* \equiv \frac{t\alpha}{w^2}, \quad L^* \equiv \frac{L}{w}, \quad P^* \equiv \frac{P}{Kw} \quad (2.27)$$

The temperature can be written as:

$$T(r^*, z^*, t^*; L^*, P^*) = \left[\frac{P^*}{2\pi^{1/2}} \right] [\eta(r^*, z^*, t^*; L^*)] \quad (2.28)$$

where η , the normalized temperature, is defined as:

$$\eta(r^*, z^*, t^*; L^*) = \frac{2}{\pi} \int_0^{2\sqrt{t^*}} \exp \left(\frac{-r^{*2}}{1 + \beta^2} \right) \sum_{n=-\infty}^{\infty} \exp \left(-\frac{(z^* - 2nL^*)^2}{\beta^2} \right) \frac{1}{1 + \beta^2} d\beta \quad (2.29)$$

2.1. ANALYTICAL SOLUTIONS TO THE HEAT EQUATION

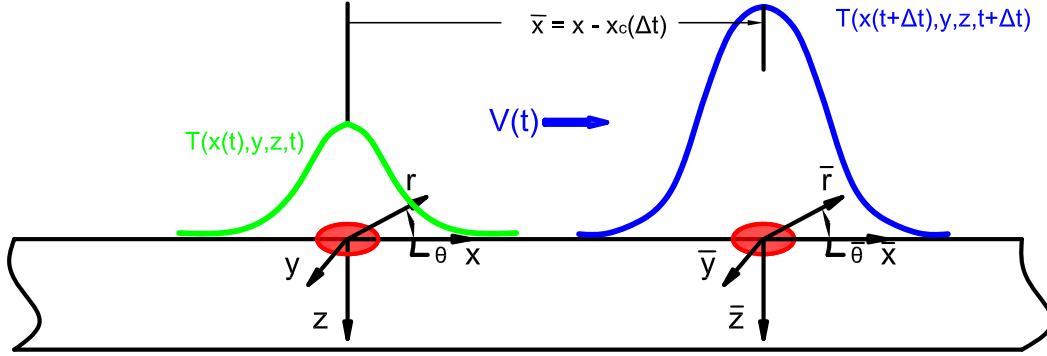


Figure 2.6: Coordinate transformation for a beam moving with an arbitrary velocity

For a semi-infinite geometry, the steady state value of the normalized temperature reaches unity at the center on the surface, i.e. $\eta(0, 0, \infty, \infty) = 1$. Eq. 2.29 can be integrated once for all for different values of the non-dimensional variables and be subsequently used to get the temperature for a specific material or geometry. Looking at the non-dimensional variables, it is seen that all the dimensions scale with the beam width and that the time scales with the beam width and the material thermal diffusivity. Moreover, the temperature increase is proportional to the ratio of the absorbed power to the thermal conductivity. For the same absorbed power, a slab of aluminum will heat about 9 times less than one made of stainless steel.

Fig. 2.7 shows the temperature distribution inside a semi-infinite body at different values of t^* for a beam applied at the origin. For a beam of 4 mm in diameter, (such that $w = 2/\sqrt{2}$), $t^* = 25$ corresponds roughly to $t = 0.7$ s for aluminum and $t = 11$ s for stainless steel. A slab of aluminum will, therefore, reach a steady state temperature about 16 times faster compared to one made out of stainless steel. The following observations can be made from Eq. 2.29 and Fig. 2.7:

- 0.94% of the steady state temperature increase is achieved after $t^* = 25$
- The temperature distribution is not one-dimensional (as seen from the curved isotherm)
- Close to the beam center, (r^* and $z^* < 1$) the radial diffusion is greater than the axial diffusion (z-direction), whereas farther away, both are equivalent.
- The temperature doesn't significantly change at a distance greater than about $5w$, (r^* and $z^* > 5$)

Next, the effect of thickness is investigated. Fig. 2.8 presents results of the normalized

2.1. ANALYTICAL SOLUTIONS TO THE HEAT EQUATION

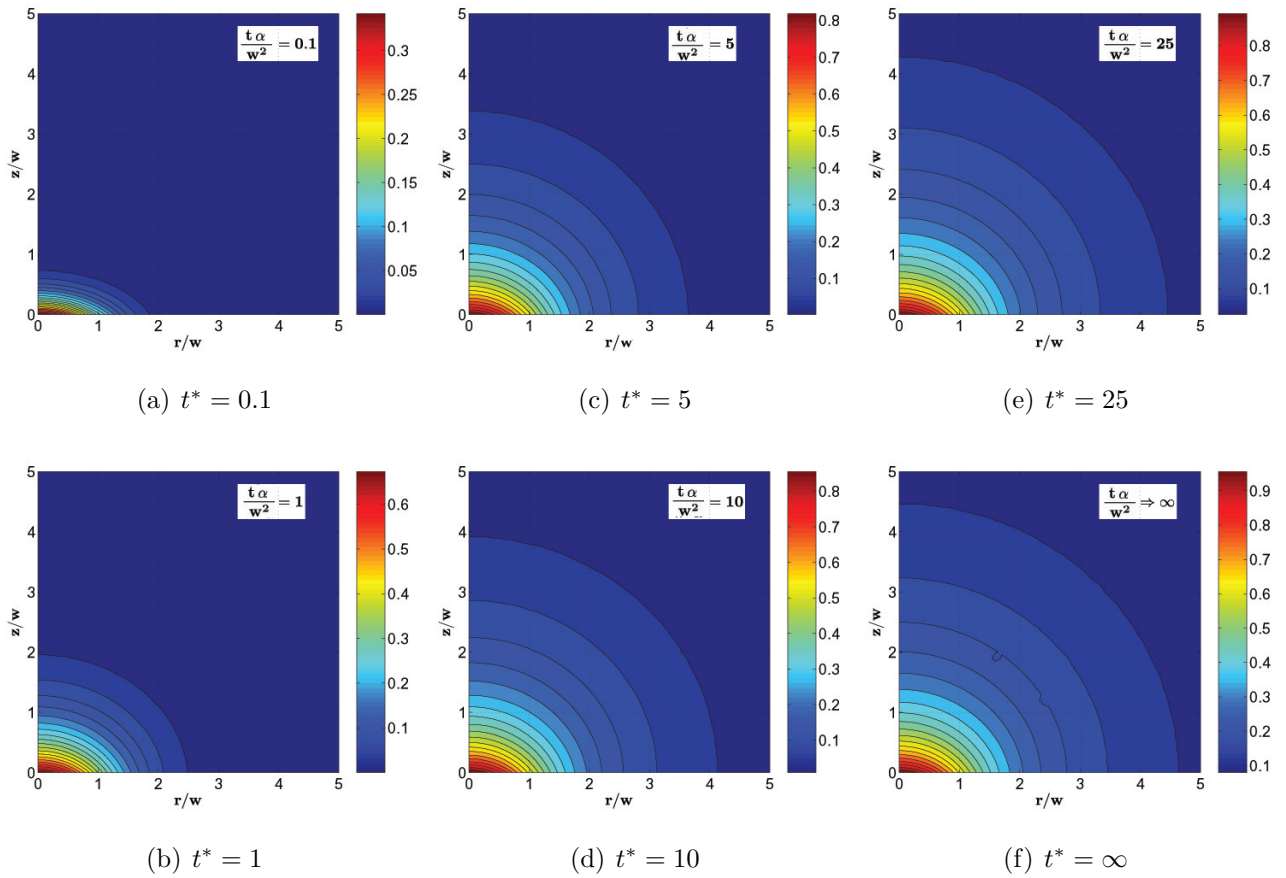


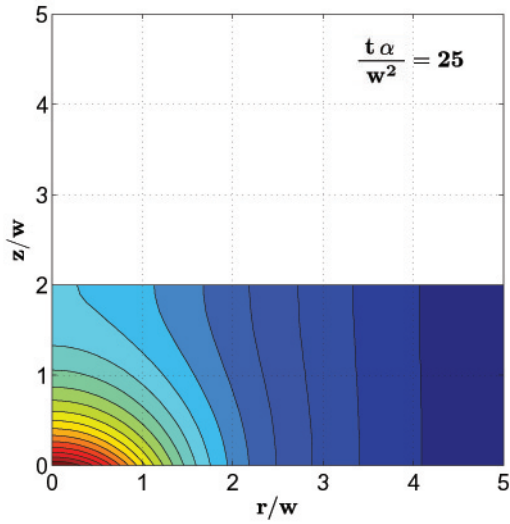
Figure 2.7: Normalized temperature for a semi-infinite geometry

temperature at $t^* = 25$ for different values of L^* . The following observation can be made from Fig. 2.8:

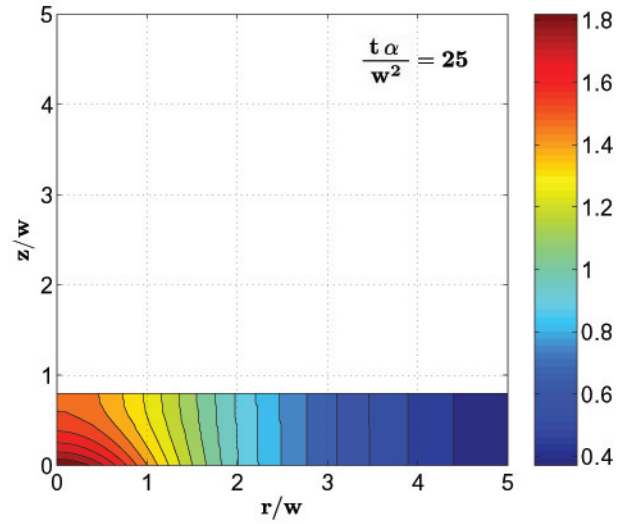
- The surface temperature increases when L^* decreases
- As L^* decreases, the temperature distribution tends towards being one-dimensional for $r > w$
- As L^* decreases, radial diffusion increases and the change in temperature becomes significant for $r^* > 5w$

The effect of L^* on the maximum surface temperature, (at $r=z=0$) is seen in Fig. 2.1.4:

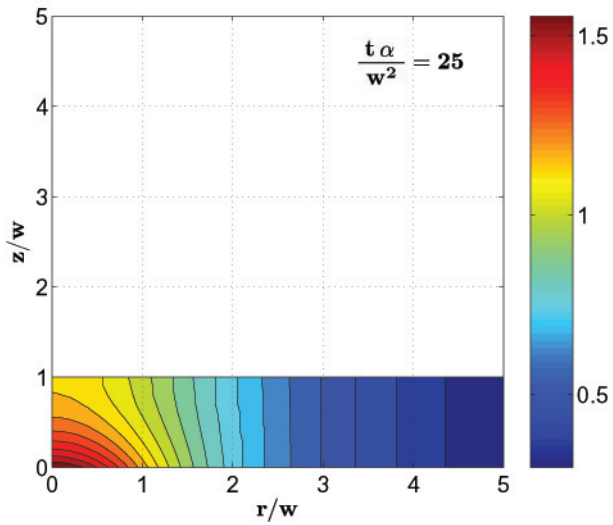
2.1. ANALYTICAL SOLUTIONS TO THE HEAT EQUATION



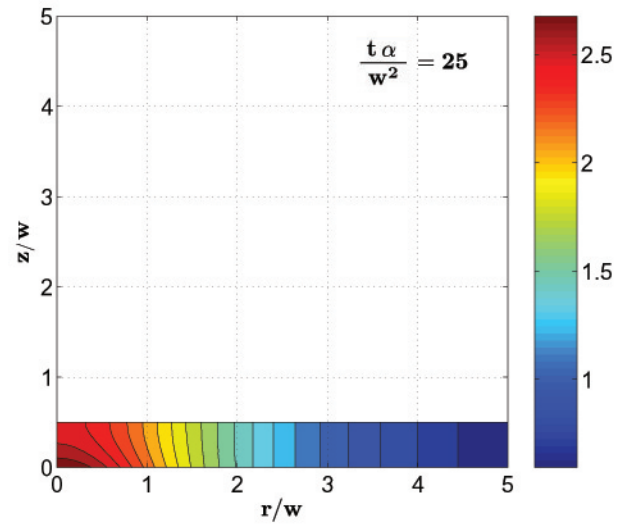
(a) $L^* = 2$



(c) $L^* = 0.8$



(b) $L^* = 1$



(d) $L^* = 0.5$

Figure 2.8: Effect of L^* on the normalized temperature at $t^* = 25$

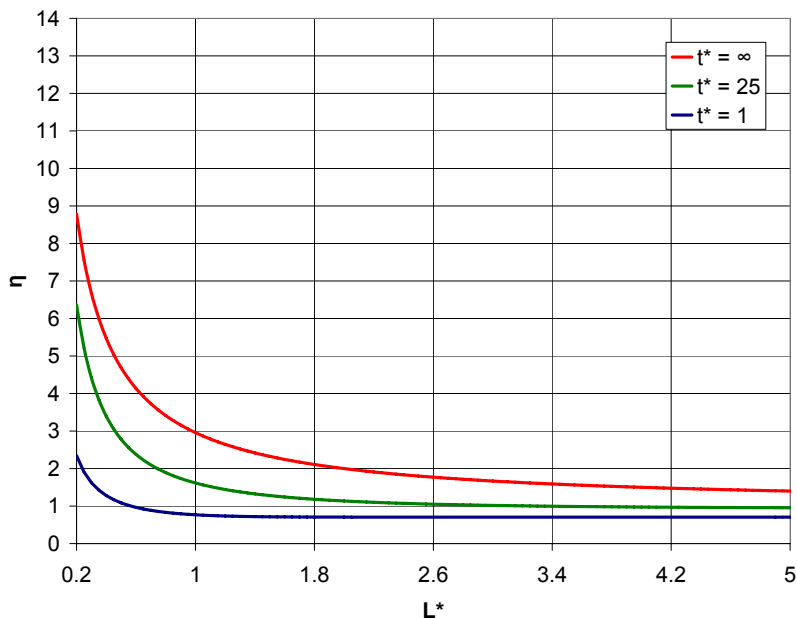


Figure 2.9: Effect of the target thickness on the maximum surface temperature

2.2 Numerical Solutions to the Heat Equation

The analytical solution previously developed is useful as it gives general results which helps to understand the influence of each parameter on the temperature distribution. However, it is limited to simple geometries and doesn't easily allow the introduction of a convective boundary condition and radiation losses at the surface. A numerical approach is, therefore, used. The numerical algorithm also makes it possible to relax the constant thermal diffusivity assumption. Variable thermal conductivity, density and specific heat can be used as long as their variations with temperature are known.

Here, an orthotropic material is assumed meaning that the material properties are the same in all directions. This assumption is valid for metals. The temperature distribution in the solid is obtained by solving Eq. 2.1. The equation is integrated over the computational domain and the Divergence Theorem is used to introduce the heat flux across the boundary leading to:

$$\rho c_v \frac{\partial}{\partial t} \iiint T dV = \oint_A (k(\nabla T \cdot \hat{\mathbf{n}}) dA + \iiint g dV \quad (2.30)$$

which lends itself to the finite volume implementation. In the finite volume solver, the temperature is cell volume averaged. This can be expressed as,

$$\bar{T} = \frac{1}{V} \iiint T dV \quad (2.31)$$

2.2. NUMERICAL SOLUTIONS TO THE HEAT EQUATION

where the bar over T indicates a volume average. The diffusive term (heat flux) is computed in the same fashion as the viscous terms in the Navier-Stokes solver. This yields a second order accurate central difference formulation for the diffusive flux. More details on the finite volume method are given in Section 4.3 where the fluid solver is discussed.

Chapter 3

Boundary Layers and Convective Heat Transfer

This chapter presents a review of the turbulent boundary layer theory for compressible flow. This theory is useful, since it can be used to identify the parameters affecting the film coefficient on a flat plate subjected to turbulent supersonic flow. The film coefficient as a function of distance is computed for a flat plate located inside the Virginia Tech supersonic wind tunnel. An analytical method used to compute the film coefficient on a wall with an arbitrary temperature distribution will be given. Finally, the transition problem in supersonic flow will be briefly discussed. Relevant experimental results enabling the estimation of the transition location inside the Virginia Tech supersonic wind tunnel result will be presented.

3.1 Turbulent Boundary Layers

Turbulent flows are characterized by time and length scales. By making the flow variables non-dimensional using the appropriate length and time scales it is possible to find universal laws collapsing the experimental data [60].

It is convenient to introduce the friction velocity:

$$u_\tau = \sqrt{\frac{\tau_w}{\rho_w}} \quad (3.1)$$

which can be used to make the u-velocity non-dimensional:

$$u^+ = \frac{u}{u_\tau} \quad (3.2)$$

Similarly, a non dimensional wall distance can be expressed as

$$y^+ = \frac{yu_\tau}{\nu} \quad (3.3)$$

3.1. TURBULENT BOUNDARY LAYERS

Table 3.1: Universal Scaling Laws for Turbulent Boundary Layers

Region	Law	Location	Velocity	Length	Comments
Laminar sublayer	Linear	$0 < y^+ < 5$	u^+	y^+	$\tau = \tau_w$ $\tau_t \approx 0$
Buffer layer		$5 < y^+ < 30$	u^+	y^+	$\tau = \tau_w$ $\tau_t \nearrow$
Log	Log	$30 < y^+ < 300$	u^+ $(u - u_e)/u_\tau$	y^+ y/δ	$\tau = \tau_w$ $\tau_l \ll \tau_t$
Outer	Defect	$y^+ > 300$	$(u - u_e)/u_\tau$	y/δ	80 to 90% of total thickness

The turbulent length, y^+ , can be seen as a Reynolds number based on the wall distance and friction velocity. The thermal field is characterized by the friction temperature which is defined as:

$$T_\tau = \frac{q_w}{\rho_w C_p u_\tau} \quad (3.4)$$

The time and length scales are not constant throughout the flow, but vary according to the region. Therefore, the turbulent boundary layer is divided in four distinct regions listed in Table 3.1.

In the laminar sublayer, the mechanism for momentum diffusion is entirely viscous. This sublayer is so thin that the total shear is constant and, therefore, equal to the wall shear $\tau = \tau_w$. Using those assumptions the momentum equation can be integrated to give a linear relation between velocity and wall distance:

$$u^+ = y^+ \quad (3.5)$$

In the buffer layer, the momentum diffusion by turbulent eddies progressively increases with distance from the wall. This effect which is due to wall damping of eddies was modelled by Van Driest [60] using the solution for an oscillating plate and was included in the logarithmic Law of the Wall. The log region extends all the way to the outer region where the velocity defect $(u - u_e)/u_\tau$ can be used to correlate the experimental data. Therefore, in the log region, the velocity scales to either u_τ or $u - u_e$ and either y^+ or y/δ can be used as a non-dimensional length. The satisfaction of both the length and velocity scales leads to the well-known logarithmic Law of the Wall.

An explicit expression for the law-of-the-wall in the inner region and law-of-the-wake in the outer region is proposed by Musker [49]:

$$u^+ = 5.424 \tan^{-1} \left[\frac{2y^+ - 8.15}{16.7} \right] + \log_{10} \left[\frac{(y^+ + 10.6)^{9.6}}{(y^{+2} - 8.15y^+ + 86)^2} \right] - 3.52 + 2.44 \left\{ \Pi \left[6 \left(\frac{y}{\delta} \right)^2 - 4 \left(\frac{y}{\delta} \right)^3 \right] + \left(\frac{y}{\delta} \right)^2 \left(1 - \frac{y}{\delta} \right) \right\} \quad (3.6)$$

3.1. TURBULENT BOUNDARY LAYERS

where Π is the Wake parameter [10] defined as:

$$\Pi = 0.55 \left[1 - \exp \left(-0.24\sqrt{Re_\theta} - 0.298Re_\theta \right) \right] \quad (3.7)$$

This expression is useful in generating velocity profiles and was used in the algorithm presented in Appendix A to generate the missing information at the inflow boundary in computational fluid dynamics CFD computations.

All the previous results apply to incompressible boundary layers and need to be extended to the compressible case. Experimental results and analysis have shown that the compressible boundary layer follows the Law of the Wall and the Law of the Wake when the velocity is transformed according to:

$$u_c = \int \left(\frac{\rho}{\rho_w} \right)^{\frac{1}{2}} du = \int \left(\frac{T_w}{T} \right)^{\frac{1}{2}} du \quad (3.8)$$

Starting from the momentum and the energy equation for a two-dimensional boundary layer without a pressure gradient, a relation between the temperature and the velocity field can be obtained by acknowledging that the convective terms are negligible close to the wall. This simplification makes it possible to integrate the momentum equation which now states that the total stress is constant across the boundary layer:

$$(\mu + \mu_t) \frac{\partial u}{\partial y} = \tau_w \quad (3.9)$$

This result can be substituted into the energy equation which is integrated twice, yielding Crocco's integral:

$$T = T_w - \frac{Pr_m q_w u}{c_p \tau_w} - \frac{Pr_m u^2}{2c_p} \quad (3.10)$$

where the mixed Prandtl number, Pr_m , defined as:

$$Pr_m = c_p \frac{\mu + \mu_t}{k_f + k_t} \quad (3.11)$$

is assumed constant to perform the integration. In practice for a wall-bounded turbulent flow of air $Pr_m \approx Pr_t \approx r \approx 0.9$, where r is the recovery factor. For that case, Eq. 3.10 can be written as:

$$\frac{T}{T_e} = \frac{T_w}{T_e} + \frac{T_r - T_w}{T_e} \left(\frac{u}{u_e} \right) - r \frac{\gamma - 1}{2} M_e^2 \left(\frac{u}{u_e} \right)^2 \quad (3.12)$$

The temperature profile is directly obtained from the velocity profile using Eq. 3.10 or 3.12.

Using Eq. 3.12, Eq. 3.8 can be analytically integrated to obtain the Van Driest transformation

$$u_c = \sqrt{B} \left[\sin^{-1} \left(\frac{A + u}{D} \right) - \sin^{-1} \left(\frac{A}{D} \right) \right] \quad (3.13)$$

3.2. FILM COEFFICIENTS

where

$$A = \frac{q_w}{\tau_w} \quad (3.14)$$

$$B = \frac{2c_p T_w}{Pr_t} \quad (3.15)$$

$$D = \sqrt{A^2 + B} \quad (3.16)$$

The inverse transformation is given by

$$\frac{u}{u_\tau} = \frac{1}{R} \sin\left(\frac{Ru_c}{u_\tau}\right) - H \left[1 - \cos\left(\frac{Ru_c}{u_\tau}\right)\right] \quad (3.17)$$

where

$$R = \frac{u_\tau}{\sqrt{B}} \quad (3.18)$$

$$H = \frac{A}{u_\tau} \quad (3.19)$$

This result is important as it makes it possible to compute the boundary layer profile for a compressible boundary from an incompressible velocity distribution (Eq. 3.6). The result is applicable to non-adiabatic walls since the heat flux at the wall is included in the formulation of Eq. 3.13

3.2 Film Coefficients

For high free-stream velocity, the effect of compressibility must be considered when evaluating the film coefficient. Even if no heat transfer takes place (adiabatic wall), the wall temperature may be considerably greater than the free stream temperature. This is due two distinct causes:

1. The increase in temperature resulting from the conversion of kinetic energy into internal thermal energy when the flow slows down
2. The heating effect due to viscous dissipation

Moreover, this variation in the temperature introduces a local change in the fluid properties. For high-velocity boundary layers, the film coefficient, h , must be defined on the basis of the difference between the surface temperature and the recovery temperature. Therefore, for high-velocity boundary layers, the wall heat transfer is given by:

$$q_w = -K \left(\frac{\partial T}{\partial y}\right)_w \equiv h(T_w - T_r) \quad (3.20)$$

3.2. FILM COEFFICIENTS

The dimensionless form of the heat transfer coefficient is known as the Stanton number which is defined as:

$$St \equiv \frac{h}{\rho u_e C_p} \quad (3.21)$$

Many correlations for computing the skin friction of low speed boundary layer have been developed over the years. A simple expression known to be valid for Reynolds number up to 10^9 was proposed Schultz-Grunow [55]:

$$\frac{c_f}{2} = 1.60 (\ln Re_x)^{-2.58} \quad (3.22)$$

This correlation can be used to compute the Stanton number by using the similarity between the momentum and heat diffusion. Reynolds analogy was first derived for $Pr = 1$. For that case, the momentum and energy equation have a similar form which leads to

$$St = \frac{C_f}{2} \quad (3.23)$$

And expression for an arbitrary Prandtl number was derived by von Karman [55]:

$$St = \frac{\frac{C_f}{2}}{1 + \sqrt{\frac{C_f}{2}} [5Pr + 5 \ln(5Pr + 1) - 14]} \quad (3.24)$$

Again, the low-speed correlation must be extended to the compressible case. Three approaches are described next and used to estimate the heat transfer coefficient prevailing on a flat plate inside the Virginia Tech supersonic wind tunnel at Mach 4.

3.2.1 Reference Properties Approach

When the specific heat is approximately constant throughout the boundary layer, the constant property solution can be used to obtain an approximate solution when all properties are evaluated at a reference temperature T^* . The same expression for T^* can be used for both laminar and turbulent flows. However, different values of the recovery factor r must be used. For laminar flows, $r = Pr^{1/2}$ whereas $r = Pr^{1/3}$ for turbulent flows. Eckert [23] proposed the following expression:

$$T^* = T_e + 0.5(T_w - T_e) + 0.22(T_r - T_e) \quad (3.25)$$

3.2.2 Temperature-Ratio Correction Approach

Another approach is to use the temperature-ratio correction [39]. It is found that an increase in Mach number decreases the Stanton number. For a given value of T_w/T_r , the Mach number

3.2. FILM COEFFICIENTS

influence may be seen by introducing the ratio of T_r/T_e which obviously is a function of the Mach number. The effect of the Mach number for high-velocity convection is similar to that of the large temperature difference at low velocities. It is found that the effect of T_w/T_r and T_r/T_e can be separately correlated and that correlation may be simplified by noting that T_r has only a minor influence. We get the following expression:

$$\frac{St}{St_i} = \left(\frac{T_e}{T_w} \right)^{-0.5} \quad (3.26)$$

Where St_i is the value of the Stanton number evaluated at the free-stream condition.

3.2.3 Van Driest II Correlation

A more physical approach consists in using the Van-Driest transformation of the log Law of the Wall with the momentum integral equation for a flat plate:

$$\frac{d\theta}{dx} = \frac{C_f}{2} \quad (3.27)$$

to obtain a skin friction law for compressible flow [60]:

$$\frac{0.242}{B_1 \sqrt{C_f (T_w/T_e)}} \left[\sin^{-1} \left(\frac{2B_1^2 - B_2}{\sqrt{B_2^2 + 4B_1^2}} \right) + \sin^{-1} \left(\frac{B_2}{\sqrt{B_2^2 + 4B_1^2}} \right) \right] = 0.41 + \log(Re_x C_f) - \omega \log \left(\frac{T_w}{T_e} \right) \quad (3.28)$$

where

$$B_1 = \sqrt{\frac{((\gamma - 1)/2) M_e^2 r}{T_w/T_e}} \quad (3.29)$$

$$B_2 = \frac{1 + ((\gamma - 1)/2) M_e^2 r}{T_w/T_e} - 1 \quad (3.30)$$

3.2.4 Film Coefficient in the Virginia Tech Supersonic Wind Tunnel

The reference properties approach, the temperature-ratio correction approach and Van Driest correlation are used to compute the film coefficient on a flat plate inserted inside the test section of the Virginia Tech Supersonic wind tunnel at Mach 4. It is important to mention that the presented results are only valid for a flat plate Boundary Layer. For instance,

the boundary layer found on the floor of the wind tunnel will have a different turbulent structure, since it is developed through a converging diverging nozzle (see Appendix B). The expansion through the nozzle will reduce the turbulence intensity leading to a lower skin friction coefficient and, therefore, a reduced Stanton number. Results are found in Fig. 3.1.

We notice that the film coefficient obtained using the reference properties and temperature-ratio correction are about 40% higher than those obtained with the Van Driest correlation. The Van Driest correlation should give a better estimate as it is based on stronger physical arguments. The results show that the film coefficient decreases with distance which also implies that it decreases with an increase in the boundary layer thickness. We also notice that the film coefficient increases sharply for $x < 0.1$ m. Physically, the boundary layer might not be turbulent at such a short distance. It is, therefore, important to predict the transition location. This aspect is covered in section 3.3 where the transition location on a flat plate located in the Virginia Tech supersonic wind tunnel is estimated.

3.2.5 Film Coefficient for an Arbitrary Wall Temperature Distribution

The irradiation of the target with a powerful laser beam will surely produce a large localized temperature variation on the wall. The correlations presented previously are only valid for a wall at a constant temperature. Here, some correlations used to analyze a wall subjected to an arbitrary temperature distribution are given.

Reynolds et. al [56] have used a $1/7^{th}$ power law for the boundary layer velocity and temperature profiles to get an expression valid for a temperature step:

$$St(\xi; x) = St_T(x) \left[\xi - \left(\frac{\xi}{x} \right)^{\frac{9}{10}} \right]^{-\frac{1}{9}}, \quad x > \xi \quad (3.31)$$

where St_T is the Stanton number for a constant wall temperature. The Stanton number for an arbitrary wall temperature can be computed using the superposition of an infinite number of differential steps. This leads to:

$$St(x) = \int_0^x St(\xi; x) \frac{dT_w(\xi)}{d\xi} + d\xi + \sum_{n=l}^N St(l_n; x) [T_w(l_n^+) - T_w(l_n^-)] \quad (3.32)$$

where the Kernel function $St(\xi, x)$ is from Eq. 3.31 and $[T_w(l_n^+) - T_w(l_n^-)]$ corresponds to the rise across the n^{th} temperature step when the wall temperature is discontinuous. This approach was successfully used by Reynolds et. al [56] to compute the heat flux on a wall with an arbitrary temperature distribution. It is agreed that the previous expression fails to accurately predict the Stanton number very close to the step. Mukerji et. al [47] et. al have reported that the film coefficient is under-predicted by 25% at one boundary layer thickness

3.2. FILM COEFFICIENTS

downstream ($x/\delta_0 = 1$) and is under-predicted by more than 30% at $x/\delta_0 = 0.25$. compared to experimental data. This shows without any doubt that the wall temperature distribution has as a large influence on the film coefficient. This large discrepancy could possibly be explained by the non-applicability of the boundary layer equations close to a sharp step due to their parabolic nature which doesn't allow upstream influence. For example, it is well known that the boundary layer equations will fail at a leading edge of a flat plate. Here, a similar situation arises for a large and abrupt heat disturbance. Mukerji et. al [47] have proposed a correction that improves the agreement close to the step:

$$St(\xi; x) = St_T(x) \left[\xi - \left(\frac{\xi}{x} \right)^{\frac{9}{10}} + \phi(\xi, x, Re_\xi) \right]^{-\frac{1}{9}}, \quad x > \xi \quad (3.33)$$

where:

$$\phi = (-0.0139 \ln(Re_\xi) + 0.246) \left(\frac{\xi}{x} \right)^2 \frac{1}{\sqrt{1 - \left(\frac{\xi}{x} \right)}} \quad (3.34)$$

We notice that ϕ tends to zero when the distance from the step is increased such that the original expression Eq. 3.31 is recovered.

Experimental data for a supersonic boundary layer subjected to a sharp variation in wall temperature are uncommon. To our knowledge and that of Debieve et al. [20] only one case of a supersonic heated turbulent flow is found in the literature. Debieve et al. [20] have made detailed temperature and velocity boundary layer surveys for three supersonic cases namely, an adiabatic wall and a step in the wall temperature with ratios of wall to recovery temperature, T_w/T_r , of 1.5 and 2 respectively. Those cases are used as validation cases for the present convection heat transfer methods in Section 4.4.2.

Using the measured velocity and temperature profiles Debieve et al. [20] also have developed a methodology to compute the skin friction coefficient and Stanton number. The starting point of their analysis is the fact that the time scale for the relaxation of the velocity field downstream of the perturbation varies approximately as the turbulent kinetic energy divided by the rate of its production. This implies that the relaxation time varies approximately as $\frac{\partial u}{\partial y}^{-1}$ meaning that the flow adjusts quickly near the wall. Therefore, a limited region of equilibrium flow can exist close to the wall. In that region, the shear stress is constant and Crocco's integral can be used to relate the temperature field to the velocity field if the upper limit of integration is the edge of the constant stress region noted s instead of the edge of the boundary layer. We then have,

$$\frac{T}{T_s} = \frac{T_w}{T_s} + \frac{T_r - T_w}{T_s} \left(\frac{u}{u_s} \right) - r \frac{\gamma - 1}{2} M_s^2 \left(\frac{u}{u_s} \right)^2 \quad (3.35)$$

Similarly in that region, the velocity profile will follow the logarithmic Law of the Wall. The friction velocity u_τ is determined by fitting the experimental velocity profile to the Law of the Wall transformed using Eq. 3.8. Similarly, the friction temperature is found by fitting

the experimental data to the Crocco's integral Eq. 3.35. Since the velocity and temperature profiles are coupled, an iterative process must be used. Also, since the extent of the constant stress region isn't known in advance, its determination is also part of the iterative process. The extent of the constant stress region simply specifies the number of experimental data points included in the least-square fit. At convergence, the friction velocity and temperature profile are determined such that the skin friction coefficient and Stanton number can be computed. Devieve et. al [20] have used this analysis to show that an increase in the temperature step decreases both the skin friction coefficient and the Stanton number.

3.3 Overview of Transition to Turbulence

Transition to turbulence is a complex topic as the physical process leading to transition is not fully understood. A common approach is to use an empirical correlation such as the Re_θ/M_e algebraic correlation [60]. However, since transition is a function of various problem specific parameters such as the leading edge bluntness, the surface roughness, the free stream Reynolds and Mach numbers, the disturbance and noise levels in the facility, the algebraic correlation approach isn't always reliable. Methods based on the linear stability theory such as the e^N method are commonly used. Chen et. al [13] have used $N = 10$ to accurately predict transition on flat plates and cones in the LaRC low disturbance Mach 3.5 wind tunnel. They also report transition data for flat plates in three conventional supersonic facilities. This data found in Fig. 3.2 is useful in estimating transition location in the Virginia Tech supersonic Wind Tunnel. We arrive to a conservative estimate of $Re_T = 2.5 \times 10^6$ which correspond to a distance of $0.05m$. Using the correlation for the transition region length from Whitfield and Potter reported in Schetz [60], we expect a fully turbulent boundary layer at $9cm$ from the leading edge.

3.3. OVERVIEW OF TRANSITION TO TURBULENCE

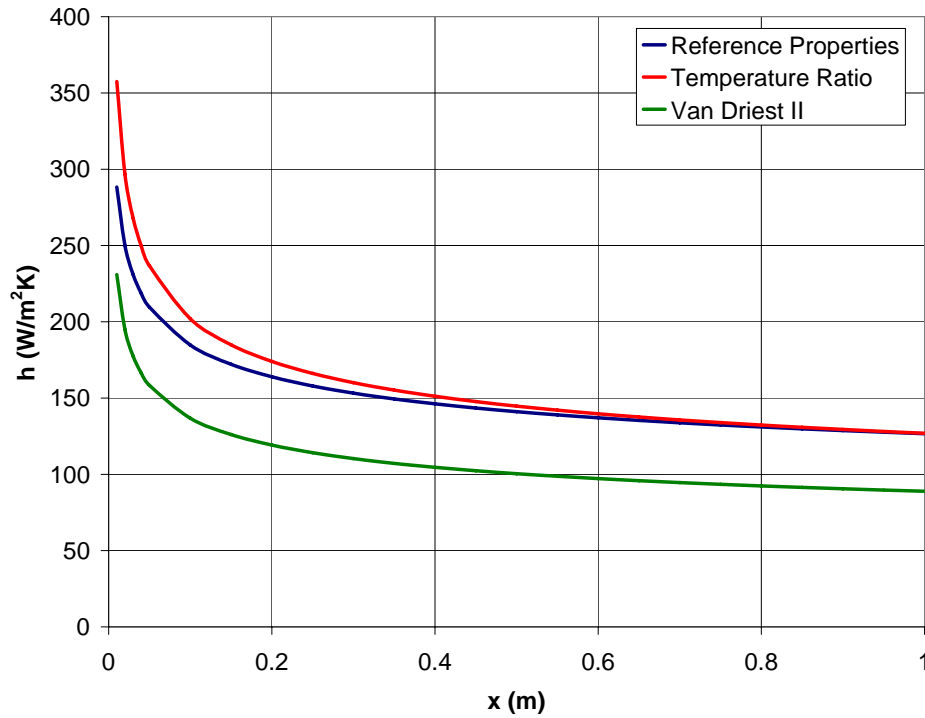


Figure 3.1: Film coefficient for a flat plate inside the Virginia Tech supersonic wind tunnel at Mach 4

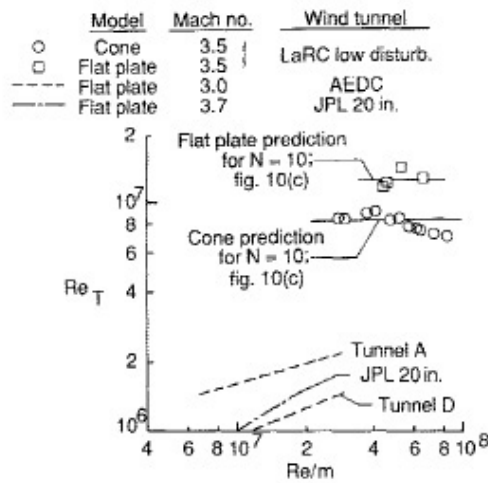


Figure 3.2: Transition Reynolds Number (from Chen et. al [13])

Chapter 4

Numerical Convective Heat Transfer

This section presents the governing equation for the motion of a Newtonian fluid, the modeling assumptions and the numerical methods used to integrate these equations. An accurate resolution of the equations of motions is essential in obtaining an accurate prediction of the convective heat transfer.

4.1 Conservation Equations

The Navier-Stokes equations state the conservation of mass, momentum and energy for a fluid [25]:

$$\frac{\partial \rho}{\partial t} + \nabla \cdot (\rho \mathbf{u}) = 0 \quad (4.1)$$

$$\frac{\partial \rho \mathbf{u}}{\partial t} + \nabla \cdot (\rho \mathbf{u} \mathbf{u}) = -\nabla p + \nabla \cdot \boldsymbol{\tau} \quad (4.2)$$

$$\frac{\partial (\rho e_0)}{\partial t} + \nabla \cdot (\rho e_0 \mathbf{u}) = -\nabla p \cdot \mathbf{u} + \nabla \cdot (\boldsymbol{\tau} \cdot \mathbf{u} + \mathbf{q}) \quad (4.3)$$

where:

$$e_0 = e + \frac{1}{2} \mathbf{u} \cdot \mathbf{u} \quad (4.4)$$

For a Newtonian fluid, the shear rate is proportional to the strain rate such that:

$$\boldsymbol{\tau} = \mu \left(\nabla \mathbf{u} + \nabla \mathbf{u}^T - \frac{2}{3} \nabla \cdot \mathbf{u} \mathbf{1} \right) \quad (4.5)$$

The heat flux is modelled using Fourier's law of conduction.

$$\mathbf{q} = -K \nabla T \quad (4.6)$$

4.1. CONSERVATION EQUATIONS

The variable thermal conductivity and viscosity are evaluated using Sutherland's law. Two equations of state are needed to close the system. The thermal and caloric equations for a perfect gas are:

$$p = \rho RT \quad (4.7)$$

$$e = c_v T \quad (4.8)$$

The Navier-Stokes equations contain all the physics required to model both laminar transitional and turbulent flows. However, since in general no closed-form solution exists, those equations must be discretized on a grid and solved numerically. We are interested in high Reynolds number flows such as found in the Virginia Tech supersonic wind tunnel. For high Reynolds flows the viscous dissipation of turbulent eddies occurs at a very small scale. At the present time, resolving the smallest eddies leads to a unmanageable number of cells meaning extravagant memory and CPU time requirement.

For this study, turbulence is modeled using a statistical approach where each flow variable is decomposed into a mean part and a fluctuating part. For a laser irradiated target, we expect the mean flow to be unsteady such that the ensemble averaging must be used, which under the ergodicity condition is equivalent to a time average. This leads to:

$$\bar{a} = \frac{1}{\Delta t} \int_{t_0}^{t_0+\Delta t} a \, dt \quad (4.9)$$

where the time interval must be large compared to the time of random fluctuations associated with turbulence, but small compared to the temporal fluctuation of the mean flow variables. For a laser heated target, we expect that the heat induced change in the flow variables will be fast but slower than the eddy frequency and most likely monotonic such that the decomposition can be performed. We define the fluctuating quantity as:

$$a = \bar{a} + a' \quad (4.10)$$

by definition the Reynolds average of a fluctuation vanishes:

$$\bar{a}' = 0 \quad (4.11)$$

For compressible flow, it is convenient to use a mass-weighted average also called a Favre average which is defined as [25]:

$$\tilde{a} \equiv \frac{\overline{\rho a}}{\bar{\rho}} \quad (4.12)$$

The fluctuations are then defined as

$$a = \tilde{a} + a'' \quad (4.13)$$

For compressible flow, the use of Favre average has the virtue of leading to a simpler form of the conservation equations which helps in extending incompressible turbulence models to

4.1. CONSERVATION EQUATIONS

compressible flows. Decomposing the variables according to Eq. 4.13 and taking the time average leads to

$$\frac{\partial \bar{\rho}}{\partial t} + \nabla \cdot (\bar{\rho} \tilde{\mathbf{u}}) = 0 \quad (4.14)$$

$$\frac{\partial \bar{\rho} \tilde{\mathbf{u}}}{\partial t} + \nabla \cdot (\rho \tilde{\mathbf{u}} \tilde{\mathbf{u}}) = -\nabla \bar{p} + \nabla \cdot \bar{\boldsymbol{\tau}} + \nabla \cdot \left(-\bar{\rho} \widetilde{\mathbf{u}'' \mathbf{u}''} \right) \quad (4.15)$$

$$\begin{aligned} \frac{\partial \bar{\rho} \tilde{e}_0}{\partial t} + \nabla \cdot (\bar{\rho} \tilde{e}_0 \tilde{\mathbf{u}}) &= -\nabla \bar{p} \cdot \tilde{\mathbf{u}} + \nabla \cdot \left(-\rho \widetilde{\mathbf{u}'' \mathbf{u}''} \cdot \tilde{\mathbf{u}} \right) + \nabla \cdot (\bar{\boldsymbol{\tau}} \cdot \tilde{\mathbf{u}}) \\ -\nabla \cdot (\bar{\boldsymbol{\tau}} \cdot \mathbf{u}'') &- \nabla \cdot \left(\bar{\rho} \widetilde{\mathbf{u}'' \mathbf{u}''} \cdot \mathbf{u}'' + \frac{1}{2} \bar{p} \widetilde{\mathbf{u}'' \mathbf{u}''} \cdot \mathbf{u}'' \right) - \nabla \cdot (\bar{\mathbf{q}} + \bar{\rho} \widetilde{\mathbf{u}'' h''}) \end{aligned} \quad (4.16)$$

The thermal and caloric equation of state become:

$$\bar{p} = \bar{\rho} R \bar{T} \quad (4.17)$$

$$\tilde{e}_0 = \bar{c}_v \bar{T} + \frac{1}{2} \tilde{\mathbf{u}} \cdot \tilde{\mathbf{u}} + \frac{1}{2} \widetilde{\mathbf{u}'' \cdot \mathbf{u}''} \quad (4.18)$$

The previous equations are still exact from a physical stand point, but some information is lost in the averaging process. It is also important to mention that the previous equations are valid for constant density flows. In that case, Favre averages simply reduce to Reynolds averages. The nonlinearity of the convective terms introduces new terms in the equations among them, the Reynolds stress:

$$-\bar{\rho} \widetilde{\mathbf{u}'' \mathbf{u}''} \quad (4.19)$$

and the turbulent heat flux:

$$-\bar{\rho} \widetilde{\mathbf{u}'' h''} \quad (4.20)$$

such that we have now more unknowns than equations meaning that more modeling is required to close the system. This will be discussed in the next sections.

4.1.1 Transport of the $\mathcal{TK}\mathcal{E}$ and of the Mean Dissipation Rate

The turbulent kinetic energy $\mathcal{TK}\mathcal{E}$ is a measure of the energy contained in the turbulent eddies. It is useful to look at how this quantity evolves in order to understand turbulence.

The Favre averaged value of the $\mathcal{TK}\mathcal{E}$ is expressed as:

$$\tilde{k} = \widetilde{\mathbf{u}'' \cdot \mathbf{u}''} \quad (4.21)$$

4.1. CONSERVATION EQUATIONS

The following equation:

$$\begin{aligned}
 \bar{\rho} \frac{D\tilde{k}}{Dt} &= \nabla \cdot \left[\underbrace{-\overline{\mathbf{u}'' p'' \mathbf{1}}}_{(1)} + \underbrace{\overline{\boldsymbol{\tau} \cdot \mathbf{u}''}}_{(2)} - \frac{1}{2} \overline{\rho \mathbf{u}'' \mathbf{u}'' \cdot \mathbf{u}''} \right] + \underbrace{\overline{p'' \nabla \cdot \mathbf{u}}}_{(3)} \\
 &\quad - \underbrace{\overline{\rho \mathbf{u}'' \mathbf{u}''} : \nabla \cdot \mathbf{u}}_{(4)} - \underbrace{\bar{\rho} \epsilon}_{(5)} + \underbrace{\frac{\overline{\rho'' \mathbf{u}''}}{\bar{\rho}} \cdot \nabla \bar{p}}_{(6)}
 \end{aligned} \tag{4.22}$$

expresses the change in the Favre averaged $\mathcal{TK}\mathcal{E}$ from:

1. the motion along the Favre averaged trajectory
2. the rate of work produced from turbulent motion \mathbf{u}'' by the pressure fluctuation p' ; by the viscous shear stress $\boldsymbol{\tau}$; by the instantaneous Reynolds stress $\rho \mathbf{u}'' \mathbf{u}''$. Those terms have a divergence form such that when Eq. 4.22 is integrated over a control volume, using the Divergence Theorem, these terms represent the flux of $\mathcal{TK}\mathcal{E}$ across the boundary. Therefore they can't change the total amount of $\mathcal{TK}\mathcal{E}$ in the flow.
3. the rate of work produced by the pressure fluctuations in the turbulent volume fluctuations
4. the production attributed to the mean velocity gradient
5. the mean dissipation into heat
6. the production or destruction related to the velocity pressure gradient correlation.

This expression states that turbulence extracts energy from the mean flow at the larger scales and gives it back through heat at the smaller scales. The mean dissipation into heat is expressed as:

$$\bar{\rho} \epsilon \equiv \overline{\boldsymbol{\tau} : (\nabla \mathbf{u})^T} \tag{4.23}$$

This term can be expressed as the sum of three part such that:

$$\overline{\boldsymbol{\tau} : (\nabla \mathbf{u})^T} = \bar{\rho} [\epsilon_1 + \epsilon_2 + \epsilon_3] \tag{4.24}$$

Where parts two and three are due to viscosity fluctuations we have:

$$\bar{\rho} \epsilon_1 = \overline{\bar{\mu} \nabla \mathbf{u}' : \left((\nabla \mathbf{u}') + (\nabla \mathbf{u}')^T \right)} - \frac{2}{3} \overline{\bar{\mu} Tr(\nabla \mathbf{u}') \nabla \cdot \mathbf{u}'} \tag{4.25}$$

$$\bar{\rho} \epsilon_2 = \overline{\mu' \nabla \mathbf{u}' : \left((\nabla \mathbf{u}') + (\nabla \mathbf{u}')^T \right)} - \frac{2}{3} \overline{\mu' Tr(\nabla \mathbf{u}') \nabla \cdot \mathbf{u}'} \tag{4.26}$$

$$\bar{\rho} \epsilon_3 = \overline{\mu' \nabla \cdot \mathbf{u}' : \left(\nabla \bar{\mathbf{u}} + (\nabla \bar{\mathbf{u}})^T \right)} - \frac{2}{3} \overline{(\mu' \nabla \cdot \mathbf{u}') Tr(\nabla \cdot \bar{\mathbf{u}})} \tag{4.27}$$

4.1. CONSERVATION EQUATIONS

and ϵ_1 can be expressed as the sum of three parts [35]: the solenoidal and dilational contributions to dissipation, and an inhomogeneous term:

$$\epsilon_1 = \epsilon_s + \epsilon_d + \epsilon_{nh} \quad (4.28)$$

where the solenoidal dissipation is:

$$\epsilon_s = 2\bar{\nu}\overline{\boldsymbol{\omega}' \cdot \boldsymbol{\omega}'} \quad (4.29)$$

where:

$$\boldsymbol{\omega}' = \nabla \times \mathbf{u}' \quad (4.30)$$

is the vorticity fluctuation; and the dilational part is given by:

$$\epsilon_d = \frac{4}{3}\bar{\nu}\overline{\nabla \cdot \mathbf{u}' \nabla \cdot \mathbf{u}'} \quad (4.31)$$

It is easy to see that ϵ_d is equal to zero when the fluid is incompressible. Here, a Reynolds decomposition is used to express the dissipation rate as it leads to simpler equations compared to using the Favre decomposition [25].

The following equation can be obtained by taking the Lagrangian derivative of Eq. 4.29 :

$$\frac{D\epsilon_s}{Dt} = \frac{D\overline{\boldsymbol{\omega}' \cdot \boldsymbol{\omega}'}}{Dt} + \bar{\rho} \frac{D\bar{\nu}}{Dt} \overline{(\boldsymbol{\omega}' \cdot \boldsymbol{\omega}')} \quad (4.32)$$

The transport equation for ϵ_s can therefore be expressed as a transport equation for the enstrophy $\overline{\boldsymbol{\omega}' \cdot \boldsymbol{\omega}'}$ and a contribution from the viscosity variations. An equation for ϵ_s could be directly derived without using enstrophy but this leads to an equation which is more difficult to interpret. The Enstrophy equation takes the following form [37]:

$$\frac{D\overline{\boldsymbol{\omega}' \cdot \boldsymbol{\omega}'}}{Dt} = P_\omega^1 + P_\omega^2 + P_\omega^3 + P_\omega^4 + T_\epsilon + D_\epsilon + Y_\epsilon + T_\epsilon^c + B_\epsilon + C_\epsilon \quad (4.33)$$

where the terms have the following form and significance.

Mixed production:

$$P_\omega^1 = 2\bar{\omega}\overline{\boldsymbol{\omega}' : \mathbf{s}'} - 2\bar{\omega} \cdot \overline{\boldsymbol{\omega}' \nabla \cdot \mathbf{u}'} \quad (4.34)$$

Production by mean rate of strain:

$$P_\omega^2 = 2\overline{\boldsymbol{\omega}' \boldsymbol{\omega}'} : \mathbf{s} - 2\overline{\boldsymbol{\omega}' \cdot \boldsymbol{\omega}'} \nabla \cdot \bar{\mathbf{u}} \quad (4.35)$$

Gradient production:

$$P_\omega^3 = -2\overline{\mathbf{u}' \boldsymbol{\omega}'} : \nabla \bar{\boldsymbol{\omega}} \quad (4.36)$$

4.1. CONSERVATION EQUATIONS

Turbulent production:

$$P_\omega^4 = 2\overline{\boldsymbol{\omega}'\boldsymbol{\omega}' : \mathbf{s}'} - 2\overline{\boldsymbol{\omega}' \cdot \boldsymbol{\omega}' \nabla \cdot \mathbf{u}'} \quad (4.37)$$

Turbulent transport:

$$T_\omega = -\overline{\nabla \cdot (\mathbf{u}'\boldsymbol{\omega}' \cdot \boldsymbol{\omega}')} \quad (4.38)$$

Viscous diffusion:

$$D_\omega = \nu \nabla^2 \overline{(\boldsymbol{\omega}' \cdot \boldsymbol{\omega}')} \quad (4.39)$$

Viscous dissipation:

$$Y_\omega^c = 2\overline{\boldsymbol{\omega}' \nabla \boldsymbol{\omega}' : \nabla \boldsymbol{\omega}'} \quad (4.40)$$

Compressible transport term:

$$T_\omega^c = \overline{\boldsymbol{\omega}' \cdot \boldsymbol{\omega}' \nabla \cdot \mathbf{u}'} \quad (4.41)$$

Baroclinic term:

$$B_\omega = -2\overline{\boldsymbol{\omega}' \cdot (\nabla \rho^{-1} \times \nabla p)} \quad (4.42)$$

Spatial viscosity variation term:

$$C_\omega = 2\nu' \overline{(\boldsymbol{\omega}' \cdot \nabla^2 \boldsymbol{\omega}')} + 2\boldsymbol{\omega}' \cdot \nabla \nu \cdot (\nabla \boldsymbol{\omega}' - (\nabla \boldsymbol{\omega}')^T) - \quad (4.43)$$

$$2\boldsymbol{\omega}' \cdot \nabla^2 \mathbf{u} \times \frac{4}{3} \nabla \nu + 2\boldsymbol{\omega}' \cdot \nabla \times \frac{\nabla \mu}{\rho} \cdot (\nabla \mathbf{u} + (\nabla \mathbf{u})^T) - 2\boldsymbol{\omega}' \cdot \frac{2}{3\rho} \nabla \times \nabla \mu \nabla \cdot \mathbf{u}$$

The terms in the solenoidal dissipation rate are related to those in the enstrophy equation using Eq. 4.32:

$$A_\epsilon = \bar{\nu} A_\omega \quad (4.44)$$

The spatial viscosity variation term becomes:

$$C_\epsilon = \bar{\nu} C_\omega \overline{\boldsymbol{\omega}' \cdot \boldsymbol{\omega}'} \quad (4.45)$$

In most turbulence models, the solenoidal dissipation rate in a compressible flow is computed from a modeled transport equation for incompressible flow where turbulence is assumed isotropic such that:

$$\epsilon_s \cong \epsilon_I \cong \overline{\nu \mathbf{u}' \cdot \mathbf{u}'} \quad (4.46)$$

The validity of this approximation was tested by Sinha and Candler [37] by computing a budget of the various terms in the solenoidal dissipation rate equation using DNS data for a Mach 4 boundary layer. They found the two quantities are equivalent with the exception of an additional term caused by the variation of the viscosity in the compressible case. The approximation introduced in Eq. 4.46 seems justified for boundary layer flows.

It will be seen that k and ϵ can be used to provide the turbulent time and length scales. Since from now on, the Favre averaged equations are only dealt with, the $(\bar{\bullet})$ and $(\tilde{\bullet})$ notation will be omitted for the average quantities with the exception to the turbulence correlations.

4.2 Turbulence Modeling

Most turbulence models were first developed for incompressible flows, since more experimental information was available due to the increased complexity of measurement in compressible flow and the simpler form of the equations.

Compressible turbulence models found in the literature are extensions of their incompressible counterparts. The main assumption leading to this extension is called Morkovin hypothesis. Based on experimental evidence, Morkovin [46] assumed that in a boundary layer, the effects of density fluctuations on turbulence can be neglected as long as the Mach number remains below 5. This also implies that the solenoidal dissipation rate is equivalent to the dissipation rate for incompressible flow as stated in the previous section.

As mentioned before, the time averaging of the equations leads to more unknowns than equations. Two strategies can be used to close the system; eliminate unknowns or introduce new equations linking unknowns to the mean flow variables. In practice a combination of the two is used since each time a new equation is introduced, new unknowns arise.

4.2.1 Eddy Viscosity Formulation

It is agreed upon that Boussinesq was the first to introduce the concept of an eddy viscosity which makes an analogy with the molecular viscosity. For a two-dimensional incompressible boundary layer this leads to:

$$-\overline{u'v'} = \nu_t \frac{\partial u}{\partial y} \quad (4.47)$$

For three-dimensional compressible flow Eq. 4.47 takes the form:

$$-\bar{\rho} \widetilde{u''u''} = \rho \nu_t \left(\nabla \mathbf{u} + \nabla \mathbf{u}^T - \frac{2}{3} \nabla \cdot \mathbf{u} \mathbf{1} \right) - \frac{2}{3} \rho k \mathbf{1} \quad (4.48)$$

Similarly, the turbulent heat flux is related to the mean temperature field:

$$-\bar{\rho} \widetilde{u''h''} = K_T \nabla T = \frac{\rho \nu_t C_p}{Pr_t} \nabla T \quad (4.49)$$

Where the turbulent Prandtl number Pr_t is usually set to 0.9 for wall bounded flows. This is equivalent to saying that the eddy heat diffusivity is proportional to the eddy viscosity. The velocity fluctuation of the $\mathcal{TK}\mathcal{E}$ -velocity moment is modelled as:

$$\bar{\rho} \frac{1}{2} \mathbf{u}'' \cdot \widetilde{\mathbf{u}''\mathbf{u}''} = \frac{\rho \nu_t}{Pr_k} \nabla k \quad (4.50)$$

where Pr_k is a constant

Originally, Boussinesq assumed that the eddy viscosity ν_t was a constant. This assumption isn't valid such that ν_t must be modelled. Using dimensional analysis, we see that ν_t the product of a velocity times a length both characterizing turbulence. ν_t can therefore be computed if the length and times scales are determined. Next, an overview of the different turbulence models used is given.

4.2.2 Spalart-Allmaras One-equation Turbulence Model

The Spalart-Allmaras one equation turbulence model [65] directly solves an equation for the eddy-viscosity. The effect of the wall is taken into account by adding a damping function. The transport equation takes the following form:

$$\frac{D\check{\nu}}{Dt} = C_{b1}\check{S}\check{\nu} + \nabla \cdot \left[\frac{1}{\sigma} (\nu + \check{\nu}) \nabla \check{\nu} \right] + \frac{C_{b2}}{\sigma} \nabla \check{\nu} \cdot \nabla \check{\nu} - C_{w1} f_w \frac{\check{\nu}^2}{d^2} \quad (4.51)$$

$$(4.52)$$

The eddy viscosity is expressed as:

$$\nu_t = \check{\nu} f_{v1} \quad (4.53)$$

where:

$$f_{v1} = \frac{\chi^3}{\chi^3 + C_{v1}} \quad \chi = \frac{\check{\nu}}{\nu} \quad (4.54)$$

Moreover:

$$\check{S} = f_{v3}(\chi) \mathbf{S} + \frac{\check{\nu}}{\kappa^2 d^2} f_{v2}(\chi) \quad (4.55)$$

where:

$$f_{v2} = \left(1 + \frac{\chi}{c_{v2}} \right) \quad f_{v3} = \frac{(1 + \chi f_{v1})(1 - \chi f_{v2})}{\chi} \quad (4.56)$$

insures that \check{S} remains positive and:

$$f_w = g \left(\frac{1 + C_{w3}^6}{g^6 + C_{w3}^6} \right)^{\frac{1}{6}} \quad r + C_{w2} (r^6 - r) \quad r = \frac{\check{\nu}}{\check{S} \kappa^2 d^2} \quad (4.57)$$

where S is the norm of the shear rate tensor. The constants of the model are:

$$C_{b1} = 0.1355 \quad \sigma = \frac{2}{3} \quad C_{b2} = 0.622 \quad C_{w2} = 0.3 \quad C_{w3} = 2$$

$$C_{w1} = \frac{C_{b1}}{\kappa^2} + \frac{1 + C_{b2}}{\sigma} \quad C_{v1} = 7.1 \quad C_{v2} = 5 \quad \kappa = 0.41$$

The model possesses a damping function which requires the computation of the distance d to the closest wall.

4.2.3 Two-equation Turbulence Models

Two-equation turbulence models require solving two transport equations in order to determine the length and time scales of turbulence.

Chien $k - \epsilon$ Model

Initially the $k - \epsilon$ Model was developed for free shear flows, such that the effect of the wall wasn't taken into account. The application of the $k - \epsilon$ model to wall bounded flows requires the introduction of a damping function to modify the dissipation term near the wall. Different flavors of the $k - \epsilon$ model exist depending on the damping functions used. Chien [14] used a Taylor expansion of the eddy viscosity, k and ϵ to get the right asymptotic behavior near the wall. The model is expressed as:

$$\rho \frac{Dk}{Dt} = P_k - \rho\epsilon - 2\mu \frac{k}{d^2} + \nabla \cdot \left[\left(\mu + \frac{\mu_t}{\sigma_k} \right) \nabla k \right] \quad (4.58)$$

$$\rho \frac{D\epsilon}{Dt} = C_{\epsilon_1} P_k \frac{\epsilon}{k} - C_{\epsilon_2} f_2 \rho \frac{\epsilon^2}{k} - 2\mu \frac{\epsilon}{d^2} \exp(-0.5d^+) + \nabla \cdot \left[\left(\mu + \frac{\mu_t}{\sigma_\epsilon} \right) \nabla \epsilon \right] \quad (4.59)$$

$$\nu_t = C_\mu f_\mu \frac{k^2}{\epsilon} \quad (4.60)$$

where d is the wall distance. The turbulent production is defined as:

$$P_k = \rho \nu_t \nabla \mathbf{u} : \mathbf{u} \quad (4.61)$$

And the damping function f_μ and f_2 are the following:

$$f_\mu = 1 - \exp(-0.0115y^+) \quad (4.62)$$

$$f_2 = 1 - \frac{0.4}{1.8} \exp\left(\frac{-R_t^2}{36}\right) \quad R_t = \frac{\rho k^2}{\mu \epsilon} \quad (4.63)$$

and the model constants are:

$$C_\mu = 0.09 \quad C_{\epsilon_1} = 1.35 \quad \sigma_k = 1.0 \quad \sigma_\epsilon = 1.3$$

Wilcox $k - \omega$ Model

The main advantage of the $k - \omega$ formulation is that it doesn't require any damping function, since it uses a transport equation for the specific dissipation defined as:

$$\omega = \frac{\epsilon}{\beta^* k} \quad (4.64)$$

4.2. TURBULENCE MODELING

The 1998 model [70] proposes improvement for free shear flow over the 1988 model [69]. For wall-bounded flows, both models are equivalent. The equations for the 1988 model are presented next:

$$\rho \frac{Dk}{Dt} = P_k - \beta^* \rho \omega k + \nabla \cdot [(\mu + \sigma^* \mu_t) \nabla k] \quad (4.65)$$

$$\rho \frac{D\omega}{Dt} = -\gamma P_k \frac{\omega}{k} - \beta \rho \omega^2 + \nabla \cdot [(\mu + \sigma \mu_t) \nabla \omega] \quad (4.66)$$

$$\nu_t = \gamma^* \frac{k}{\omega} \quad (4.67)$$

$$(4.68)$$

the model constants are:

$$\beta = 0.075 \quad \beta^* = 0.09 \quad \gamma = \frac{5}{9} \quad \gamma^* = 1 \quad \sigma = \sigma^* = 0.5$$

Menter SST Model

Menter showed the sensitivity of the $k - \omega$ model to the value of ω specified in the free stream. Menter SST (Shear Stress Transport) turbulence model is equivalent to the $k - \omega$ model in the inner region and to the $k - \epsilon$ in the outer region of the boundary layer. The transition between the two models is performed using a blending function. The equations are the following:

$$\rho \frac{Dk}{Dt} = P_k - \beta^* \rho \omega k + \nabla \cdot [(\mu + \sigma_k \mu_t) \nabla k] \quad (4.69)$$

$$\rho \frac{D\omega}{Dt} = -\frac{\sigma}{\nu_t} P_k - \beta \rho \omega^2 + \nabla \cdot [(\mu + \sigma_\omega \mu_t) \nabla \omega] + 2(1 - F_1) \rho \sigma_w \frac{1}{\omega} \nabla k \cdot \nabla \omega \quad (4.70)$$

$$\mu_t = \frac{\rho k}{\omega} \quad (4.71)$$

$$(4.72)$$

Where, the coefficients vary according to:

$$\Phi = F_1 \Phi_1 + (1 - F_1) \Phi_2 \quad (4.73)$$

4.2. TURBULENCE MODELING

and subscript 1 refers to the value corresponding to the $k - \omega$ model and subscript 2 to the $k - \epsilon$ model. The blending function takes the form:

$$F_1 = \tanh (arg_1^4) \quad (4.74)$$

$$arg_1 = \min \left[\max \left(\frac{\sqrt{k}}{\beta^* \omega d}; \frac{500\mu}{\rho \omega d^2} \right); \frac{4\rho \sigma_{\omega_2} k}{CD_{k\omega} d^2} \right] \quad (4.75)$$

$$CD_{k\omega} = \max \left(2\rho \omega_2 \frac{1}{\omega} \nabla k \cdot \nabla \omega; 10^{-20} \right) \quad (4.76)$$

Considering the limiter, the eddy viscosity takes the form:

$$\mu_t = \frac{\rho a_1 k}{\max (a_1 \omega; \nabla \times \mathbf{u} F_2)} \quad a_1 = 0.31 \quad (4.77)$$

and F_2 is defined as:

$$F_2 = \tanh (arg_2^4) \quad arg_2 = \max \left(\frac{2\sqrt{k}}{\beta^* \omega d}; \frac{500\mu}{\rho \omega d^2} \right) \quad (4.78)$$

4.2.4 Analysis of Turbulence Models in Compressible Boundary Layers

To facilitate the analysis of any two-equation models, Huang et al. [33] have proposed the following generalized length scale:

$$\phi = \rho^n k^m \epsilon^l \quad (4.79)$$

Governed by the following transport equations:

$$\rho \frac{\partial k}{\partial t} = P_k - \rho \epsilon + \nabla \cdot \left(\frac{\nu_t}{\alpha_k} \nabla k \right) \quad (4.80)$$

$$\rho \frac{\partial \phi}{\partial t} = C_1 P_k \frac{\phi}{k} - C_2 \rho \epsilon \frac{\phi}{k} + \nabla \cdot \left(\frac{\nu_t}{\alpha_\phi} \nabla \phi \right) \quad (4.81)$$

$$\nu_t = C_\mu \rho \frac{k^2}{\epsilon} \quad (4.82)$$

We can show that the constants of the $k - \epsilon$ model are related by the constants of the other models by the following equations:

$$C_1 = lC_{\epsilon_1} + m \quad (4.83)$$

$$C_2 = lC_{\epsilon_2} + m \quad (4.84)$$

Using 5 equations, namely, the momentum equation, the Eqs 4.80, 4.81 and 4.82 with the Boussinesq and Bradshaw hypothesis (assuming the proportionality of the turbulent shear

4.2. TURBULENCE MODELING

and the $\mathcal{TK}\mathcal{E}$ [9]) and neglecting convection and viscous shear in the log region the following equation was obtained by Huang:

$$\frac{\sqrt{C_m u \sigma_\phi}}{l^2 \kappa^2} (C_2 - C_1) = 1 + \frac{1}{l^2} \left[d_1 \frac{y}{\rho} \frac{\partial \rho}{\partial y} + d_2 \frac{y^2}{\rho} \frac{\partial^2 \rho}{\partial y^2} + d_3 \left(\frac{y}{\rho} \frac{\partial y}{\partial \rho} \right)^2 \right] \quad (4.85)$$

where

$$d_1 = \left(n - m - \frac{3}{2}l \right) (1 - 2l) - \frac{1}{2}l + C_1 \frac{\sigma_\phi}{\sigma_k} \quad (4.86)$$

$$d_2 = n - m - \frac{3}{2}l + C_1 \frac{\sigma_\phi}{\sigma_k} \quad (4.87)$$

$$d_3 = \left(n - m - \frac{3}{2}l \right) \left(n - m - \frac{3}{2}l - \frac{1}{2} \right) - \frac{3}{2}C_1 \frac{\sigma_\phi}{\sigma_k} \quad (4.88)$$

For incompressible flow, the viscosity is constant such that for incompressible flow Eq. 4.85 reduces to

$$\frac{\sqrt{C_m u \sigma_\phi}}{l^2 \kappa_i^2} (C_2 - C_1) = 1 \quad (4.89)$$

Where $1/\kappa_i$ is the value of the slope of the logarithmic Law of the Wall for incompressible flow. Solving for κ_i in Eq. 4.89 and substituting into eqn. 4.85 yields:

$$\left(\frac{\kappa_i}{\kappa} \right) = 1 + \frac{1}{l^2} \left[d_1 \frac{y}{\rho} \frac{\partial \rho}{\partial y} + d_2 \frac{y^2}{\rho} \frac{\partial^2 \rho}{\partial y^2} + d_3 \left(\frac{y}{\rho} \frac{\partial y}{\partial \rho} \right)^2 \right] \quad (4.90)$$

A similar analysis for the Spalart-Almaras model was performed by Catris [9] and gives:

$$\left(\frac{\kappa_i}{\kappa} \right) = 1 + \frac{\kappa_i^2}{\sigma C_{b1}} \left[(1 + C_{b2}) \frac{y}{\rho} \frac{\partial \rho}{\partial y} + \frac{1}{2} \frac{y^2}{\rho} \frac{\partial^2 \rho}{\partial y^2} - \left(\frac{1}{4} C_{b2} + \frac{1}{2} \right) \left(\frac{y}{\rho} \frac{\partial y}{\partial \rho} \right)^2 \right] \quad (4.91)$$

Since compressibility doesn't change the value of the slope ($\kappa_i = \kappa$), Eq. 4.91 shows that in order for a model to predict the right slope of the Law of the Wall it must have $d_1 = d_2 = d_3 = 0$. However, no combination of n, m, l meets that condition. Assuming that the order of terms in front of the d_i is the same, by computing the term $d_1 - d_2 + d_3$, we can assess how well a model should perform. Results for Chien $k - \epsilon$, Wilcox $k - \omega$ and Spalart-Allmaras are shown at Table 4.1. Looking at this results we expect that Chien's model will perform the worst for a compressible boundary layer flow.

This is actually the case as seen in Fig. 4.1, where computations of a compressible turbulent boundary layer are made and compared with experimental results from Mabey et al. [29] for a Mach 4 boundary layer on an adiabatic wall with Re_θ varying between 3100 and 5000. The $k - \omega$ and Spalart-Allmaras model are found to perform much better. Also on Fig. 4.1 are shown results for modified models. It is seen that modifications proposed by Catris [9]

Table 4.1: Contribution from $d_1 - d_2 + d_3$ adapted from Catris [9]

Model	$k - \epsilon$	$k - \omega$	ν_t
Worker	Chien	Wilcox	Spalart-Allmaras
$d_1 - d_2 + d_3$	2.58	0.54	0.87

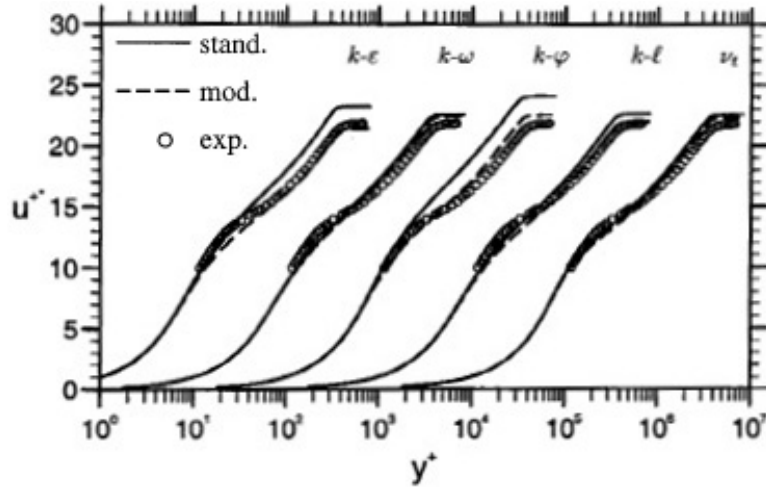


Figure 4.1: Comparison between original and modified turbulence models and experiment of Mabey et. al (figure adapted form Catris [9])

improve the predictions for all the models considered. The main inconsistency noticed by Catris when extending the incompressible turbulence models to compressible flow is the loss of the equilibrium between the production and the dissipation of the $\mathcal{TK}\mathcal{E}$ in the log region. This arise from the fact that in a compressible boundary layer the $\mathcal{TK}\mathcal{E}$ is not constant in the logarithmic region such that ∇k doesn't vanish in the transport equation for the $\mathcal{TK}\mathcal{E}$ (Eq. 4.80). This introduces an imbalance between the production and dissipation of the turbulent kinetic energy in the log region. In a compressible flow, k isn't constant, but ρk is such that a simple fix can be made by replacing ∇k with $\frac{1}{\rho}\nabla(\rho k)$ in Eq. 4.80. In order to get a constant slope in the log region, a modification is also applied to Eq. 4.81 such that d_1 , d_2 and d_3 can all vanish. The modified transport equations are now written as:

$$\rho \frac{\partial k}{\partial t} = P_k - \rho \epsilon + \nabla \cdot \left(\frac{\nu_t}{\rho \alpha_k} \nabla(\rho k) \right) \quad (4.92)$$

$$\rho \frac{\partial \phi}{\partial t} = C_1 P_k \frac{\phi}{k} - C_2 \rho \epsilon \frac{\phi}{k} + \nabla \cdot \left(\frac{\nu_t}{\sqrt{\rho} \alpha_\phi} \nabla(\sqrt{\rho} \phi) \right) \quad (4.93)$$

It is found that the $k - \omega$ model is the one that requires the least amount of modifications.

4.3 Finite Volume Discretization and GASP Solver

An overview of the numerical methods used to solve the conservation equations is given next. First, the integral form of the conservation equations and the finite volume discretization is presented. Version 4 of the commercial flow solver GASP [2] from Aerosoft, Inc. is the basic tool used here.

4.3.1 Finite Volume Discretization

Expressing the Navier Stokes equations in hypervector form we get

$$\frac{\partial \mathbf{Q}}{\partial t} + \nabla \cdot (\mathbf{F} + \mathbf{F}_v) = 0 \quad (4.94)$$

where the conserved variables are:

$$\mathbf{Q} = \begin{Bmatrix} \rho \\ \rho \mathbf{u} \\ \rho e_0 \end{Bmatrix} \quad (4.95)$$

\mathbf{F} the inviscid flux takes the form:

$$\mathbf{F} = \begin{Bmatrix} \rho \mathbf{u} \\ \rho \mathbf{u} \mathbf{u} + p \mathbf{1} \\ \rho \mathbf{u} h_0 \end{Bmatrix} \quad (4.96)$$

\mathbf{F}_v and the viscous flux is expressed as:

$$\mathbf{F}_v = \begin{Bmatrix} 0 \\ \boldsymbol{\tau}_G \\ \mathbf{q}_G \end{Bmatrix} \quad (4.97)$$

where

$$\boldsymbol{\tau}_G = \rho (\nu_t + \nu) \left(\nabla \mathbf{u} + \nabla \mathbf{u}^T - \frac{2}{3} \nabla \cdot \mathbf{u} \mathbf{1} \right) + \frac{2}{3} \rho k \mathbf{1} \quad (4.98)$$

and

$$\mathbf{q}_G = \left(k + \frac{\rho \nu_t C_p}{Pr_t} \right) \nabla T + \rho \left(\nu + \frac{\nu_t}{Pr_k} \right) \nabla k \quad (4.99)$$

and e_0 now includes the $\mathcal{TK}\mathcal{E}$:

$$e_0 = e + \frac{1}{2} \mathbf{u} \cdot \mathbf{u} + k \quad (4.100)$$

and the stagnation enthalpy is defined as:

$$h_0 = e_0 + \frac{p}{\rho} \quad (4.101)$$

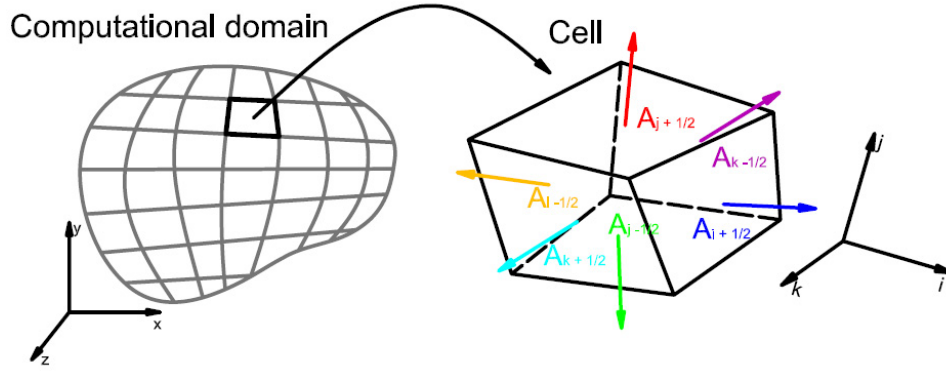


Figure 4.2: Finite volume discretization

Integrating Eq. 4.94 over the computational domain using the Divergence Theorem yields:

$$\frac{\partial}{\partial t} \iiint_V \mathbf{Q} dV + \oint_A (\mathbf{F} + \mathbf{F}_v) \cdot \mathbf{n} dA = 0 \quad (4.102)$$

To evaluate the flux integrals, the domain is split into six-sided cells of arbitrary shape, each acting as a control volume (see Fig. 4.2). Integrating Eq. 4.102 over each face of a cell and using the chain rule to express the equations in term of the primitive variable we get:

$$\begin{aligned} V \left(\frac{\partial \bar{\mathbf{Q}}}{\partial \mathbf{q}} \right) \frac{\partial \mathbf{q}}{\partial t} + [(\mathbf{F} + \mathbf{F}_v) \cdot \mathbf{n}]_{i+1/2} \Delta A_{i+1/2} + \\ [(\mathbf{F} + \mathbf{F}_v) \cdot \mathbf{n}]_{i-1/2} \Delta A_{i-1/2} + [(\mathbf{F} + \mathbf{F}_v) \cdot \mathbf{n}]_{j+1/2} \Delta A_{j+1/2} + \\ [(\mathbf{F} + \mathbf{F}_v) \cdot \mathbf{n}]_{j-1/2} \Delta A_{j-1/2} + [(\mathbf{F} + \mathbf{F}_v) \cdot \mathbf{n}]_{k+1/2} \Delta A_{k+1/2} + \\ [(\mathbf{F} + \mathbf{F}_v) \cdot \mathbf{n}]_{k-1/2} \Delta A_{k-1/2} = 0 \end{aligned} \quad (4.103)$$

where in cartesian coordinates, the primitive variable vector is simply:

$$\mathbf{q} = \begin{Bmatrix} \rho \\ u \\ v \\ w \\ e_0 \end{Bmatrix} \quad (4.104)$$

4.3.2 Spatial Reconstruction and Flux Computation

In order to evaluate the flux, the primitive variables must be evaluated at each face of the control volume. This situation is shown in Fig. 4.3. This requires expressing the

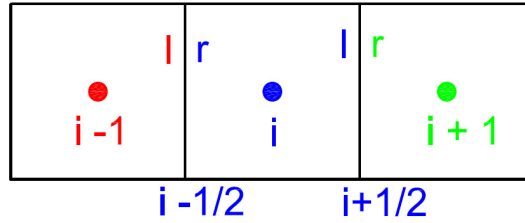


Figure 4.3: Spatial reconstruction is needed to express the face values as a function of the cell-centered values. The computation of the inviscid flux requires a left and a right state at each faces.

face values as a function of the cell averaged values. This process is called the spatial reconstruction. Viscous and inviscid fluxes are different mathematical animals that require a different treatment. The inviscid flux is computed using an upwind flux function which requires two states at each faces namely the left and the right state. Whereas the viscous flux is evaluated using a centered scheme such that only one state is required at the face. In GASP, the spatial reconstruction is obtained from the Monotonic Upstream-centered Scheme for Conservation Laws (MUSCL) [1]. The values of the left and right states in the i direction are represented as:

$$\begin{aligned}
 q_{i+1/2}^l &= \mathbf{q}_i + \frac{\phi}{4} [(1 - \kappa) \nabla \mathbf{q}_i + (1 + \kappa) \Delta] \\
 q_{i-1/2}^r &= \mathbf{q}_i - \frac{\phi}{4} [(1 + \kappa) \nabla \mathbf{q}_i + (1 - \kappa) \Delta]
 \end{aligned}
 \tag{4.105}$$

The value of κ determines the order of the spatial reconstruction and $\phi = 0$ simply give a first order scheme whereas $\phi = 1$ enables higher order accuracy. The forward and backward difference operators are defined as:

$$\begin{aligned}
 \Delta \mathbf{q}_i &= \mathbf{q}_{i+1} - \mathbf{q}_i \\
 \nabla \mathbf{q}_i &= \mathbf{q}_i - \mathbf{q}_{i-1}
 \end{aligned}
 \tag{4.106}$$

For the inviscid flux, the face values are evaluated using $\phi = 1$ and $\kappa = 1/3$ leading to a third-order reconstruction, whereas for the viscous flux, $\phi = 1$ and $\kappa = 1$ are used leading to a second order central difference scheme. The reconstruction must be modified near a wall to incorporate the specified wall value. When shocks are present in the flow, a high-order scheme can introduce an unreasonable reconstruction for which the computed face values don't lie between the values of the adjacent cell averages. Limiters are then required to maintain numerical stability and eliminate numerical oscillation in the solution. For shock-free boundary layer flows, no limiters are required.

The Roe flux-difference splitting [59] is used to compute the inviscid flux since it contains less numerical dissipation than Van Leer flux-vector splitting leading to more accurate boundary

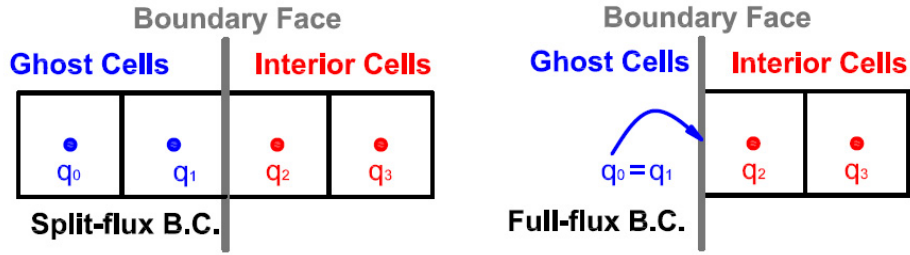


Figure 4.4: Nomenclature for the boundary conditions. When the Full is used the ghost cells values are applied directly on the boundary

layer computation. This method exactly solves an approximate Riemann problem at every face based on the reconstructed left and right states at each face. When computing the viscous flux, the velocity, temperature and turbulent gradients in the (x, y, z) frame must be evaluated. The Gradient Theorem can be used to obtain the component of the gradient without requiring any coordinate transformation between the cell (ξ, η, ζ) and the cartesian coordinate (x, y, z) frame. The Gradient Theorem is expressed as:

$$\frac{1}{V} \iiint_V \nabla \phi dV = \frac{1}{V} \oint_A \phi \mathbf{n} dA \quad (4.107)$$

Here ϕ represents an arbitrary scalar. The surface integral is approximated in the usual way by taking the contribution over each face of the six-sided control volume. The face value of the scalar ϕ is taken as the average of the adjacent cell center. The face value of the gradient is also computed by taking the average of the value of adjacent cells center.

4.3.3 Boundary Condition

GASP contains a large number of boundary conditions. The ones used in our investigation are presented next. Two ghost cells are used in GASP. The ghost cells are denoted as q_0 and q_1 whereas the interior cells are denoted as q_2 and q_3 as shown in Fig. 4.4.

For a supersonic outlet flow, the first-order extrapolation boundary condition is used since the outside information can't travel upstream. In that case:

$$\mathbf{q}_0 = \mathbf{q}_1 = \mathbf{q}_2 \quad (4.108)$$

For a subsonic outlet flow, it is often convenient to specify the back pressure. For the outflow with a specified back pressure, the boundary condition is written as:

$$\mathbf{q}_0 = \mathbf{q}_1 = \mathbf{q}_2 \quad \text{except} \quad p_0 = p_1 = p_b \quad (4.109)$$

This boundary condition can be used to simulate a pressure-gradient-free boundary layer by setting the exit pressure to the free stream value. For a supersonic inflow the inside

information can't travel upstream and modify the value on the boundary. This condition is called fixed at q in GASP. In that case, the boundary values simply take the values specified by the user:

$$\mathbf{q}_0 = \mathbf{q}_1 = \mathbf{q}_\infty \quad (4.110)$$

For a subsonic inlet, this boundary condition cannot be used as a wave coming from the computational domain can travel upstream. In that case the Riemann invariants are used. Denoting a forward moving wave with a plus and a backward-moving wave with a minus, we express the Riemann invariants as:

$$R^\pm = u \pm \frac{2a}{\gamma - 1} \quad (4.111)$$

This information is used to compute the normal boundary velocity and speed of sound.

$$R_\infty^+ = \bar{u}_\infty + 2\frac{a_\infty}{\gamma - 1} = \bar{u}_1 + 2\frac{a_1}{\gamma - 1} \quad (4.112)$$

$$R_\infty^- = \bar{u}_2 - 2\frac{a_2}{\gamma - 1} = \bar{u}_1 - 2\frac{a_1}{\gamma - 1} \quad (4.113)$$

The two previous equations are used to determine the speed of sound and the velocity normal to the cell face at the boundary as a function of the free stream properties. In order to fix the state at 1 another property must be known. It is assumed that the flow is isentropic near the boundary such that

$$s_1 = s_\infty \Rightarrow \frac{p_1}{\rho_1}^\gamma = \frac{p_\infty}{\rho_\infty}^\gamma \quad (4.114)$$

Since two thermodynamic variables are known at 1, all the other thermodynamic variables can be computed using the equations of state.

At the wall, the no-slip boundary condition is used such that:

$$u = v = w = 0 \quad (4.115)$$

For an adiabatic wall also have:

$$\rho_1 = \rho_2 \quad (4.116)$$

$$e_1 = e \quad (4.117)$$

whereas, for a fixed wall temperature we have:

$$\begin{aligned} \rho_1 &= \rho_2 \\ T_1 &= T_w \end{aligned} \quad (4.118)$$

4.3.4 Linearization and Time Integration

The finite volume discretization process leads to a non-linear system of ODE's in time. For a single cell this system is given by eqn. 4.103. Here the system is rewritten in compact form as:

$$V \frac{\partial \bar{Q}}{\partial \mathbf{q}} \frac{\partial \mathbf{q}}{\partial t} + \mathbf{R}(\mathbf{q}) = 0 \quad (4.119)$$

where the residual is expressing the balance of the fluxes on a cell and can be written as:

$$\mathbf{R}(\mathbf{q}) = \oint_A \mathbf{F} \cdot \mathbf{n} dA - \oint_A \mathbf{F}_v \cdot \mathbf{n} dA \quad (4.120)$$

Here, the fluxes are discretized by the finite volume method as seen in Eq. 4.103. When the steady state is reached, the residual needs to be zero in order for the conservation equations to be satisfied. Many solution strategies are available in GASP. In this study, an implicit method of solution is used to get a good computational efficiency. For this approach, the system is linearized about a given time level $t = n\Delta t$:

$$\left[\frac{V}{\Delta t} \frac{\partial \bar{Q}}{\partial \mathbf{q}} + \frac{\partial \mathbf{R}}{\partial \mathbf{q}} \right] \Delta \mathbf{q} = -\mathbf{R}(\mathbf{q}^n) \quad (4.121)$$

where $\Delta \mathbf{q} = \mathbf{q}^{n+1} - \mathbf{q}^n$ represents the change in the primitive variables between two successive iterations, and the time derivative is approximated to first order. The linearization process introduces the Jacobian matrix which is the derivative of the fluxes with respect to the primitives variables. The Jacobian of the viscous and inviscid flux must therefore be computed. In GASP the first-order expression of the jacobian is coded in. To make the method fully implicit, the jacobian of the boundary conditions must also be evaluated.

All problems are treated as 3-Dimensional in GASP such that each cell is part of a computational molecule containing a total of 7 cells (center cell plus the 6 neighboring cells). A different time step can be used for each cell by specifying the value of the CFL number.

The size of the jacobian matrix depends of the number of primitive variables in the vector q as seen is Eq. 4.104. We note that the turbulence variables are not included in q , since the system resulting for the turbulence equations is treated as uncoupled and therefore solved separately using the same numerical algorithm. Here, we have 5×5 block as q contains 5 variables. The bandwidth of the matrix increases with the number of cells in the domain.

The problem ultimately resides in solving efficiently a linear system of equations at each time step. Here, the block diagonal structure of the system is considered in choosing an efficient solution method. The linear system is solved in a iterative manner using the Gauss-Seidel method. This iterative solving of the linear system at a given time step is refereed as the inner problem. The system doesn't need to be solved exactly as long as when steady state is reached the residual is driven to zero. Here we have used the default value of 10 inner iteration cycles with a convergence tolerance of 0.01.

As seen in Eq. 4.121, reducing the time step increases the importance of the first term on the left hand side which increases the block diagonal dominance of the linear system. Therefore, for stiffer problems, the use of a small time step can be necessary. For most of the cases solved in our investigation, an infinite time step was used such that the solution to the system reduces to Newton's method:

$$\frac{\partial \mathbf{R}}{\partial \mathbf{q}} \Delta \mathbf{q} = -\mathbf{R}(\mathbf{q}^n) \quad (4.122)$$

Using an infinite time step increases the computational efficiency as quadratic convergence can be obtained.

When a time-accurate solution is required, GASP offers the choice between the explicit Runge-Kutta method or the implicit dual-time stepping method. Here, the dual-time stepping method is used as it allows for a greater time step. This method introduces a fictional time τ to reformulate the problem as

$$V \frac{\partial \bar{Q}}{\partial \mathbf{q}} \frac{\partial \mathbf{q}}{\partial \tau} = V \frac{\partial \bar{Q}}{\partial \mathbf{q}} \frac{\partial \mathbf{q}}{\partial t} + \mathbf{R}(\mathbf{q}) = \mathbf{R}^*(\mathbf{q}, t) \quad (4.123)$$

The goal is to drive $\mathbf{R}^*(\mathbf{q}, t)$ to zero at a fixed value of the physical time t . The strength of the method lies in the fact that the exact same algorithm (as the one used for steady flow) can be used, since the problem is transformed into a sequence of steady-state computations in the fictional time domain. For this approach, the system is linearized about a given fictional time level $\tau = n\Delta\tau$:

$$\left[\frac{V}{\Delta\tau} \frac{\partial \bar{Q}}{\partial \mathbf{q}} + \frac{\partial \mathbf{R}^*}{\partial \mathbf{q}} \right] \Delta \mathbf{q} = -\mathbf{R}^*(\mathbf{q}^n, t) \quad (4.124)$$

Once $\mathbf{R}^*(\mathbf{q}, t)$ is driven down, the value of \mathbf{q} of the current time step t is obtained and the original equation recovered. The new value of q is used to update the time dependent terms in the residual $\mathbf{R}^*(\mathbf{q}, t)$ advancing the solution in time. In GASP, those terms can be evaluated using a first-, second- or third-order method. Essentially, the values of past time steps are used to compute the time derivatives of the primitive variables by finite differencing. In most cases considered here, an infinite value of the fictional time τ is used such that a Newton iteration is performed.

4.4 Validation Studies

Validation studies of the GASP flow solver for cases with complex wall temperature variations were conducted by comparing the solutions with experimental data.

For both the high- and low-speed cases, the grid is clustered normal to the surface using an hyperbolic tangent distribution such that $y^+ < 1$ for the first cell from the wall. Uniform spacing is used in the x direction and the grid density is set such that the cell aspect ratio

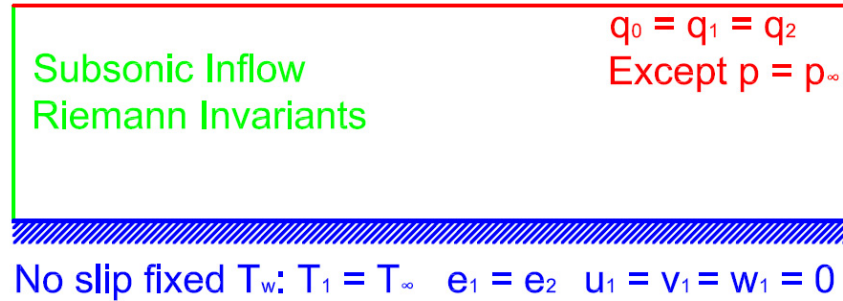


Figure 4.5: The inlet boundary condition permits upstream influence. Fixing the pressure at the outlet and on the top surface insure no pressure gradient.

is kept under 1000. At least 40 cells were located inside the boundary layer. For each case, a grid-convergence study was performed by using mesh sequencing. Either two or three grid levels were used and created by removing every other grid point from the previous grid level. The solutions on each grid level were then compared to each other to determine if the grid level was sufficient to resolve all the relevant flow physics. In some cases the final grid was determined by going through several cycles of the grid-convergence study. For all simulations Roe’s flux difference splitting scheme [59] was used with third-order spatial accuracy. For all cases, a steady-state solution is obtained and converged to a global residual of 10^{-12} . The boundary conditions used for all the low-speed cases are shown in Fig. 4.5.

4.4.1 Low Speed Validation Cases

The subsonic inlet boundary condition at the inflow allows upstream influence to reflect this physical reality in subsonic flows. Fixing the pressure at the outlet and on the top surface insure that no pressure gradients in the flow. Three cases of low velocity turbulent flow over a flat plate are studied [57, 56]. For these cases no significant difference was found among the turbulence models used. Therefore, only the Wilcox $k-\omega$ turbulence model solutions are shown. A constant value of the turbulent Prandtl number, Pr_t , of 0.9 was used.

The wall temperature distribution is set by using heated strips as shown in Fig. 4.6. First, a heated wall at constant temperature is considered. The wall temperature is imposed as a boundary condition. Predicted Stanton numbers (S_t) are compared against experimental data from Reynolds et al. [57, 56]. Both Menter’s SST and Wilcox’s 1998 $k-\omega$ two-equation turbulence models are used as well as the Spalart-Allmaras (S-A) one-equation turbulence model.

The simplest case considered is a wall maintained at a uniform temperature. The free stream properties are:

4.4. VALIDATION STUDIES

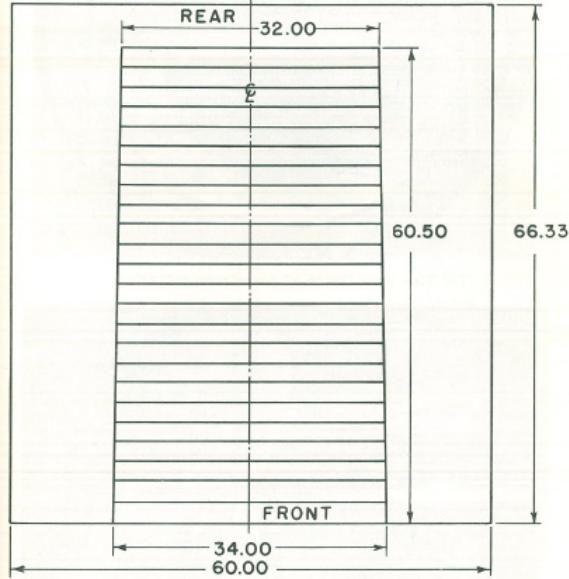


Figure 4.6: Experimental Apparatus: The wall temperature distribution is obtained with heated strips [57]

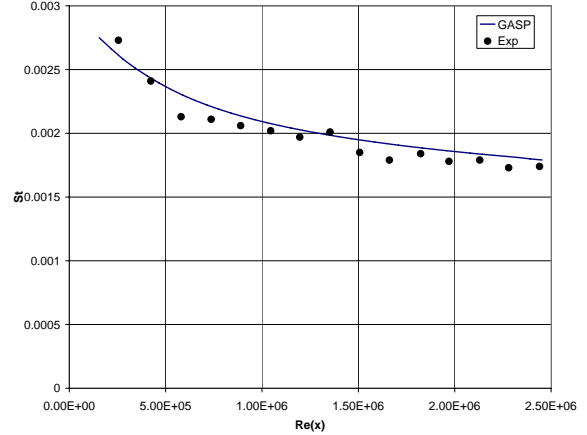


Figure 4.7: Stanton number for low velocity boundary layer on a heated wall with constant $T_w - T_e = 12.8K$ compared with experiment from Reynolds et al. [57]

- $T_e = 300.7K$
- $M_e = 0.111$
- $\rho_e = 1.168 \frac{kg}{m^3}$

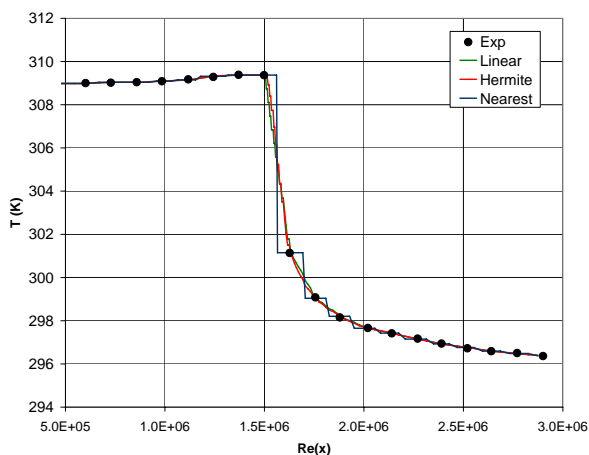
The temperature of the heated wall is maintained constant at $12.8K$ above the fluid free stream temperature. Results for S_t are depicted in Fig. 4.7 which generally matches experimental data.

The second low-speed case considered is a plate with an isothermal portion followed by an adiabatic region. The free stream conditions are the following:

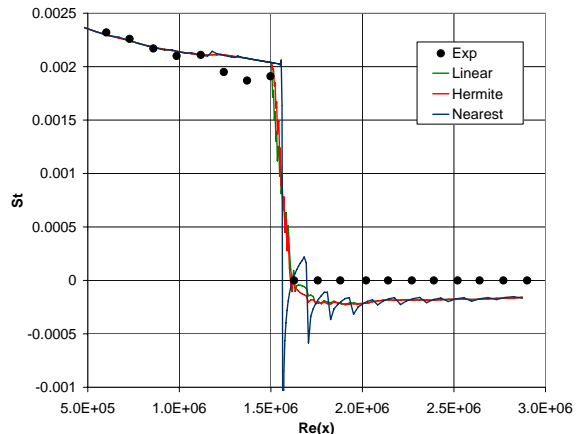
- $T_e = 294.7K$
- $M_e = 0.089$
- $\rho_e = 1.197 \frac{kg}{m^3}$

This case displays a sharp temperature gradient between the isothermal and adiabatic region. Over both the adiabatic and isothermal portions, the wall temperature is set to that measured by Reynolds et. al [56]. Since the grid density is greater than the density of

4.4. VALIDATION STUDIES



(a) Interpolation of the wall temperature



(b) Stanton number the different interpolation methods

Figure 4.8: Effect of wall temperature interpolation on Stanton number wall temperature. Results are compared with experiment from Reynolds et al. [56]

the measurements, interpolation is required. Different interpolation methods, namely linear interpolation, hermite polynomial and nearest neighbor are used. The interpolated wall temperature and the computed Stanton number are presented in Fig. 4.8. Some sensitivity to the interpolation method is found. The nearest neighbor method creates artificial temperature jumps that introduce oscillations in the solution. Oscillations could therefore show up for an insufficient grid resolution when using a first-order scheme. Linear interpolation is subsequently used, as it is simple and yields satisfactory results. Next, the effect of grid clustering near the adiabatic/isothermal interface is investigated. Figure 4.9 shows results for a fine uniform grid as well as for a medium and a fine grid with clustering around the isothermal/adiabatic interface. Clustering slightly increases the Stanton number ahead of the interface. Overall, for a fixed number of grid points, clustering near the interface showed no improvement. Figure 4.10 shows both the experimental wall temperature, used as a boundary condition, and the Stanton number. As in the previous case, turbulence modeling doesn't significantly impact the results. It is important to note that in the experimental setup, the wall section labelled as adiabatic wasn't insulated; the heaters were simply turned off [56]. This explains the negative value of the Stanton number over that portion as the flow heated over the isothermal region heats up the wall located downstream. To assess this effect, a simulation was performed with an adiabatic wall boundary condition instead of specifying the wall temperature throughout. As seen in Fig. 4.11, the computed wall temperature is compared to the one measured by Reynolds et. al [56]. We notice that by using an adiabatic wall, we compute a higher temperature than the measurement. A higher temperature is perfectly logical since for a "truly" adiabatic wall, no heat can leave the flow to penetrate the wall.

The next case considered is a flat plate with a double pulse in wall temperature with the

4.4. VALIDATION STUDIES

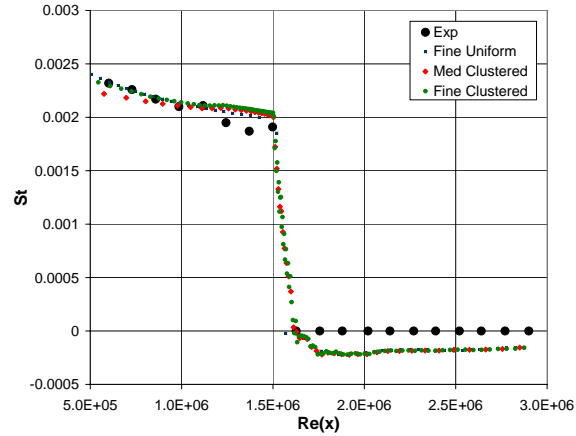
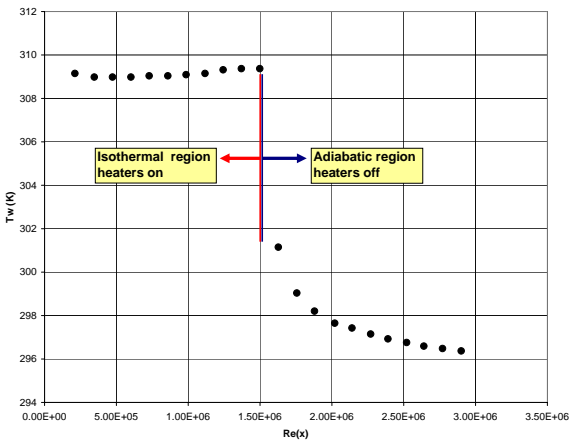
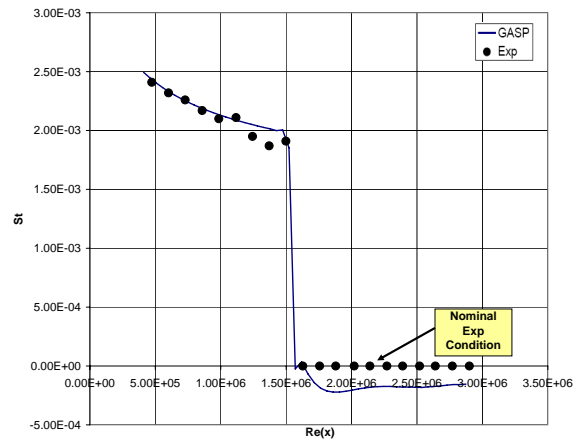


Figure 4.9: Effect of grid clustering



(a) Wall temperature boundary condition



(b) Stanton number for a wall temperature step

Figure 4.10: Stanton number for a low velocity boundary layer subjected to wall temperature step compared with experiment from Reynolds et al. [56]

4.4. VALIDATION STUDIES

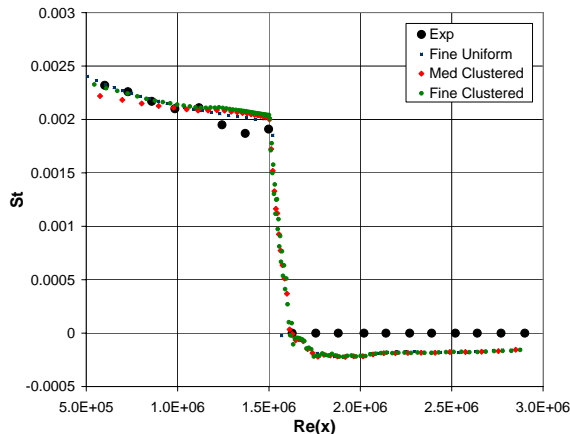


Figure 4.11: Computed wall temperature over the adiabatic portion of the wall compared with experiment from Reynolds et al. [56]

following free stream conditions

- $T_e = 293.3K$
- $M_e = 0.108$
- $\rho_e = 1.213 \frac{kg}{m^3}$

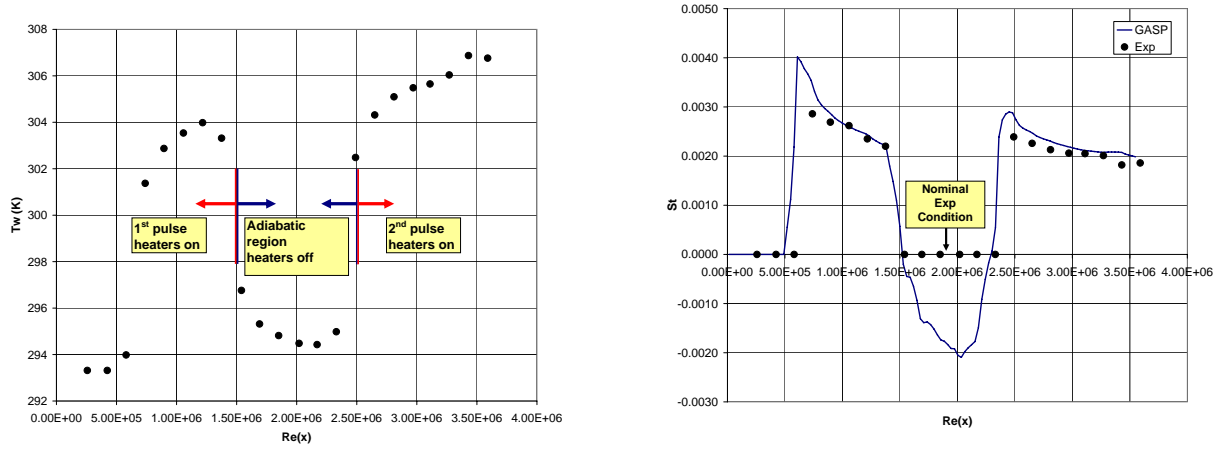
The experimental wall temperature was again used to set the numerical boundary condition. This data along with the results for Stanton number are shown in Fig. 4.12. As for the previous case, the heaters where turned off over the section labelled adiabatic such that the flow transfers heat to the wall in that region which explains the negative Stanton number. Again good agreement is seen between the numerical simulation and the experimental results.

4.4.2 Supersonic Validation Cases

Three supersonic cases are considered which include an adiabatic wall case and a step in the wall temperature with ratio of wall to recovery temperature, T_w/T_r , of 1.5 and 2 respectively. Skin friction, Stanton number and velocity and temperature profiles are compared to experimental results from Debieve et al. [20]. To the authors knowledge, these experimental results are the only one for a heated turbulent boundary layer subjected to a step in wall temperature. The flow conditions and initial boundary layer parameters are:

- $T_0 = 300K \pm 5K$

4.4. VALIDATION STUDIES



(a) Wall temperature boundary condition

(b) Stanton number for a double wall temperature pulse

Figure 4.12: Stanton number for a low velocity boundary layer subjected to double pulse in wall temperature compared with experiment from Reynolds et al. [56]

- $p_0 = 0.5 \times 10^5 Pa \pm 3\%$
- $M_e = 2.3$
- $\delta_0 = 10.2mm$
- $Re_\theta = 4200$

The experimental configuration is depicted in Fig. 4.14. Total temperature and velocity profiles were measured using hot wire anemometry. The method developed in Appendix A was used to generate the missing variables at the domain inlet. The boundary condition used are shown in Fig. 4.13. Since the inlet is supersonic, this fixed at Q boundary condition is used such that there is no upstream influence on the boundary. Similarly since the outlet is supersonic the first order extrapolation is used such that the boundary doesn't have an upstream influence. On the top surface, the velocity gradient in the normal direction is zero such that the first order extrapolation boundary condition can be used there. On the wall, no-slip boundary condition is enforce and the temperature specified.

The first case considered is an adiabatic wall. Good agreement is found for the skin friction as seen in Fig. 4.15. Computed velocity profiles are compared to experimental results in Fig. 4.16. At a downstream location of 8 cm, good agreement is found close to the wall. The discrepancy away from the wall is probably due to the effect of pressure gradients in the nozzle. Since the relaxation rate varies proportionally to the inverse of $(\partial u / \partial y)$, the flow adjusts more quickly close to the wall [20] explaining the better agreement in the near wall region. At 46 cm, the agreement is better throughout the boundary layer, since the flow has had more time and distance to relax. Overall, better agreement is found when using

4.4. VALIDATION STUDIES

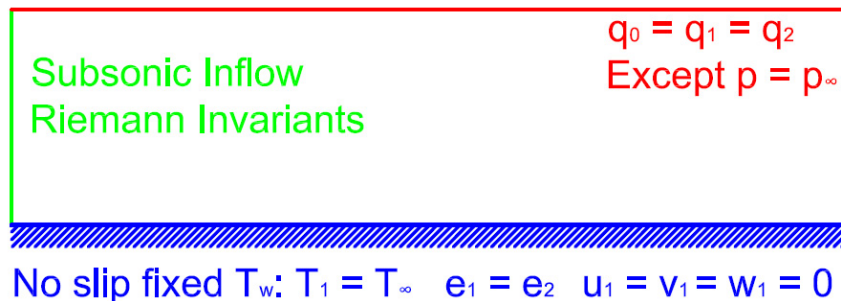


Figure 4.13: The inlet boundary condition doesn't permit upstream influence. Extrapolation at the outlet insure no influence from the boundary on the inside domain

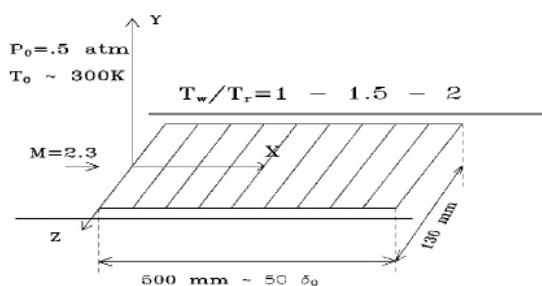


Figure 4.14: Experimental configuration taken from Debieve et al. [20].

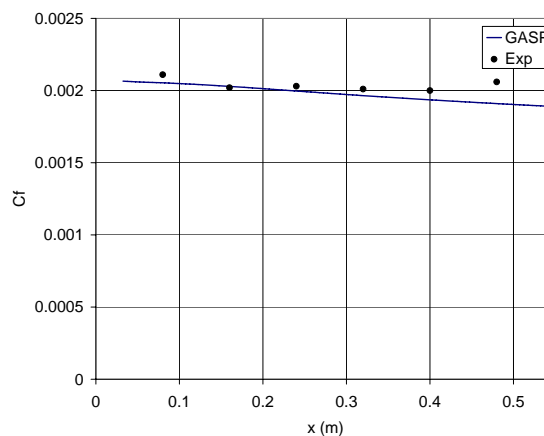


Figure 4.15: Skin friction coefficient for a supersonic boundary layer with an adiabatic wall compared with results from Debieve et al. [20].

the experimental velocity profile as a boundary condition as opposed to a flat plate profile. The Menter SST turbulence model gives better agreement than Wilcox $k-\omega$. The Menter SST model and the boundary condition based on the experimental velocity profile are used for the two subsequent cases.

For the next two cases, a step change in wall temperature is applied at $x = 0$ with respective ratios in wall temperature to recovery temperature, T_w/T_r equal to 1.5. and 2. Turbulent Prandtl numbers of 0.9 and 0.86 are used. It is observed that such a change doesn't significantly modify the velocity and temperature profile. However, a change in turbulent Prandtl number introduces a variation in the Stanton number. Good agreement is found for the skin friction coefficient and Stanton number for both cases as shown in Figs. 4.17 and 4.18 where the computed values are compared to those of Debieve et al. [20]. The variation in Pr_t shifts

4.4. VALIDATION STUDIES

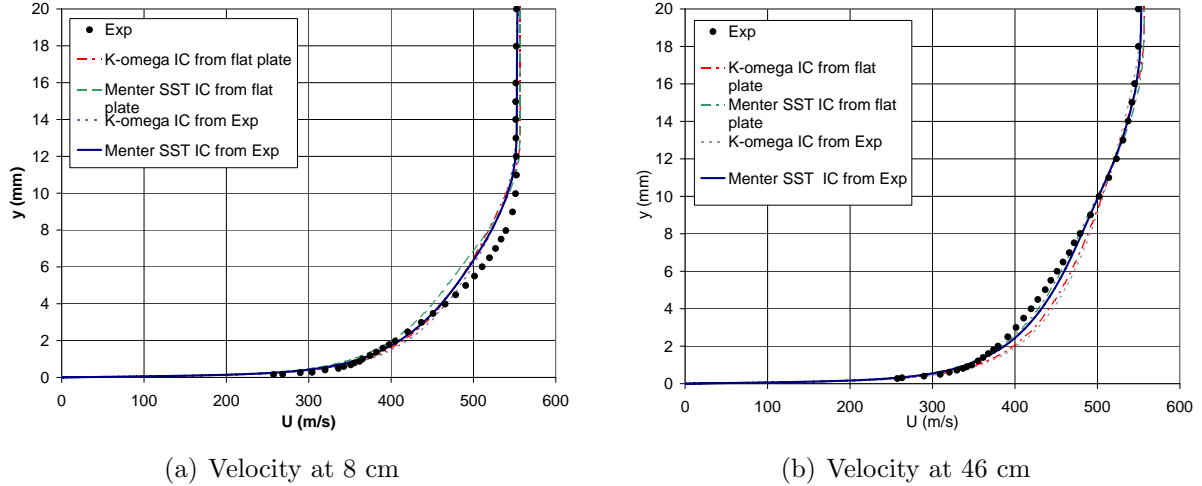


Figure 4.16: Velocity profiles for a supersonic boundary layer on an adiabatic wall compared with experiment from Debieve et al. [20]

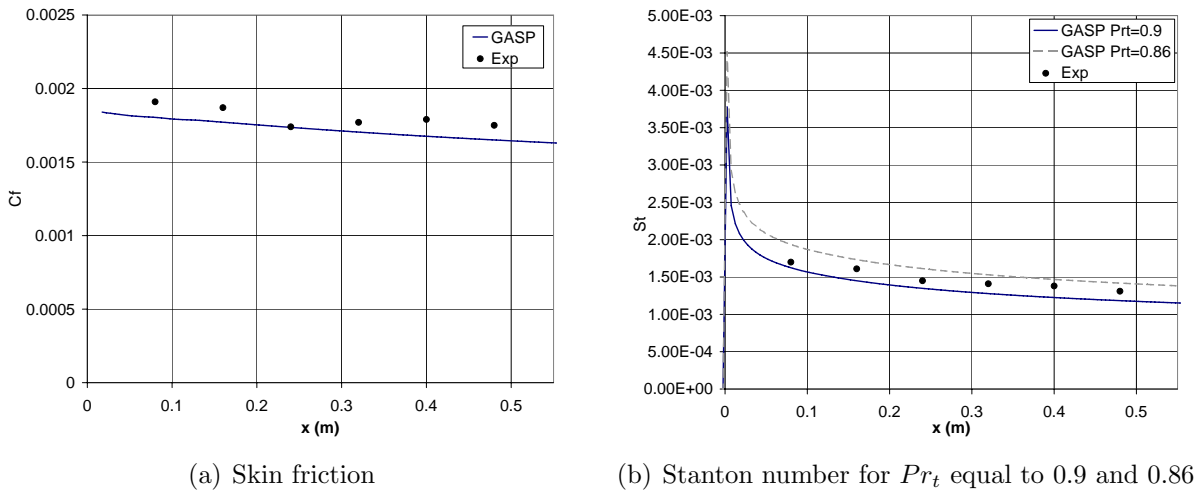
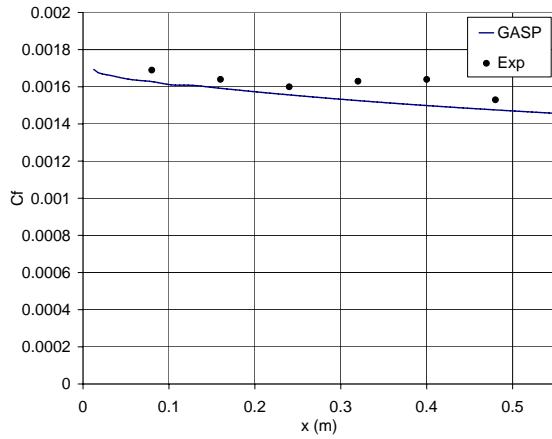
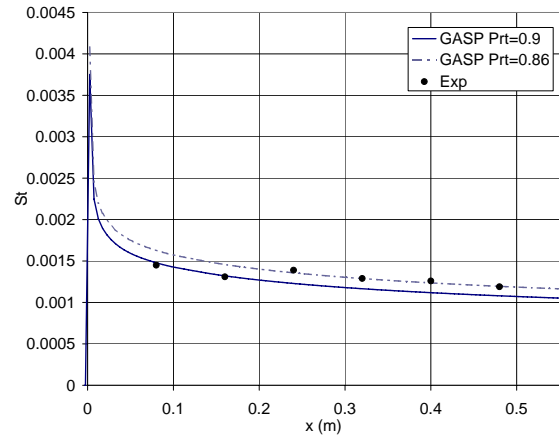


Figure 4.17: Skin friction coefficient and Stanton number for a supersonic boundary layer with a step in wall temperature with $T_w/T_r = 1.5$ compared with results from Debieve et al. [20]

4.4. VALIDATION STUDIES



(a) Skin friction



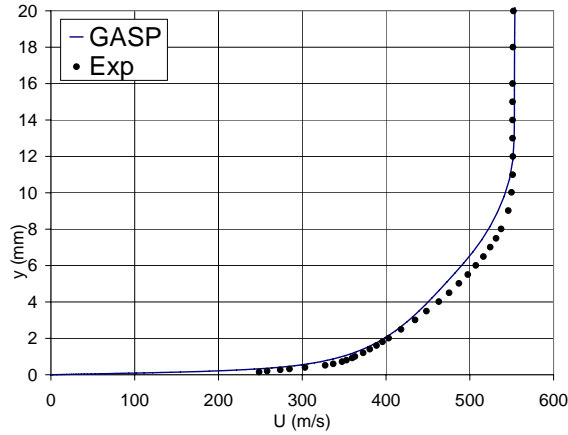
(b) Stanton number for Pr_t equal to 0.9 and 0.86

Figure 4.18: Skin friction coefficient and Stanton number for a supersonic boundary layer with a step in wall temperature with $T_w/T_r = 2$ compared with results from Debieve et al. [20]

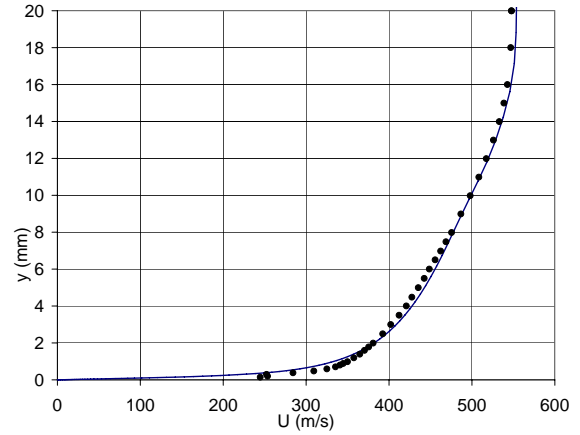
the S_t curve. The two turbulent Prandtl number solutions bracket the experimental data.

Velocity and temperature profiles are shown in Figs. 4.19 and 4.21. We notice that for both T_w/T_r ratios, the agreement in velocity is better at 8 cm. Agreement in temperature is good at both stations for both T_w/T_r ratios. Temperature profiles at both stations closely matches experimental results.

4.4. VALIDATION STUDIES

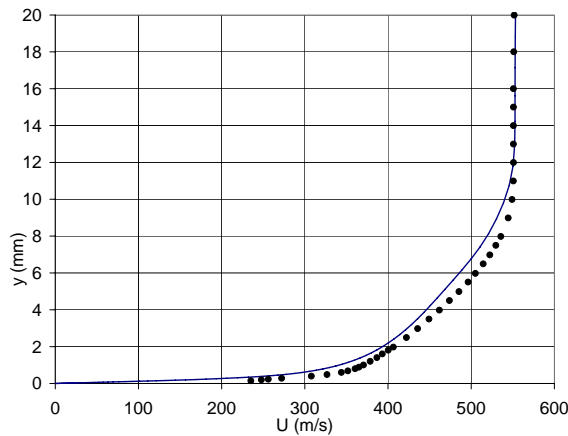


(a) Velocity at 8 cm $T_w/T_r = 1.5$

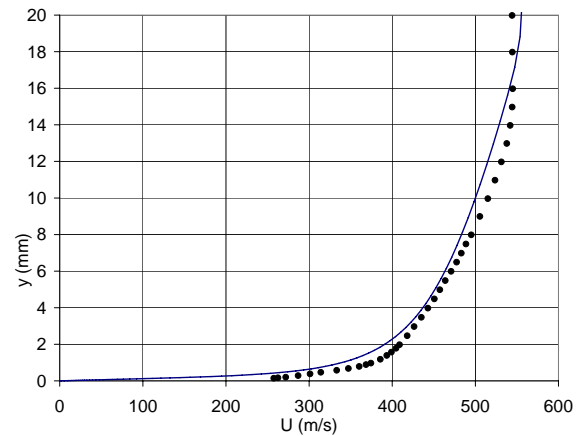


(b) Velocity at 46 cm $T_w/T_r = 1.5$

Figure 4.19: Velocity profiles for a supersonic boundary layer with a step in wall temperature at $x=0$ for ratios of $T_w/T_r = 1.5$ compared with experiment from Debieve et al. [20]



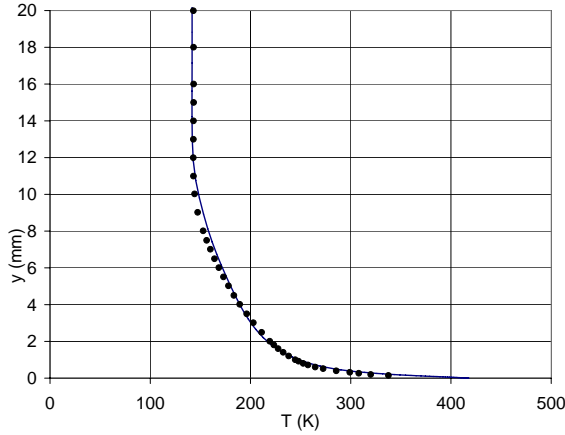
(a) Velocity at 8 cm $T_w/T_r = 2$



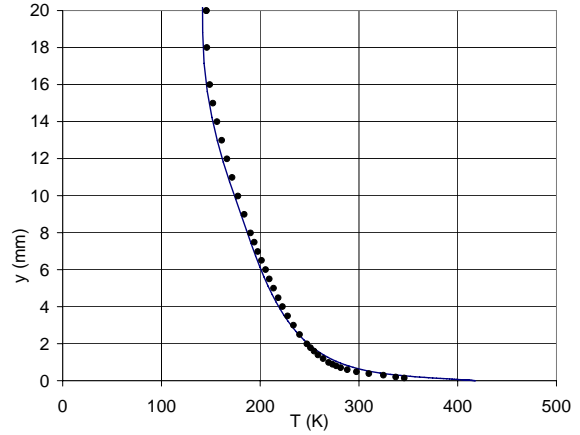
(b) Velocity at 46 cm $T_w/T_r = 2$

Figure 4.20: Velocity profiles for a supersonic boundary layer with a step in wall temperature at $x=0$ for ratios of $T_w/T_r = 2$ compared with experiment from Debieve et al. [20]

4.4. VALIDATION STUDIES

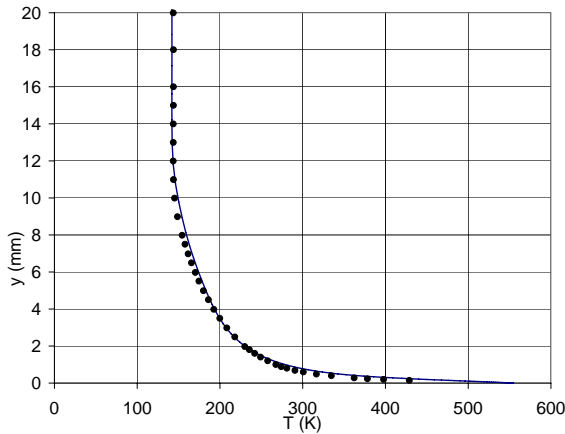


(a) Temperature at 8 cm $T_w/T_r = 1.5$

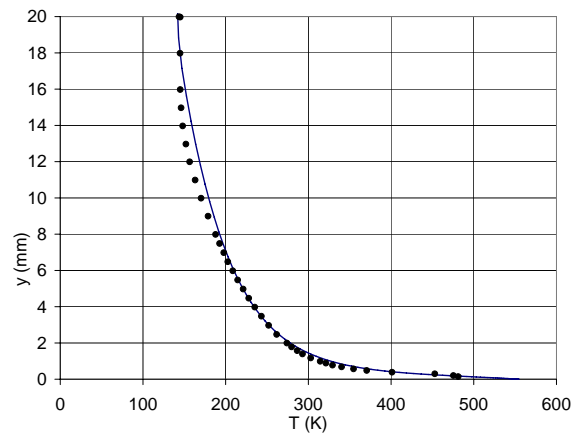


(b) Temperature at 46 cm $T_w/T_r = 1.5$

Figure 4.21: Temperature profiles for a supersonic boundary layer with a step in wall temperature at $x=0$ for ratios of $T_w/T_r = 1.5$ compared with experiment from Debieve et al. [20]



(a) Temperature at 8 cm $T_w/T_r = 2$



(b) Temperature at 46 cm $T_w/T_r = 2$

Figure 4.22: Temperature profiles for a supersonic boundary layer with a step in wall temperature at $x=0$ for ratios of $T_w/T_r = 2$ compared with experiment from Debieve et al. [20]

Chapter 5

Conjugate Heat Transfer

Conjugate heat transfer (CHT) pertains to heat transfer between a fluid and a solid in which the condition at the interface must be determined as a part of the solution. CHT problems are commonly found in real-world applications such as turbo-machinery, reentry vehicles, laser irradiation applications, deicing of aircraft wings, electronic cooling and more. First, the condition linking the fluid and the solid at the interface is described. Then, dimensional analysis is used to introduce the conjugate Peclet number. Results from a simplified theory are given as they help understand the influence of the key parameters. Finally, a new numerical treatment implemented in GASP is presented and validation results are shown.

5.1 CHT Theory

In conjugate heat transfer problems, the fluid and solid domains are interdependent and, must, therefore be coupled. The geometry for a laser irradiated target is shown in Fig. 5.1 as an example of particular interest here. The plate is irradiated by the laser beam and cooled by a fluid flow. The laser is modelled as a surface heat flux. A thermal and velocity boundary layer are growing on the plate when the heated spot generates a new thermal boundary layer imbedded inside the thicker boundary layer. This new boundary layer has its own time and length scales. The coupling between the fluid and the solid is done using the matching condition which expresses the continuity of the temperature and the conservation of energy at the solid-fluid interface. The matching condition is written as:

$$T_s|_w = T_f|_w \quad (5.1)$$

$$K_s \left. \frac{\partial T_s}{\partial z_s} \right|_w + K_f \left. \frac{\partial T_f}{\partial z_f} \right|_w = -I_0 f(x, y) \quad (5.2)$$

Since in general, the solid and fluid thermal conductivities are different, the temperature gradient is discontinuous at the wall. The function $f(x, y)$ varies from 0 to 1 to express the

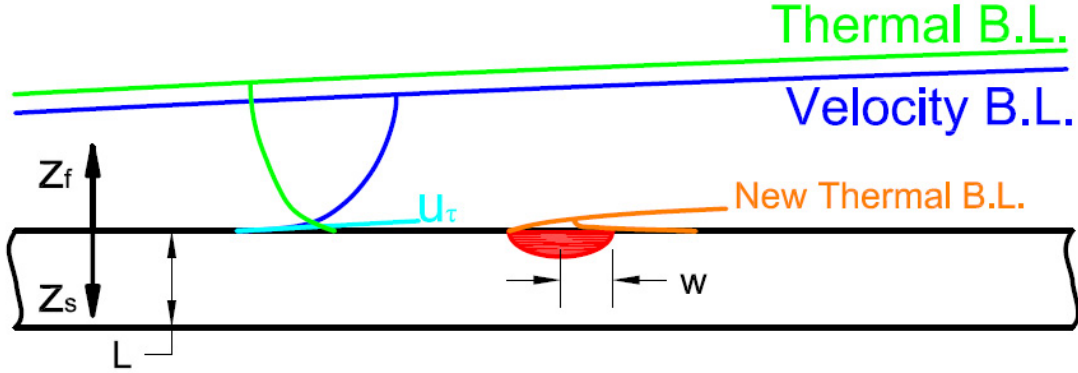


Figure 5.1: Geometry for the CHT problem of a laser irradiated flat plate

spatial variation of the laser intensity on the surface. For a Gaussian beam, the right hand side of Eq. 5.2 is given by Eq. 2.6. Next, dimensional analysis is used to gain some insight into the conjugate heat transfer problem.

5.1.1 Dimensional Analysis

Dimensional analysis is useful as it reduces the number of parameters needed to describe the temperature and introduces dimensionless groups that help shed light of the CHT problem. The following dimensionless variables are introduced:

$$\begin{aligned}
 x^* &\equiv \frac{x}{w}, & y^* &\equiv \frac{y}{w}, & z_s^* &\equiv \frac{z_s}{w}, & z_f^* &\equiv \frac{z_f}{w} (Pe)^{1/3}, & L^* &\equiv \frac{L}{w} \\
 T_s^* &\equiv \frac{T_s - T_r}{I_0 w / K_s}, & T_f^* &\equiv \frac{T_f - T_r}{I_0 w / K_s} \\
 q_s^* &\equiv -\frac{K_s}{I_0} \frac{\partial T_s}{\partial z_s} \Big|_w, & q_f^* &\equiv -\frac{K_f}{I_0} \frac{\partial T_f}{\partial z_f} \Big|_w
 \end{aligned} \tag{5.3}$$

Where the Peclet number, Pe is a dimensionless number that relates the heat convection to the heat diffusion inside the fluid. Here, the slope of the velocity profile at the wall times the beam width is chosen as the velocity scale and the beam width is chosen as the length scale leading to:

$$Pe \equiv \frac{\text{heat convection}}{\text{heat diffusion in the fluid}} = \frac{\frac{\partial u}{\partial y} \Big|_w w^2}{\alpha_f} \tag{5.4}$$

In Eq. 5.4, the Peclet number is raised to the 1/3 power to be consistent with the conjugate heat transfer literature. Historically, this exponent was introduced for convenience since it

is found in the solution in a line heat source. Substituting Eq. 5.4 into Eq. 5.2 using Eq. 5.4 leads to the dimensionless matching condition.

$$T_f^*|_w = T_s^*|_w \quad (5.5)$$

$$\Lambda \frac{\partial T_f^*}{\partial y_f^*} + \frac{\partial T_s^*}{\partial y_s^*} = -f(x, y) \quad (5.6)$$

where the conjugate Peclet number first introduced by Cole [16] is defined as:

$$\Lambda = \left(\frac{K_f}{K_s} \right) Pe^{\frac{1}{3}} \quad (5.7)$$

The conjugate Peclet number is important as it directly influences the balance of energy at the fluid solid interface. It contains both the properties of the fluid and the solid.

The Nusselt number is often used in conjugate heat transfer to present results in dimensionless form. This parameter isn't a direct parameter as it doesn't appear in the conservation equations [16]. The Nusselt number is defined as:

$$Nu_L \equiv \frac{\text{convection}}{\text{conduction in the fluid}} = \frac{hL}{K_f} \quad (5.8)$$

Generally, this parameter is averaged over the heated surface leading to the spatially averaged Nusselt number:

$$\overline{Nu_L} = \frac{\overline{h}L}{K_f} \quad (5.9)$$

where \overline{h} is the spatially average heat transfer coefficient over the heated surface. Using dimensional analysis it can be shown that $\overline{Nu_L} = \overline{Nu_L}(\lambda, \frac{L}{w}, Pe)$. Lee and Ju [41] have shown that a modified Nusselt number defined as

$$\overline{Nu_L^*} = \frac{K_f}{K_s} \overline{Nu_L} \quad (5.10)$$

is better suited as it is a function of less dimensional parameters since, $\overline{Nu_L^*} = \overline{Nu_L^*}(\Lambda, \frac{L}{w})$.

5.1.2 Effect of Conjugate Peclet Number

Cole [16] has used a surface element method to compute the steady state two-dimensional temperature distribution inside a plate with a small heated strip of length $2w$ for a wide range of conjugate Peclet number λ and geometric ratio $\frac{L}{w}$. A linear velocity profile was assumed. This simplified example is useful in assessing the effect of the conjugate Peclet number and the geometric ratio. Values of Λ ranging from 10^{-3} to 100 were studied. Large values of Λ can't be obtained in a flow of air on a metallic plate, since the value of the fluid

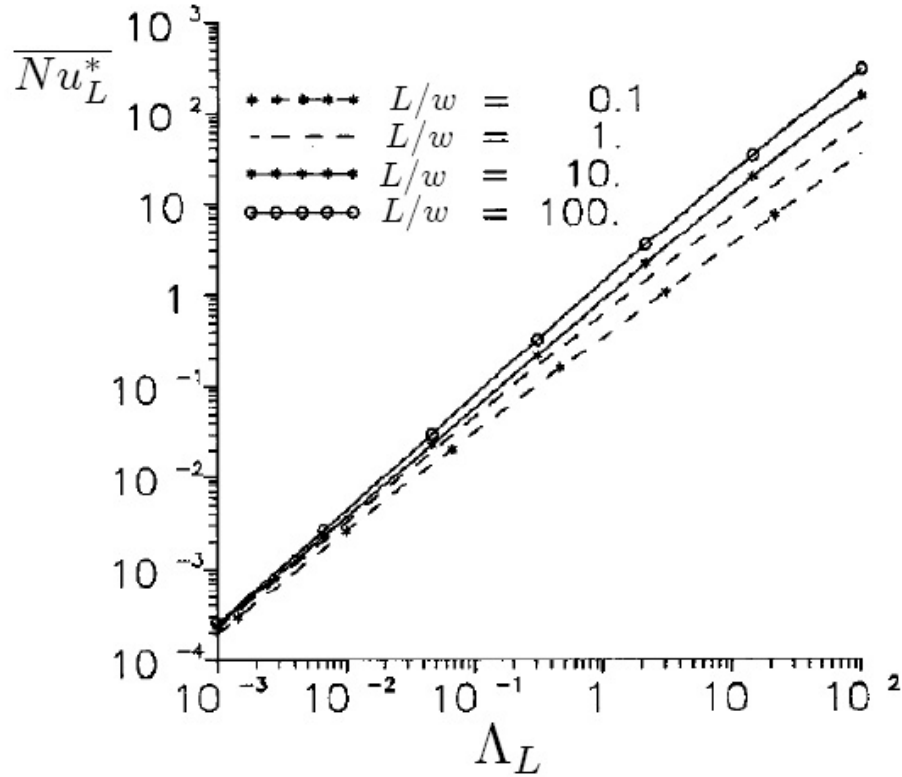


Figure 5.2: Spatially averaged modified Nusselt number based of the plate thickness L vs conjugate Peclet number based on the plate thickness L taken from Cole [16]

thermal conductivity K_f is much lower than that of the solid K_s . For a small value of Λ it is found that the data correlates better when using a value of the Conjugate Peclet number based on the plate thickness L .

$$\Lambda_L = \frac{K_f \left. \frac{\partial u}{\partial y} \right|_w L^2}{K_s \alpha_f} \quad (5.11)$$

Results obtained by Cole are shown in Fig. 5.2

Using the results from Fig. 5.2, the effect of the plate thickness and material is assessed for the flow conditions prevailing in the Virginia Tech supersonic wind tunnel. It is assumed that the heat spot has a diameter of $w = \sqrt{2}/2 \text{ mm}$ and is located at 0.1 m from the plate leading edge. In the computation of the conjugate Peclet number, the slope of the velocity profile is computed from the skin friction coefficient using Van Driest II correlation. (see section 3.2.3) Results are compiled in Table 5.1.

It is seen that the wall thickness and material has a significant impact on the heat transfer coefficient meaning that a conjugate heat transfer analysis must be performed as the actual

5.1. CHT THEORY

Table 5.1: Effect of plate thickness and material on heat transfer coefficient

Material	L [inch]	Λ_L	$\Lambda_L w/L$	h [$W/m^2 K$]	q_f/q_0 [%]
Stainless	5.6×10^{-3}	0.01	0.5	350	5
Aluminum	5.6×10^{-3}	0.0013	0.06	187	1.2
Stainless	0.1	0.07	0.19	250	3.6
Aluminum	0.1	0.008	0.02	174	1.1
Stainless	1	0.32	0.09	233	3.4
Aluminum	1	0.036	0.01	139	0.9

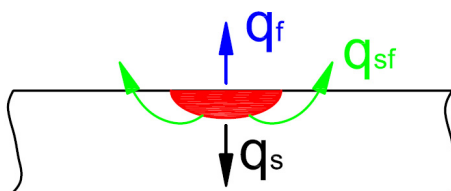


Figure 5.3: Heat balance at the surface

heat transfer coefficient doesn't only depend on the fluid flow but also on the physical properties and geometry of the solid. It is found that an aluminum plate has a lower film coefficient than stainless steel plate. The film coefficient also reduces with an increase in the plate thickness. Those trends can be understood by looking at the fate of the heat deposited on the surface by the laser beam. As seen in Fig. 5.3 part of the heat is directly transferred to the fluid (q_f), whereas another part is absorbed by the solid. Since the heat flows both axially and radially in the solid, part of it will be reabsorbed (q_{sf}) by the fluid such that the balance for a steady state is the following:

$$q_0 = q_s + q_f + q_{sf} \quad (5.12)$$

For a material with a lower thermal conductivity, less diffusion occurs inside the material such that more heat can directly be extracted by the flow over the heated area. The same thing can be said of a thinner plate. Moreover, for a thinner plate, the heated area increases such that more heat can be extracted. In Table 5.1 the ratio q_f/q_0 is computed for the different material/plate thickness combinations for a target temperature of 1000 K. A thin plate of stainless steel will have the greatest ratio of q_f/q_0

As seen in Table 5.1, the film coefficient doesn't vary monotonically with the conjugate Peclet number. Since w/L has a strong influence on the film coefficient, the conjugate Peclet number is multiplied by w/L to try scaling the data. The film coefficient is plotted as a function of $\Lambda_L w/L$ in Fig. 5.4

It is found that the film coefficient scales reasonably well with $\Lambda_L w/L$ when using a power law as seen in Fig. 5.4. Along the same line of thought, Li and Ortega [43] have formulated

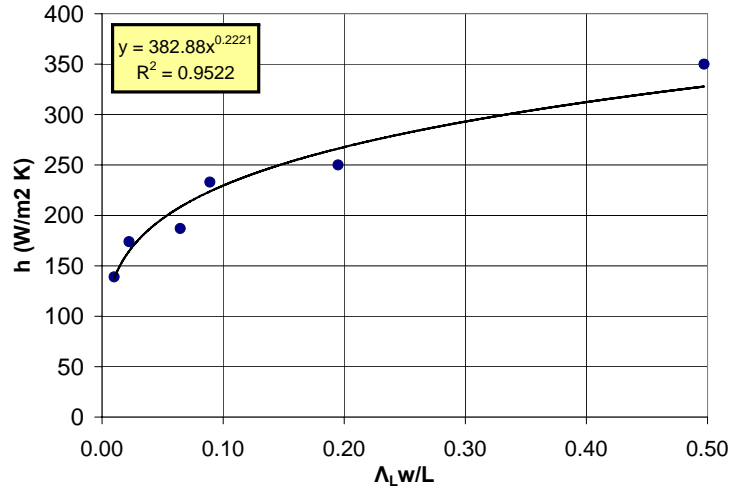


Figure 5.4: Correlation for the film coefficient as a function of $\Lambda_L w/L$

a conjugate Peclet number which includes w/L :

$$Pe^* = \frac{K_f w}{K_s L} Pe^{\frac{2}{3}} = \frac{K_f w}{K_s L} \left(\frac{u_\tau w}{\alpha_f} \right)^{\frac{2}{3}} \quad (5.13)$$

Here, the Peclet number is computed using the friction velocity instead of the slope at the wall. The 2/3 exponent is included since it appears in the solution of two-dimensional strip source. For a thin plate, Yiming and Ortega have found that Nu^* scales with Pe^* where Nu^* is defined as:

$$Nu^* = \frac{K_f w}{K_s L} Nu \quad (5.14)$$

Even if the preceding analysis is useful in understanding the effect of the key parameters namely the geometric ratio and the conjugate Peclet number, it can't be used to give a precise prediction of the surface temperature for a laser irradiated target. This is because a simple 2-D geometry, with linear velocity profile and a steady state are assumed in the preceding analysis. The actual irradiated target will generate an unsteady three-dimensional temperature distribution subjected to a supersonic turbulent flow. A numerical algorithm is then developed to included all those important features. This algorithm is presented in the next section.

5.2 Numerical Algorithm

The conjugate heat transfer algorithm needs to insure the conservation of energy and continuity of the temperature at the interface. Here, the fluid and solid domains are tightly

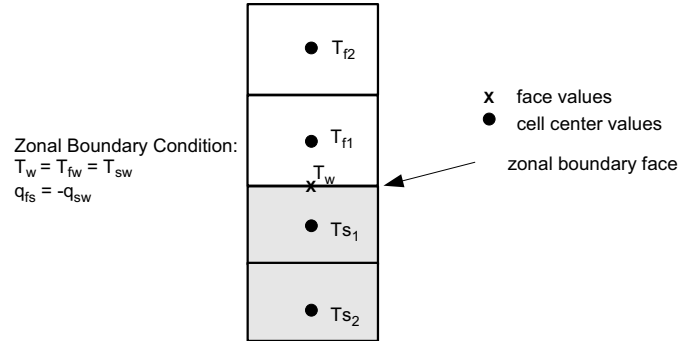


Figure 5.5: Schematic of the conjugate heat transfer problem

coupled using the matching condition (Eq. 5.2) [44]. In the following description, it may be helpful to refer to Fig. 5.5 for terminology. In this figure, the fluid dynamics zone (or grid) is on top and the shaded zone on bottom is the solid material zone. The boundary condition at a zonal boundary face (face common to both a fluid zone and a solid zone) is:

$$T_{fw} = T_{sw} = T_w \quad (\text{wall temperatures equal})$$

and

$$q_{fw} = -q_{sw} \quad (\text{heat fluxes equal and opposite})$$

where

$$q_{fw} = -k_f \left. \frac{\partial T}{\partial n} \right|_{fw} \quad q_{sw} = -k_s \left. \frac{\partial T}{\partial n} \right|_{sw}$$

When a surface heat source is present, the boundary condition becomes

$$q_{fw} = -q_{sw} - q_o$$

where q_o is an additional heat flux specified by the user. The above condition states the conservation of energy at the surface. The algorithm implemented here covering one iteration cycle is as follows (see fig 5.6):

1. The wall temperature along the zonal boundary is computed at each boundary face. This is done by setting the heat flux for the fluid face equal to the heat flux for the solid face and solving for temperature. This results in a temperature that satisfies the constraint of an equal and opposite heat flux for each zonal boundary face. The heat flux uses a second-order, one-sided stencil for the temperature gradient at the boundary face.
2. The fluid zone is then solved for. Fluxes are computed for each face and boundary conditions are applied. The unknowns (ie, density, velocity, pressure, turbulence quantities) at each cell center are updated.

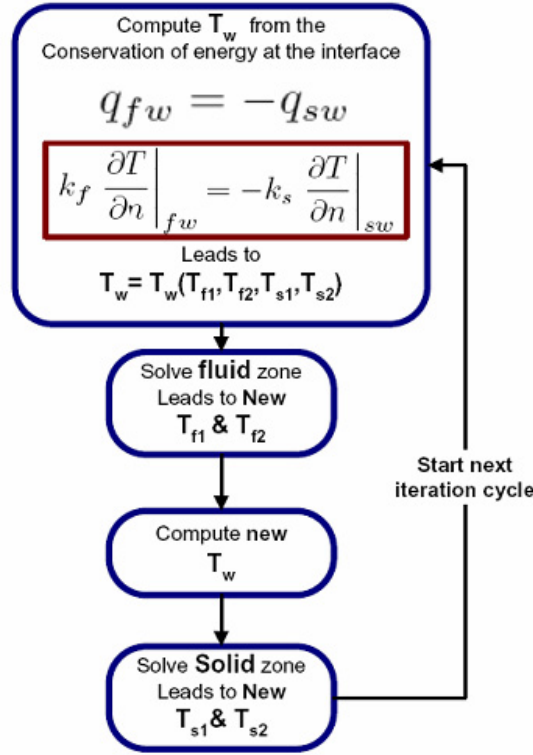


Figure 5.6: Conjugate heat transfer iterative algorithm

3. The wall temperature is then updated along the zonal boundary due to the updated fluid dynamic solution. Again, the condition of an equal and opposite heat flux is imposed to compute the wall temperature.
4. The solid zone is then solved for. Fluxes are computed for each face and boundary conditions are applied. The unknowns (temperature) at each cell center are updated.

This completes one iteration cycle. At convergence, a common wall temperature is converged to which satisfies the condition that the wall temperature for the fluid is equal to the wall temperature for the solid ($T_{fw} = T_{sw}$), as well as equal and opposite heat transfer fluxes. For a time-accurate solution, the algorithm is performed on the fictional time at the inner iteration level using the dual time stepping algorithm.

5.3 Validation Study

Supersonic flow inside a cooled axisymmetric convergent divergent nozzle is investigated next (see Fig. 5.7). The analysis is based on the experimental data reported by Back et al. [3] Prior to expansion in the nozzle, the air is heated by the combustion of methanol and

5.3. VALIDATION STUDY

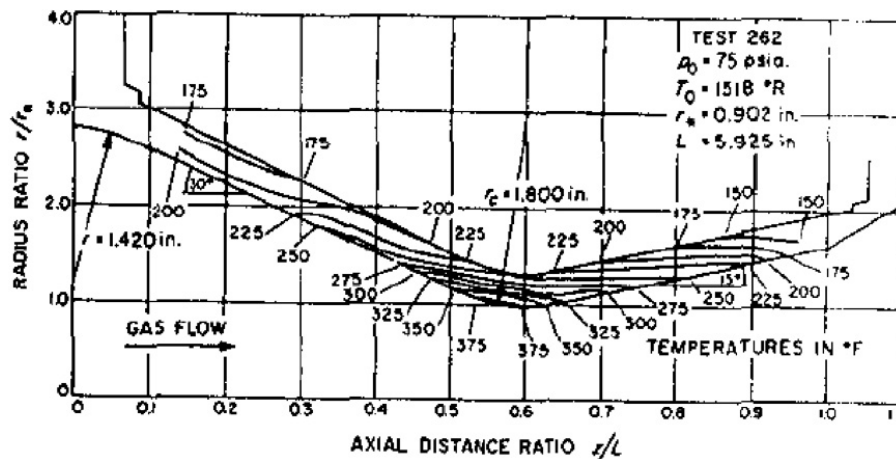


Figure 5.7: Temperature distribution ($^{\circ}F$) inside the nozzle from thermocouple measurements by Back et al. [3] reported by Delise and Naraghi [21]

directed through a calming section followed by a cooled approach section of 18 inch. The mass fraction of the methanol being small (compared to air), the real gas mixture can be approximated as a perfect gas. The nozzle and the approach section are water-cooled on the outside of the wind tunnel wall. The temperature distribution inside is experimentally obtained by using sets of three thermocouples embedded in the wall (the first on the flow side, the second at the wall center and the third on the cooled side) at 22 locations along the nozzle wall. The uncertainty on the temperature measurements is approximately 2% [3]. The temperature distribution inside the wall is depicted in Fig. 5.7 by Back et al. [3] reported by Delise and Naraghi [21]. The following flow conditions prevail.

- $T_0 = 843.33 \text{ K}$
- $p_0 = 5.171 \times 10^5 \text{ Pa}$

This case has previously been analyzed by Delise and Naraghi [21] and Liu [54] et al.. Delise and Naraghi didn't model the heat transfer inside the solid by directly using the wall temperature on the flow side as a boundary condition. Their analysis is useful as their results show that an algebraic turbulence model can't be used to accurately model heat transfer in the vicinity of the throat since the favorable pressure gradient causes a reduction in turbulence intensity which in turn causes a reduction of heat transfer. This phenomenon can't be modeled using an algebraic turbulence model (mixing length) or an empirical correlation (N-R correlation). Over predictions of heat transfer of 20% and 70% are obtained by Delise and Naraghi [21] for the mixing length turbulence model and the N-R correlation respectively.

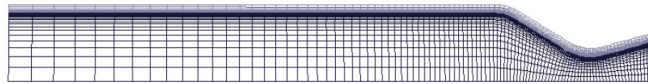


Figure 5.8: Cooled nozzle grid containing 6800 cells

The wall material wasn't specified by Back et. al. [3]. However, the thermal conductivity of the material K_w can be determined from the temperature gradient and the heat flux provided by Back et al. [3].

$$q = K_w \frac{\partial T}{\partial n} \Rightarrow K_w = \frac{q}{\frac{\partial T}{\partial n}} \approx \frac{q \Delta n}{\Delta T} \quad (5.15)$$

where q is the heat flux and K_w the thermal conductivity of the wall material. From Fig. 5.7, k_w is computed by approximating the temperature using the temperature difference between two isotherms separated by a known distance in a region where all the isotherms are parallel to the wall. In that case the heat conduction is 1-D such that the heat flux is constant across the wall. The following value was obtained

- $K_w = 27 \frac{W}{mK}$ corresponding to AISI 405 stainless steel

The conjugate heat transfer problem is solved by imposing the temperature at the outside wall taken from Fig. 5.7. The inside wall temperature doesn't need to be imposed since the boundary condition for conservation of energy at the interface is used as described in Section 5.2. The temperature distribution inside the wall as well as the flow field are being determined. The problem was modeled as axisymmetric. The grid containing 6800 cells is depicted in Fig. 5.8.

As for the previous cases, a grid independent solution was achieved by performing a grid refinement study. Four turbulence models were used namely, Spalart-Allmaras, 1998 Wilcox $k - \omega$, Menter's SST and Chien's $k - \epsilon$. Here, turbulence modeling has an impact on wall temperature (and therefore heat transfer rate) as each model reacts differently to the nozzle favorable pressure gradient which reduces turbulence. The ratio of eddy-viscosity to laminar viscosity is shown in Fig. 5.9. The Spalart-Allmaras model results displays a lower initial amount of eddy viscosity and a fast decrease from the favorable pressure gradient starting upstream of the throat, whereas the $k - \epsilon$ displays a much higher initial level of eddy-viscosity as well as a significant increase near the throat. The Spalart-Allmaras model offers the best agreement with the experimental data as seen in Fig. 5.10 where the computed internal wall temperature is compared with the experimental results. The nozzle Mach number and the nozzle wall temperature contours are depicted in Fig. 5.11. We notice that the wall temperature distribution (Fig. 5.11) is similar to the one obtained by Back (Fig. 5.7).

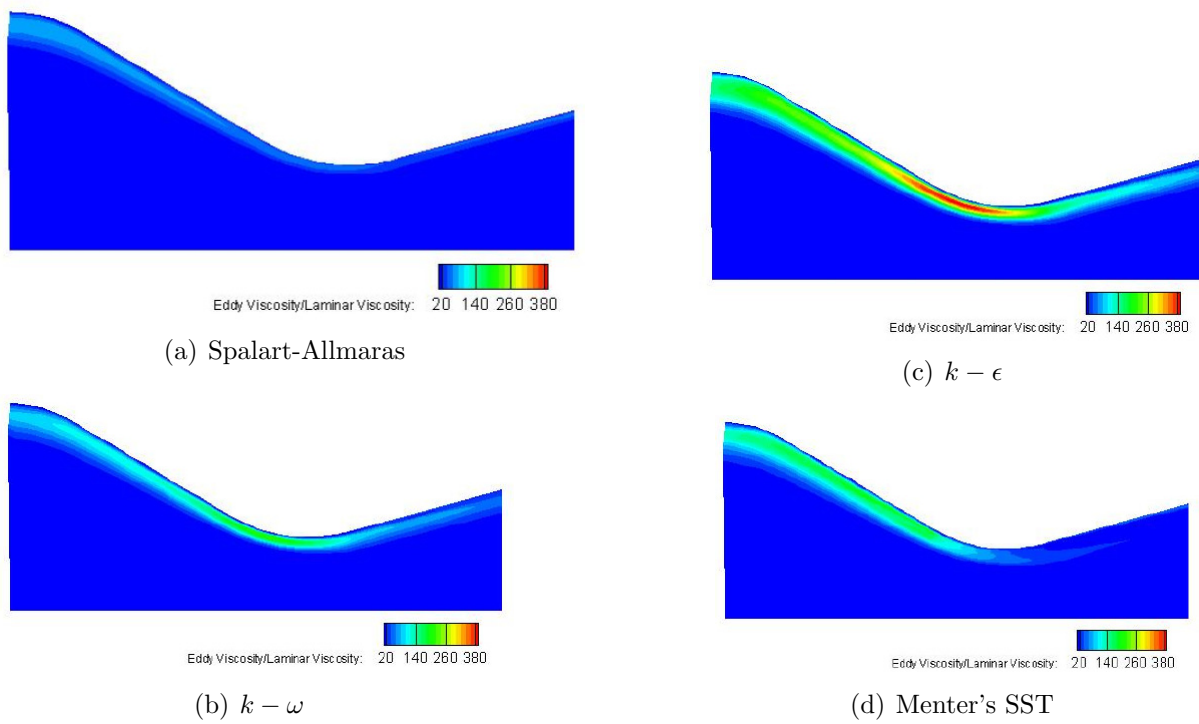


Figure 5.9: Ratio of eddy to laminar viscosity for a cooled axisymmetric nozzle

5.3. VALIDATION STUDY

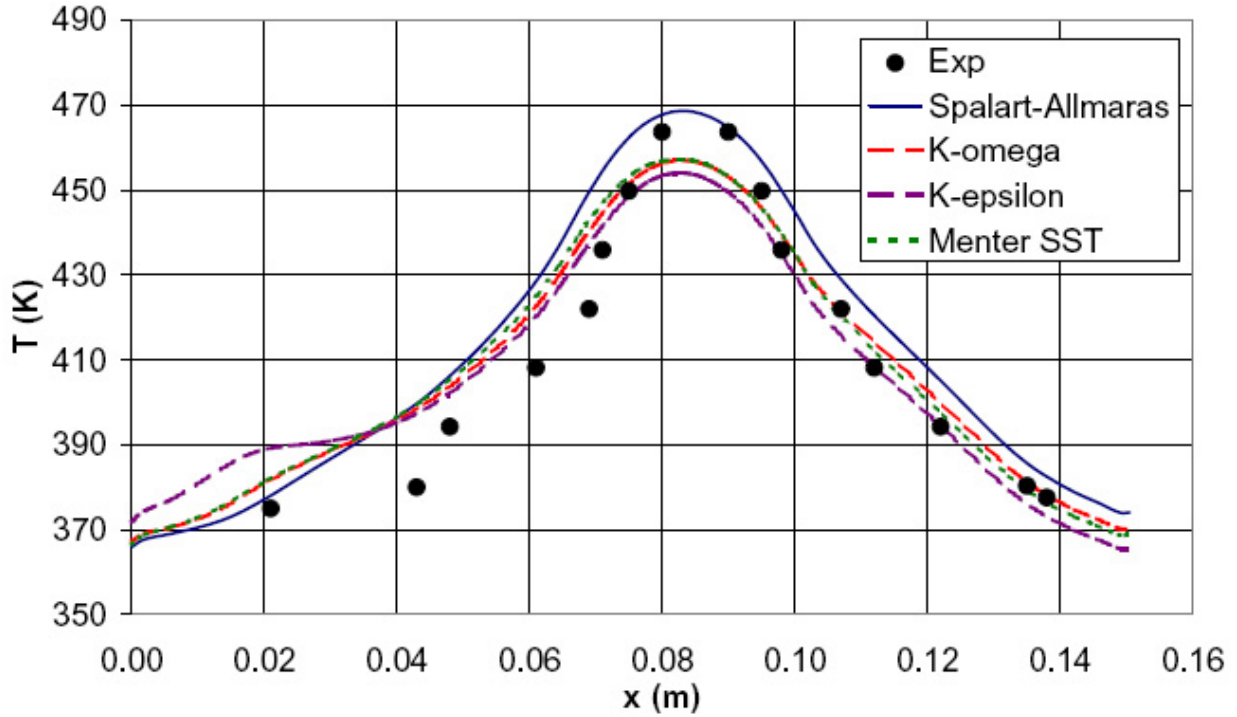


Figure 5.10: Inside wall temperature for a cooled axisymmetric nozzle compared with experiment from Back et al. [3]

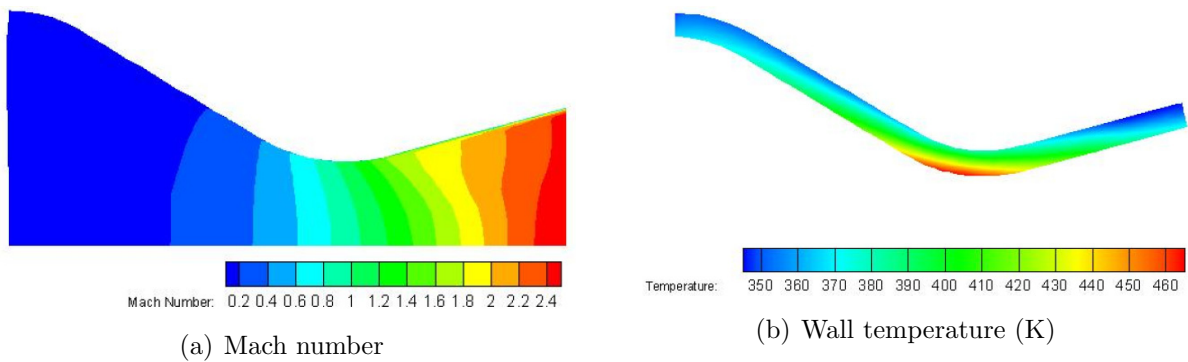


Figure 5.11: Mach number and wall temperature contour for a cooled axisymmetric nozzle using Spalart-Allmaras turbulence model

Chapter 6

Experimental Apparatus and Methods

The experimental setup required to investigate the effect of supersonic flow over a laser heated target is detailed in this chapter. First, the methodology used in the design of the experiment is illustrated. Then, each critical component is detailed and an uncertainty analysis is performed.

6.1 Design Methodology

The objective of the experiment is to investigate the effect of a supersonic flow field over a laser irradiated target. To our knowledge this is the first time that such an experiment is performed.

The measurement of the temperature distribution on a laser irradiated target is a difficult task due to the large temporal and spatial gradients over a very small area. This means that the measurement must provide an adequate spatial resolution and an adequate time response. Preliminary two-dimensional simulations have shown a small convective cooling varying from 20 to 40 K compared to the no-flow case. The small value of the predicted cooling contributes to the difficulty as experimental uncertainties can reach the same magnitude as the predicted cooling.

Analytical methods and numerical simulations were used to design the experiment. Our goal was to generate reliable measurements that can be used to validate the conjugate heat transfer model. In order to lower the experimental uncertainties, the convective cooling has to be maximized. We have seen in Section 5.1.2 that this implies a maximization of the conjugate Peclet number Λ_L and the beam geometric ratio w/L . This introduces the following requirements:

1. Thin turbulent boundary layer

6.2. OVERVIEW OF PREVIOUS EXPERIMENTS

2. Low solid thermal conductivity
3. Thin plate and/or large beam diameter

Each requirement is discussed next. A thin turbulent boundary layer can't be obtained on the floor or on the wall of the wind tunnel since the boundary layer grows over a large distance and is expanded through a nozzle. A detailed experimental and numerical analysis of the of the boundary layer in the Virginia Tech supersonic wind tunnel at Mach 4 is given in Appendix B. To get a thin boundary layer, a flat plate must be inserted into the flow. This configuration is referred to a splitter-plate. If the target is positioned too close to the leading edge, the boundary layer could be laminar or transitioning. In section 3.3, the transition phenomenon was looked at and it was determined that the boundary layer will be fully turbulent at $0.09m$ from the leading edge. Therefore, the laser beam center was located after $0.1m$ from the leading edge. By using a splitter plate configuration instead of the performing the experiment on the tunnel floor, the film coefficient is almost doubled.

The effect of the material was investigated in Section 5.1.2 where it was found that stainless steel leads to a much greater conjugate Peclet number due to it's low thermal conductivity. Stainless steel also as the advantage of sustaining high temperature. AISI-303 stainless steel was chosen as the plate material.

The geometric ratio w/L can be made large by increasing the beam width or by making the plate thin. Here to facilitate repeatability, we chose to avoid using any external optics. The thickness of the plate near the target center fixed to 0.1 inch.

6.2 Overview of Previous Experiments

Since this was the first time that such an experiment was to be performed by our research group, a literature review is made to asses the effectiveness of some previous designs. By reading various papers, we notice that very few researchers present a detailed and rigorous uncertainty analysis. Moreover, to our knowledge, no experimental study of the temperature distribution on a laser heated target submitted to a supersonic flow is available in the literature. Experiments on a laser heated ceramic disk have been performed at Oak Ridge Laboratory [26, 27]. The surface temperature was measured using a Radiance 1T infrared camera. For this problem, the temperature variation across the thickness is insignificant such that the temperature on only one side is measured. The calibration procedure of Ferber [27] consists in using thermocouple readings on an electrically heated plate to relate the temperature to pixel value. The temperature is varied by varying heater input voltage. This calibration procedure isn't the best as infrared cameras and thermocouple have similar precisions. One would prefer using a more precise standard for calibration. Furthermore, if the plate temperature isn't uniform, the location of the thermocouples needs to be precisely located on the image in order to assign the proper temperature value to the proper

pixel. The authors didn't report the accuracy of their system. A more accurate calibration methodology requires the use of a blackbody source. Most factory calibrations are performed in that way.

Schultz [61] used infrared thermography to measure film cooling of gas turbine components. An *in situ* calibration was performed using thermocouples in order to find the three coefficients of the camera calibration function. Sargent et al. [67] used a similar procedure. Once again the accuracy is limited to the accuracy of the thermocouples.

6.3 Design Overview and Selection of Components

6.3.1 Design Overview

The main components of the proposed measurement system are depicted in Fig. 6.1. As we can see, the system uses both infrared thermography and thermocouples mounted on the splitter plate. Three data acquisition and control modules are present. Each are linked to a different computer. Next, a description of each component is given and the selection process explained.

6.3.2 Splitter Plate and Paint

A drawing of the splitter plate is shown in Fig. 6.2. The plate contains two inserts that can be removed if damaged. The laser hits the first insert which is 0.1 inch thick. The second insert can be used to mount a Pitot tube. The strut-mounted plate can be located on the side wall or on the test section floor plate which allows taking Schlieren or shadowgraph images. A picture of the splitter plate fixed to the tunnel wall is shown in Fig. 6.3.

The inserts are mounted on a 0.25 inch thick plate. In order to get good repeatability, the surface must be consistent from run-to-run. It is well known that metals oxidize at high temperature. The oxidation process changes the absorptivity of the target such that the absorbed power varies. A protective coating must, therefore, be used to insure good repeatability. To be effective, this coating must be able to withstand high temperature above 1000 K. The plate was painted using Pyromark 2500 flat black paint. This silicon based paint has an absorptivity of 95% and emissivity of 0.85 [50] and can sustain a temperature of 1350K.

A structural analysis was performed to make sure that the aerodynamic loads could be sustained. The absolute load case used corresponds to a dual starting of the wind tunnel (nonsymmetric starting). The stresses in the bolts were analyzed using the methods found in ESDU 67019 [24]. Shear stress, bearing and tearout failure modes are analyzed. A factor of safety of 9 is found for the design.

6.3. DESIGN OVERVIEW AND SELECTION OF COMPONENTS

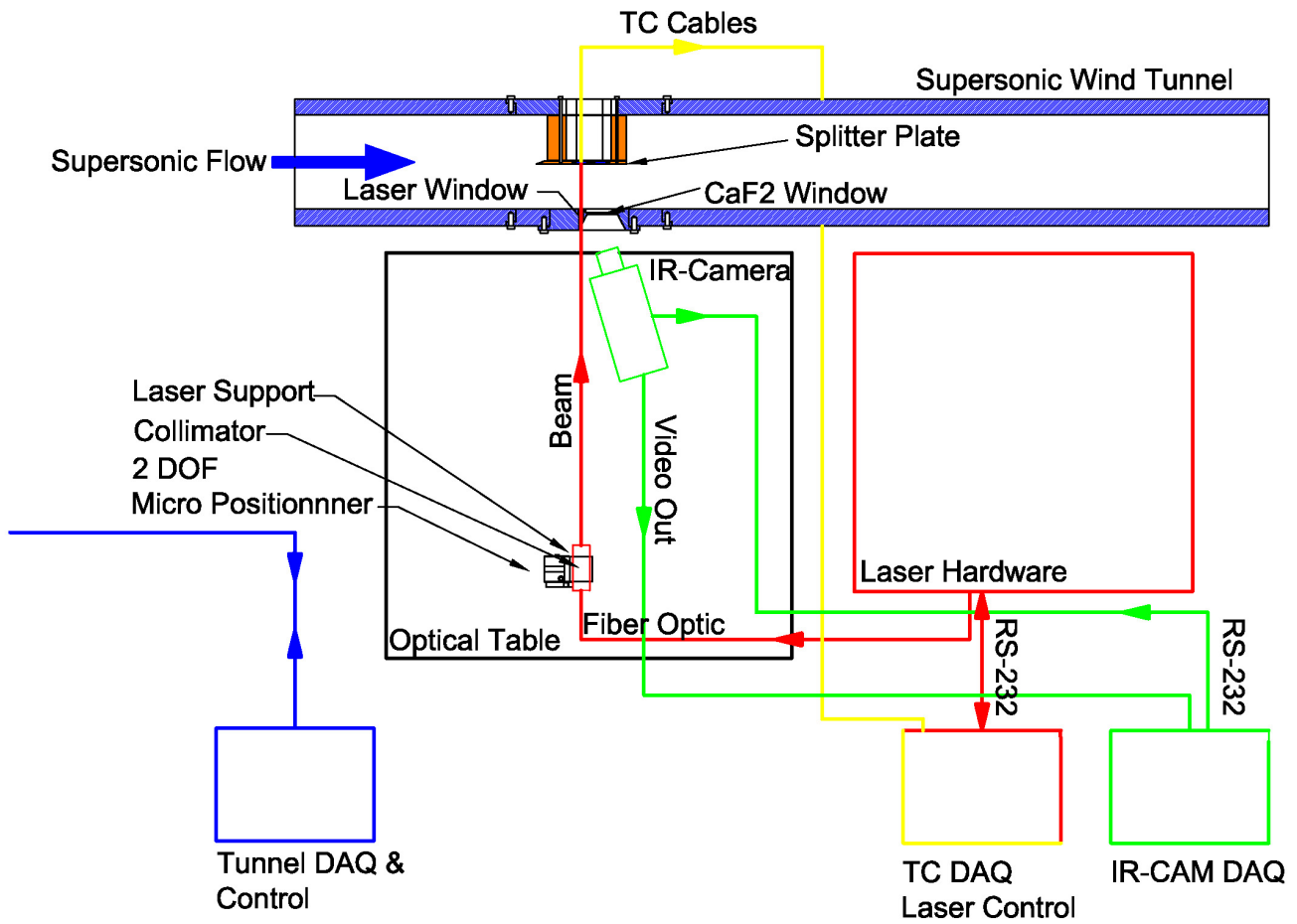


Figure 6.1: Overall experimental layout

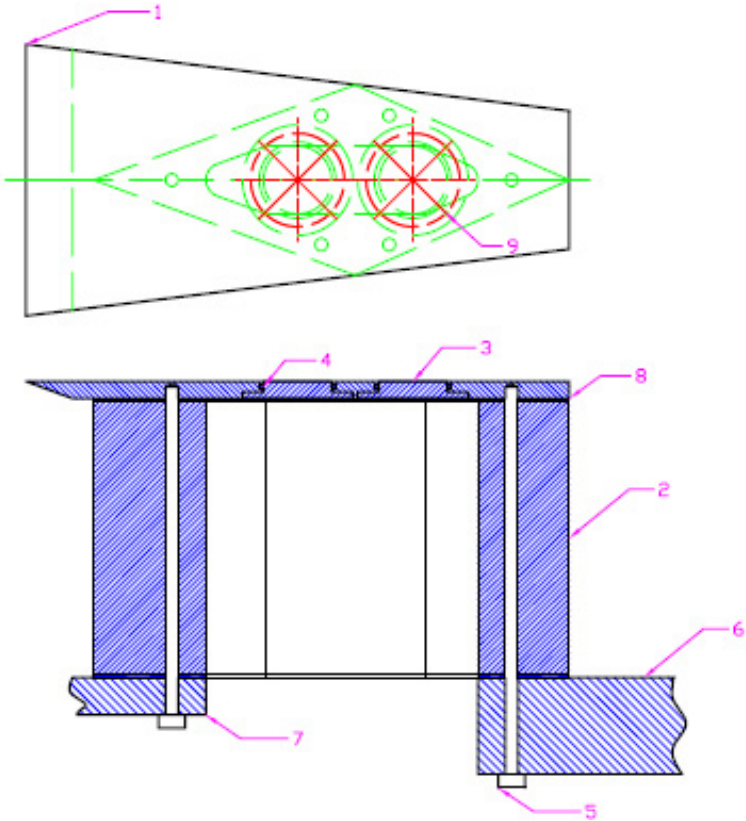


Figure 6.2: Splitter plate and strut mount assembly

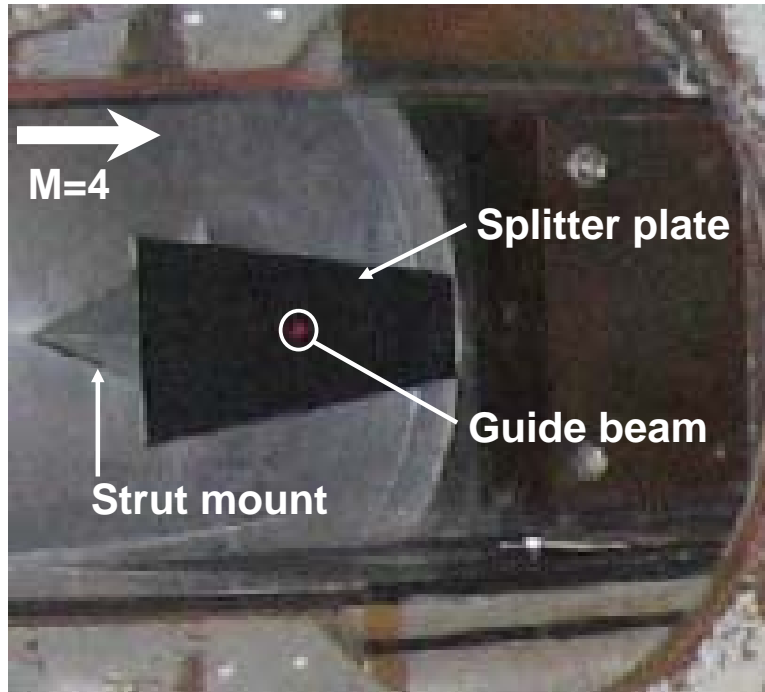


Figure 6.3: Splitter plate fixed on the wind tunnel wall irradiated with the guide beam

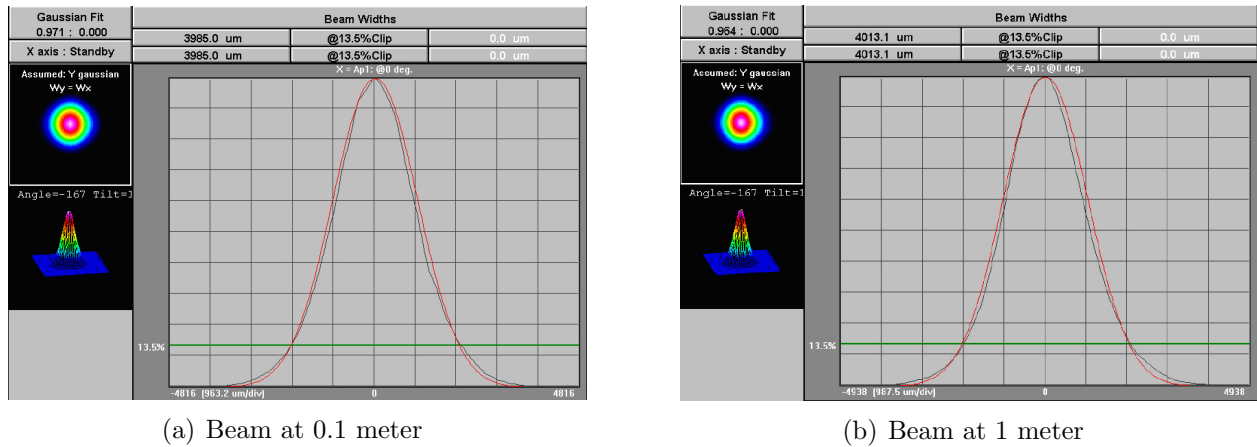
In section 2.1.4, the analytical solution for the temperature distribution caused by a Gaussian heat source was given. This solution can be used to quickly predict the target temperature. Using Fig. 2.1.4 for $L^* = 1.8$ which corresponds to the ratio L/w for our geometry, we get a normalized temperature of $\eta = 1.18$ at $t^* = 25$. For a power of 81 Watts this give a temperature increase of 960 K after 11 seconds. This time roughly corresponds to the tunnel run time. This estimate of the temperature increase is conservative since the material properties are assumed constant. In reality, the thermal conductivity of stainless steel increases with temperature such that the temperature raise is reduced. This phenomenon was observed by making numerical simulations. An absorbed power 81 Watts is the maximum power that can be used without damaging the paint.

Surface temperature measurements were made on both side of the plate. Since the temperature distribution inside the wall is tree-dimensional, the use of thermocouples can be problematic as they can modify the temperature inside the solid. Moreover, since the heated area is less than 1 square inch with a beam radius of 4 mm it is physically difficult to insert a large number of thermocouples inside such a small area. Infrared thermography was therefore used as it offers a better spatial resolution and doesn't interfere with the heat conduction inside the solid. The time evolution of the temperature needs to be accurately captured as the heating occurs . Dynamic response of the measurement system is therefore of primary importance. The surface was heated with a continuous beam Ytterbium fiber laser emitting at 1.08 micron with a maximum power of 300 Watts such that safety is a primary issue.

6.3. DESIGN OVERVIEW AND SELECTION OF COMPONENTS

Table 6.1: Laser Specifications

Manufacturer	IPG Photonics
Model	YLR-300-SM
Maximum Optical Power	300 W
Minimum Optical Power	30 W
Output Optical Power Accuracy	2%
Central Emission Wavelength	$1083 \pm 2nm$
Beam Diameter at e^{-2} level	$4 \pm 0.015mm$
Guide Beam	1 mW @ 640-660 nm
Cooling	Filtered Tap Water
Interface	Handheld or RS-232



(a) Beam at 0.1 meter

(b) Beam at 1 meter

Figure 6.4: Beam Quality: The Gaussian fit is found on the upper left as well as the beam diameter

6.3.3 Laser

A 300 W single-mode, continuous-wave Ytterbium fiber laser is used for this experiment. The laser characteristics are found in Table 6.1. This laser is made for industrial application such that it is relatively simple and safe to operate. Being in the infrared range, the beam can't be seen with the naked eyes so a guide beam is provided for alignment. The beam quality can be appreciated in Fig. 6.4 (provided by IPG Photonics) which shows that the Gaussian beam used in our analysis is valid and that the beam diameter doesn't significantly change with distance. The laser can be controlled using a handheld device or with a computer using the RS-232 standard. The main advantage of using computer control is that laser emission can be synchronized with data acquisition.

A LabVIEW program used to control and display the state of the laser was written by Steve Edwards the wind tunnel electronic engineer according to our specifications. This program

has the following functionality

- Turn emission on and off
- Turn guide beam on and off
- Check laser status
 - Back reflection
 - Temperature
 - Power
- Set the power level
- Synchronize the data acquisition with the emission

A screen shot of the program interface is shown in Fig. 6.5.

6.3.4 Optical Table

The laser collimator was mounted on an optical table and positioned with two degrees of freedom using two translation stages each with a resolution of $3\mu m$. The collimator is fixed using a laser holder. For static testing, the instrumented model is also fixed on the table to facilitate the alignment and insure perpendicularity of the beam. Components are illustrated in Fig. 6.6.

6.3.5 Infrared Camera

The infrared camera has to satisfy the following requirements.

- Temperature calibration up to 1500 K
- Good spatial resolution
- High frame rate

The Indigo Merlin InSb camera was chosen, since it is able to meet the previous requirements. The main specifications of this camera are shown in Table 6.2. Next, the implication of each requirement is explained and related to the characteristics of the camera.

The maximum temperature that can be recorded is limited by the saturation of a given photodetector cell. This happens when all the electrons of a cell are released. The maximum

6.3. DESIGN OVERVIEW AND SELECTION OF COMPONENTS

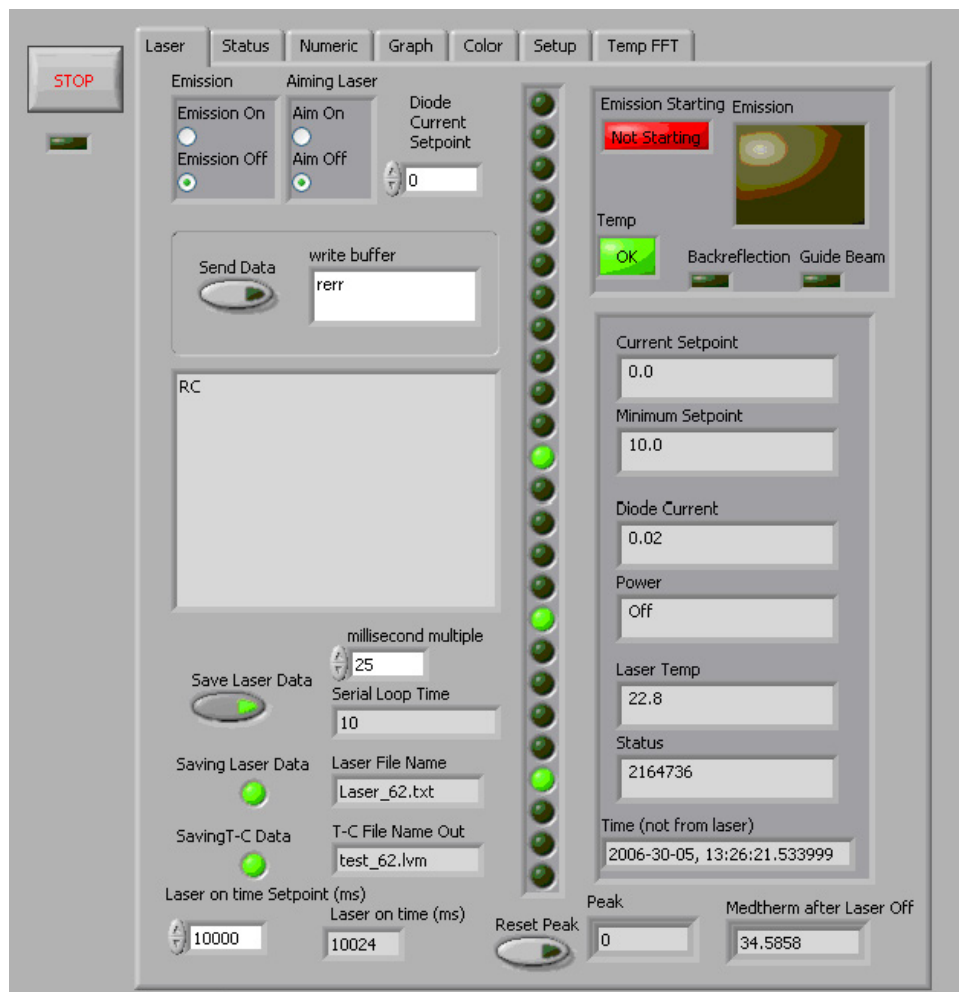


Figure 6.5: Laser LabVIEW control program GUI

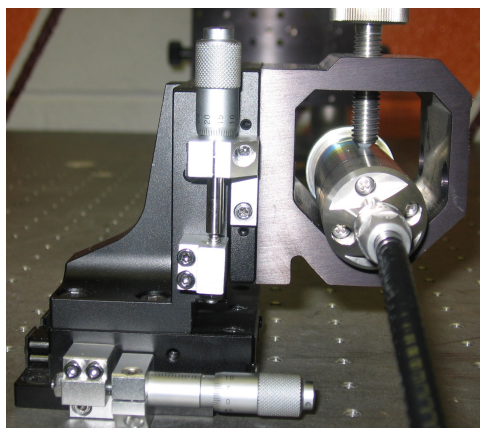


Figure 6.6: Optical table setup

6.3. DESIGN OVERVIEW AND SELECTION OF COMPONENTS

number of electrons that can be released is called the well capacity of the detector. One electron is released about 0.85 times a photon hits the photodetector where 0.85 is the quantum efficiency of the detector. In order to increase the maximum temperature, the integration time can be reduced. The integration time corresponds to the period of time elapsed before a "new" supply of electron is available. For such a period, a voltage is output and converted to a digital number so that the current temperature can be computed. However, a shorter integration time decreases the sensitivity of the camera as explained in Appendix C. The Merlin camera uses a Indium antimonide (InSb) detector which helps achieve a high sensitivity. Typically, a the Merlin camera can detect a temperature change as small as $0.025^{\circ}C$. However, InSb detectors have the inconvenience that they must constantly cooled to $77 K$ to operate properly. The cooling system limits the maximum angle of the camera such that the camera must be maintained close to the horizontal. This limitation is not problematic in our setup. The second option available to increase the maximum temperature is to add a filter to reduce the number of photons reaching the detector. Typically, neutral density filters was used. Those filters have a uniform spectral transmissivity. Here, a ND2 filter is used to achieve high temperature measurements. Such a filter possess a transmissivity of 10^{-2} . For each integration time, filter and lens combination, a radiometric calibration must be performed. This calibration is obtained by comparing the digital output of the camera to the known temperature of a uniform blackbody. The Indium antimonide detectors are known to display some significant variability such that each cell of the photodetector needs to have its own calibration. For this camera, the variability of each cell is corrected for using non-uniformity correction table (NUC). The NUC are generated during the calibration process. The precision of the system is therefore dependant on the uniformity of the blackbody. Six calibrations, NUC, are performed for a $25mm$ lens by the manufacturer and checked in house using a blackbody. The integration time and temperature range corresponding to each NUC are shown in Table 6.3.

The spatial resolution is now discussed. The greatest achievable spatial resolution called the pixel pitch is a function of the size of each photodetector cell and the wavelength of the infrared radiation sensed. The Merlin camera is sensitive to radiation in the mid-infrared range between 3 and 5 microns. The pixel pitch to $30 \times 30 \mu m$ for this camera. However, in practice, the spatial resolution is limited by the lens used and the distance from the target. Here, a $25mm$ lens was used and located about 6 inches from the target leading to a spatial resolution of approximately $0.240mm$.

A greater spatial resolution could be achieved by using a $50mm$ lens with an extender ring to increase the minimum focussing distance. This option would have required a new calibration and was therefore not used.

Since the temperature range resulting from the target heating is larger than the dynamic range of the camera, many runs must be repeated to get the totality of the temperature field. For a power of 81 watts, the NUC0, NUC2, NUC3, NUC4 and NUC5 are used which means that 5 runs are required. At each instant in time, the images must be combined to give a single image. A data reduction program was designed to perform this task. A schematic of

6.3. DESIGN OVERVIEW AND SELECTION OF COMPONENTS

Table 6.2: Indigo Merlin Infrared Camera Specifications

Detector	Indium antimonide
Format	$256 \times 320 - 78720$ elements
Pixel pitch	$30 \times 30 \mu m$
hline Spectral range	$3-5 \mu m$
Sensitivity	$0.025^{\circ}C$ NETD
Dynamic range	12 bits
Frame rate	$50hz$
$25mm$ Lens	$22^{\circ} \times 16^{\circ}$ Field of View - $f/\#2.5$

Table 6.3: Infrared Camera NUC

NUC	Integration time ms	Filter	Temperature Range K
0	1.7 ms	No	253-333
1	0.4 ms	No	293-398
2	0.08 ms	No	343-493
3	0.01 ms	No	413-623
4	0.25 ms	ND2	573-1000
5	0.015 ms	ND2	873-1873

the data reduction process is found in Fig. 6.7. The data acquisition was made with the ThermaCAM Image Desk software. This software can't be used to combine images. The Image Desk images were converted in Matlab .mat format. For each image, a Matlab file must be generated. The .mat file contains information about the image such as the time and the emissivity setting as well a 256×320 array that stores the temperature of each pixel as an 8-byte, double-precision float numbers. The software doesn't allow the conversion of a sequence of image, such that each image must be converted one by one. Typically, for a given run, 500 images must be converted. To avoid having to manually perform this tedious process, the conversion is automated by imbedding the Image Desk software into Microsoft Excel. Then, a VBA script was use to loop over all the images in a sequence and save each image in a .mat file. Each .mat file is read and combined in a 3-dimensional array by the data reduction program. The pixel corresponding to the center of the images must be given in order to center the images. The time origin must also be read by the data reduction program. This time correspond to the time at which the laser is turned on.

Moreover each pixel must be mapped to a given physical coordinate. This mapping was achieved by identifying the pixel corresponding to the edge of the heated insert. An edge detection algorithm could be used, but the process was performed manually as it was judged more reliable. Since the dimension of the insert is known, the size of a given pixel can be determined.

The vertical and horizontal pixel lengths are not the same since the camera isn't perfectly perpendicular to the target. In order to combined all the images, each image must be interpolated onto a uniform grid and time. First, all the images are interpolated on a uniform time. The initial time was set and a time interval of 0.02 second was used. The interpolation on a uniform grid was performed. The image center was taken as the origin of the coordinate system. The spacing of each grid point was set to 0.2mm which is smaller that the spatial resolution to avoid introducing an excessive interpolation error. linear interpolation is used for both the temporal and spatial interpolations. Once each image is interpolated on the same time and space grid, the combination can be performed. Since the image outputs a temperature that is too low when the signal is insufficient and since it saturates when the temperature is too high, the max function can be used to easily combine the images.

6.3.6 Thermocouples

Thermocouples are used to make surface and backside temperature measurements. The characteristics of the thermocouples are detailed next.

Surface Thermocouples

Two type-K surface temperature thermocouples from Medtherm corporation [18] was used to make surface measurements. One of 0.015" in diameter was located at the center of the heated insert. The other of 0.061" in diameter was located upstream to provide an accurate wall temperature boundary condition for our numerical simulations. A hole equal to the thermocouple diameter was made and the thermocouple press fitted in. Epoxy was used on the backside to fix the thermocouple in place. The Medtherm thermocouples have many appealing characteristics:

- Microsecond response to surface temperatures
- Precise location of the thermocouple
- High maximum operating temperature of 1560 K
- Chromel tube that closely match the plate thermal properties of the plate
- Flat surface which eliminate surface protuberance (Convective flow over the surface is minimally disturbed)

A fast response time is made possible by the two micron thickness junction formed by a vacuum deposited metallic coating over the sensing end of the probe. The thermocouple construction is depicted in Fig. 6.8

Backside Thermocouples

Eight, type-K thermocouples (SRTC-TT-K-40-36 from Omega) were fixed to the backside of the plate. This amount was judged sufficient to provide an adequate resolution while keeping thermal disturbances to a minimum level. The thermocouples are made of 0.003 inch (gage 40) wires. Such fine wires enable precise, pin-point measurements and fast response time. The thermocouples also have the advantage of being ready-made meaning that they come with insulation and standard subminiature connectors. An extension thermocouple wire of greater diameter (gage 30) was used to reach the DAQ. Since the connector and the extension wires of the same material as the thermocouple wire no accidental thermal junction is created at the connection, the second junction being in the DAQ. (see section 6.3.6). Moreover the thermocouple and extension wire are "special limit of error" with calibration errors of $1.1^{\circ}C$ or 0.4% (whichever is greater).

The backside reaches high temperatures such that a high temperature cement must be used to bond the thermocouples to the surface. Omegabond 400 high temperature cement was used. This cement possesses a high thermal conductivity and a maximum service temperature of $1425^{\circ}C$. The position of the thermocouples is shown in Fig. 6.9 where the dimensions are in inches.

Thermocouples Data Acquisition

Usually, temperature data are slowly varying signals such that low sampling rates are used. When a low sampling rate is used the higher frequency noise (50 to 200 Hz) must be removed using an analog filter before the analog-to-digital conversion. It is usually recommended to amplify the signal as close as possible to the thermocouple in order to reduce the effects of the noise. [28]

Here, a different approach was needed, since the signal varies rapidly (for temperature) and because we want to have a low sampling delay between channels to simulate simultaneous sampling. The National Instrument 6036E analog-to-digital converter with the AMUX-64T multiplexer was used for thermal data acquisition. The 6036E is a 16-bit successive approximation ADC with 8 differential channels and a maximum sampling rate of 200 kS/s. The input impedance for each channel is $100G\Omega$ in parallel with $100 pF$. This insures that the voltage drop in the thermocouple wires is insignificant. The AMUX-64T was used to increase the number of channels to 10 (one for each thermocouple). It also has a temperature sensor for cold-junction compensation. A sampling rate of 1000 Hz is achievable. The input range is software selectable and was chosen to $50mV$ to make sure that the quantization error is negligible.

LabVIEW was used to acquire and save the data to the hard drive. Each experiment doesn't last more than 45 seconds such that data file size isn't a problem. Since a high sampling rate of 1000 Hz was used, it is possible to distinguish the noise from the thermocouple signals

6.3. DESIGN OVERVIEW AND SELECTION OF COMPONENTS

after the analog to digital conversion. The noise can be removed by using either a digital low pass filter or a moving average. Many filters are already implemented in LabVIEW and can be applied in real time. The eight order inverse Chebyshev low pass filter has been found very efficient to remove noise.

As previously mentioned, the AMUX-64T contains a cold junction compensation (on channel 0). A direct voltage addition method for software cold-junction is used. This was performed by a built-in LabVIEW routine. This method follow the following steps [28]

1. Measure the reference-junction temperature, T_{ref}
2. Convert this temperature into an equivalent voltage for a type K thermocouple. This is done using the NIST polynomial which assumes a reference junction at $0^{\circ}C$
3. Add this equivalent voltage to the measured voltage, V_{MEAS} , to obtain the true open-circuit voltage that the thermocouple would produce with a reference junction at $0^{\circ}C$, $V_{TC}(T_{TC})$
4. Convert the resulting voltage into a temperature (using a NIST polynomial); this value is the thermocouple temperature, T_{TC}

When performing the final conversion, care must be taken especially with high temperatures (above $500^{\circ}C$). Depending on the voltage, a different calibration curve must be applied as no NIST polynomial is valid for the whole temperature range for type K thermocouples. It was checked that the built-in LabVIEW routine has a case control structure that chooses the right polynomial for a given voltage. The error associated to this curve-fit is very small $\pm 0.05^{\circ}C$

6.3.7 Windows

The selection of the window is critical for both safety and measurement accuracy. The design of the window insert is depicted in Fig. 6.11. Two windows are used, one for the laser and another for the infrared camera. A BK7 glass window of 0.5" in diameter was chosen for the laser. This window doesn't distort the beam and minimizes reflection such that the intensity profile on the surface remains Gaussian. The properties are shown on Table 6.4 which compiles information from the manufacturer [19].

Calcium fluoride (CAF₂) was chosen as the material for the infrared camera window as it has high and flat transitivity between 3 and 5 microns as well as an intrinsically low reflectivity such that an antireflection coating is not required. The window needs to be large enough such that it doesn't block radiation from the target. However, the thickness needs to increase significantly with an increasing diameter since the window has to sustain the load arising

6.3. DESIGN OVERVIEW AND SELECTION OF COMPONENTS

Table 6.4: Laser Window Properties

Supplier	CVI
Material	BK7 glass
Wedge	< 10 arc seconds
Diameter X Thickness(inch)	0.5 X 0.250
AR Coating Wavelength (nm)	1064
Incidence Angle with Polarization:	0
Damage Threshold	1MW/cm ² CW at 1064nm
Reflectivity at 0°	< 0.1% see Fig. 6.10

Table 6.5: IR-Camera Window Properties

Supplier	Vecor
Material	CaF ₂ IR grade multocrystal
Surface quality	60/40 (Precision optics)
Diameter X Thickness(mm)	75 X 8
Parallelism	3 arc min
Transmittance	see Fig. 6.12
Young's modulus	75.9 Gpa
Shear modulus	33.7 Gpa
Tensile Strength	36.5 Mpa

from the difference in pressure between the inside and outside of the wind tunnel. The properties of the CAF2 window are given in Table 6.5 [48, 51, 68].

The pressure difference between the outside and the inside of the wind tunnel generates a force close to 500 *lbf* for a 2.9" diameter window such that a structural analysis needs to be performed to determine the required window thickness. It is convenient to use the thinnest window possible as price drastically increases with thickness. The results of the structural analysis performed to evaluate the required thickness is presented in Appendix D.

6.3.8 Safety Considerations

It is self-evident that a 300 Watt laser capable of melting metal can be hazardous. Safety is, therefore, a key component of this project. To insure a safe environment, advice from laser manufacturer were followed and the Virginia Tech Laser Safety Program document is carefully studied. Two key safety components were identified.

1. Wear proper safety goggles
2. Contain the beam inside a safety enclosure

Trinity Glass Laser Filter 1138 goggles were worn at all time when the laser is operated. This filter has an optical density of 8 such that the maximum irradiance of the laser goes from $1.9E4W/cm^2$ to $1.9E - 4W/cm^2$. However, one need to be careful when looking at those numbers, since the eye is made to focus light such that the intensity is increased inside the eye. Another important feature is that the visibility is good with the goggles on.

A tool box was purchased and painted with Krylon 1602 ultra flat black paint to make the safety enclosure. The box was made light-tight by using metal and rubber sleeves and was mounted on the top of the optical table. The first set of static experiments was performed with everything enclosed in the box. For the wind tunnel testing, a hole was made and the box was pushed against the tunnel wall. Two persons are required to run the experiment. Our setup was reviewed and approved by the Virginia Tech Laser Safety Officer.

6.3.9 Virginia Tech Supersonic Wind tunnel

Tests were performed in the Virginia Tech supersonic 23×23 (cm) blow-down wind tunnel with a Mach 4 nozzle. A sketch of the facility is shown in Fig. 6.13. The specifications of the facility are presented in Table 6.6. The variation of the total pressure and total temperature are shown in Fig. 6.14. The pressure is maintained constant using a digital feed-back control system. Typically for the Mach 4 nozzle, a pressure of 150 *psi* is used, here a pressure of 160 *psi* was used to facilitate the startup considering the blockage of the splitter plate inside

the test section. The stagnation temperature can vary from day-to-day depending on the outside air temperature. From Fig. 6.14 we notice a sharp increase in temperature due to the starting shock followed by a steady decreasing during the run and a sharp decrease during the unstart. However, the decrease in temperature during the run has a small effect on the heat transfer over the heated spot as the wall temperature is much greater than the recovery temperature. Due to the low free stream temperature, a high Reynolds number can be achieved.

Table 6.6: Characteristics of the Virginia Tech Supersonic Wind Tunnel

Test Section $H \times W \times L$ (cm)	$23 \times 23 \times 30$
P_0	160 psi $\pm 1\%$ PID control
T_0	≈ 291 K depending on outside temperature
Nozzle	Mach 4
Run time	12 seconds
Re/m	5×10^7

6.4 Uncertainty Analysis

This section presents an uncertainty analysis for the infrared camera and thermocouples temperature measurements. To cancel the bias, errors the temperature difference between the flow-off and flow-on cases was taken. For that strategy to be effective, the tests must be highly repeatable. Repeatability was quantified and the uncertainty on temperature difference between the flow-off and flow-on case was determined for both the thermographic and thermocouples measurements.

6.4.1 Sources of Bias Error

The sources of bias errors for the infrared thermography and the thermocouples measurements are fundamentally different, since the infrared camera is based on radiation heat transfer and the thermocouple is based on conduction heat transfer.

An infrared camera doesn't directly measure temperature but irradiance coming from a target. The proper calibration makes it possible to relate the digital output of the camera (which is proportional to radiance) to the temperature. For a properly calibrated camera, the calibration error is around 0.75% [31] of the temperature reading. However, the irradiance reaching the photodetector isn't only due to the target and can be expressed as [53].

$$I_e = \epsilon_0 \tau I_0 + \tau(1 - \epsilon_0) \epsilon_{sur} I_{sur} + (1 - \tau) I_{atm} \quad (6.1)$$

6.4. UNCERTAINTY ANALYSIS

where I is the radiance, ϵ the emissivity, τ the atmosphere transmission and the subscript 0, refers to the object, sur to the surroundings, e to the detector and atm to the atmosphere. The second term on the right hand side expresses the irradiance from the surroundings which after reflecting on the object reaches the detector whereas the last term corresponds to the atmospheric irradiance. For short distances (especially in the 3-5 waveband where almost no absorption occurs) $\tau \approx 1$ such that the last term vanishes. When the emissivity of the measured object is low and the temperature of the object is similar to the temperature of the surroundings, the temperature of the surroundings has an influence on the irradiance reaching the detector. This is taken into account by the software which asks the user for the surroundings temperature. However, if the temperature of the surroundings changes when a measurement is taken, an error can be introduced. For our measurements, the emissivity of the object is large (0.85) and the object temperature is much greater than that of the surrounding such that $I_{sur} \ll I_0$. This implies that a variation of the surrounding temperature will not introduce a significant error. Eq. 6.1 also shows that the irradiance reaching the detector is a function of the object emissivity.

To assess the effect of the emissivity on the measured temperature, the value of the emissivity was varied in the Image Desk data analysis program. A emissivity of 0.85 ± 0.09 was used as reported in [50] for the Pyromark paint. The effect of a change in emissivity is seen in Fig. 6.15 for a mean temperature of $1099K$.

Next, the effect of the laser power was investigated. It is known from the analytical solution that the temperature increase is proportional to the laser power. Again $T_{mean} = 1099K$ is chosen as the value of the laser power was varied by $\pm 5\%$ as reported by the manufacturer.

The sources of uncertainty leading to a bias error when comparing the numerical solution with the infrared camera temperature measurements are the following:

1. Laser power uncertainty is $U_p = 5\%$. Since the temperature increase is proportional to the laser power, we have $\Delta T_{power} = 3.75\%$
2. Surface absorptivity uncertainty is $U_{absorptivity} = 3\%$. Since the temperature increase is proportional to the laser power, we have $\Delta T_{absorptivity} = 2.25\%$
3. Surface emissivity uncertainty is $U_{emissivity} = 10\%$. Using the data analysis software: $\Delta T_{emissivity} = 3\%$
4. Infrared camera calibration error is $\Delta T_{calibration} = 0.75\%$

The uncertainties are combined using the root-mean-square formula to leading the following cumulative bias error for the infrared camera measurements:

$$\Delta T_{IR} = \sqrt{\Delta T_{power}^2 + \Delta T_{absorptivity}^2 + \Delta T_{emissivity}^2 + \Delta T_{calibration}^2} = 5.35\% \quad (6.2)$$

The thermocouples are subjected to the laser power uncertainty and to a calibration uncertainty which is due to the variability of the thermocouple as the same calibration curve is used for all thermocouples. The calibration error is estimated to 0.5 %. Obviously, the thermocouples are not affected by the emissivity of the surface. However, since the thermocouple is in contact with the surface, its presence can modify the temperature locally as the heat flows into the thermocouple wire. The thermocouple can, therefore, modify the temperature through heat conduction losses. This implies that the temperature measured by the thermocouple is lower than what the temperature would be if the thermocouple wasn't attached to the surface. It was found that conduction losses play an important role for the backside thermocouple located close to the center. This makes sense as close to the center, a greater axial temperature gradient prevails. The conduction loss error is difficult to quantify since it depends on the temperature distribution in the solid. This error is not included in the evaluation of the cumulative uncertainty for the thermocouples measurement but will be considered when comparing the thermocouple measurements with the infrared measurements and the computed temperature. Since large temperatures are measured, the error introduced by the uncertainty in the cold-junction compensation can be neglected. The cumulative bias error on the thermocouple measurements is equal to:

$$\Delta T_{TC} = \sqrt{\Delta T_{power}^2 + \Delta T_{absorptivity}^2 + \Delta T_{calibration}^2} = 3.8\% \quad (6.3)$$

The bias error for both the thermocouples and infrared measurements are very large in comparison to the expected cooling due to the flow field. By performing a temperature measurement without the flow and subtracting this measured temperature from the temperature measured under the same laser setting but with the flow over the target it is possible to cancel the bias errors as the absorptivity, emissivity and calibration doesn't change. In order for bias errors to cancel, very good repeatability must be achieved. For instance, the laser must deliver the same power from run-to-run and the surface properties must remain constant. The uncertainty on the temperature difference is evaluated next.

6.4.2 Uncertainty on the Temperature Difference

An uncertainty analysis was performed for the temperature difference on the surface and backside for the thermocouple and the infrared camera. For the infrared camera, the following source of errors were considered separately.

- Misalignment: the position of the center needs to be the same when subtracting the flow-on temperature from the flow-off temperature
- Repeatability: the laser power output and wind tunnel flow condition needs to be consistent from run-to-run, and the initial temperature need to be precisely known.
- Timing error: the flow-on and flow-off image needs to have the same initial time

6.4. UNCERTAINTY ANALYSIS

The uncertainty arising from each source was considered separately and combined using the root-mean-square formula.

The uncertainty in position U_r was estimated to $0.02mm$. From this value, the resulting error in temperature was computed from the radial temperature gradient at any given location on the surface or the backside. The gradient was computed using the analytic solution Eq. 2.16.

The flow-on and flow-off case measurements were performed in sequence such that the position of the camera wasn't changed. However, some adjustment of the image was sometimes required to locate the maximum temperature at the center of the image.

The repeatability was quantified from a statistical analysis of the temperature recorded on the backside for three runs performed at the same laser power. To avoid including any positioning error, the maximum temperature measurements were used. The mean and standard variation were computed at each value of time. To consider the small number of samples available, a Student's t-distribution was used such that the uncertainty of the mean for a 95% confidence interval is multiplied by 2.353. The uncertainty varies with time and is greater for a small value of time. This is most likely due to the timing error. Since, we do not want to include the timing error in the random error, a constant value corresponding to a greater value of the time was chosen. A random temperature error of $2 K$ was computed and taken twice in the root mean square formula since it arises for the flow-on and flow-off cases. Here, it was assumed that the random error for the flow-off condition is equal to the random error for the flow-on condition. This is probably a conservative estimate since the change in the tunnel condition should contribute to the random error such that the random error for the flow-off condition should be smaller.

The timing error is assumed to be equal to $0.02s$ since the camera outputs 50 images per second. The temperature error resulting from the timing error is obtained by multiplying the timing error by the time rate of change in temperature. This implies that the temperature error due to the timing error is both a function of time and position. The global error was obtained using the root-mean square formula

$$\Delta T_{IR}(r, z, t) = \sqrt{\left(U_r \frac{\partial T}{\partial r}\right)^2 + \left(U_t \frac{\partial T}{\partial t}\right)^2 + 2\Delta T_{ran}^2} \quad (6.4)$$

The uncertainty for the temperature difference measured by the infrared camera on the surface and backside as function of distance for $t = 1s$ and $t = 10s$ is found in Fig. 6.16 We notice that uncertainty is a function of position and time. At the surface center, the uncertainty is smaller due to the absence of the positioning error. The positioning error is approximatively equal to zero at the center since it corresponds to a maximum in the temperature distribution. On the surface, the positioning error is the greatest at $1 mm$ from the center due to the large radial temperature gradient. From that position, the positioning error progressively decreases with distance such that away from the center the uncertainty is

6.4. UNCERTAINTY ANALYSIS

mainly due to the random errors. The timing error is maximum at the center where the time rate of change in temperature is the greatest. As time increases, the timing error becomes negligible. This is seen at the center by the reduction of the uncertainty from 8 K at $t = 1s$ to 8 K at $t = 10s$. On the backside, the radial temperature gradient is smaller than on the surface such that positioning error is small. This explains why at $t = 10s$ error is almost constant with distance as it is almost uniquely due to the random errors. For $t = 1s$, the timing error is important at the center which explains the greater uncertainty.

Next, the uncertainty of the backside thermocouples was investigated. Here it is difficult to separate the different sources. We assume the random error on the temperature difference will encompass the repeatability, positioning and timing error.

The temperature results from six runs performed at 81 Watts were used to compute the random error. Here, the statistical analysis was made directly on the temperature difference such that the error doesn't need to be multiplied by 2. The random error is computed for each thermocouple. Again the Student's t-distribution was used to compute the uncertainty on the mean from the standard deviation for a 95% confidence interval. The error is shown in Fig. 6.17.

Here the uncertainty is greater for thermocouples 3 and 8 which are the closest to the center. For most thermocouples the uncertainty increases with time. This could be due to conduction losses in the wires.

6.4. UNCERTAINTY ANALYSIS

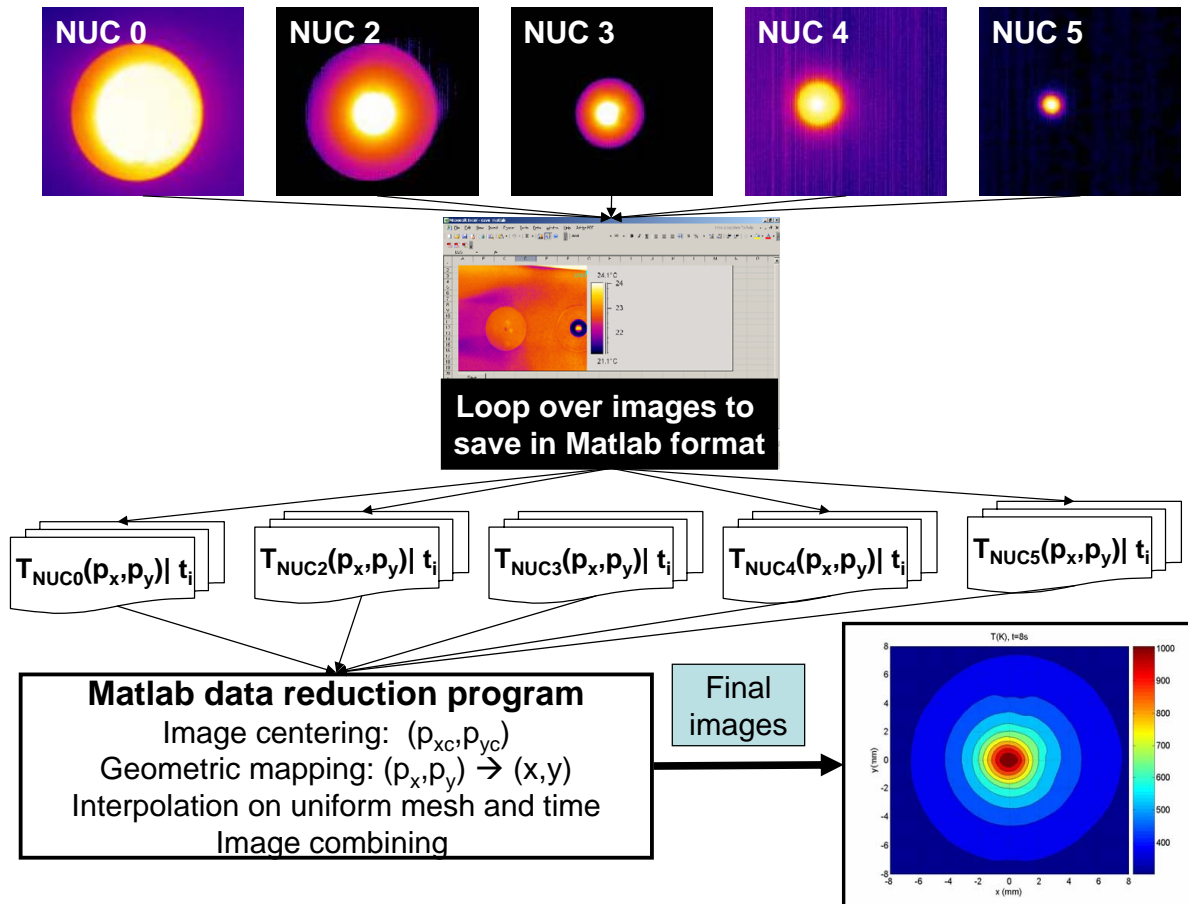


Figure 6.7: Data reduction of infrared camera images

6.4. UNCERTAINTY ANALYSIS

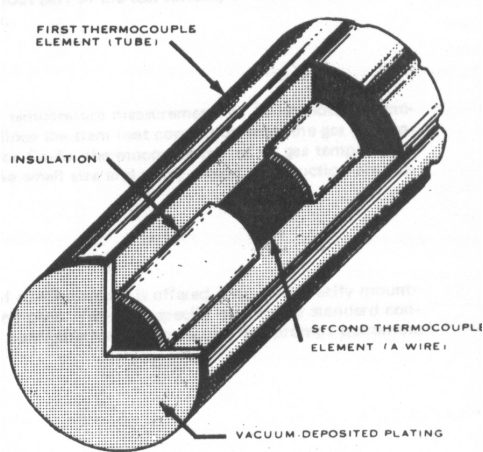


Figure 6.8: Medtherm thermocouple detail taken from [18]

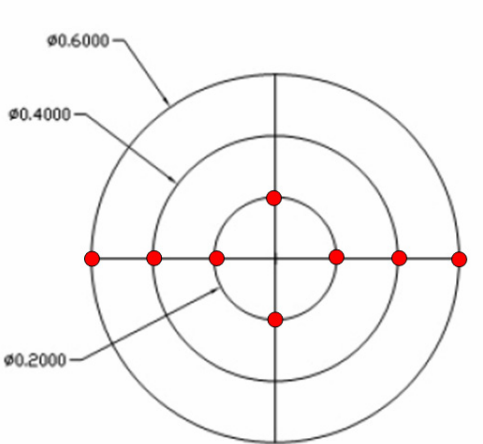


Figure 6.9: Backside thermocouple position

6.4. UNCERTAINTY ANALYSIS

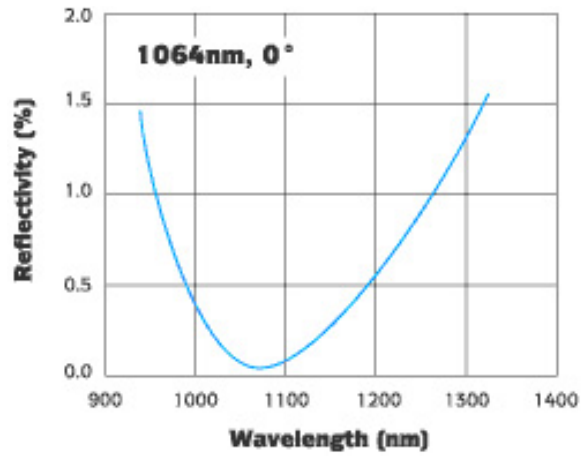


Figure 6.10: Reflectivity for 1064 nm coating at 0° [19]

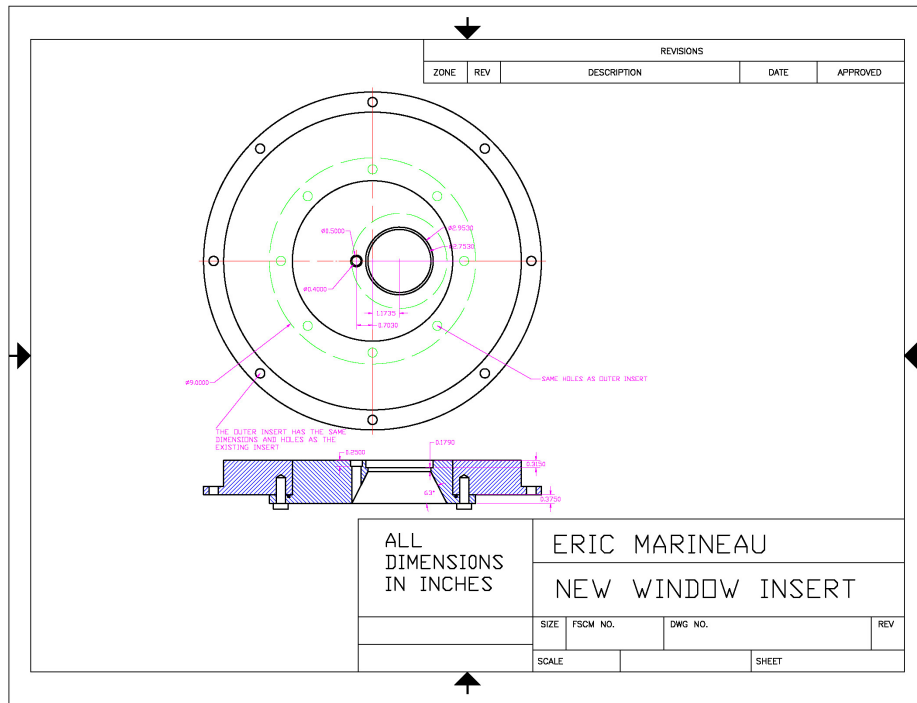


Figure 6.11: Window insert

6.4. UNCERTAINTY ANALYSIS

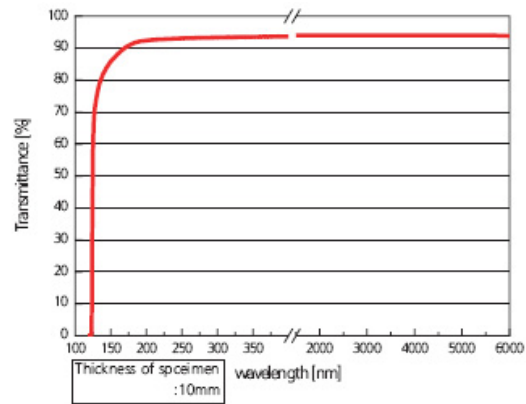


Figure 6.12: Transmissivity of calcium fluoride [51]

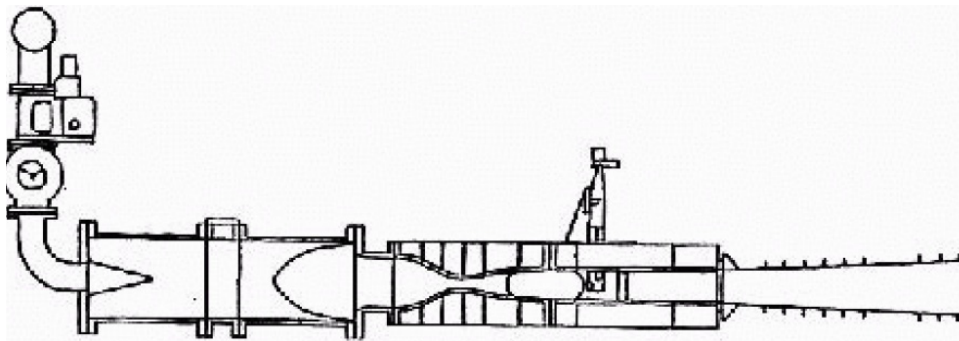


Figure 6.13: Side-view sketch of the Virginia Tech Supersonic Wind tunnel

6.4. UNCERTAINTY ANALYSIS

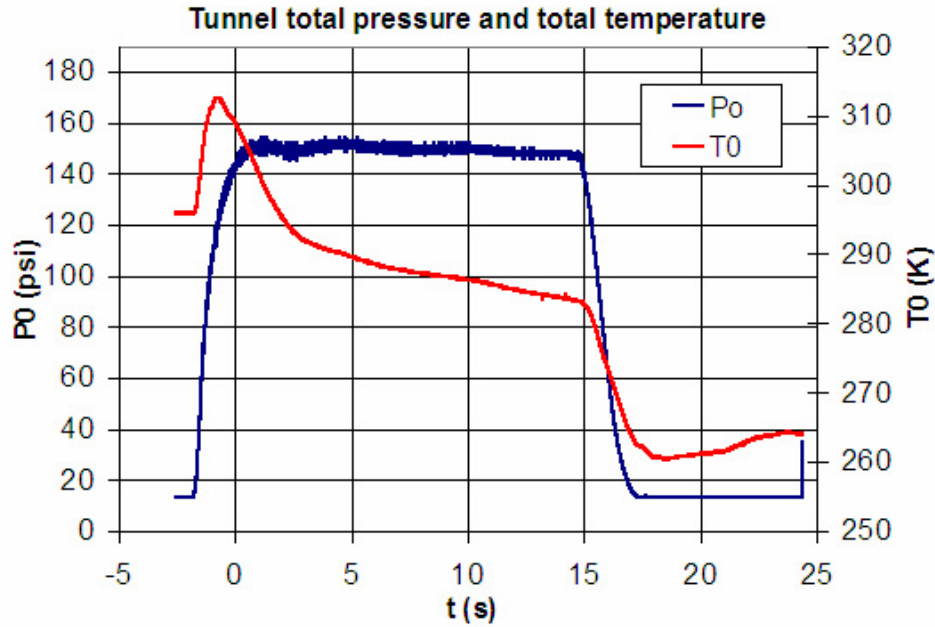
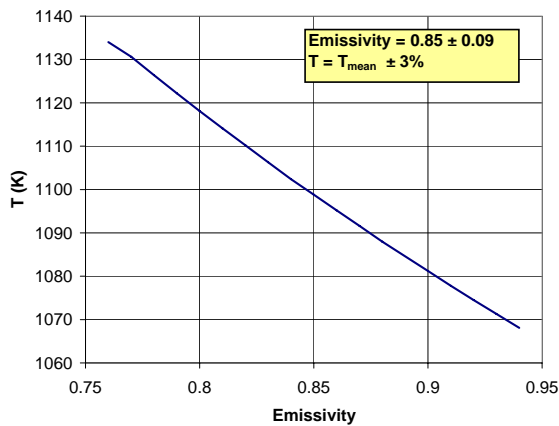
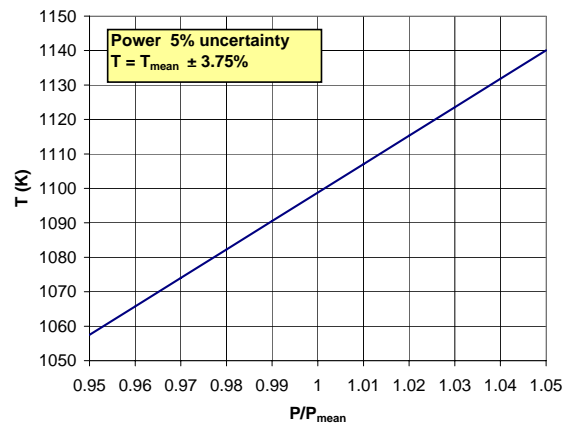


Figure 6.14: Total pressure and total temperature as a function of time for a typical run



(a) Bias error introduced by the emissivity uncertainty



(b) Bias error introduced by the laser power uncertainty

Figure 6.15: An uncertainty in the emissivity of 0.09 unit introduces a temperature error of 3% (of the temperature in K) whereas an uncertainty on the laser power of 5% (of the temperature in K) introduces temperature error of 3.75%

6.4. UNCERTAINTY ANALYSIS

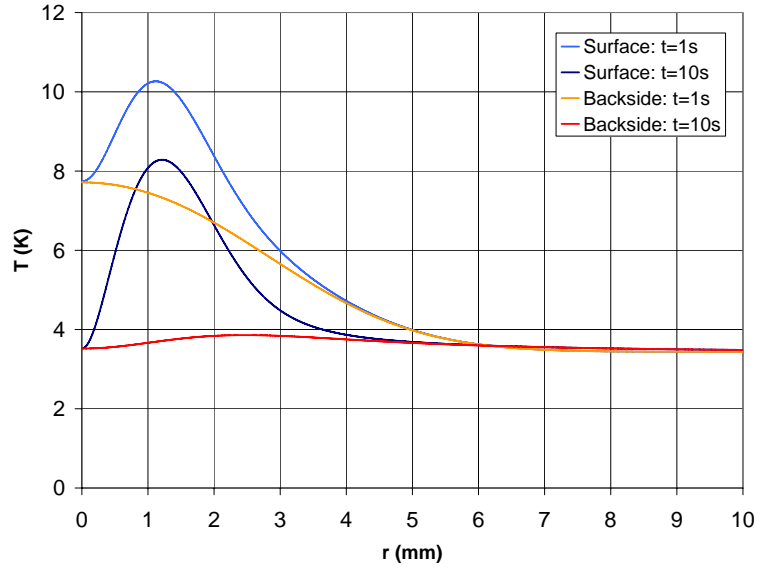


Figure 6.16: Uncertainty on the temperature difference measured by the infrared camera on the surface and backside as a function of distance for $t = 1s$ and $t = 10s$ for $P=81 W$

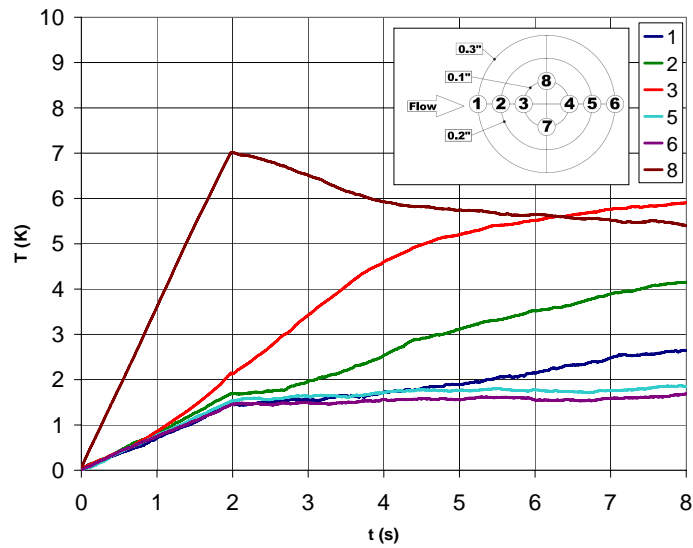


Figure 6.17: Uncertainty on the temperature difference measured by the thermocouples as a function of time.

Chapter 7

Experimental Results

Experimental results are presented in this chapter. The objective of the experiment is to quantify the effect of the supersonic flow-on the temperature distribution over the target. The experimental results are used in the validation of the conjugate heat transfer model. First, static (no-flow) testing was performed. Second a flow survey was performed.

7.1 Static Testing Results

Before carrying out the wind tunnel tests, static testing was performed to assess the proper functioning of the experimental setup. The target was fixed on the optical table inside the safety enclosure as shown in Fig. 7.1. Two rounds of testing are performed in May-June and July 2006 respectively. The tests had the following objectives.

- Test the laser control software
- Test the paint resistance to the thermal shock
- Learn the laser starting characteristics
- Assess the repeatability of the experiment

It was found that after the "emission on" command is sent, the laser takes between 3 and 4 seconds to start. Also, the requested power isn't achieved instantaneously but progressively increases to full power. This is depicted in Fig. 7.2. The exact shape of the ramp is unknown as the laser doesn't send the value of the power when below 25% ("low" is outputted). We see that the startup time is a function of the power output, but that repeatability is good for any given power value. The relation between the diode current (the quantity set by the laser control program) and the laser power was determined. Both are proportional in the

7.1. STATIC TESTING RESULTS

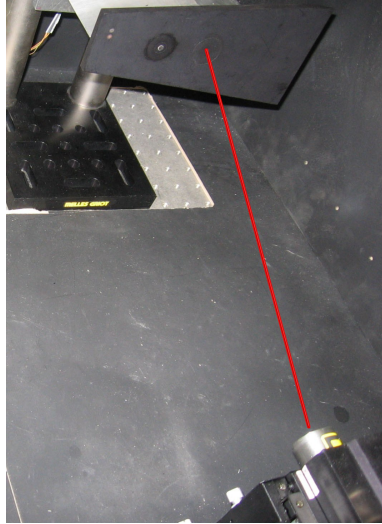


Figure 7.1: Picture of the static setup where the laser beam (simulated) is aimed at the splitter-plate insert

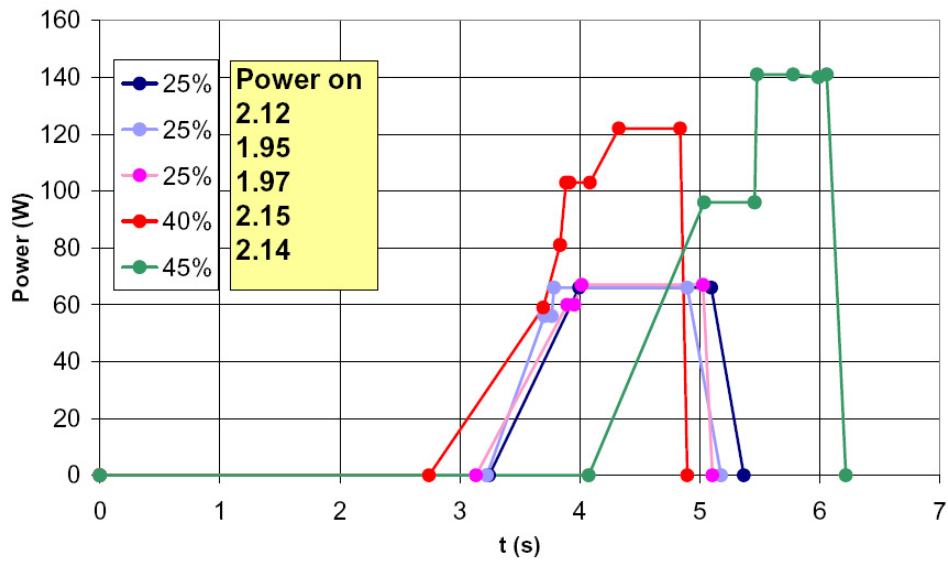


Figure 7.2: Starting characteristic of laser for different values of power

7.1. STATIC TESTING RESULTS

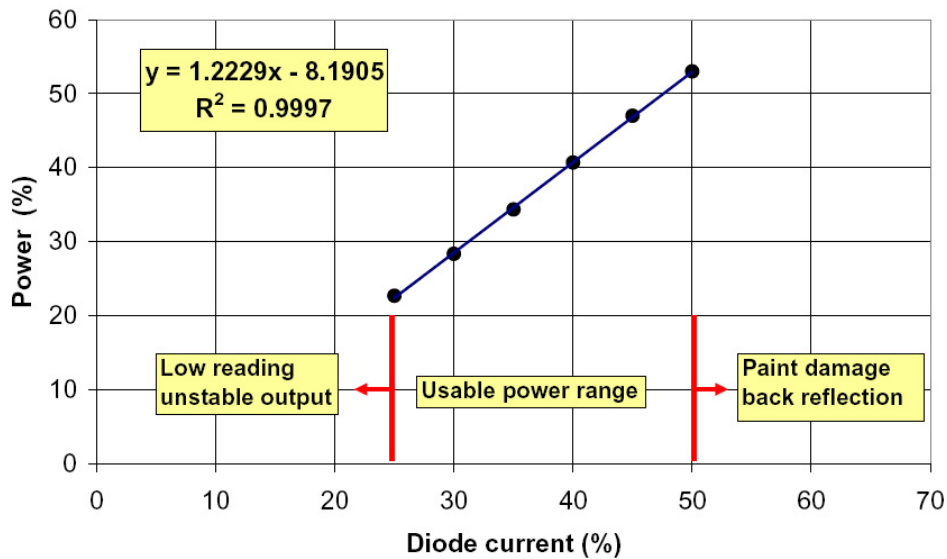


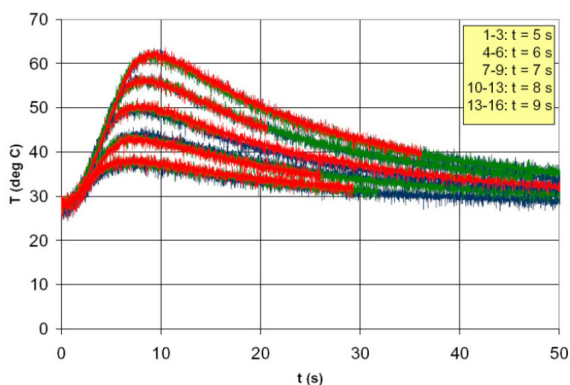
Figure 7.3: Relation between diode current and laser power

usable power range. The generated calibration curve is presented in Fig. 7.3. We have seen that the maximum usable diode current for a 2-second run is 50%. This value was obtained by performing a series 2-second tests at the back of the plate with an increasing power until the paint sublimated (the two spots are visible in Fig. 7.1). On the heated insert, great care was taken as the plate is first heated at a lower power. This heating changed the paint characteristics. We noticed that the paint got paler and then stabilized. No significant impact on the measured temperature was found once the paint stabilizes. We believe that this corresponds to the vitrification of the paint due to heating. To see if this change in the aspect of the paint influences the plate temperature, successive tests were performed on a spot of "new" (not previously irradiated) paint located at around 0.25 inch above the target center. Five groups of three runs were performed for a fixed amount of time. After each group, time is increased by one second. The power was kept constant at 67 Watts. Again, the aspect of the paint changes over the irradiated area, however as seen in Fig. 7.4 no significant effect on the temperature measurements was observed. The repeatability of the laser power output and the paint stability are therefore excellent.

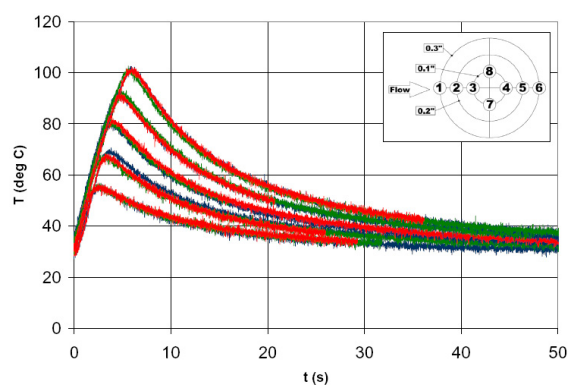
7.1. STATIC TESTING RESULTS

Table 7.1: Power Output

Date	P($\pm 1W$) for 25 % diode current	P ($\pm 1W$) for 30 % diode current
05-25-06	67	85
05-26-06	68	84
06-19-06	65	—
07-10-06	62	—
07-12-06	62	80
07-13-06	63	81
07-14-06	64	82
07-14-06	—	82



(a) Temperature for thermocouple 2



(b) Temperature for thermocouple 7

Figure 7.4: Good repeatability of backside temperature seen for successive irradiation at a fixed location

However, reproducibility isn't perfect since the power output for a given diode current was different for the tests performed in July in comparison with those performed in May and June. The reason is unknown, but we believe that it might be due to an increase in room and/or cooling water temperature. Power values are found in Table 7.1.

In both tests, the Medtherm surface thermocouples developed problems. Since the surface temperature is lower than the thermocouple maximum operating temperature, we believe that the failure can be attributed to a reaction between the thin thermocouple junction and the silicone-based paint. Moreover, another problem related to the use of a painted thermocouple for surface measurements is the effect of the paint thickness on the temperature. For laser heating, the surface heat flux is large which directly translates into a large temperature gradient near the surface such that a thin coating of paint can introduce a large temperature error. A simple way to get a feel for the order of magnitude of this error was obtained by looking at the temperature at a small distance δ below the surface (corresponding to the

paint thickness). For $\delta = 5 \times 10^{-3}$ in., we get a temperature difference of about $75K$ for a power of $81W$ (the difference doesn't vary significantly with time). This difference increases with a reduction of the paint thermal conductivity. The effect of the paint could be modeled using the GASP solid conduction solver if the paint thickness and properties were known. The paint thickness can be measured accurately using a paint thickness gauge which uses an Eddy-current transducer. Since no data on the thermal properties of the paint are available, this effect cannot be modeled. In subsequent tests, most of the surface temperature measurements were made using infrared thermography.

7.2 Flow Survey

The splitter plate was mounted on the wind-tunnel floor and tested without heating from the laser. The objectives of this test were the following:

- Check the structural integrity of the system
- Assess the flow quality over the plate
- Estimate the boundary layer thickness and turbulent nature at the heated insert position.
- Estimate the free stream Mach number over the plate
- Test the temperature measurement system

The first test was a success as no structural problem were detected on the plate and wedge. The thermocouples and the acquisition system performed properly. The boundary layer thickness was estimated using Schlieren imagery, whereas the shock on the plate leading edge is visualized best by using the Shadowgraph method as seen in Fig. 7.5. Fig. 7.5 (a) shows that the boundary layer is turbulent over the plate since eddies are easily identified. Fig. 7.5 (b) shows that the shock isn't two-dimensional at the leading edge of the plate due to the corners. The free stream Mach number is also obtained by measuring the static pressure on the plate wall and the total pressure in the free stream. The Mach number was computed using the Rayleigh Pitot formula. The estimated boundary layer thickness at the location of the heated insert and free stream Mach number (from the shock angle) obtained from the shadowgraph and pressure measurement are found at Table 7.2. The estimated boundary layer thickness is greater than that obtained numerically running a flat plate simulation up to the same length. We believe that this difference is attributable to an initial boundary layer thickness at the leading edge caused by the small bluntness. Both values of the Mach number agree well such that we are confident that the measured value is accurate.

7.3. TEST MATRIX AND PROBLEM TYPE

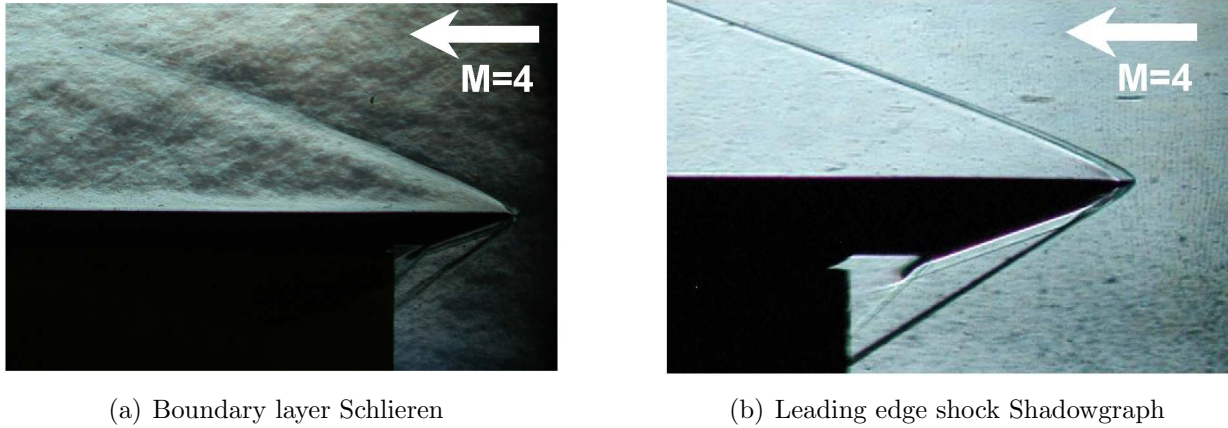


Figure 7.5: Flow visualization in used in determining the free stream Mach number and boundary layer thickness

Table 7.2: Flow Survey Results

δ from Schlieren (mm)	4
M_e from Shadowgraph	3.8
M_e from Pressure	3.75

7.3 Test Matrix and Problem Type

After obtaining excellent repeatability on the static testing, the test program was pushed forward. The test matrix is presented in Table 7.3. Different laser power values were used to evaluate the effects of the power on the target cooling. Test at a lower power are performed fist to avoid damaging the paint. For the 101 Watt test, some paint damage was visible whereas for the 120 Watt test the paint got progressively sublimated. Two different types of test were performed which are referred as Type 1 and Type 2. For Type 1, two tests are made, one with the flow-on the other with the flow-off. For the flow-on case, the laser is turned on after the tunnel starts and the flow reaches a steady state. The laser is turned off before the tunnel unstarts. For the flow-off case the plate is heated at the same power but

Table 7.3: Test Matrix

Power (W)	Maximum Intensity (W/cm^2)	Time on (s)	Type
65	1035	10.8	1
81	1289	10.8	1
101	1607	10.8	1
120	1910	10.8	1
50	796	80	2

without the supersonic flow over the target. The cooling effect is seen by subtracting the flow-off temperature from the flow-on temperature.

For Type 2 testing, the laser is turned on first as the plate is preheated for 70 seconds. This created a pseudo-steady temperature distribution on the plate. The tunnel was then started and run for approximately 10-15 seconds in an attempt to reach a new steady condition at a lower temperature. Experimental results are presented next. Infrared temperature measurements were made for the 65 Watt, 81 Watt and 120 Watt cases only. Those values correspond to the absorbed power which is 95% of the emitted power.

7.4 65 Watt Case

The experimental results for 65 Watt of absorbed power are presented. For this power setting both infrared thermography and thermocouple measurements were made. Thermocouple results are presented first.

7.4.1 Thermocouple Results

The experimental data is visualized by looking at the temperature as well as the temperature difference between the flow-off and flow-on cases. The temperature plots are presented first. The flow-off case is located on the left hand side and the flow-on case on the right hand side.

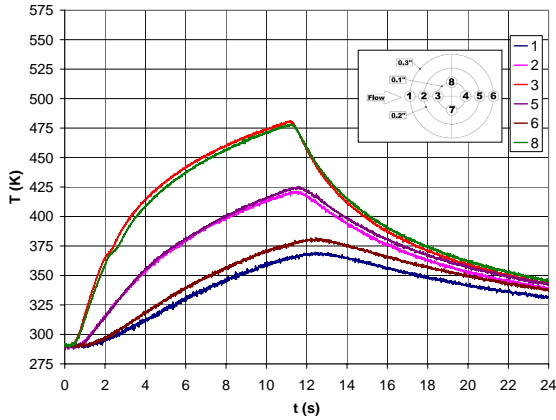
Temperature Plots

Fig. 7.6 presents the temperature increase recorded by the thermocouple on the backside of the plate. For the flow-off case, a perfectly symmetric temperature distribution is expected. However, due to the uncertainty in the positioning of the thermocouples and the laser alignment the recorded temperature isn't perfectly symmetric. The asymmetry is small with the exception of the thermocouples located at 0.3 inch from the center for which a difference of 12 K is found. For both the flow-on and flow-off cases, the laser is turned off after 11 seconds of irradiation. After the laser is turned on, it takes about 0.6 seconds before the temperature of thermocouples 3 and 8 start increasing, as some time is required for the heat to diffuse through the solid. As expected, more time is required for the heat to reach the thermocouples located at 0.2 inch and 0.3 inch from the center. When the laser is stopped, the temperature of thermocouples 3 and 8 drops faster as they are located closer to the surface heat source. The drop in temperature for thermocouples 1 and 6 is slower since heat diffuses radially from the center of the plate.

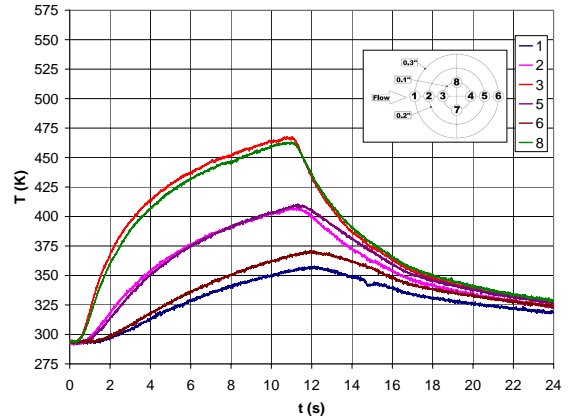
The decrease in temperature is visible when comparing the flow-off and flow-on cases. However, the difference is better seen when taking the difference between the flow-off and flow-on

7.4. 65 WATT CASE

cases.



(a) Backside Temperature flow-off at P=65W



(b) Backside Temperature flow-on at P=65W

Figure 7.6: Thermocouple temperature measurements at P=65W

Temperature Difference Plots

In order to facilitate the interpretation of the results and cancel the bias error, the flow-on temperature is subtracted from the flow-off temperature. Results are shown in Fig. 7.7. For this case, the cooling from all the thermocouples is similar and reaches 10 K to 15 K after 10 seconds.

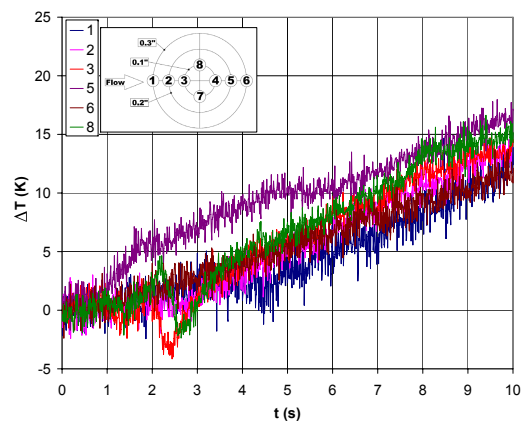


Figure 7.7: Temperature difference between flow-off and flow-on condition at P=65

7.4.2 Infrared Camera Results

Infrared thermography was used to measure the temperature on the surface and backside of the plate. Temperature contours taken at a 1 second interval are shown and discussed in the next section.

Temperature Plots

Fig. 7.8 shows the surface temperature contours for the flow-on and flow-off cases at a one second interval. The flow is directed from left to right. The upper half of each contour plot corresponds to the flow-off case and the lower part corresponds to the flow-on case.

For the flow-off cases, the temperature contours are symmetric. For the flow-on cases, we notice some asymmetry at the center. This can be clearly seen in Figs. 7.8 (h),(g) and (i) where the maximum temperature contours are slightly shifted downstream. Without flow, the temperature reaches 975 K at the center after 10 seconds compared to 925 K with the flow-on.

7.4. 65 WATT CASE

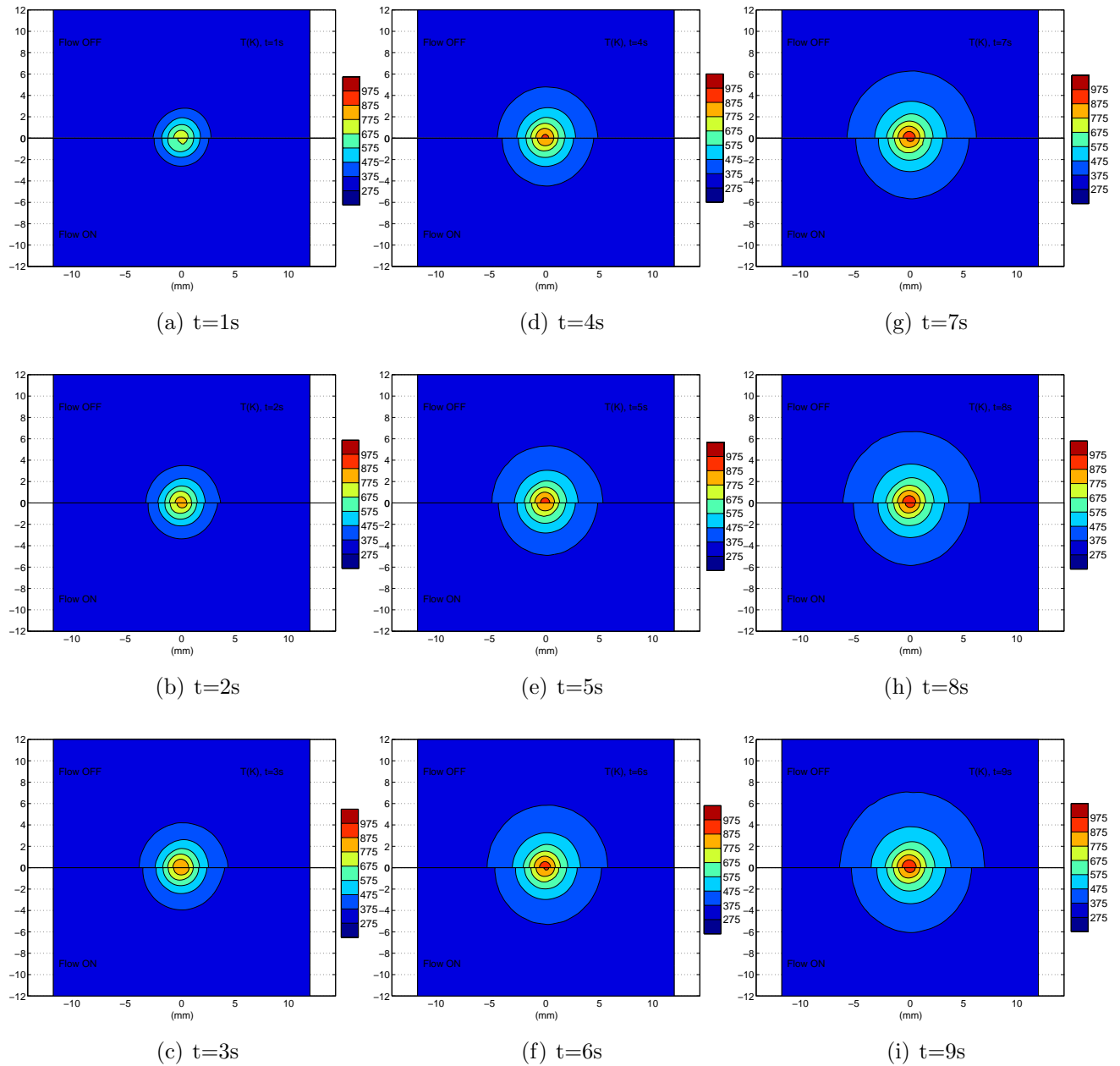


Figure 7.8: Surface temperature for $P=65$ W with the flow going from left to right

The backside temperature is shown in Fig. 7.9. Here, the temperature distribution appears symmetric for both the flow-on and flow-off cases. Again, the maximum temperature difference between the flow-on and flow-off cases is found at the center. For the flow-off case, the maximum temperature reaches 600 K after 8 seconds compared to 575 K with flow-on. The temperature difference between flow-on and flow-off on the backside at the center is roughly one half of that found on the surface.

7.4. 65 WATT CASE

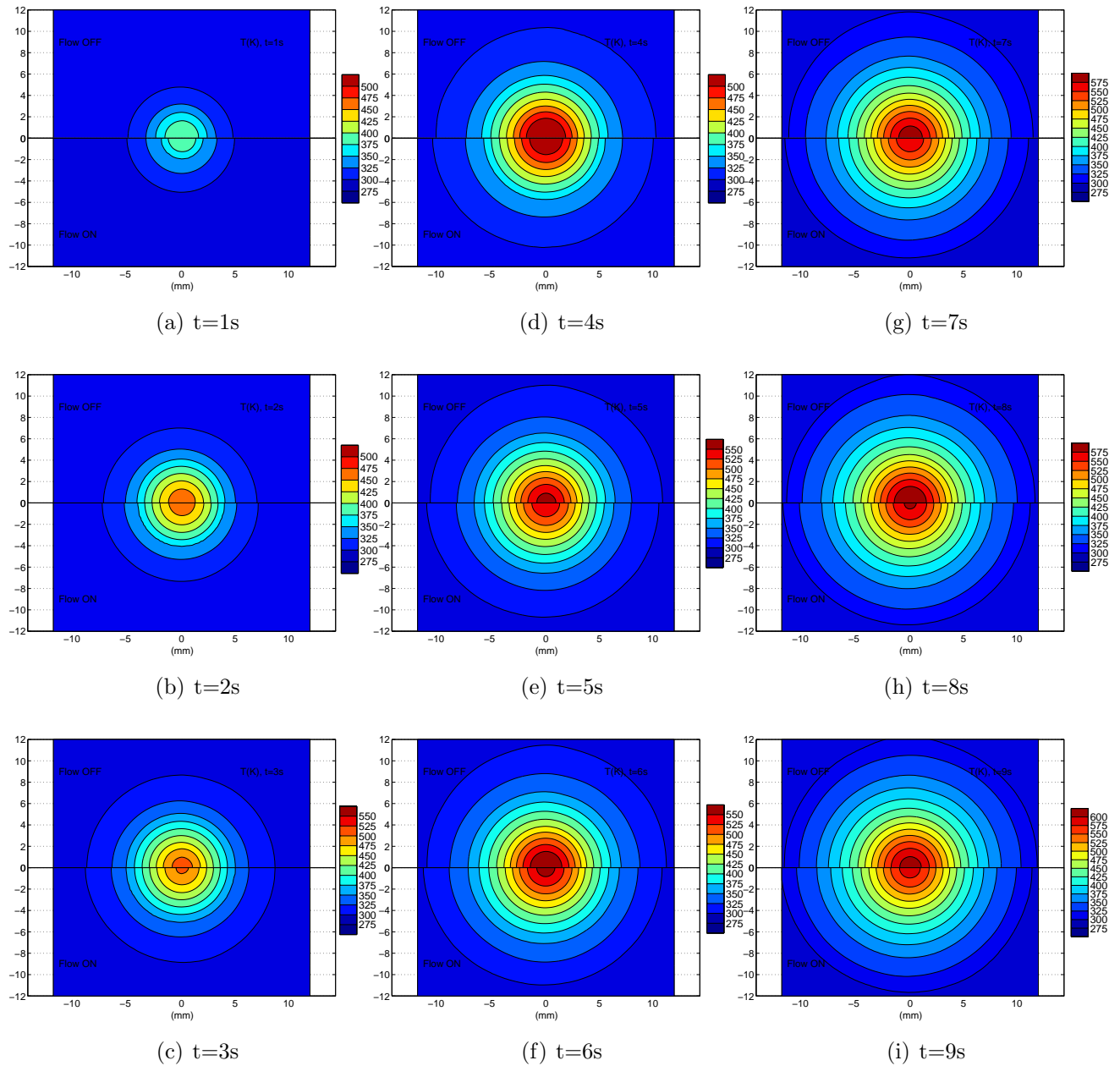


Figure 7.9: Backside temperature for $P=65$ W with the flow going from left to right

Temperature Difference Plots

As was seen for the thermocouple data, the cooling effect of the flow-on the temperature distribution is best seen by subtracting the flow-on temperature from the flow-off temperature. Fig. 7.10 shows the surface temperature between $t = 1s$ and $t = 9s$ at 1 second intervals.

NUC0 was not used such that the temperature difference is set to zero when the temperature is below 333 K .

At $t = 1s$, the maximum temperature difference reaches 60 K . As seen in the uncertainty analysis, the uncertainty is greater at a small value of time due to the increase in the timing error from the large time rate of change of the temperature. Also, the flow-on and flow-off cases are on a different calibration for that value of time such that the bias error does not cancel. It is, therefore, believed that the temperature difference is over predicted at $t = 1s$. At $t = 2s$ we notice a region of intense cooling right in front of the center followed by a region of heating aft. This is logical, since heat is convected downstream by the flow. Further away from the center for $2mm < |r| < 4mm$ the cooling is almost uniform and greater than for $1.5mm < |r| < 2mm$. A strong increase in the maximum temperature difference is seen between 3 and 5 seconds as it rises from 20 K to 50 K . At a larger time, the maximum cooling oscillates around 50 K . For $2mm < |r| < 4mm$ the temperature difference steadily increases from 15 K to 30 K degrees between $t = 3 s$ and $t = 9 s$. Over that area, a region of reduced cooling is seen towards the back for $4 < t < 7$.

7.4. 65 WATT CASE

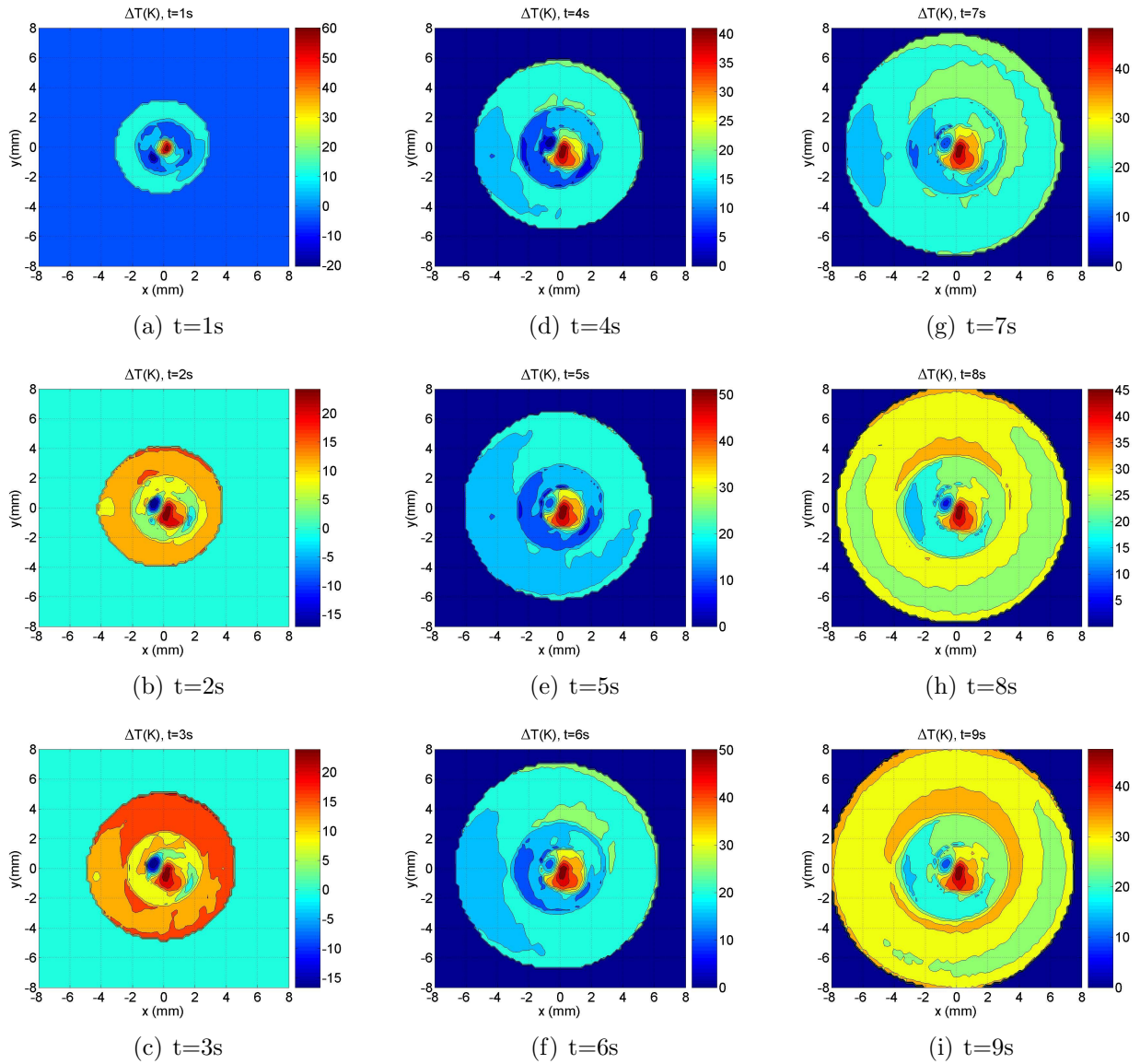


Figure 7.10: Surface temperature difference for $P=65$ W with the flow going from left to right (Note: the temperature difference is set to zero for temperatures below 333 K)

The temperature difference on the backside is shown at a 1 second intervals in Fig. 7.11 for $1s < t < 9s$. The effect of the mismatching calibration can be seen on all the images. For instance, at $t = 1$, a disk of high cooling is seen at $r = 2mm$. This cooling isn't real as it is produced from the non-cancellation of the bias error for mismatching integration time. As time increases, the radius of the disk increases.

Maximum cooling is seen in front of the center for $-2mm < x < 0mm$. It increases steadily and reaches 25 K at $t = 9s$. For $2mm < |r| < 4mm$ the temperature is almost uniform for

7.4. 65 WATT CASE

short time values and, a region of reduced cooling is seen aft for a large values of time.

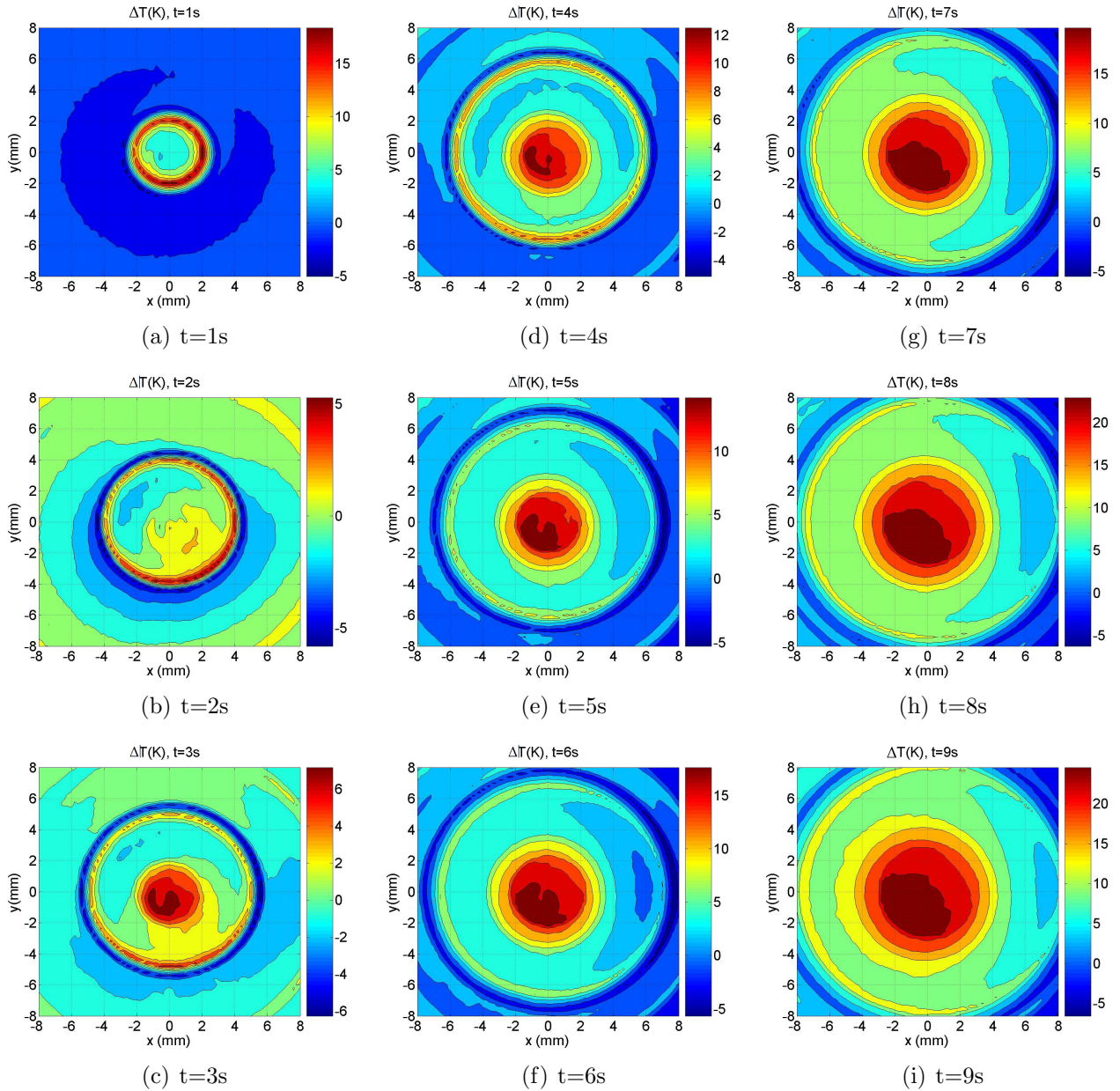


Figure 7.11: Backside temperature difference for $P=65$ W with the flow going from left to right

7.5 81 Watt Case

The same study as performed for a power of 81 Watts. Again, the thermocouple results are shown first followed by the infrared measurements.

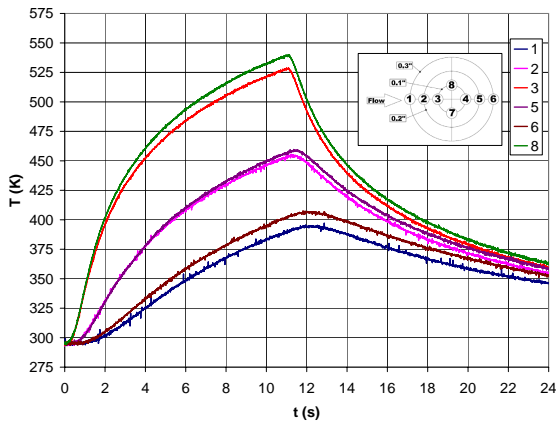
7.5.1 Thermocouple Results

A total of 6 runs were performed at the same power setting to assess the repeatability of the experiment. Those results were used in the uncertainty analysis to quantify the random error.

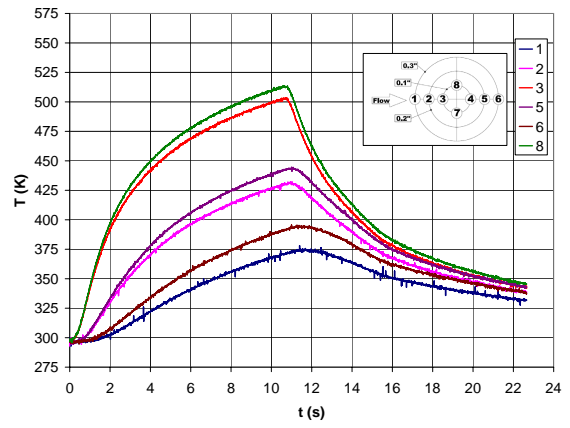
Temperature Plots

Figs. 7.12 to 7.17 present the backside temperature for 6 runs performed at the same power setting. The flow-off case is located on the left whereas the flow-on case is located on the right. The laser was kept on for about 11 seconds. As seen for the 65 W case, the temperature distribution isn't perfectly symmetric for the flow-off case as would be expected. Again, the greatest difference is seen between thermocouple 1 and 6 located at 0.3 inch from the center. For runs 1 through 3, the laser isn't perfectly aligned such that a temperature difference is seen for thermocouples 3 and 8. The alignment was subsequently improved for runs 4 through 6. However, since the alignment was kept the same for the flow-on and flow-off cases, the effect of the slight misalignment should only introduce a small difference when the temperature difference between the flow-off and flow-on cases is taken. Overall, repeatability is very good as the run-to-run temperatures are close except for run 4 where the laser stopped short on the flow-on case. Nevertheless, run 4 gives good data before $t = 8s$.

7.5. 81 WATT CASE

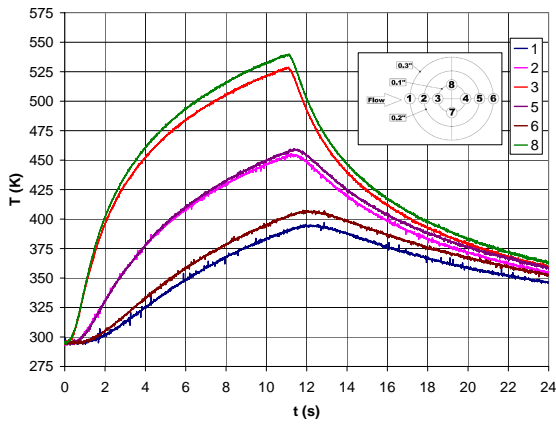


(a) Backside temperature flow-off at P=81W

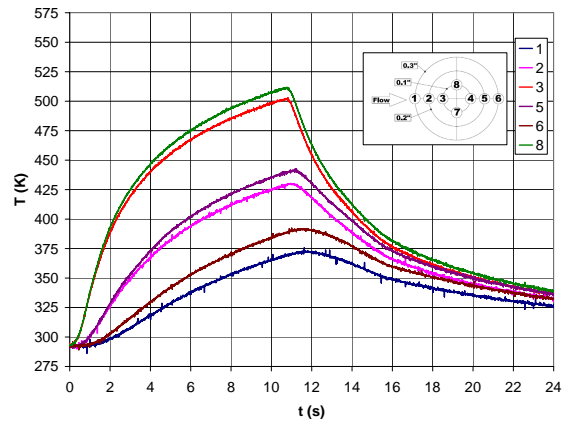


(b) Backside temperature flow-on at P=81W

Figure 7.12: Backside thermocouple temperature measurements for run 1 at P=81W



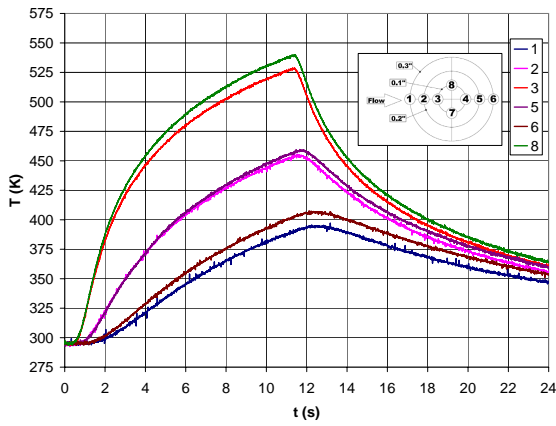
(a) Backside temperature flow-off at P=81W



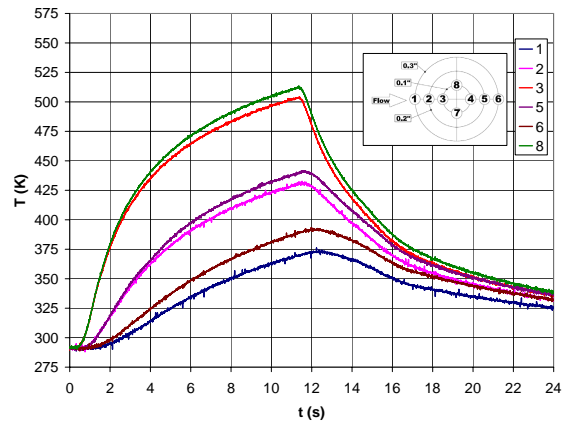
(b) Backside temperature flow-on at P=81W

Figure 7.13: Backside thermocouple temperature measurements for run 2 at P=81W

7.5. 81 WATT CASE

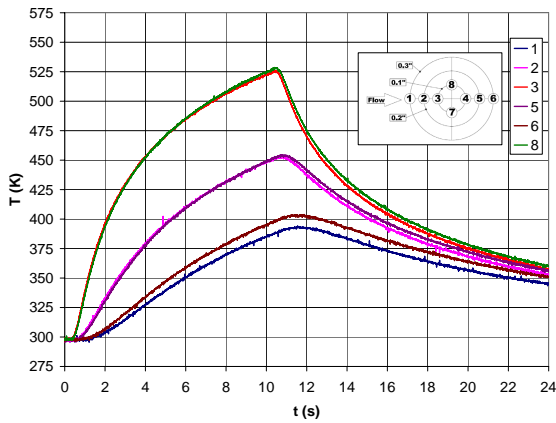


(a) Backside temperature flow-off at P=81W

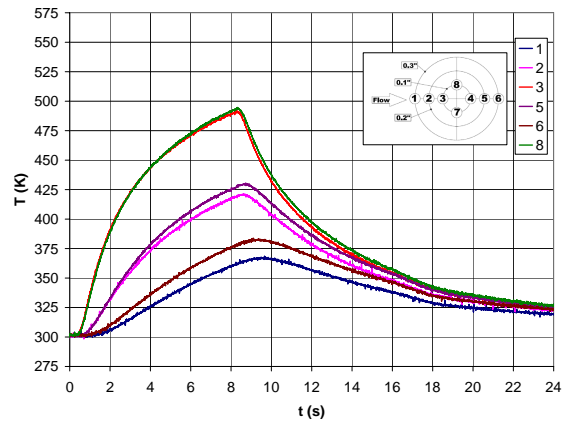


(b) Backside temperature flow-on at P=81W

Figure 7.14: Backside thermocouple temperature measurements for run 3 at P=81W



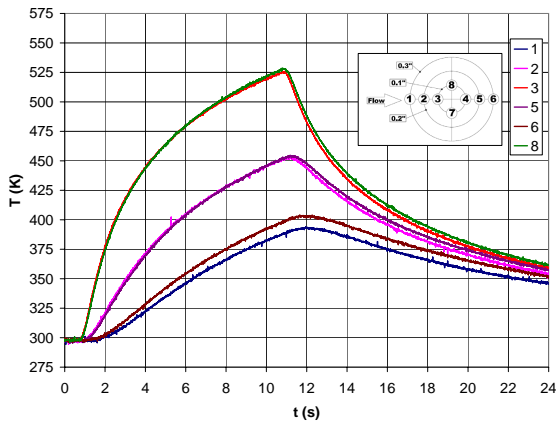
(a) Backside temperature flow-off at P=81W



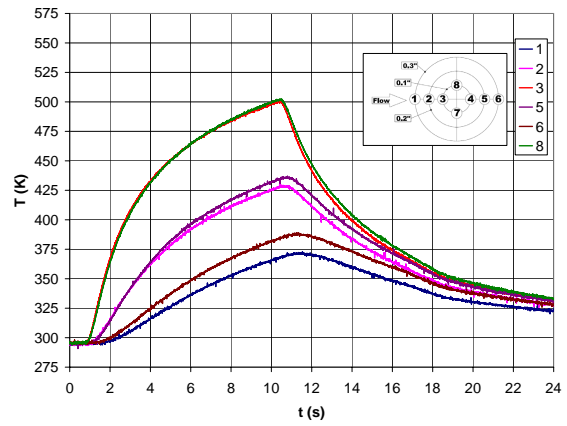
(b) Backside temperature flow-on at P=81W

Figure 7.15: Backside thermocouple temperature measurements for run 4 at P=81W

7.5. 81 WATT CASE

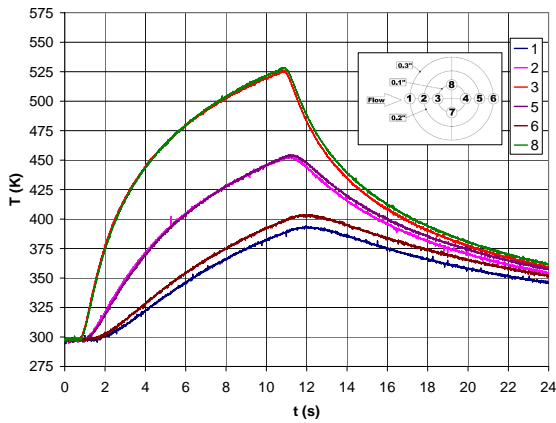


(a) Backside temperature flow-off at $P=81W$

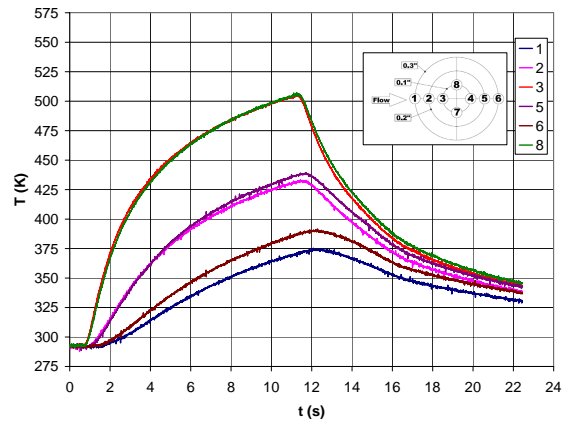


(b) Backside temperature flow-on at $P=81W$

Figure 7.16: Backside thermocouple temperature measurements for run 5 at $P=81W$



(a) Backside temperature flow-off at $P=81W$



(b) Backside temperature flow-on at $P=81W$

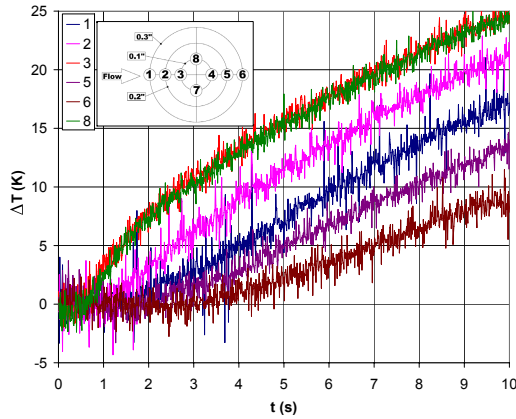
Figure 7.17: Backside thermocouple temperature measurements for run 6 at $P=81W$

Temperature Difference Plots

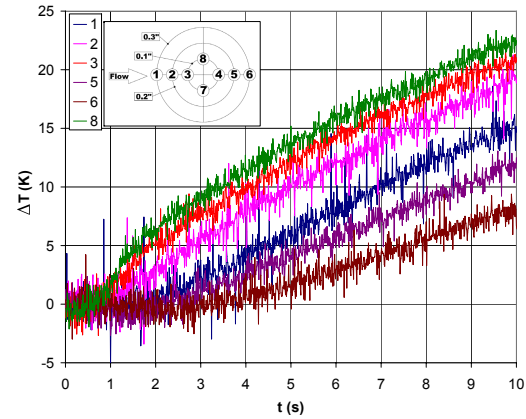
The temperature difference between the flow-off and flow-on cases was computed and plotted in Figs. 7.18 to 7.20. More cooling is seen for run 1 compared to run 5 and run 6 which displayed the least amount of cooling. Overall, repeatability is good as the run-to-run difference is less than $5 K$. Contrary to the $65 W$ case, a noticeable difference is found among the different thermocouples. The greatest cooling is seen close to the center for thermocouples 3 and 8. The maximum cooling is between $20K$ and $25K$ at the center. We clearly notice some asymmetry by looking at the thermocouples pairs 1-6 and 2-5. The

7.5. 81 WATT CASE

difference between thermocouples 2 and 5 reached almost 10 K at $t = 10\text{ s}$. As expected, thermocouple 5 cools less than thermocouple 2, since heat is convected downstream. The same situation arises when comparing thermocouples 1 and 6 as the difference in cooling is close to 10 K at $t = 10\text{ s}$. Clearly, a steady state was not achieved during the run as the temperature difference for all the thermocouples keep increasing.

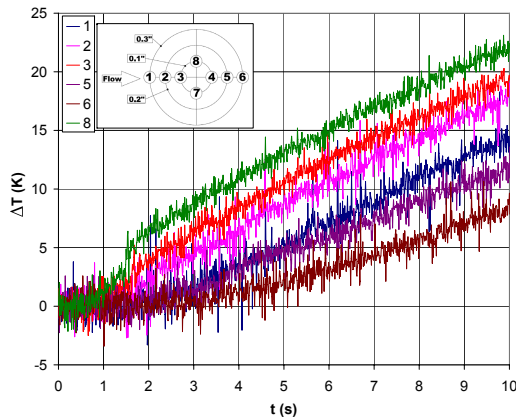


(a) Backside temperature difference for run 1 at $P=81\text{ W}$

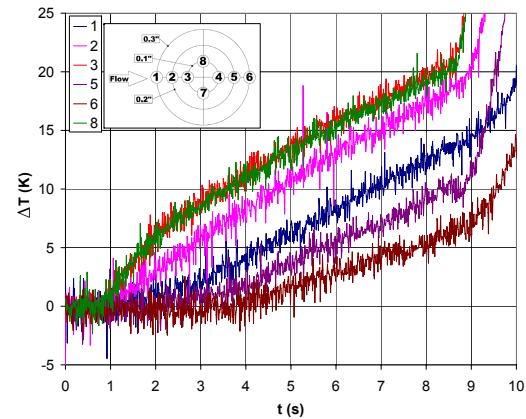


(b) Backside temperature difference flow for run 2 at $P=81\text{ W}$

Figure 7.18: Backside temperature difference between flow-off and flow-on condition at $P=81\text{ W}$



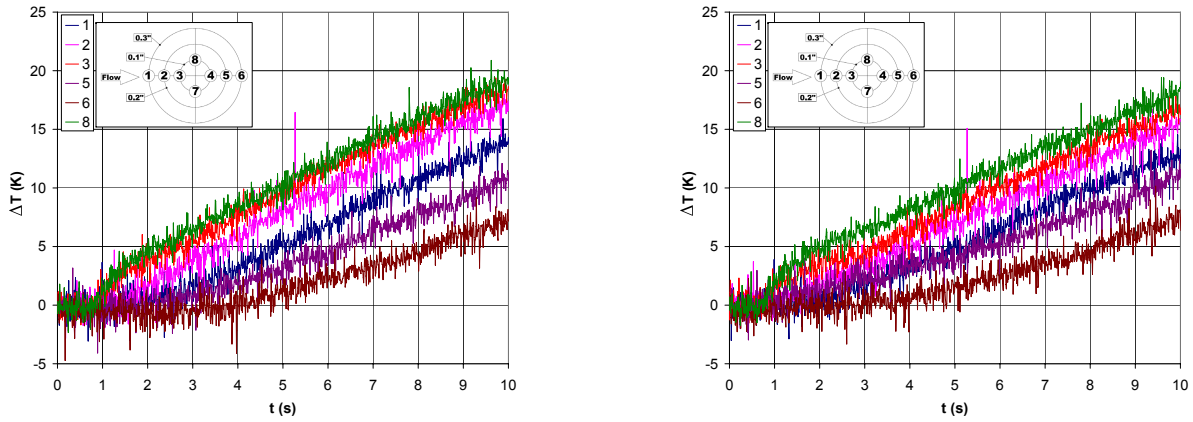
(a) Backside temperature difference for run 3 at $P=81\text{ W}$



(b) Backside temperature difference for run 4 at $P=81\text{ W}$

Figure 7.19: Backside temperature difference between flow-off and flow-on condition at $P=81\text{ W}$

7.5. 81 WATT CASE



(a) Backside temperature difference for run 5 at $P=81W$

(b) Backside temperature difference for run 6 at $P=81W$

Figure 7.20: Backside temperature difference between flow-off and flow-on condition at $P=81W$

7.5.2 Infrared Camera Results

The infrared camera was used to measure the temperature on the target surface and backside. Temperature results are presented first.

Temperature Plots

Fig. 7.21 shows the surface temperature contours for the flow-on and flow-off cases at a 1 second interval. The flow is directed from left to right. The upper half of each contour plot corresponds to the flow-off case and the lower part corresponds to the flow-on case.

Some disturbance in the temperature contours can be seen on the upper part around $r = 4mm$ due to paint damage. Over the damaged area, the emissivity is less which explains the disturbance. For the flow-off, case the temperature reaches $1175 K$ after 10 seconds. The maximum temperature reaches $1115 K$ after 10 seconds for the flow-on cases. As for the 65 Watt case, the maximum cooling was achieved at the center. More cooling can be seen upstream of the heated spot compared to downstream where the isolines almost coincide.

7.5. 81 WATT CASE

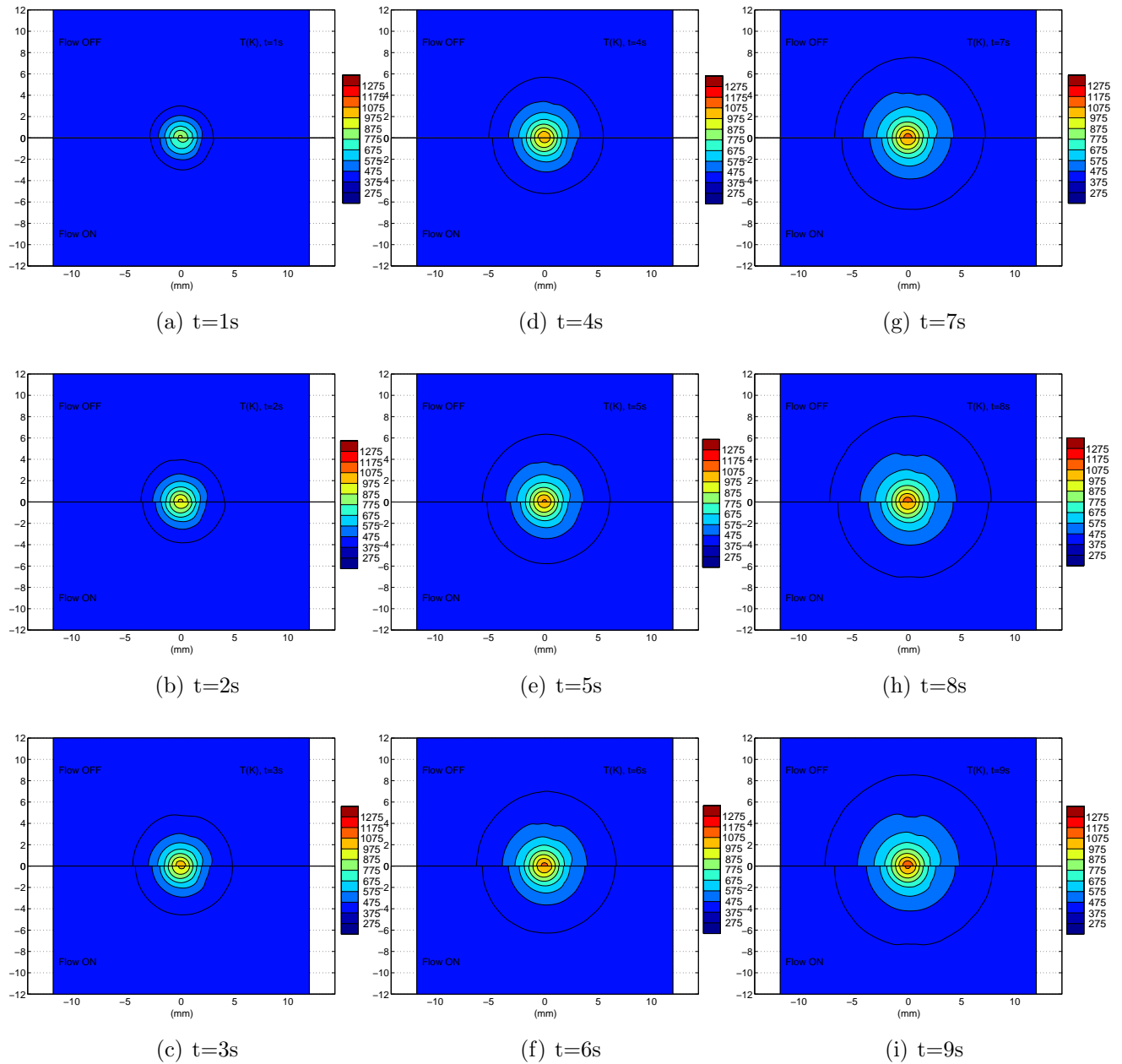


Figure 7.21: Surface temperature for $P=81$ W with the flow going from left to right

Figure 7.22 shows the temperature distribution on the backside. The asymmetry is difficult to notice from the temperature plots. The maximum temperature at the center reaches 675 K after 8 seconds for the flow-off case and 650 K for the flow-on case. At the center, the infrared camera gets saturated past $t = 8s$ for the flow-off case. This can be seen close to the center when looking at the temperature difference in Fig. 7.22(i).

7.5. 81 WATT CASE

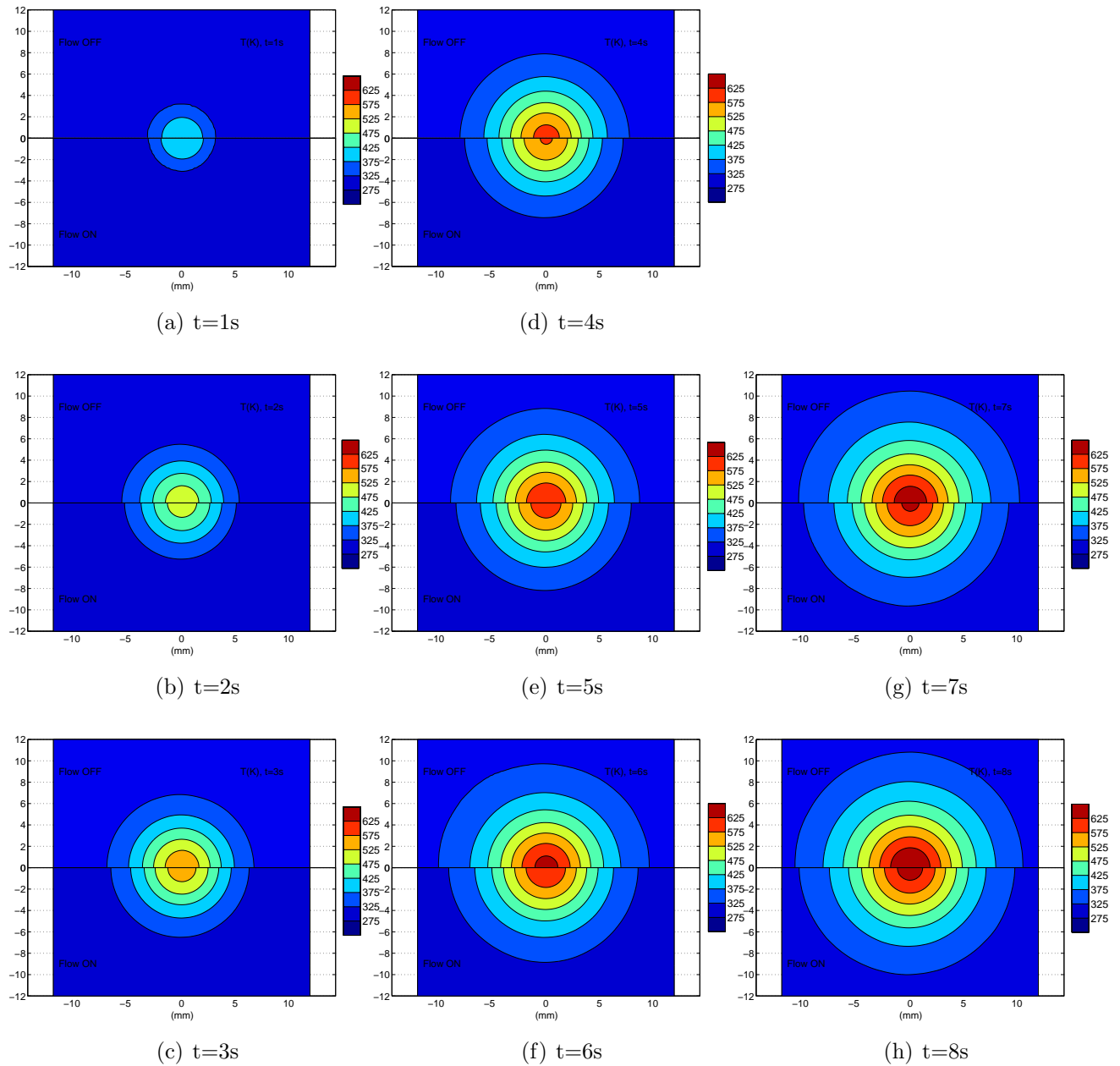


Figure 7.22: Backside temperature for $P=81$ W with the flow going from left to right

Temperature Difference Plots

The asymmetry in cooling is better seen when looking at the temperature difference between the flow-on and flow-off cases. The temperature difference on the surface is found in Fig. 7.23 and Fig. 7.24 for the backside. On the surface, a region of increased cooling is seen

7.5. 81 WATT CASE

upstream which is followed by a region of reduced cooling right before the center. At the center, the cooling reaches about 50 K after 9 seconds. For the 81 Watt case, the temperature distribution is more asymmetric compared to the 65 watt case. The increase in asymmetry is also seen on the backside as clearly, more cooling occurs upstream than downstream.

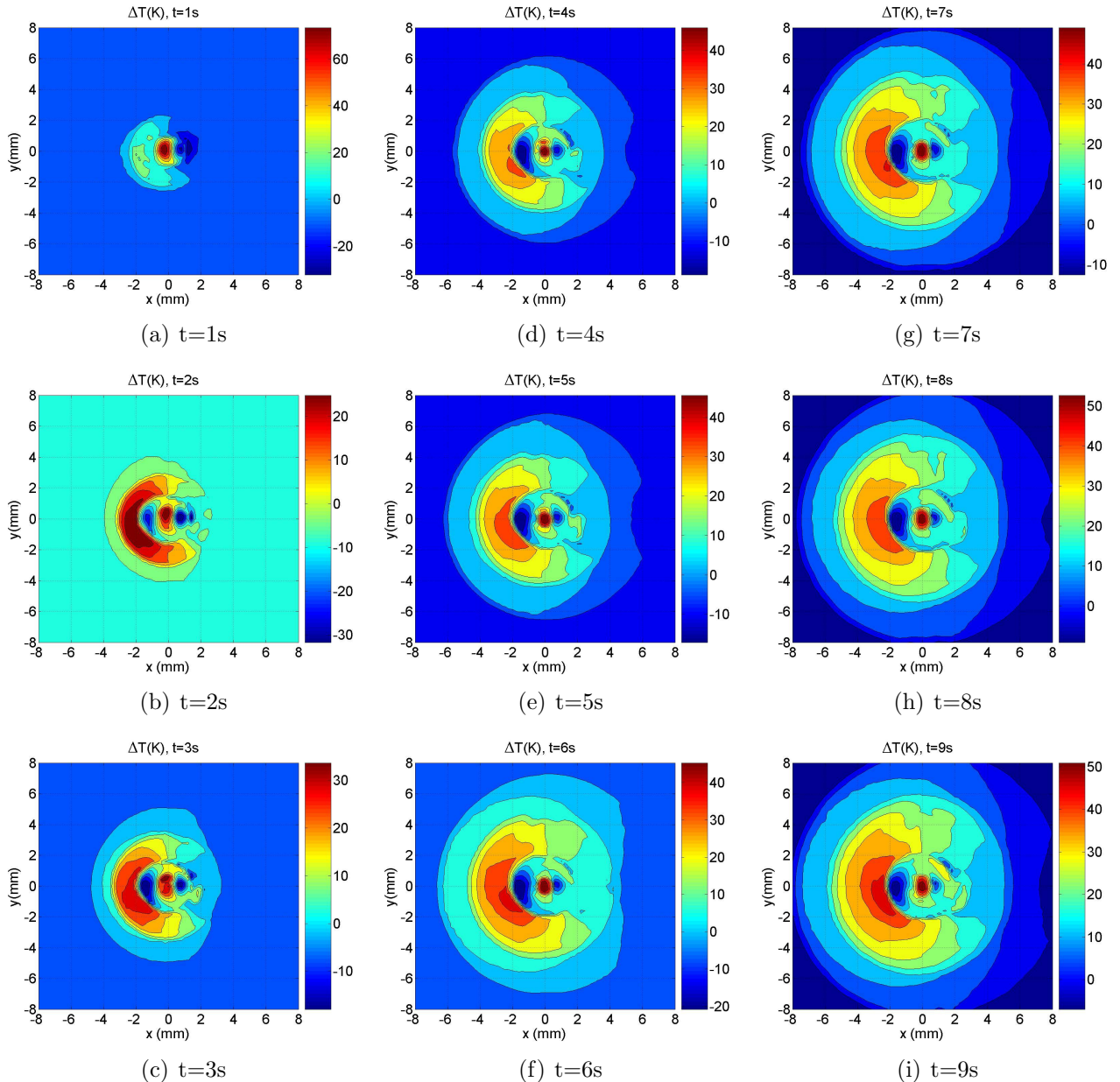


Figure 7.23: Surface temperature difference for $P=81$ W with the flow going from left to right

7.6. 101 WATTS CASE

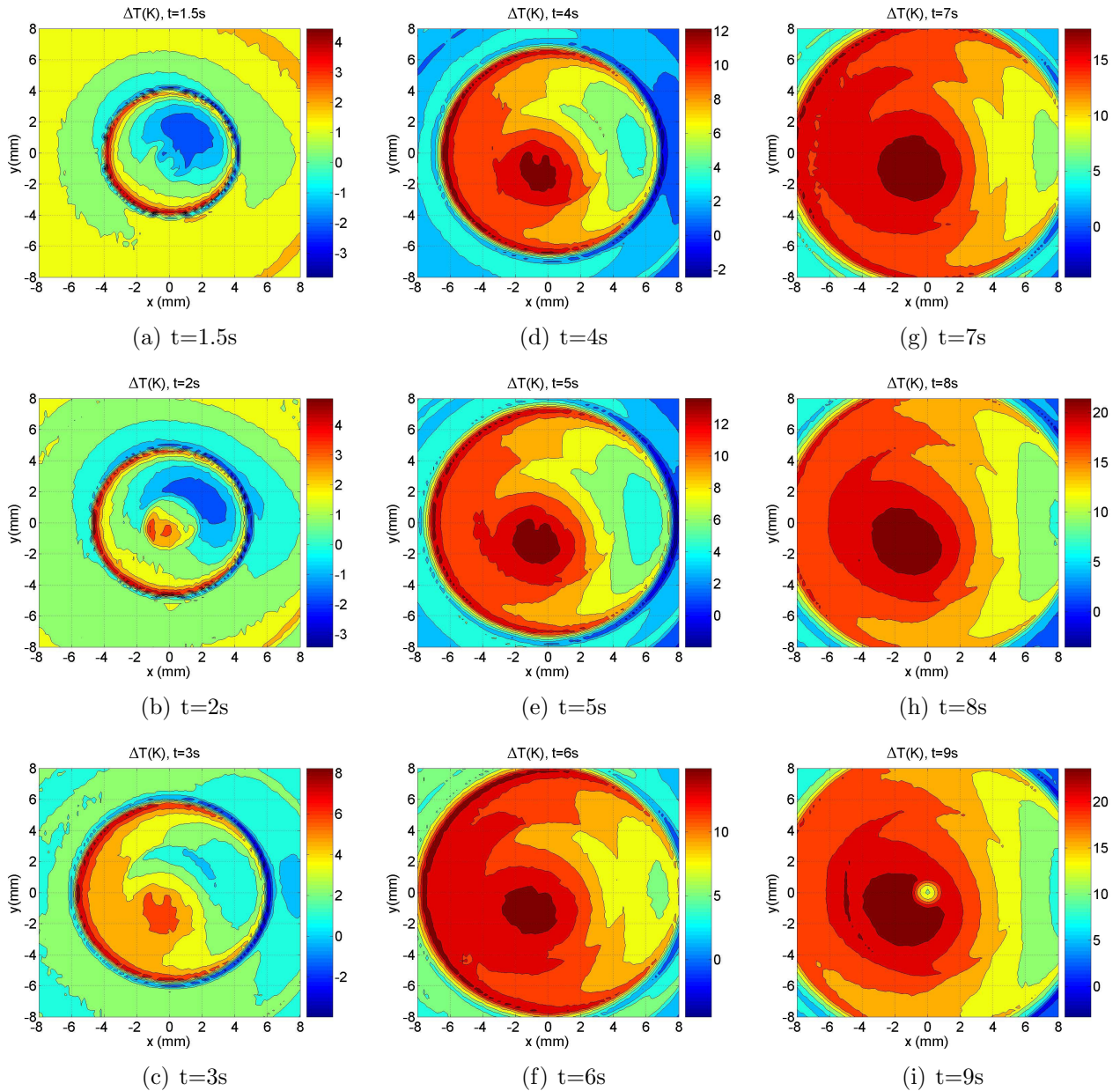


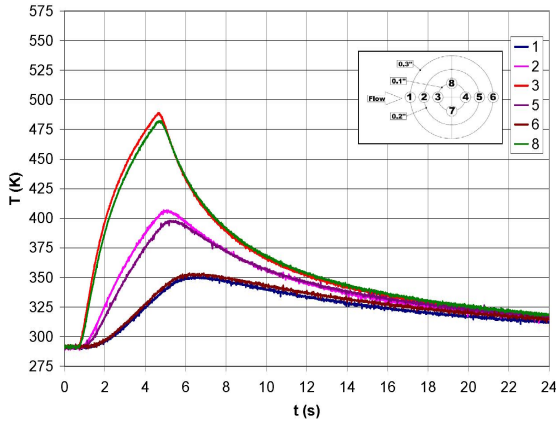
Figure 7.24: Backside temperature difference for $P=81$ W with the flow going from left to right

7.6 101 Watts Case

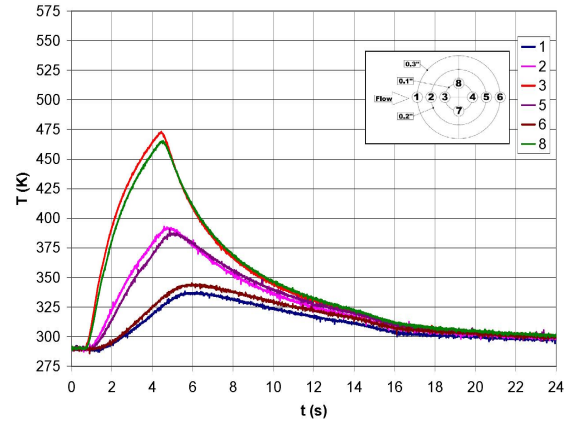
For the 101 Watt tests, the laser was turned on for only 4.5 seconds to avoid damaging the paint. Two runs were performed at this setting, and the temperature was recorded using the

7.6. 101 WATTS CASE

backside thermocouples. Temperature results for run 1 are shown in Fig. 7.25 and in Fig. 7.26 for run 2. At 0.1 inch from the center a maximum temperature of 488 K is recorded for the flow-off case and 475 K for the flow-on case.

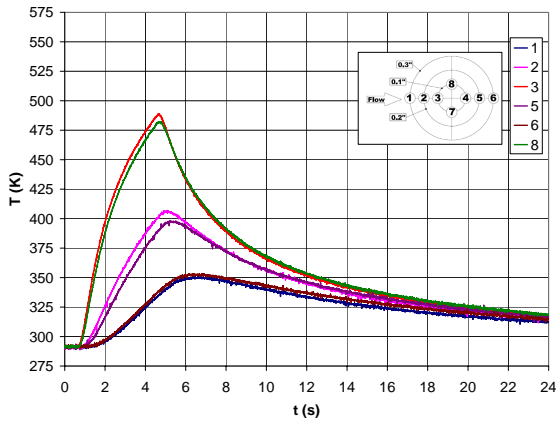


(a) Backside Temperature flow off for run 1 at P=101W

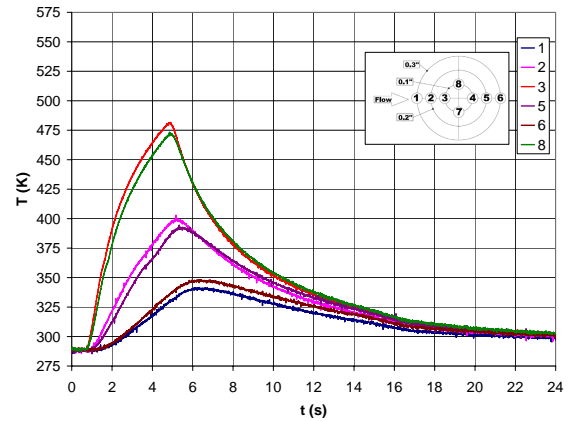


(b) Backside Temperature flow on for run 1 at P=101W

Figure 7.25: Backside thermocouple temperature measurements at P=101W



(a) Backside Temperature flow off for run 2 at P=101W

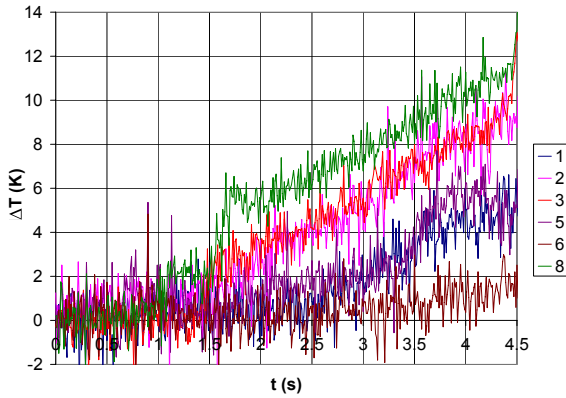


(b) Backside Temperature flow on for run 2 at P=101W

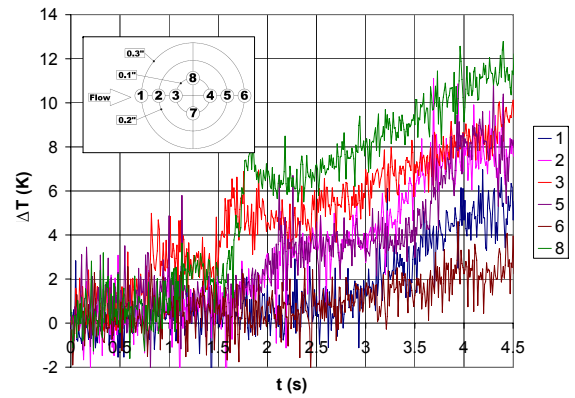
Figure 7.26: Backside thermocouple temperature measurements at P= 101 W

Temperature difference results are found at Fig. 7.27. Overall good repeatability is achieved with the exception of thermocouple 5 which displays a jump of 4K at $t = 3.5s$ in run 2. Thermocouple 8 displays the maximum cooling followed by thermocouples 2 and 3. Thermocouple 6, located 0.3 inch downstream, displays almost no cooling. At $t = 4.5$ the

7.7. 120 WATT CASE



(a) Backside Temperature difference for run 1 at $P=101W$



(b) Backside Temperature difference for run 2 at $P=101W$

Figure 7.27: Thermocouple temperature difference at $P=101 W$

maximum cooling reaches $12 K$ which is comparable to the 81 watts case which displays a cooling varying between $12 K$ and $14 K$ at that time depending on the run.

7.7 120 Watt Case

Due to limited testing time, only the highest temperature calibration was used at 120 Watt which means that only the temperature close to the center is available. For that high laser power setting, the paint showed some extensive damage. Run-to-run repeatability wasn't good until the paint got entirely removed, and the bare surface oxidized. Contours of temperature close to the center at $t = 10s$ for the flow-on and flow-off conditions are shown in Fig. 7.28. Contours of the temperature difference $t = 5s$ and $t = 10s$ are found in Fig. 7.29. The maximum cooling occurs at the center, and a region of reduced cooling is clearly observed downstream. The maximum surface temperature is plotted as a function of time for the flow-on and flow-off cases in Fig. 7.30

7.7. 120 WATT CASE

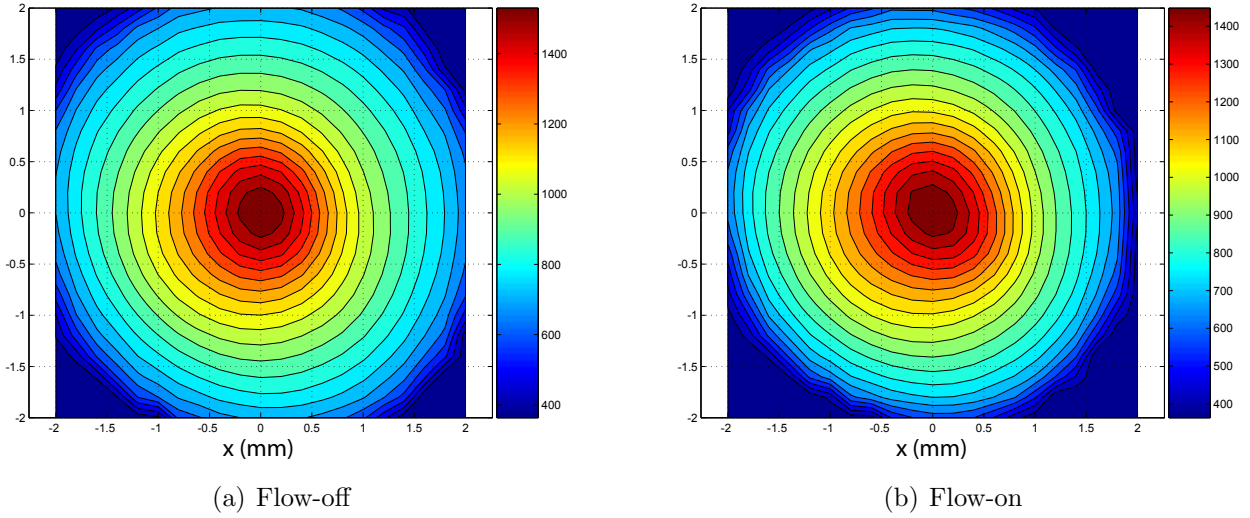


Figure 7.28: Temperature contours (K) at $t = 10s$ for $P=120 W$

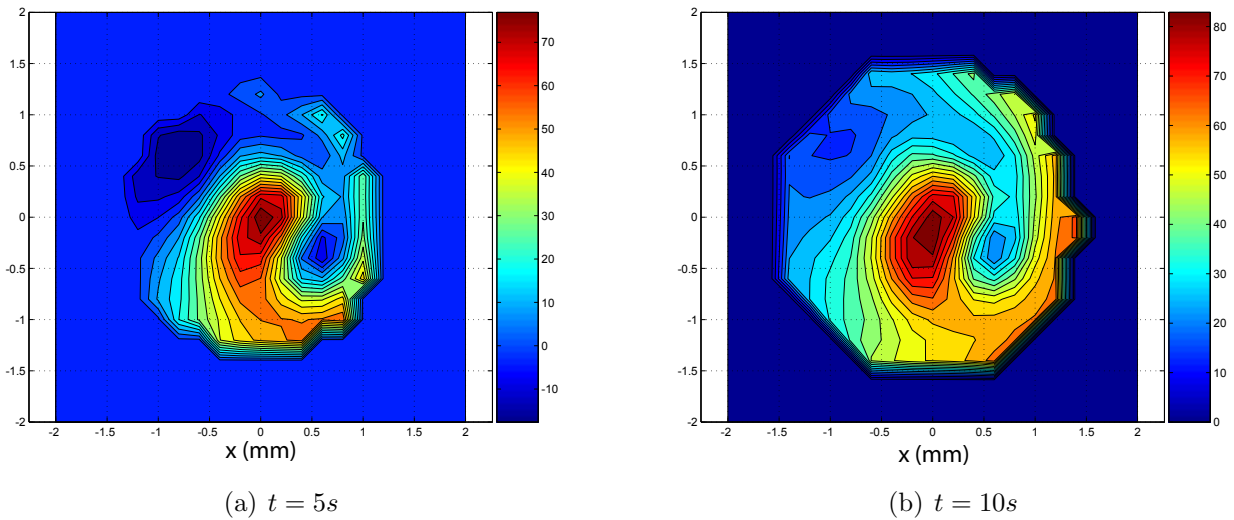


Figure 7.29: Temperature difference contours (K) for $P=120 W$

7.7. 120 WATT CASE

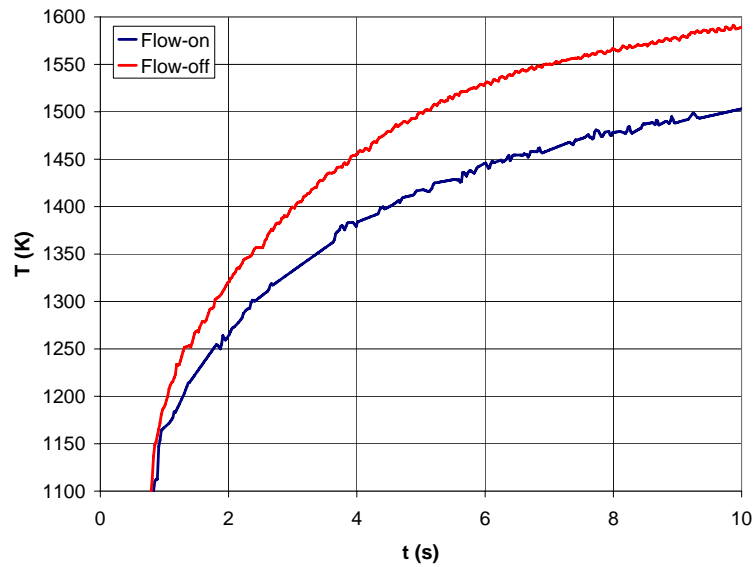


Figure 7.30: Maximum surface temperature for flow-on and flow-off conditions at $P = 120W$

After 10 seconds, a temperature difference of $90K$ was measured. As seen in Fig. 7.31, the difference between the flow-off and flow-on case remains almost constant between 6 and 10 seconds. For times below 2 seconds, the signal is too weak to get an accurate measurement. Fig. 7.31 also shows that convective cooling significantly change the time required to reach a given temperature. For example, for the flow-off case only 5 seconds are required to reach 1500 K compared to 10 seconds for the flow-on case.

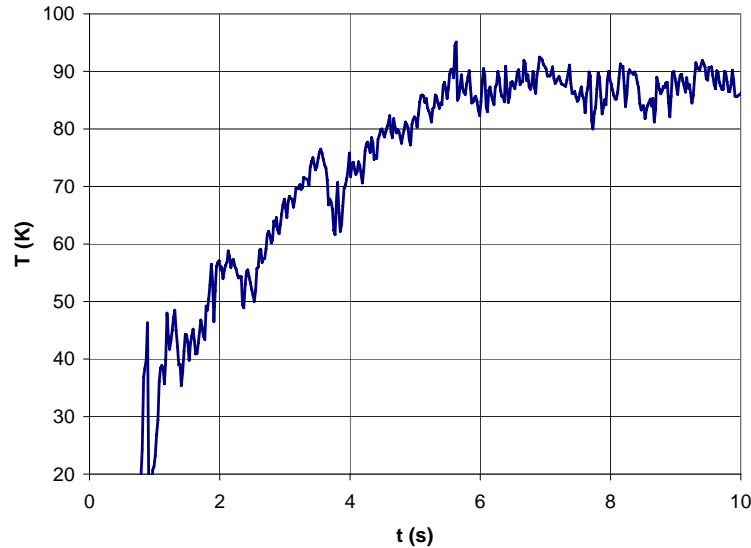


Figure 7.31: Difference in the maximum surface temperature between the flow-off and flow-on conditions at $P = 120W$

7.8 Type 2 Results

For a Type 2 run, the plate was preheated for 70 seconds before the tunnel was started while the laser was maintained on. To avoid damaging the paint, the power was limited to 50 Watt. After being preheated for 70 seconds the plate reached a quasi-steady state at the center. Thermocouples measurements were made on the back on the plate. Results are shown in Fig. 7.32. It is noticed that a steady state was almost reached as the temperature increase during the 10 seconds preceding the tunnel startup is less than 5 K. We notice a sharp decrease in temperature after the tunnel starts followed by a more moderate cooling when the supersonic flow is on. A steady state isn't reached before the tunnel unstarts. The temperature difference between the flow-off and flow-on cases is plotted in Fig. 7.33. The two thermocouples located near the center display the greatest cooling followed closely by thermocouple 2 which is located 0.2 inch upstream of the beam center. Asymmetry is noticed when comparing thermocouples 2 and 5 and thermocouples 1 and 6 as the downstream thermocouples cool down about 5 K less.

7.9 Experimental Results Summary

A summary of the experimental results is shown in Table 7.4. We notice that the maximum temperature difference at the center increases with the power. A linear relation is found

7.9. EXPERIMENTAL RESULTS SUMMARY

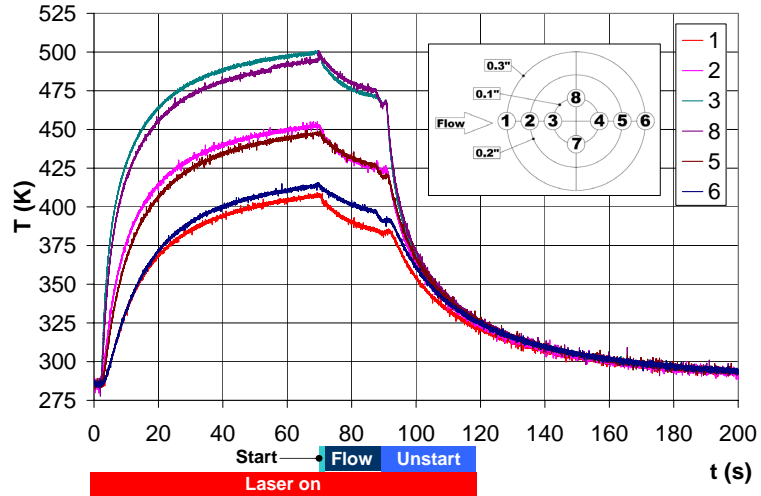


Figure 7.32: Temperature on the backside for a type 2 test for $P=50$ W. The plate is preheated for 70 seconds and the tunnel started while the irradiation is maintained

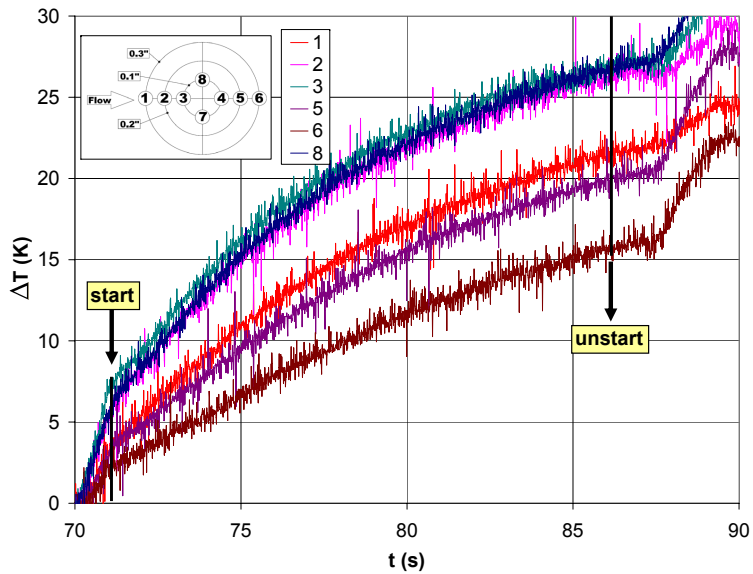


Figure 7.33: Temperature difference on the backside

7.9. EXPERIMENTAL RESULTS SUMMARY

between the maximum surface temperature and the laser power. On the backside, a similar temperature difference is observed between the 65 Watt and 81 Watt cases.

Table 7.4: Results summary for temperature and temperature difference of Surface ($|_s$) and Backside ($|_b$)

P (W)	$T_{max} _s(K)$	$t(s)$	$\Delta T_{max} _s(K)$	$t(s)$	$T_{max} _b(K)$	$t(s)$	$\Delta T_{max} _b(K)$	$t(s)$
65	975	10	50	9	600	10	27	10
81	1175	10	65	10	675	10	25	8
101	NA	NA	NA	NA	NA	NA	12	4.5
120	1589	10	90	10	NA	NA	NA	NA

Chapter 8

Computational Model and Results

Computations were performed using the GASP conjugate heat transfer solver to replicate the experimental condition for Type 1 tests. The free stream conditions used are presented in table 8.1.

The value of the free stream Mach number was obtained from the shadowgraph and Pitot measurements. The other free stream properties were obtained by assuming an oblique shock at the leading edge of the plate which brings the Mach number from 4 (the test section free stream Mach number) to 3.75. A boundary layer profile was specified at the inlet with a pointwise boundary condition. The profile was obtained by running a flat plate simulation at the free stream condition in order to get the measured boundary layer thickness over the target.

As mentioned earlier, for the Type 1 experiments, the tunnel is started and a steady state flow is achieved over the plate. After the tunnel comes to a steady state, the laser is turned on. The CFD simulation follows a similar procedure. The fluid portion of the mesh is solved with a constant wall temperature until a steady state is achieved. The steady state solution becomes the $t = 0$ solution for the time-accurate run. The steady state problem is solved using an infinite time step such that the system is solved with a Newton iteration (see Eq. 4.122) and converged to a global residual of 10^{-12} . Ten iterations are used on the inner problem.

When the laser is turned on, nearly a second passes before the laser reaches full power. The

Table 8.1: Free stream conditions

Mach Number: M_∞	3.75
Static temperature: T_∞	77.4 K
Static pressure: P_∞	9770.5 Pa

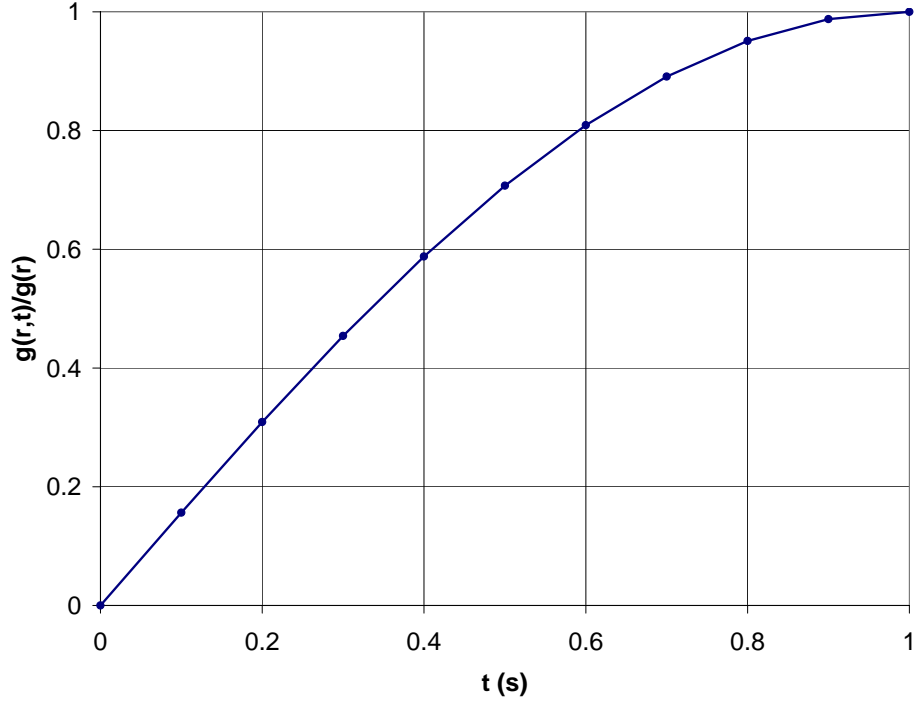


Figure 8.1: Ramp in laser power specified as a pointwise boundary condition

laser startup is modeled using the following function:

$$g(r, t) = \begin{cases} g(r) \sin\left(\frac{\pi t}{2T_s}\right) & 0 \leq t \leq T_s \\ g(r) & t > T_s \end{cases} \quad (8.1)$$

where r is the distance from the beam center, the startup time of the laser, T_s equals 1 second and the intensity (heat flux per unit area) distribution for a Gaussian beam, $g(r)$ is given by equation 2.6 where P is the laser optical power and w the beam width. The intensity was specified on the surface with a pointwise boundary condition at each 0.1 seconds as seen in Fig. 8.1. Linear interpolation is used by the solver in between the specified values.

The time-accurate simulation was performed using a physical time step of 3×10^{-4} seconds. Within the dual-time-stepping formulation, 10 inner cycles are performed for each time step. The inner pseudo time step is set to infinity (ie, 10^{15}). All cases were solved with the one-equation Spalart-Allmaras turbulence model. However, to assess the sensitivity to turbulence modelling, some cases were solved using Willcox $k - \omega$ and Menter's SST turbulence models.

The grid was generated with Gridgen grid generation software. Only one half of the geometry is modelled and a symmetry boundary condition was used. Three grid densities, coarse, medium and fine were generated to perform a grid and a time refinement study in order

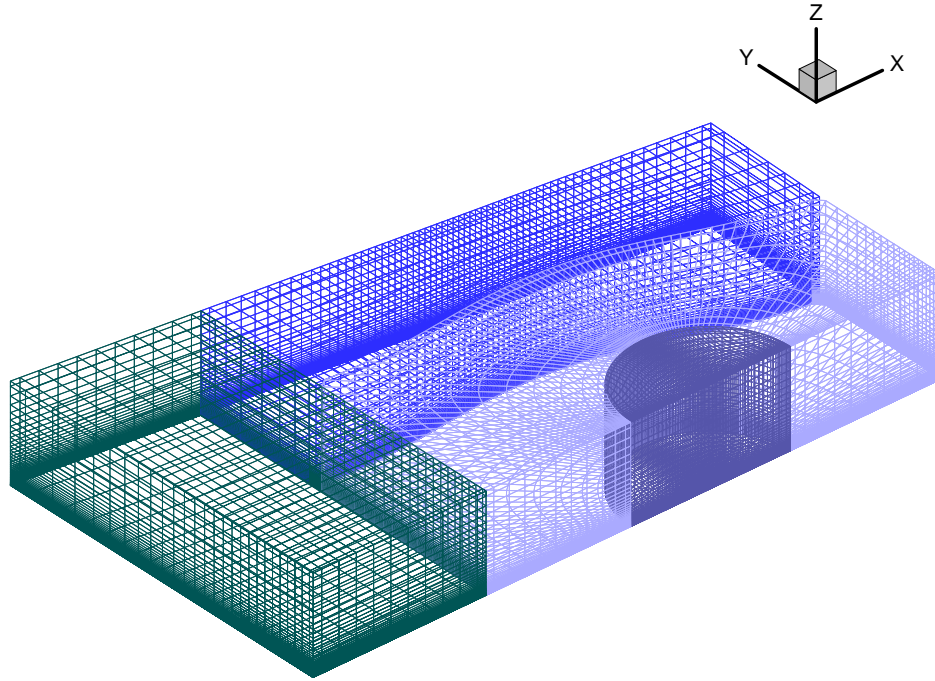


Figure 8.2: Medium grid for the fluid domain composed of four blocks. Half of the geometry is modeled due to symmetry

to estimate the spatial and temporal discretization errors. The details of the grid and time convergence study are presented in the next section. The medium grid for the fluid domain is shown in Fig. 8.2. Four blocks are used for the fluid domain and solid domain, respectively, with a matching interface between the fluid and solid zones. The conjugate heat transfer boundary condition was used at the interface and the algorithm detailed in section 5.2 is used. An adiabatic boundary condition was used and on the edge on the backside of the solid. Convective and radiative boundary conditions on the backside were tried but the effect on the temperature is insignificant (less than 0.01 K).

The surface topology is shown in Fig. 8.3. H-C-H topology is used such that an H-grid block is surrounded by a C-grid block. This topology is more efficient since it keeps the clustering localized around the target center compared to strictly using an H-grid which propagates the clustering throughout the domain. However, this H-C-H topology has the disadvantage of creating non-orthogonal cells at the junction of the H and C zones which is known to cause convergence problems. Here, no such problems were identified. To make the transition as smooth as possible, the shape of the junction between the H and C grids was kept free and the elliptical smoothing solver provided in Gridgen was used. In the fluid, hyperbolic tangent clustering is used in the z-direction to properly capture the boundary layers. For the medium grid, more than 40 points are located in the boundary layer. The center of the

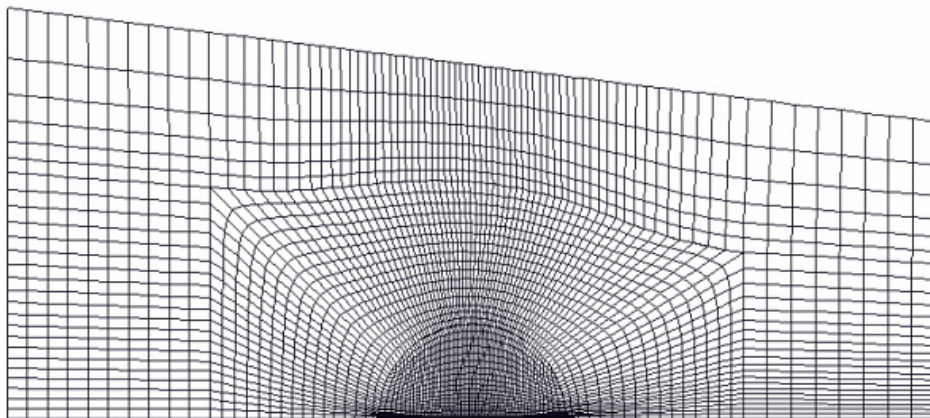


Figure 8.3: Surface grid topology

first cell of the wall is located at $2.5 \times 10^{-6}m$ from the wall to get a value of y^+ of 0.5. In the solid, hyperbolic tangent clustering was also used in the z -direction.

Most simulations were performed at AeroSoft, Inc. on a Linux cluster using between 8 and 16 processors. The other simulations were performed on the Enterprise SGI cluster using 32 processors and on the System-X Mac cluster using 16 processors, both at Virginia Tech. Typically, on 8 processors, the solution corresponding to 10 seconds of physical time takes approximately 2 weeks of computation.

8.1 Grid and Time Convergence Study

As for experimental testing, evaluating the uncertainty of the numerical simulation is of crucial interest. However as one can imagine, sources of computational and numerical uncertainties are inherently different. Here, the focus is on quantifying the spatial and temporal discretization errors. The methodology used is presented next.

8.1.1 Methodology

The generalized Richardson extrapolation method developed by Roache [58] was used to compute the spatial and temporal discretization errors. To evaluate the spatial discretization error on an arbitrary clustered grid, a characteristic grid size must be defined. For a 3-dimensional computational domain we use:

$$h = \left[\frac{V}{N} \right]^{1/3} \quad (8.2)$$

8.1. GRID AND TIME CONVERGENCE STUDY

where V is the total volume and N the total number of cells in the computation domain. It is convenient to introduce the grid refinement factor:

$$r_{ij} = \frac{h_i}{h_j} \quad (8.3)$$

which is the ratio of grid size for grid i and j . The generalized Richardson extrapolation method enables the computation of the observed convergence order by using three different grid levels. The grid used must be sufficiently clustered to get solutions that are located in the asymptotic grid convergence range. For example, when modeling wall bounded flows, a sufficient number of cells must be located in the boundary layer for each grid.

Given 3 grids with $h_1 < h_2 < h_3$, the apparent convergence order p , is computed by first choosing an important variable for the problem at hand, ϕ . Here, the maximum surface temperature is chosen. The basic idea of the method is to extrapolate the value of ϕ for $h \rightarrow 0$ to get the exact solution estimate. Using this estimate, the error can be computed for each grid. The exact value is written as the sum of the computed value and an error term of order p . For three grid levels we get:

$$\begin{aligned} \phi_{exact} &\simeq \phi_1 + Ch_1^p \\ \phi_{exact} &\simeq \phi_2 + Ch_2^p \\ \phi_{exact} &\simeq \phi_3 + Ch_3^p \end{aligned} \quad (8.4)$$

where only the dominant order terms contributing to the error are considered. It is agreed upon that this approximation is valid when the solutions are in the asymptotic range. Eq. 8.4 constitutes a nonlinear system of 3 equations and 3 unknowns C , p and ϕ_{exact} . Baker [4] showed that this system possesses a nontrivial positive root for p when monotonic convergence is observed i.e. $\phi_1 < \phi_2 < \phi_3$ or $\phi_1 > \phi_2 > \phi_3$. However, Celik et. al. [12] showed that oscillatory convergence can be observed in the asymptotic range for upwind and mixed methods. We also believe that the coupling of the fluid and solid solution could lead to an oscillatory convergence. Satisfaction of Eq. 8.4 is, therefore, desirable for a consistent scheme (stable and convergent) but not necessary. The following solution was proposed by Celik et. al [12] who have simply introduced the *sign* function to handle the negative sign in the error ratio occurring when oscillatory convergence is observed:

$$\begin{aligned} p &= \frac{1}{\ln r_{21}} \left| \ln \frac{\varepsilon_{32}}{\varepsilon_{21}} + q(p) \right| \\ q(p) &= \ln \left(\frac{r_{21}^p - s}{r_{32}^p - s} \right) \\ s &= \text{sign} \left(\frac{\varepsilon_{32}}{\varepsilon_{31}} \right) \end{aligned} \quad (8.5)$$

where $\varepsilon_{ij} = \phi_i - \phi_j$ where ϕ_i denotes the solution on the j^{th} grid. Eq. 8.5 is also valid for monotonic convergence as it simply yields the solution to the system 8.4. The observed

8.1. GRID AND TIME CONVERGENCE STUDY

Table 8.2: Number of cells for the discretization error determination

Grid	Fluid	Solid	Total
Coarse	118080	68880	186960
Medium	169200	112800	282000
Fine	336384	280320	616704

order p is computed by solving Eq. 8.5 numerically. The extrapolated value of the solution is obtained from:

$$\phi_{ext}^{21} = (r_{21}^p \phi_2 - \phi_1) / (r_{21}^p - 1) \quad (8.6)$$

The approximate relative error between grids i and j is computed according to:

$$e_a^{ij} = \left| \frac{\phi_i - \phi_j}{\phi_j} \right|, \quad i = j + 1 \quad (8.7)$$

and the true relative error corresponding to the solution on grid j is obtained from:

$$e_j^{21} = \left| \frac{\phi_{ext}^{21} - \phi_j}{\phi_{ext}^{21}} \right| \quad (8.8)$$

The same method can be used to compute the temporal discretization error by replacing h with the time step Δt .

8.1.2 Spatial Discretization Error

Using the method described in the previous section, the spatial discretization error was estimated using three different grid levels. The number of fluid, solid and total cells for each grid is shown in Table 8.2. For the 3 grids, the distance to the center of the first cell off the wall is kept constant at $2.5 \times 10^{-6}m$ to have a value of y^+ close to 0.5 as required by the turbulence models. For all three grids, at least 30 points are located in the boundary layer.

In order to avoid introducing a time discretization error, a steady state solution was obtained. The maximum surface temperature was chosen as the critical variable ϕ , and the steady state is obtained when the relative change in the maximum surface temperature becomes sufficiently small. The maximum surface temperature as a function of the number of iterations is shown in Fig. 8.4. Oscillatory convergence is noticed as the solution for the medium grid gives the highest maximum surface temperature. The computed spatial discretization error and important parameters used in the computation are reported in Table 8.3. The observed order p is equal to 6.2 which is greater than the theoretical order which should be somewhere between 2 and 3. All grids display a reasonable discretization the highest relative error being equal to 2.2% for the coarse grid. The relative error of the fine grid is much lower compared to the medium and coarse grid.

8.1. GRID AND TIME CONVERGENCE STUDY

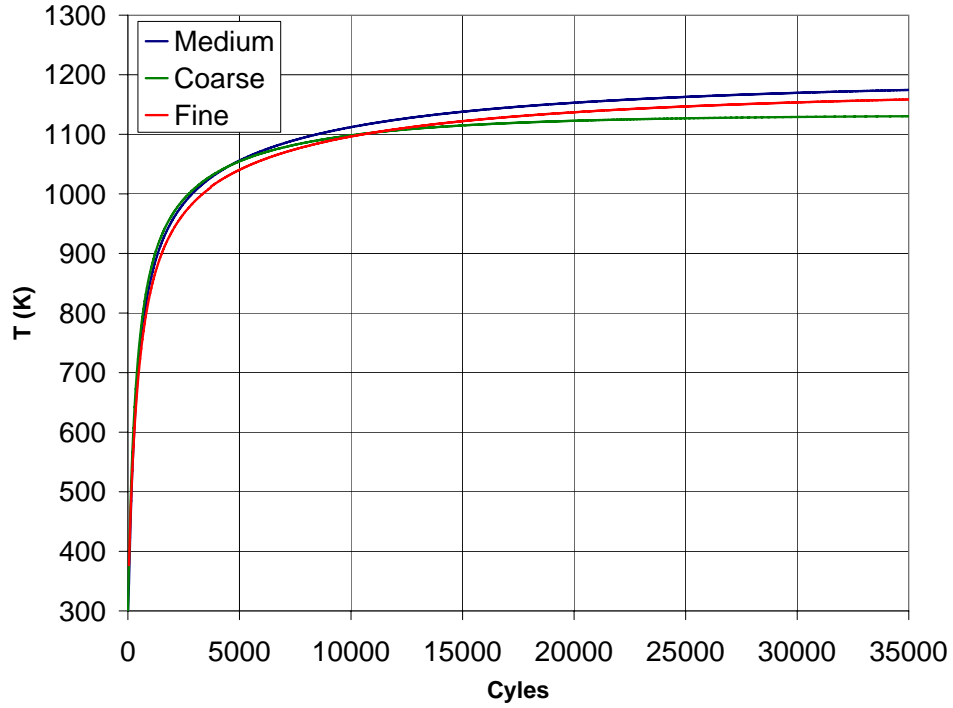


Figure 8.4: Maximum surface temperature for a steady state computation at P=81 Watts

Table 8.3: Spatial discretization error

	$\phi \equiv$ Maximum surface temperature [K]
r_{21}	1.3
r_{32}	1.15
ϕ_1	1158
ϕ_2	1174
ϕ_3	1130
p	6.2
ϕ_{ext}^{21}	1155
e_1^{21}	0.35%
e_2^{21}	1.7%
e_3^{21}	2.0%

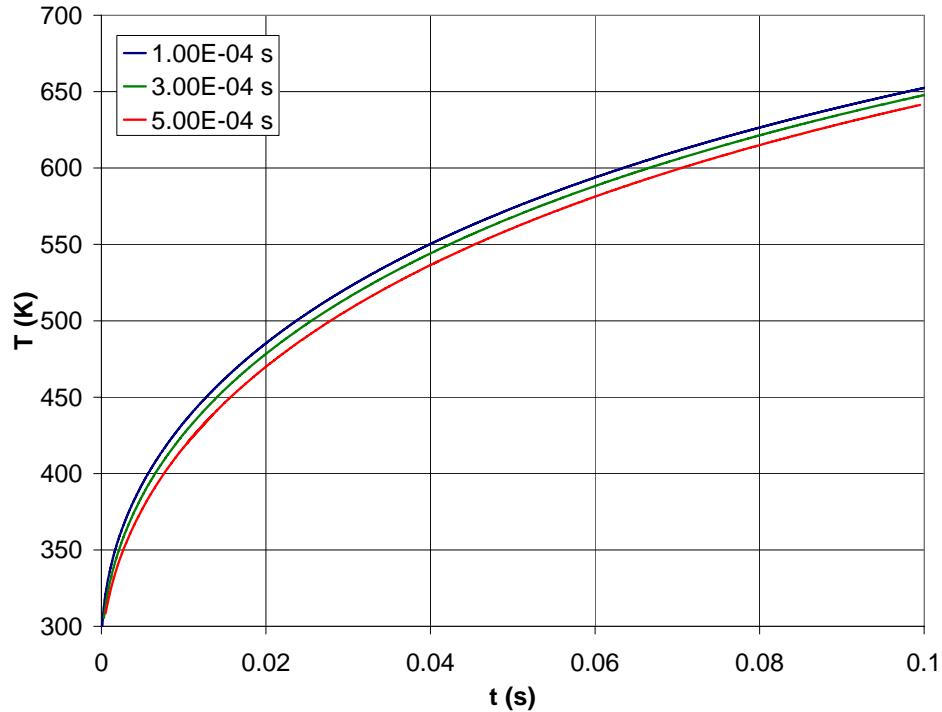


Figure 8.5: Maximum surface temperature used in the evaluation of the time discretization error

8.1.3 Time Discretization Error

The time discretization was evaluated by performing time-accurate simulations with three different time steps namely, 1×10^{-4} , 3×10^{-4} , 5×10^{-4} for a total time of 0.1 second. No ramp in the laser power was used as the full laser power is applied at $t=0$. To minimize the spatial discretization error, the fine grid was used for all time steps. The results are shown in Fig. 8.5.

The time discretization error was obtained using the same method as before. The computed discretization error is found in Table: 8.3. The magnitude of the time discretization error is similar to the spatial discretization error. The computed order of convergence is equal to 1.15 which is smaller than the theoretical value of 3. This is probably due to the coupling algorithm. However, a monotonic convergence is found in contrast which the spatial discretization. The computed temperature decreases with an increase in the time step.

Table 8.4: Time discretization error

	$\phi \equiv$ Maximum surface temperature [K] at $t = 1s$
r_{21}	3
r_{32}	1.67
ϕ_1	651.8
ϕ_2	647.3
ϕ_3	642.3
p	1.15
ϕ_{ext}^{21}	653.6
e_1^{21}	0.273%
e_2^{21}	0.97%
e_3^{21}	1.7%

8.1.4 Total Error for Flow-on and Flow-off Conditions

Considering the available computational resources and the time required to perform a numerical simulation the medium grid was chosen with a time step of 3×10^{-4} second. For the flow-on case, the total error was computed using the mean root square formula for the spatial and time discretization error. Since the error estimator neglects the iterative convergence error and roundoff errors, a safety factor of 1.25 was used as recommended by Celik [11] in the Journal of Fluids Engineering Editorial Policy Statement on the Control of Numerical Accuracy. We then have for the flow-on condition a total error equal to:

$$|\text{total error (\%)}|_{\text{flow-on}} = 2.2\%$$

It is important to mention that this error doesn't include the physical modeling error. Here the analysis is performed for the 81 Watt case and the total error is assumed the same for the 65 Watt case.

For the flow-off case, an exact solution is known (Eq. 2.16) for a material with constant properties. To get an estimate of the total error for the flow-off case, the numerical solution for a material with constant properties was compared to the analytical solution. The maximum surface temperature for the numerical and the analytical solution is plotted in Fig. 8.6. The medium grid with a time step of 1×10^{-4} was used to compute the numerical solution. We notice that the numerical computation underestimates the maximum surface temperature compared with the analytical solution. The total relative error for the flow-off case was computed by taking the difference between the numerical and the analytical solution and applying a safety factor of 1.25 which gives:

$$|\text{total error (\%)}|_{\text{flow-off}} = 1.2\%$$

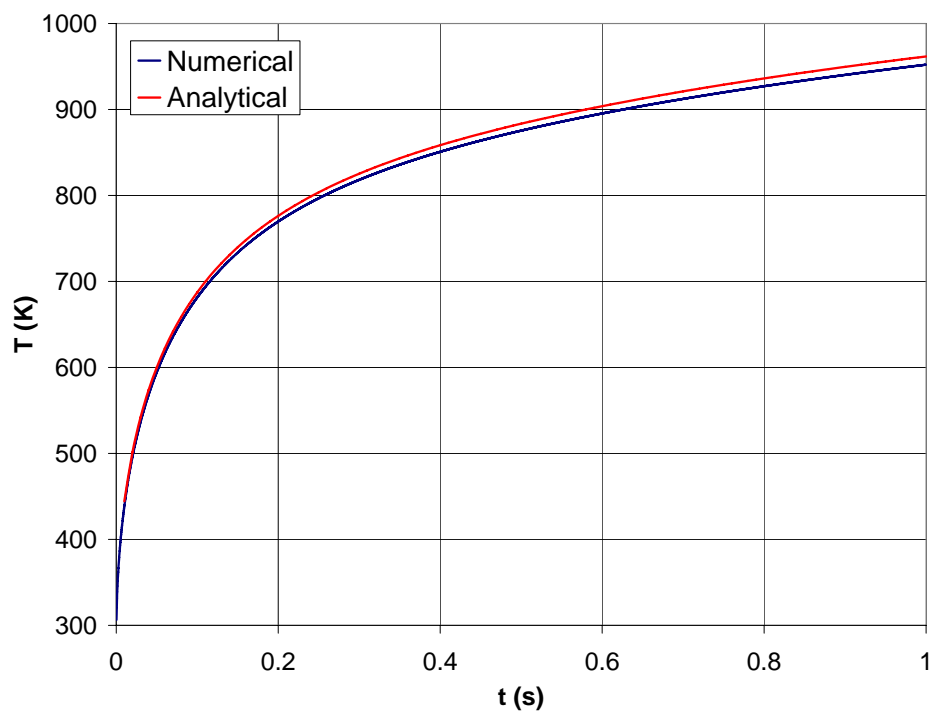


Figure 8.6: Comparison of the maximum surface temperature between the numerical and analytical solution for the medium grid at a time step of 1×10^{-4}

8.1.5 Uncertainty on the Temperature Difference

Since we are interested in the cooling effect of the flow, we need to evaluate the uncertainty of the maximum temperature difference between the flow-on and flow-off cases. Here, the effect of the temperature subtraction on the uncertainty can't be expected to act like for the experiment as we can't expect the same error cancellation. One simple-minded way to proceed is to add the discretization errors of the flow-on case to that of the flow-off case. This method leads to an overestimation of the uncertainty. Here, a sensible accurate approach was used. First, it is noticed that the time step requirements for the flow-off solution are much less than that for the flow-on case, as the time scale of the solid is much larger than the time scale of the fluid. When the same time steps are used for the flow-on and flow-off solutions, the discretization error for the flow-off solution is entirely due to the spatial discretization. The strategy used to estimate the uncertainty of the temperature difference is explained next. First, a very fine cartesian grid containing over 1 million cells was generated. Here, the number of cells increases as the clustering around the target center propagates throughout the domain. However for that simple topology, all the cells are perfectly orthogonal which should contribute to reducing the numerical error. Therefore, for such a fine orthogonal grid, a minimal spatial discretization error is expected. This grid was used to estimate the exact solution. This exact solution is generated by computing two solutions with respective time steps of $1 \times 10^{-4}s$ and $3 \times 10^{-4}s$. Using the observed temporal convergence order, the exact solution can be estimated. The temperature difference was computed by subtracting the flow-off solution obtained on the fine cartesian grid to the estimate of the exact solution. Since the time discretization error can be neglected for the flow-off solution and the spatial discretization error on the fine cartesian grid is small, they should give a good estimate of the exact temperature difference. Next, the exact temperature difference estimate was compared with the temperature difference for the medium grid with a time step of $3 \times 10^{-4}s$. Here, it is useful to look at the computed temperatures to get an idea of the temperature differences between the different solutions. Results are shown in Fig. 8.7. We notice that both the flow-on and flow-off solutions for the cartesian grids give a higher temperature compared to the medium grid. At $t = 1.2s$, the difference between the 3×10^{-4} time step and the 1×10^{-4} time step solutions reaches $0.74K$ corresponding to 5.58% of the computed temperature difference. The estimate of the exact temperature is found equal to $866.6K$. The estimate to the temperature difference is equal to 13.05. The total error for the medium grid is found equal to:

$$|\text{total error (\%)}|_{\text{temperature difference}} = 5.9\%$$

relative to the maximum surface temperature difference.

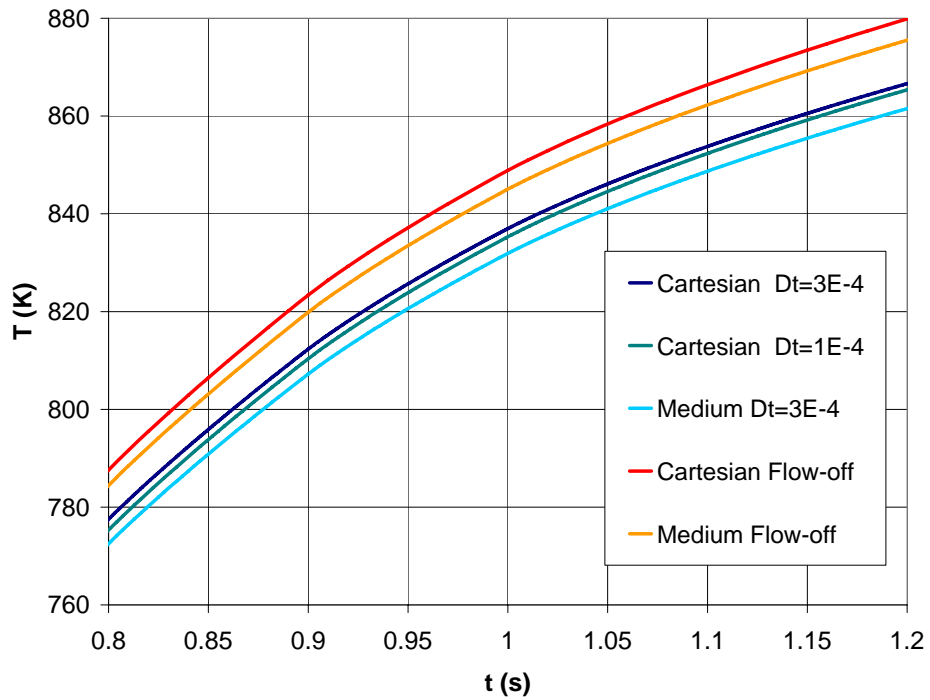


Figure 8.7: Comparison of the solutions used in the evaluation of the uncertainty on the computed difference between the flow-off and flow-on cases. In the legend, medium refers to the medium grid with a H-C-H topology (seen in Fig. 8.2) whereas the cartesian refers to a fine cartesian grid

Table 8.5: Effect of turbulence modeling

t (s)	T S-A (K)	T $k-\omega$	T M-SST
0.1	336.06	336.11	336.10
0.5	615.83	616.44	616.41
2	831.68	833.20	833.09
3	921.31	923.90	923.64
4	962.14	965.49	965.15
5	1012.48	NA	1013.32
9	1064.16	NA	1063.39

8.2 Effects of the Turbulence Model

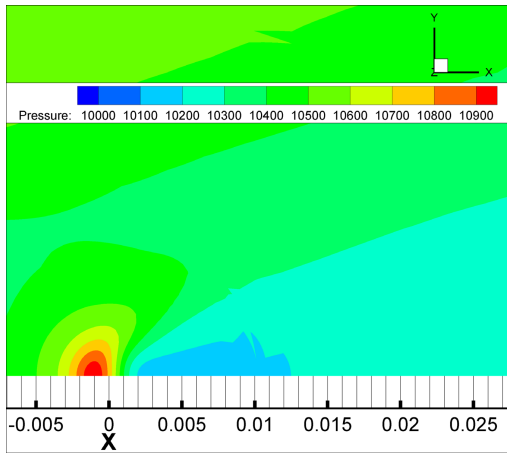
Different turbulence models were used to evaluate the sensitivity of the problem to turbulence modeling. Simulations were performed for the 81 Watt case. The Spalart-Allmaras, $k-\omega$ and Menter-SST turbulence models were used. The maximum surface temperature computed at different times for each turbulence model is found in Table 8.5. We notice that turbulence modeling has a small effect on the maximum surface temperature.

8.3 Flow Results

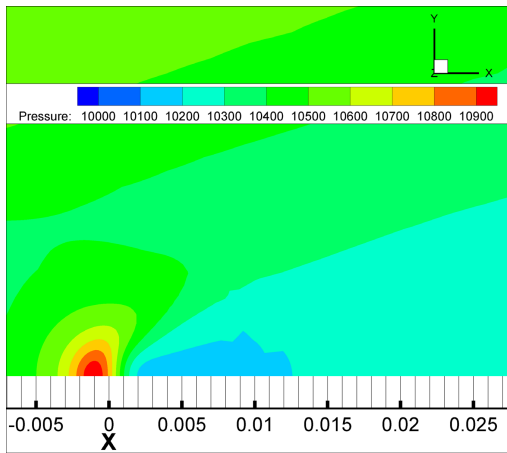
The effect of the heating on the flow variables is investigated. The use of CFD makes it possible to visualize the change produced by the wall heating on the flow field. Results for 65 Watt of laser power are presented next. Similar results are observed for the 81 Watt case.

The x-axis is aligned with the streamwise direction, the z-axis is normal to the wall and the y-axis completes the right-handed orthogonal reference frame. Fig. 8.8 presents pressure contours for slices parallel to the wall for an increasing wall distance. We notice an increase in pressure of about 5% in front of the target center and a decrease in pressure of similar magnitude downstream. The pressure disturbances emanating from the wall get convected downstream along Mach lines as seen in Fig. 8.9. The intensity of the disturbances is progressively reduced with increasing distance from the wall due to three dimensional effects.

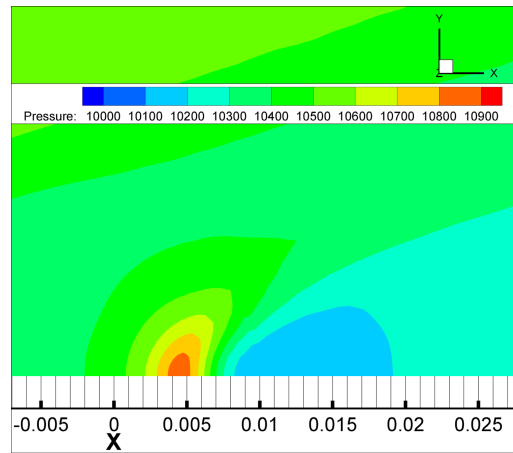
8.3. FLOW RESULTS



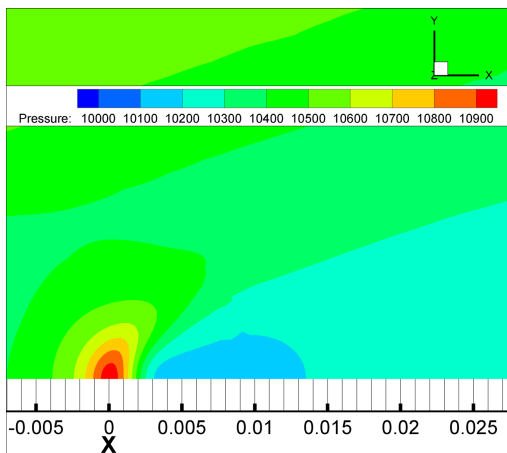
(a) wall



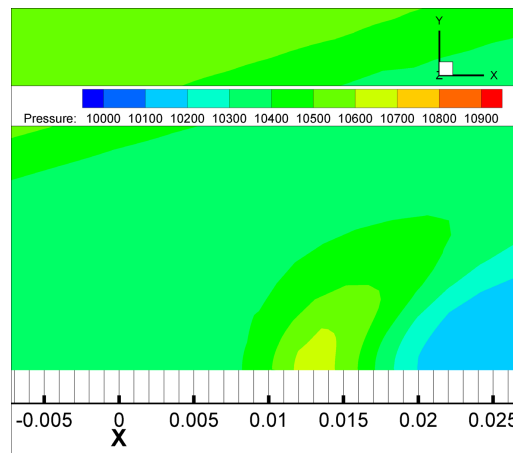
(b) $z=0.1$ mm



(d) $z=3$ mm



(c) $z=1$ mm



(e) $t=6$ mm

Figure 8.8: Pressure contours in the x-y plane. Dimensions are in *mm*

8.3. FLOW RESULTS

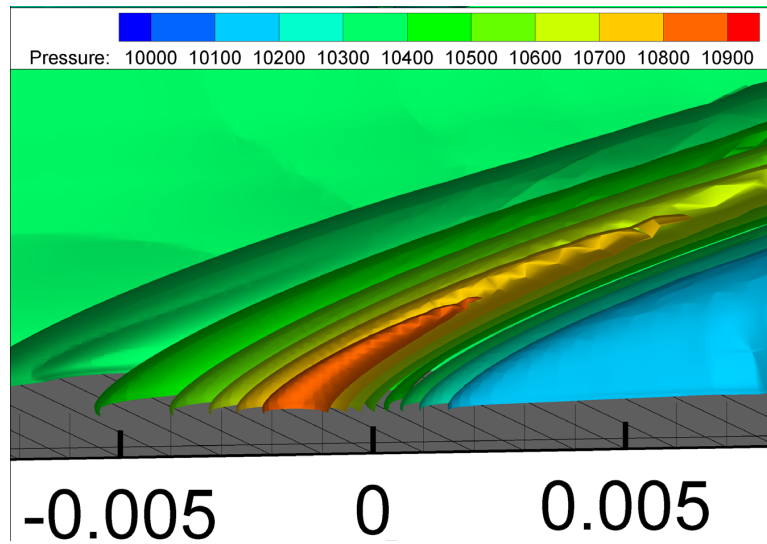


Figure 8.9: Pressure iso-contours at $t = 10s$ for $P=65$ W. A high pressure region is created upstream of the heat spot and a low pressure region is created downstream

It is noticed that the temperature disturbances are localized in a thin-near-wall region. For a maximum wall temperature of 900 K, the maximum temperature in the flow decreases to 400 K at 0.1 mm from the wall as seen in Fig. 8.10. This makes temperature measurements in the flow very difficult.

8.3. FLOW RESULTS

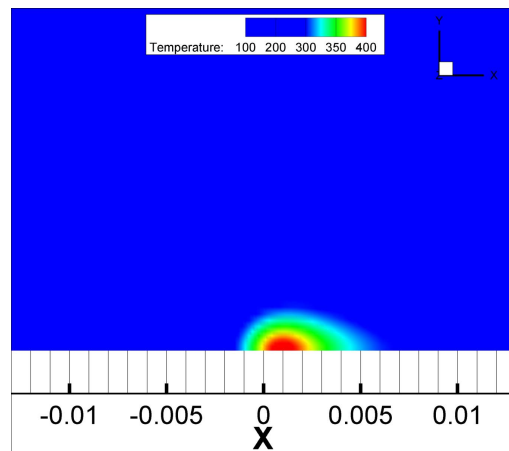
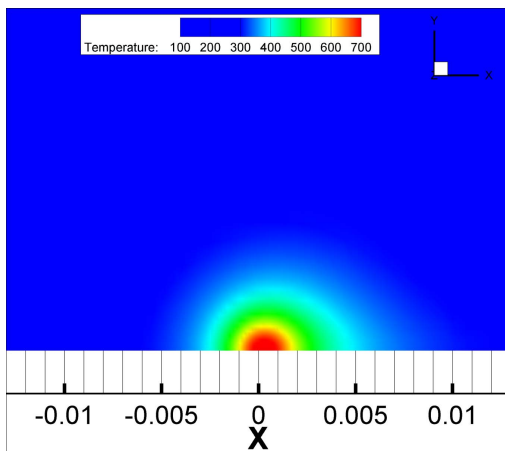
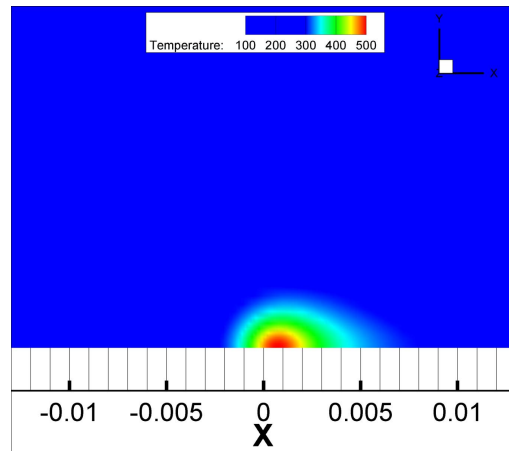
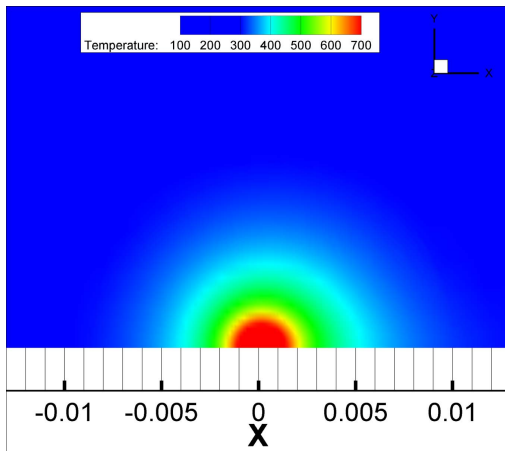
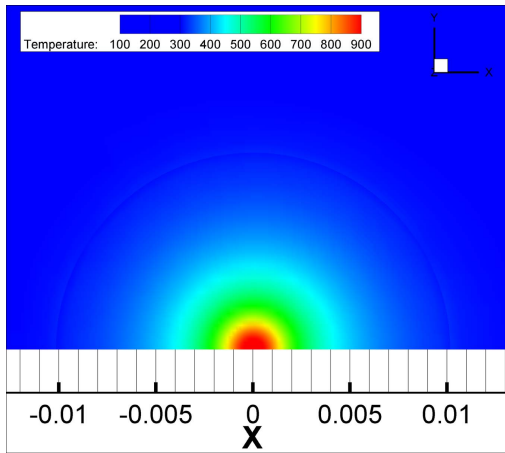


Figure 8.10: Temperature contours in the x-y plane dimensions are in mm

8.3. FLOW RESULTS

Density contours are shown in Fig. 8.11, where we notice a strong decrease in density near the wall where the maximum temperature is reached. This behavior is easily deduced from the thermal equation of state. Moving away from the wall, the density contours get elongated in the streamwise direction.

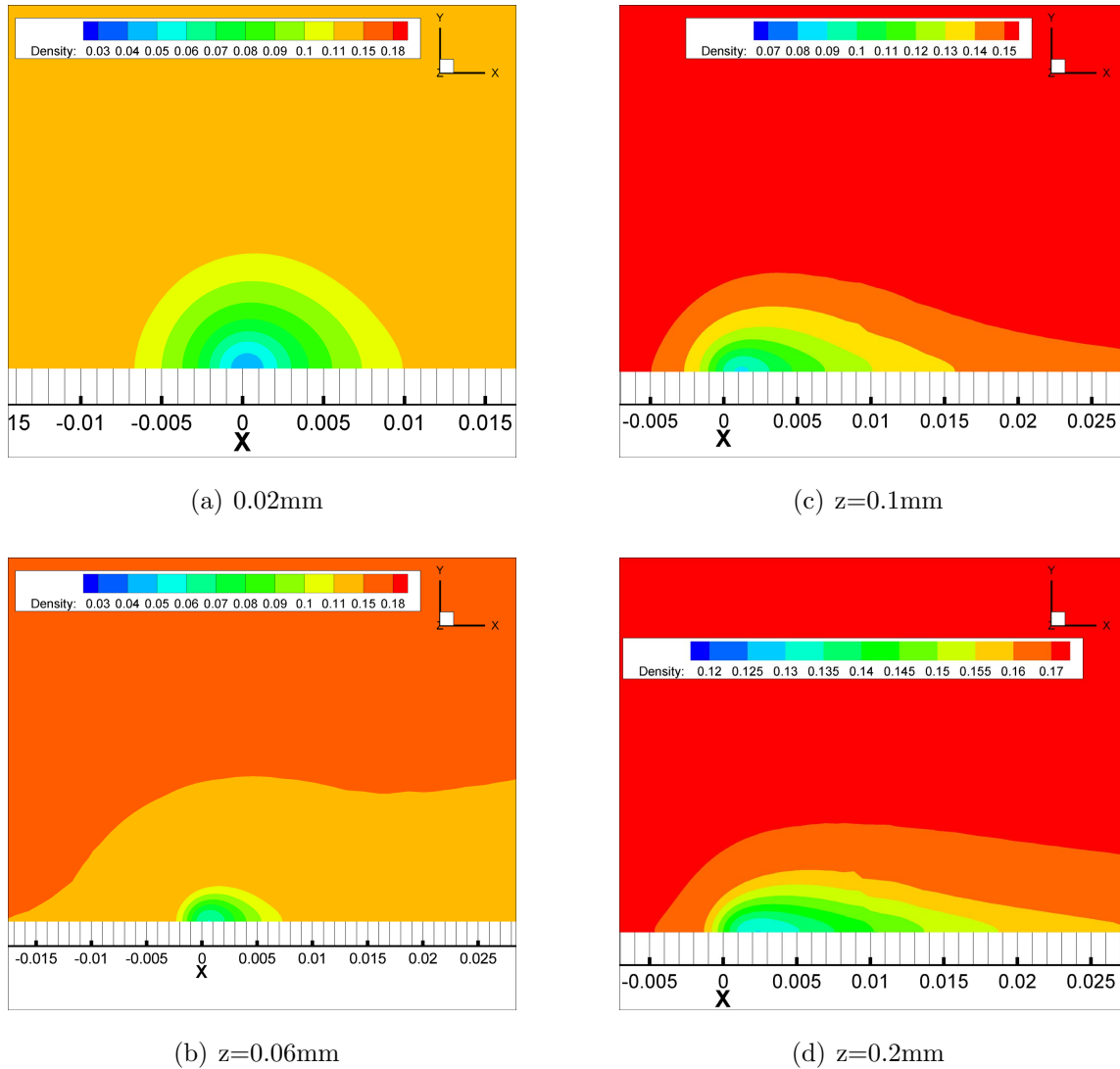


Figure 8.11: Density contours in the x-y plane dimensions are in mm

Fig. 8.12 shows the streamlines and w-velocity contours in the symmetry plane. To improve the visualization of the flow features, the scale is stretched by a factor of 20 in the z-direction. Clearly, the heated spots acts as a "bump" which slightly turns the flow upward. Very close to the wall, the flow is turned downward behind the bump as a region of negative w-velocity is seen. The positive disturbance in the w-velocity component is convected along Mach lines,

8.3. FLOW RESULTS

whereas the negative disturbance is quickly damped out such that it remains near the wall.

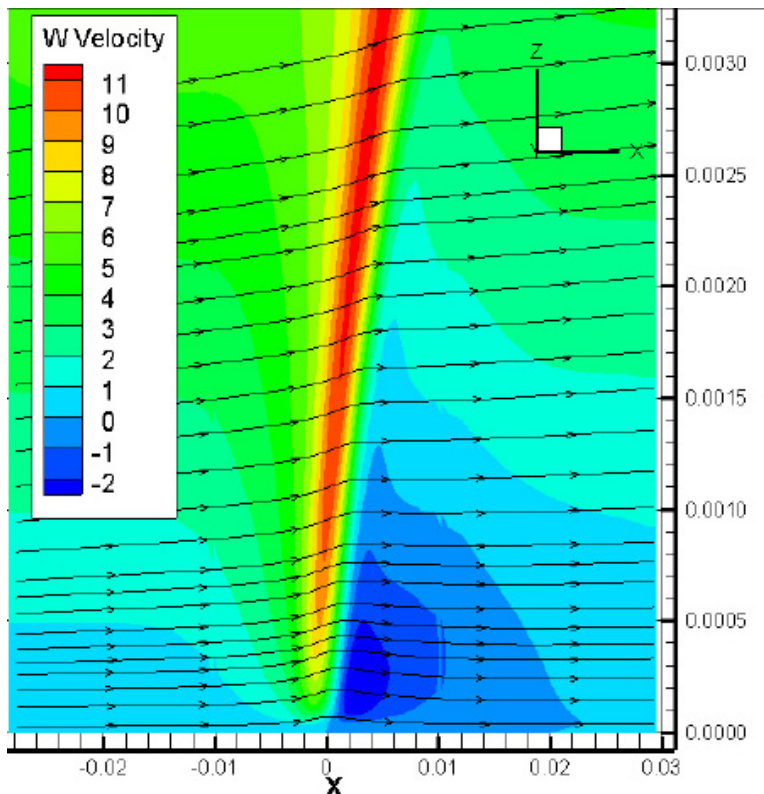


Figure 8.12: Streamlines in the x - z plane at $t = 10s$ dimensions are in mm . The heat source acts like a "bump"

It is interesting to look at the effect of the heating on the vorticity field. The vorticity transport equation is obtained by taking the curl of the momentum equation 4.2 leading to:

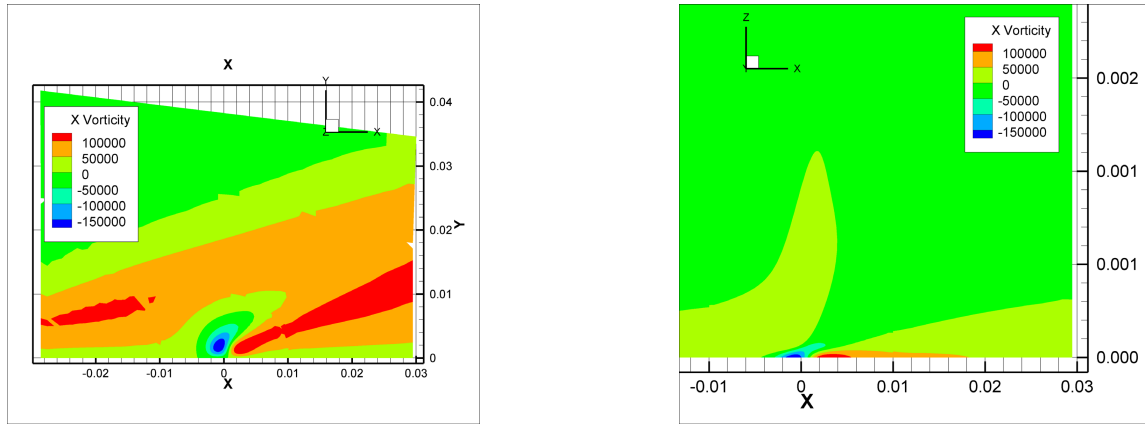
$$\frac{D\boldsymbol{\omega}}{Dt} = -\boldsymbol{\omega}\nabla \cdot \mathbf{v} + \boldsymbol{\omega} \cdot \nabla \mathbf{v} + \frac{1}{\rho^2} \nabla p \times \nabla \rho + \nu \nabla^2 \boldsymbol{\omega} \quad (8.9)$$

The first term on the LHS is the change in vorticity due to fluid dilatation. This term can't change the orientation of the vorticity vector. The second term on the LHS represent the change due to a gradient in velocity which can be decomposed in two-component one parallel to the vorticity vector called the "stretching" and one perpendicular called the "tilting". The third term known as baroclinic generation plays a role when the pressure and density gradients are misaligned. The last term is the viscous vorticity diffusion.

Since the heating expands the fluid, we expect a decrease in vorticity. In the boundary layer, most of the vorticity is in the y -direction (considering the coordinate system used) such that we expect a reduction of the y -component of the vorticity. The x , y and z components of the

8.3. FLOW RESULTS

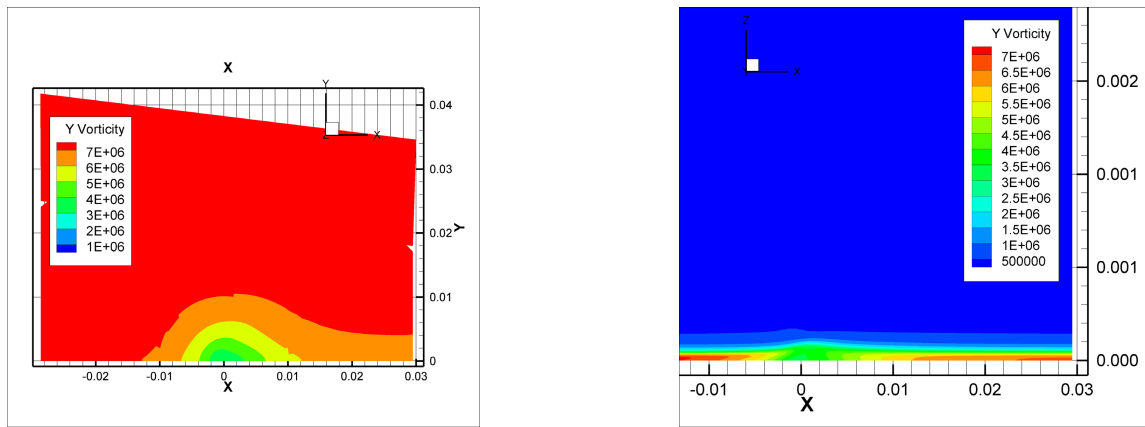
vorticity in the $x - y$ and $x - z$ planes are shown in Figs 8.13, 8.14 and 8.15. As expected, a reduction of about 45% of the y -vorticity component is seen. This translates into a reduction of the near-wall velocity gradient as seen in Fig 8.19. The x and z -vorticity components are also modified, but to a much lesser extent. It is seen that the heating creates a strong density gradient in the near wall region and a moderate pressure gradient that gets convected along Mach lines. The baroclinic term could, therefore, contribute to the change in vorticity.



(a) x -vorticity in the $x - y$ plane at $z = 1 \times 10^{-5}m$

(b) x -vorticity in the $x - z$ plane at $y = 1 \times 10^{-5}m$

Figure 8.13: x -vorticity at $t = 10s$ for P=65 W dimensions are in mm

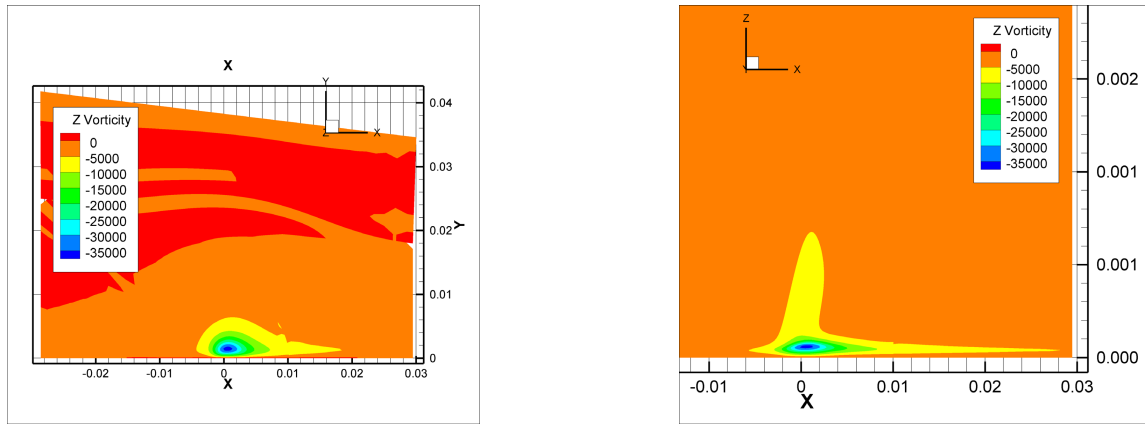


(a) y -vorticity in the $x - y$ plane at $z = 1 \times 10^{-5}m$

(b) y -vorticity in the $x - z$ plane at $y = 1 \times 10^{-5}m$

Figure 8.14: y -vorticity at $t = 10s$ for P=65 W dimensions are in mm

8.3. FLOW RESULTS



(a) z -vorticity in the $x - y$ plane at $z = 1 \times 10^{-5}m$

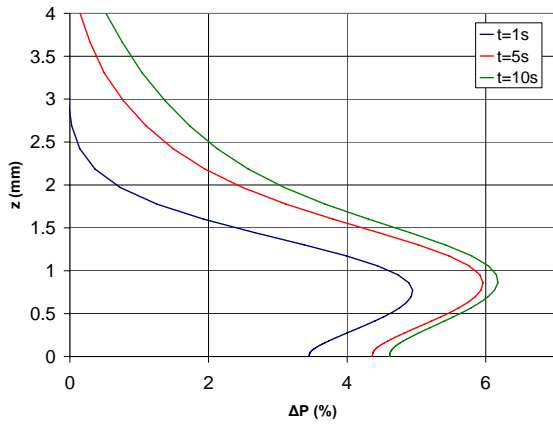
(b) z -vorticity in the $x - z$ plane at $y = 1 \times 10^{-5}m$

Figure 8.15: z -vorticity at $t = 10s$ for $P=65 W$ dimensions are in mm

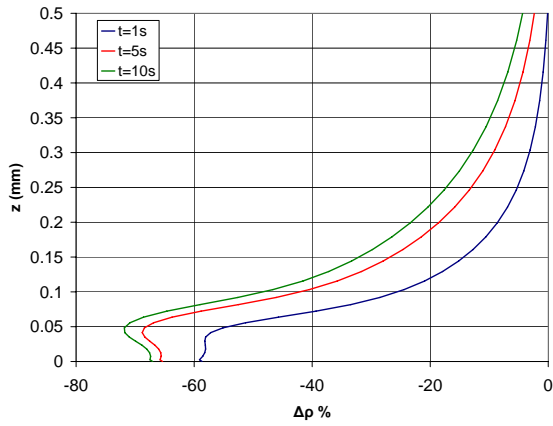
Next, the effect of heating on the flow is visualized by looking at the z -profiles of the flow variables at three locations namely, at 0.1 inch upstream, at the target center and at 0.1 inch downstream. The relative difference between the unheated ($t=0$) and heated case at $t = 1s$, $t = 5s$, and $t = 10s$ are computed for pressure, density and viscosity, whereas the absolute difference is computed for temperature and u -velocity.

At the center, an increase in pressure is seen. The maximum increase reaches 6% at 1 inch from the wall. With increasing time, the disturbance in pressure increases. A larger increase is seen in the initial 5 seconds compared to the last 5 seconds of heating. The change in density and viscosity are driven by the change in temperature as seen in Fig. 8.16 b), c) and d). The reduction in density reaches a maximum value of 70% at 0.5 mm from the wall. The greatest viscosity increase exceeds 100% at the wall. Considering the increase in pressure, it is not surprising to notice a reduction in the u -velocity component. The velocity reduction reaches $140m/s$ at $0.04mm$ from the wall.

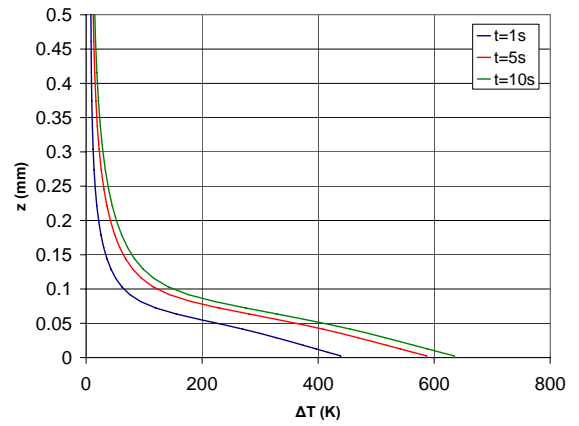
8.3. FLOW RESULTS



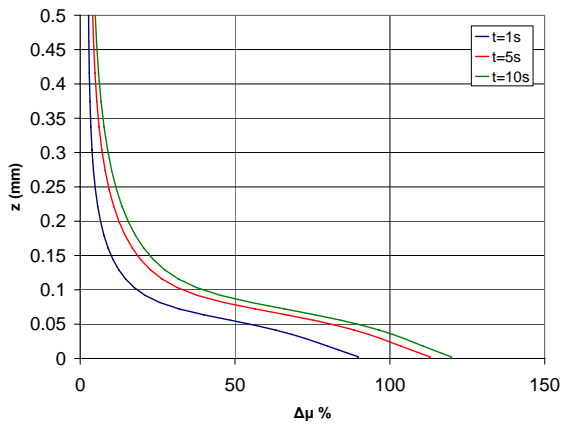
(a) Relative pressure difference at center



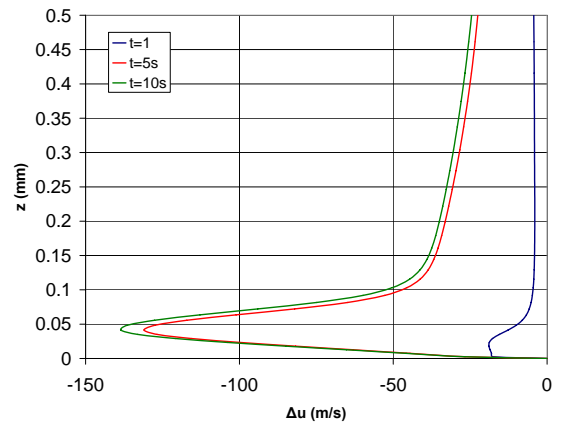
(b) Relative density difference at center



(d) Temperature difference at center



(c) Relative viscosity difference at center



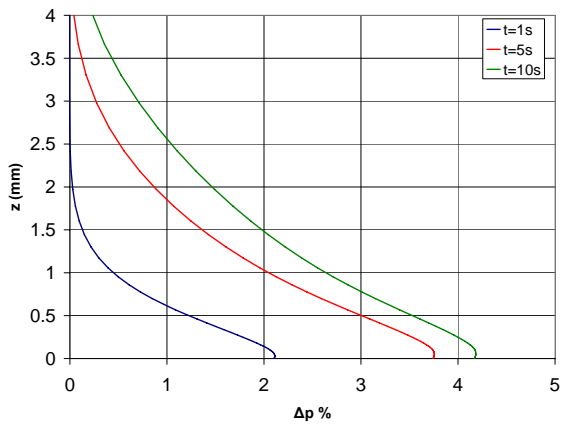
(e) Velocity difference at center

Figure 8.16: Effect of heating on flow variables for $P = 65W$ at target center

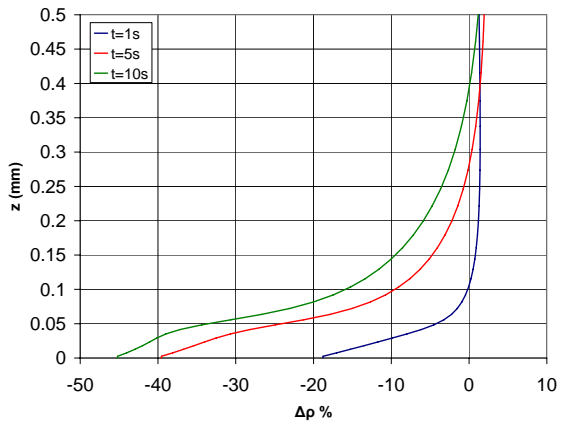
8.3. FLOW RESULTS

At 0.1 inch each upstream, the variation in the flow variables are smaller than that at the center, but the trends are the same with the exception to the density variation which is now greatest at the wall. This is shown in Fig. 8.17.

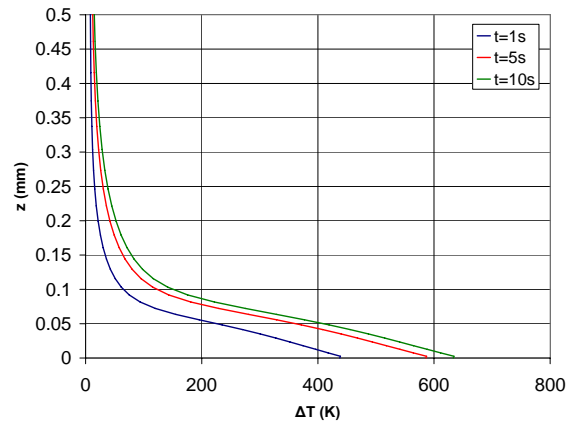
8.3. FLOW RESULTS



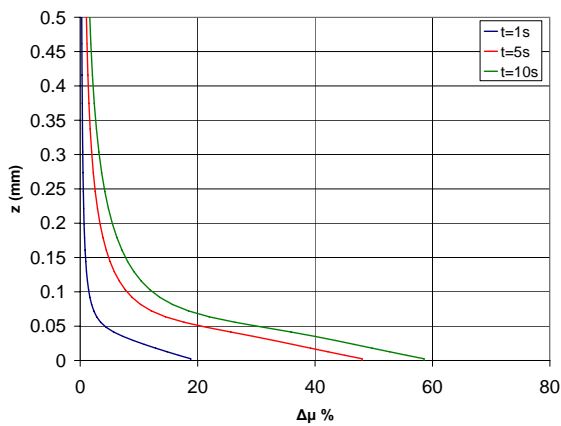
(a) Relative pressure difference 0.1 inch upstream



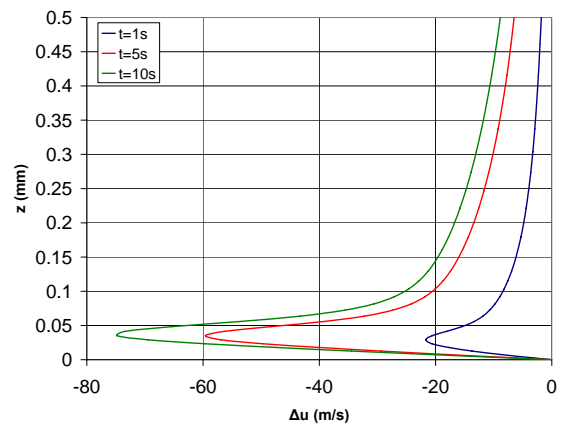
(b) Relative density difference 0.1 inch upstream



(d) Temperature difference 0.1 inch upstream



(c) Relative viscosity difference 0.1 inch upstream



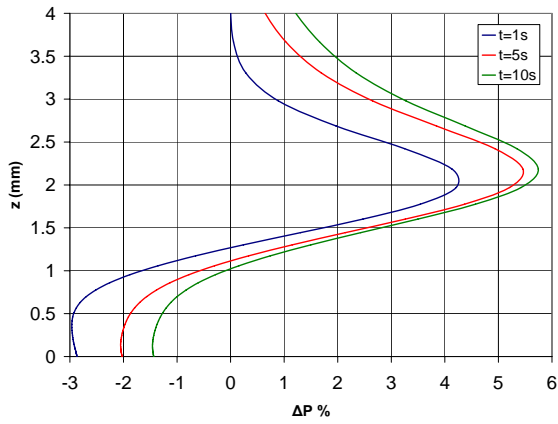
(e) Pressure difference 0.1 inch upstream

Figure 8.17: Effect of heating on flow variables for $P = 65W$ 0.1 inch upstream of target center

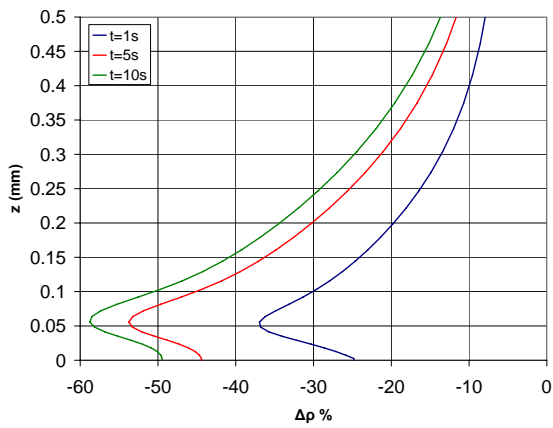
8.3. FLOW RESULTS

At 0.1 downstream, a reduction in pressure is found near the wall whereas, away from the wall pressure the increases as seen in Fig. 8.18. This increase corresponds to the upstream pressure disturbance which is transmitted along Mach lines. The reduction in velocity is smaller compared to that at the center such that the fluid is actually accelerating downstream of the target center. At $t = 1s$, the hot plume is clearly visible as the temperature increase in the flow is greater than the increase in wall temperature. The u-velocity and Mach profiles at the target center for different time values are seen at Figs. 8.19 and 8.20. A different behavior is seen for the Mach and u-velocity profiles. As noticed previously, the u-velocity is decreased near the wall. However, due to the increase in temperature, the speed of sound also increases which translates to a decrease in the Mach number near the wall. It is clearly seen at Fig. 8.20 that the sonic line is shifted up as time increases. When computing the wall shear, it is seen that the increase in viscosity is of the same order as the decrease in the velocity gradient such that the wall shear remains virtually unchanged.

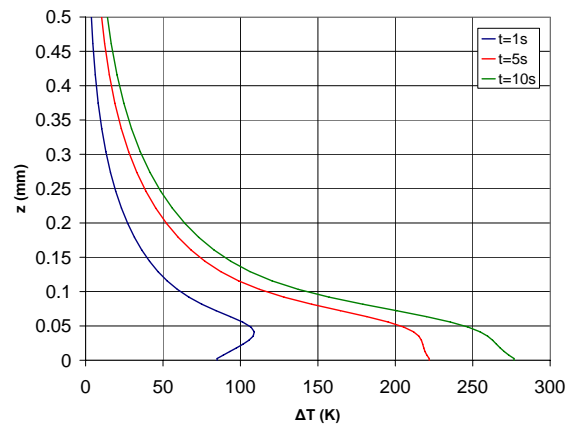
8.3. FLOW RESULTS



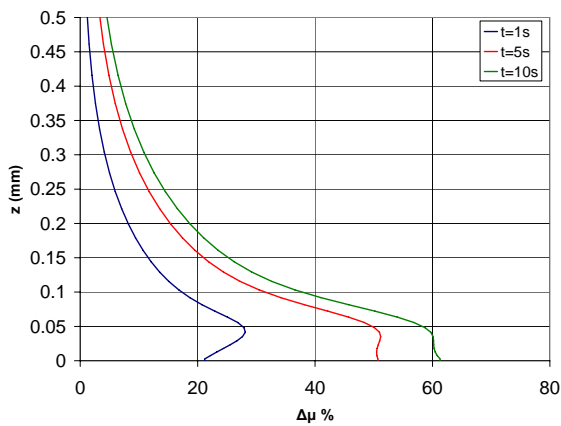
(a) Relative pressure difference 0.1 inch downstream



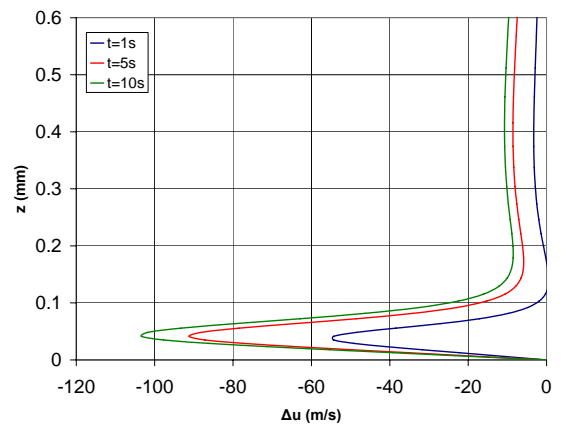
(b) Relative density difference 0.1 inch downstream



(d) Temperature difference 0.1 inch downstream



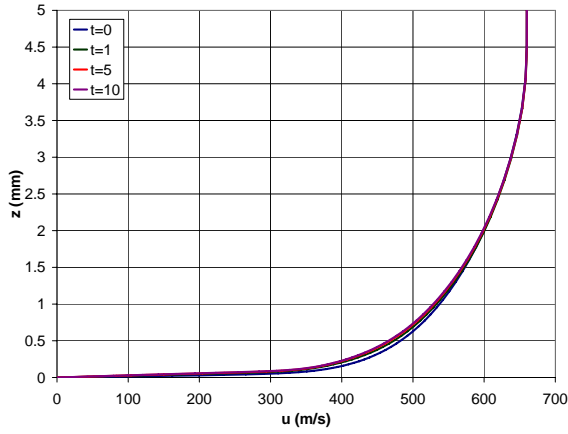
(c) Relative viscosity difference at center



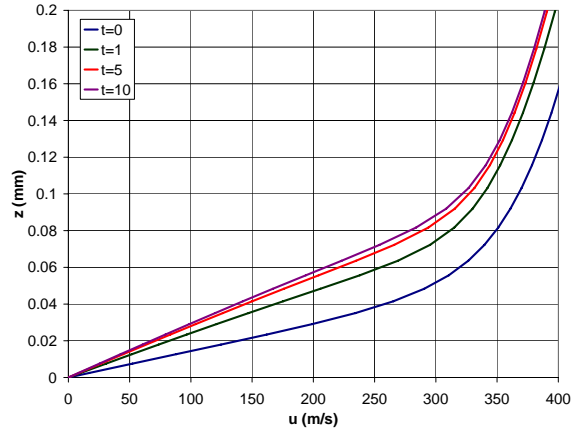
(e) Pressure difference 0.1 inch downstream

Figure 8.18: Effect of heating on flow variables for $P = 65W$ 0.1 inch downstream of target center

8.3. FLOW RESULTS

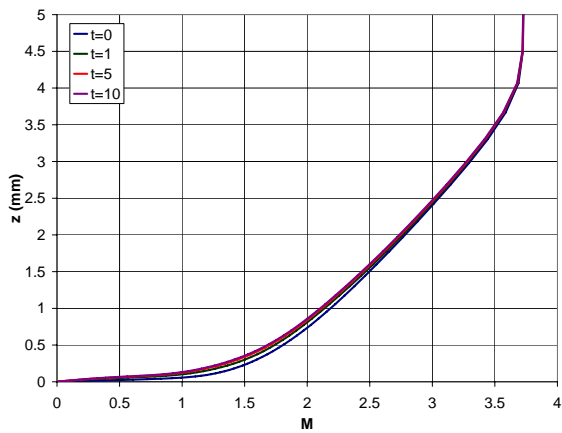


(a) Effect of heating on u-velocity profile at target center

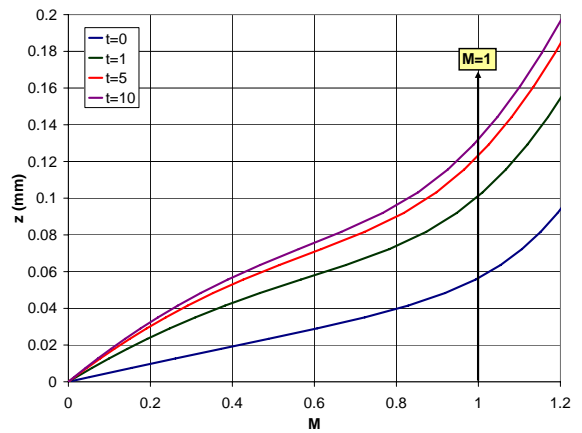


(b) Effect of heating on u-velocity profile close to wall

Figure 8.19: Effect of heating on the u-velocity profile. The velocity decreases close to the wall



(a) Effect of heating on Mach profile at target center



(b) Effect of heating on Mach profile close to wall

Figure 8.20: Effect of heating on the Mach profile. The increase in temperature increases the local speed of sound and local Mach number. The sonic line is shifted up

Chapter 9

Comparison of Computation and Experiment

A comparison of the computational and experimental results was made for the 65 Watt and 81 Watt cases. For each case, the surface temperature difference between the flow-off and flow-on case is presented for the surface and backside using contour plots at different values of time. The comparison is facilitated by plotting the numerical results on the upper half and the experimental results on the lower half. The temperature is plotted at different locations as a function of time. On the surface, numerical results are compared to the infrared measurement whereas on the backside, a comparison with thermocouple measurements is also presented when available. Temperature profiles on the symmetry plane are plotted for the surface and backside temperature.

9.1 65 Watt case

Comparison is made for the 65 Watt case. First, contour plots for the difference in the surface temperature between the flow-off and flow-on cases are presented.

9.1.1 Contour Plots of the Surface Temperature Difference

To help visualize the effect of the flow-on the target temperature, the temperature for the flow-on case is subtracted from the temperature for the flow-off case. Contours of temperature difference on the surface of the target are presented in Fig. 9.1. For that case, no data was taken with the lower temperature calibration range such that the temperature difference isn't computed away from the target center. With increasing time, as the target temperature increases, the area where the temperature difference can be computed increases.

This is clearly seen in Fig. 9.1. On the top surface, the cooling is underpredicted at the target center. The measured cooling strongly increases between $t = 3s$ and $t = 5s$ and then oscillates around 50 K for the remainder of the run whereas the computed cooling displays a more gradual increase and reaches 35 K after 10 seconds such that the difference between the computed and measured cooling decreases with time. This behavior is better seen in Fig. 9.3 a) where the time variation of the temperature at the center is plotted as a function of time.

Upstream, at $-4mm < r < -2mm$, the difference between the measured and computed cooling varies between 5K and 10K, the measured cooling being greater. Over that area, the measured temperature is almost uniform, whereas the computed temperature displays a more significant variation. Downstream, at $2mm > r > 4mm$ for $t < 7s$, the temperature difference in cooling is also close to 10K. The data do not seem as reliable for $t > 7s$ as the asymmetry between the upstream and downstream temperature disappears.

The temperature distribution on the backside is shown in Fig. 9.2. Good agreement is noticed for the temperature distribution at the center. Upstream, the measured temperature difference is lower than the computation whereas downstream, the agreement is better. The overall agreement on the backside is much better than on the top surface.

9.1.2 Time variation plot

The time variation of the temperature is better seen by looking at a fixed point in space over time. Moreover, on the backside, thermocouple measurements are also available such that the computation can be compared to two independent sources of measurements. Data is plotted at the center as well at distances equal to 0.1" and 0.2" upstream and downstream. Those position are chosen since they correspond to the location of the backside thermocouples. On the surface at 0.3", the temperature is not plotted, since this location falls right in between two calibrations for most of the run such that the bias error isn't cancelled when computing the temperature difference. This situation also arises at 0.1" and 0.2" for a time smaller than 4 to 5 seconds. The data was removed for that time range. Similarly, at the center, for $t < 2s$ the timing error is important and many different calibrations are used over a small period of time such that the data displayed an erratic behavior.

The surface temperature difference is plotted as a function of time in Fig. 9.3. At the center, a sharp increase in the measured temperature is seen between 3 and 5 seconds. Between 5 and 7 seconds the measured temperature difference rate is similar to the computed rate. At 0.2" upstream and downstream, a similar behavior is seen as the measured temperature difference is approximately 10K greater than the computed one. However, this discrepancy arises for a shorter value of time for which the calibrations are mismatched so that it impossible to see how this increase in brought about. For $t > 5s$ the rate of increase in the measured and computed temperature difference are very similar. As seen on the contour plots, much better agreement is seen at 0.1" inch from the center as both the slope and temperature

9.1. 65 WATT CASE

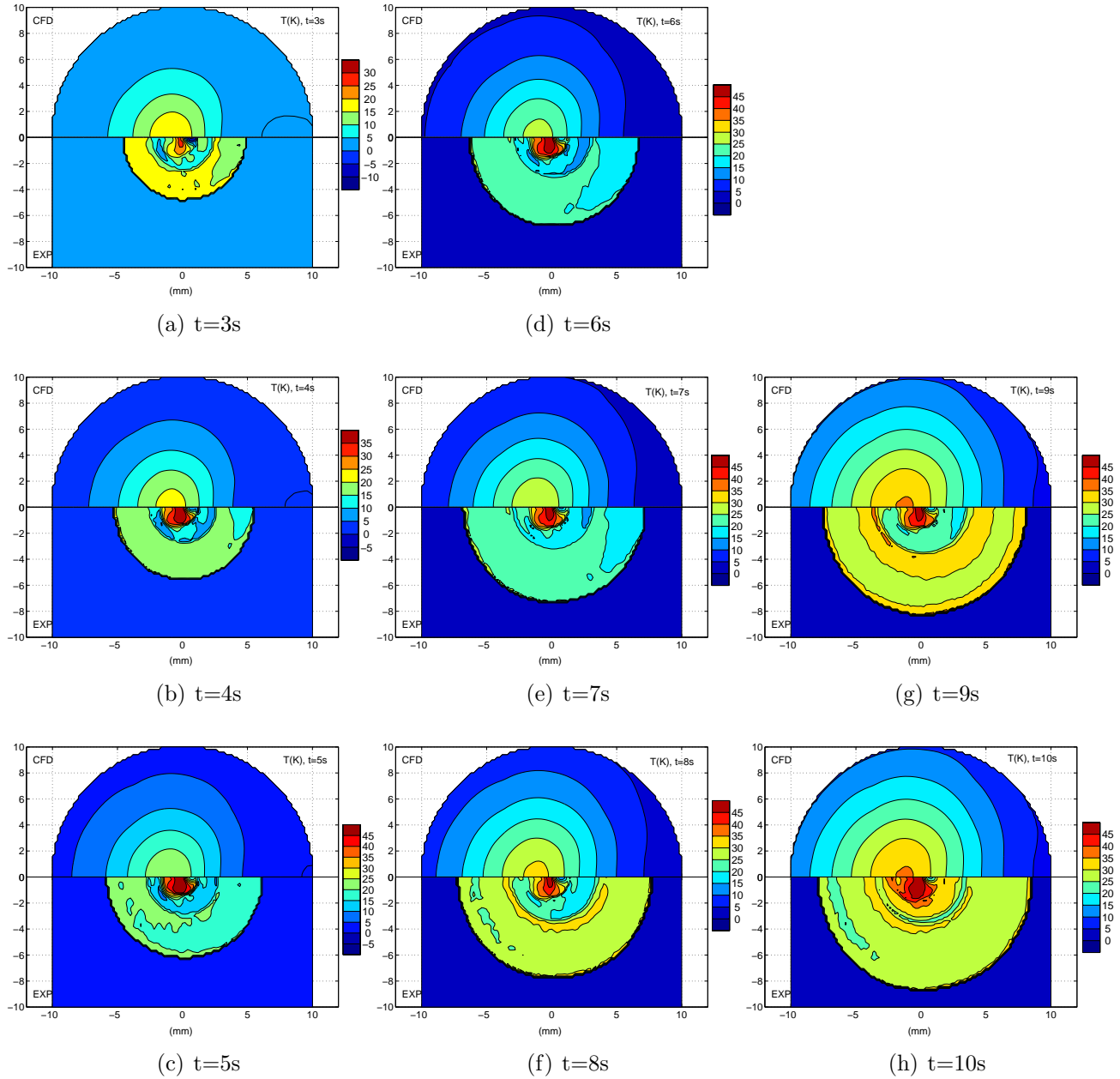


Figure 9.1: Comparison of surface temperature difference between CFD and experiment for $P=65$ W. Computation on top and experiment on bottom (Note: the experimental temperature difference is set to zero for temperatures below 333 K)

9.1. 65 WATT CASE

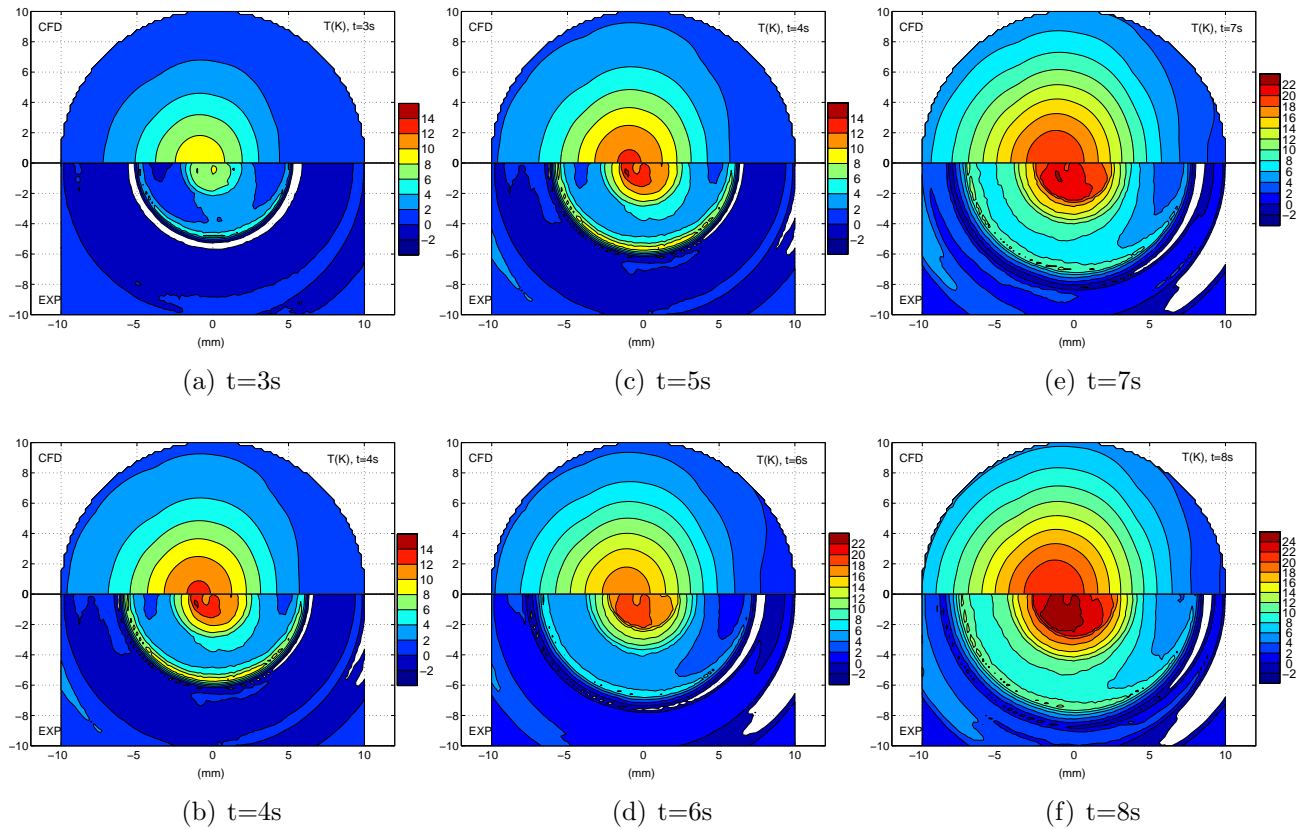


Figure 9.2: Comparison of backside temperature difference between CFD and experiment for $P=65$ W. Computation on top and experiment on bottom

difference agree well. Fig. 9.5 presents the comparison on the backside. Overall very good agreement is seen between the computation and both the thermocouple and infrared camera measurements.

9.1.3 Streamwise Temperature Profiles

A comparison in the temperature profiles was made by taking a slice at center of the target parallel with the flow direction. A comparison between the measurement and the computed surface temperature at different time values for the flow-off condition is depicted in Fig. 9.6. Plots displaying the uncertainty bars are shown in Figs. E.1 to E.6 of Appendix E for the surface and backside temperature.

Good agreement is found between the computation and the measurements. The largest discrepancy is observed for $t = 0.5$ and is probably due to the modeling of ramp in the laser power output. Fig. 9.8 displays a comparison for the flow-on case. At $t = 0.5s$, the strong asymmetry in the measured temperature profile isn't seen in the computed temperature. At $t = 4s$ and $t = 10s$, a slight asymmetry is seen close to the center as the downstream temperature is slightly higher. At these two time values, the surface temperature is overpredicted.

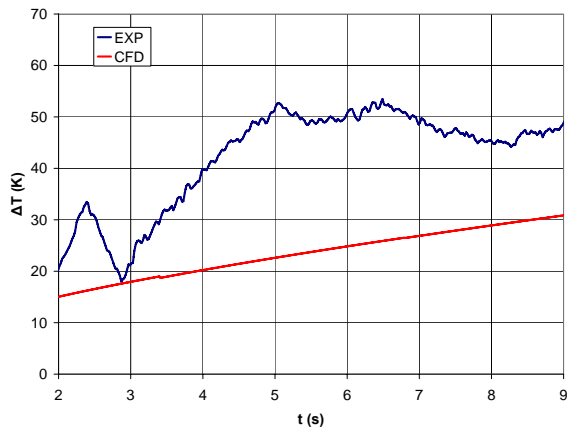
Fig. 9.8 presents the backside temperature for the flow-off case. For the backside, the greatest disagreement is seen for small values of time where the measured temperature is greater than the one computed. Again, this disagreement is most likely due to a timing error as well as the startup of the laser. The fact that the target is located inside a cavity as seen in Fig. 9.10 could increase the emissivity of the surface and explain the underprediction of the temperature. Reflection which is most likely coming from the lens of the camera is also seen in Fig. 9.10 on the top and bottom of the image. The reflection shouldn't affect the measurements as reflectivity of the optics is taken into account in the calibration.

At $t = 4s$ and $t = 8s$, agreement is very good. A notch in the temperature profile is seen close to $T = 325K$ where the images taken with NUC0 overlap the images with NUC2. The temperature close to the notch is too low for NUC2 such that the calibration error is greatly increased.

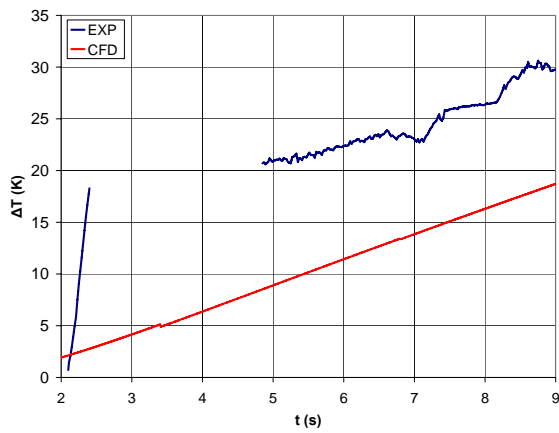
The flow-on case is depicted in Fig. 9.9. Again, agreement is good for larger values of time. At $t = 2s$, the computed temperature is again higher than the measurement. Contrarily to the flow-off case, good agreement is seen at $t = 0.5s$. However, this measurement is close to the junction between NUC2 and NUC0 and therefore not as reliable.

The temperature difference profiles are shown in Fig. 9.11 and 9.12 where the uncertainty bars are shown. On the top surface, agreement is acceptable away from the center. On the backside good agreement is found.

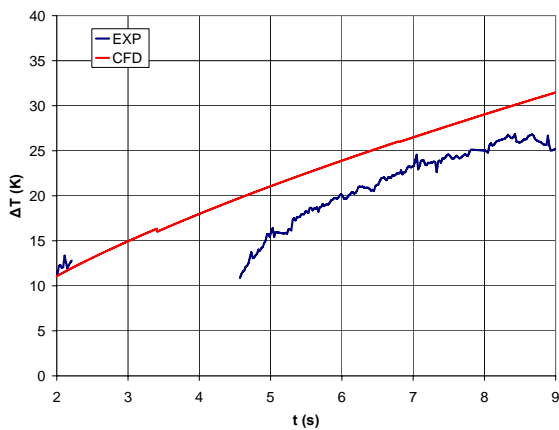
9.1. 65 WATT CASE



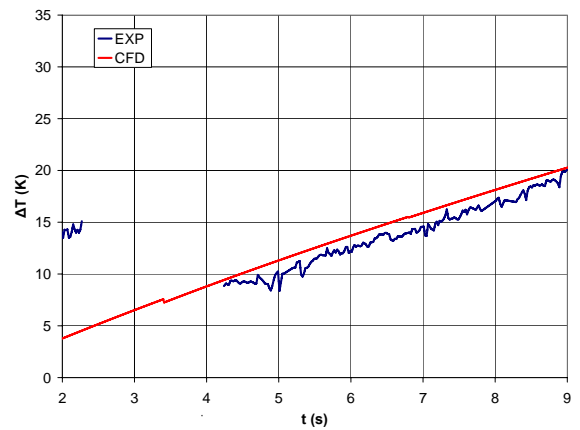
(a) Surface temperature difference at center ($x=0$ inch)



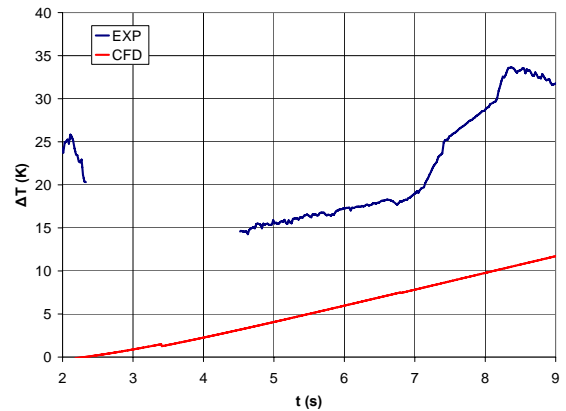
(b) Surface temperature difference at $x=-0.2$ inch



(c) Surface temperature difference at $x=-0.1$ inch



(d) Surface temperature at $x=0.1$ inch



(e) Surface temperature difference at $x=0.2$ inch

Figure 9.3: Comparison between infrared measurement and computed surface temperature difference as a function of time for $P=65$ W.

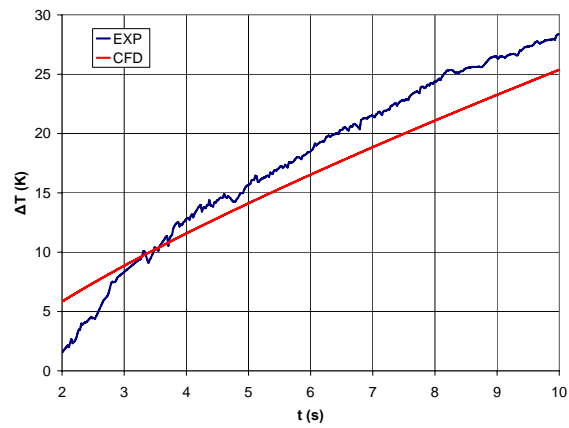
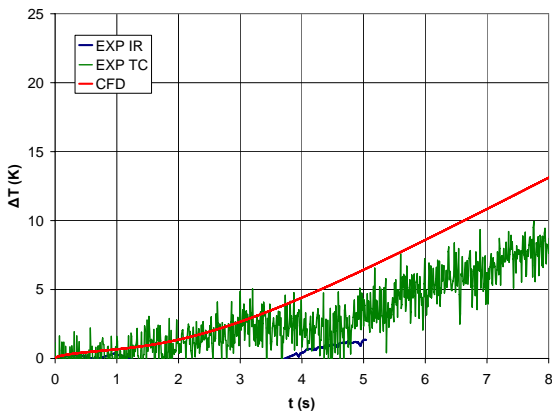
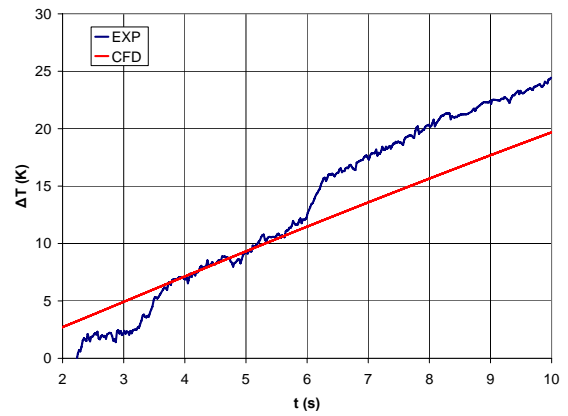


Figure 9.4: Comparison between thermocouples measurement and computed backside temperature difference as a function of time for $P=65$ W at the center

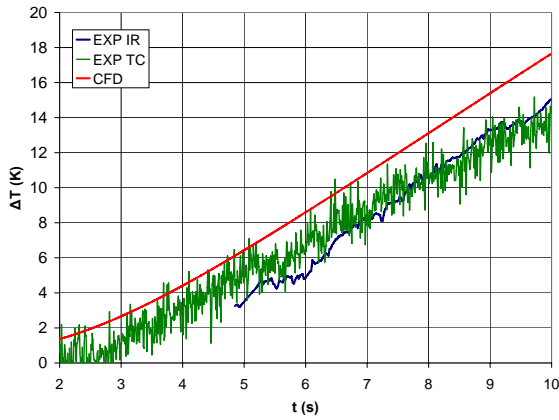
9.1. 65 WATT CASE



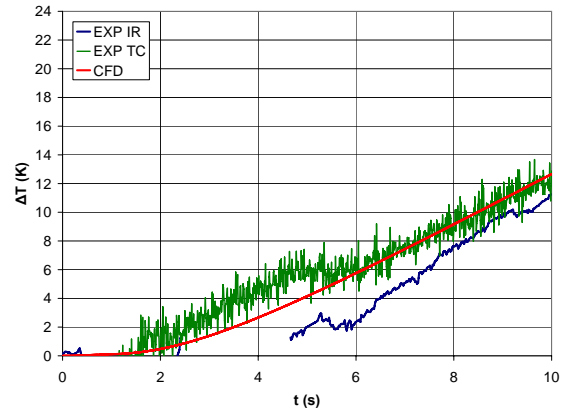
(a) Backside temperature difference at $x = -0.3$ inch



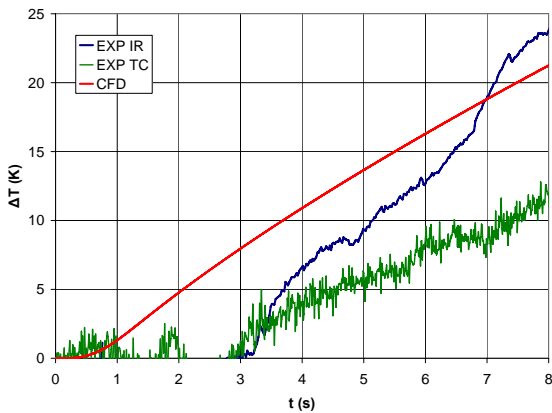
(d) Backside temperature at $x = 0.1$ inch



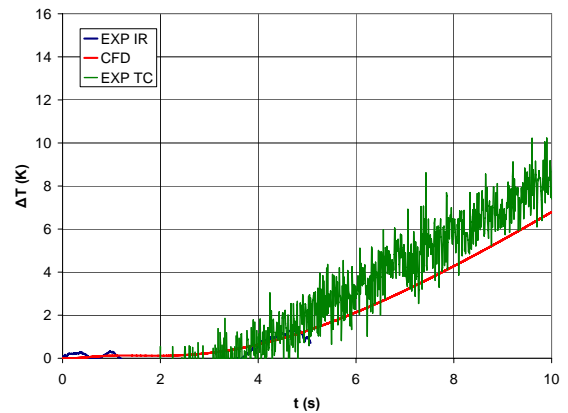
(b) Surface temperature difference at $x = -0.2$ inch



(e) Backside temperature difference at $x = 0.2$ inch



(c) Surface temperature difference at $x = -0.1$ inch



(f) Backside temperature difference at $x = 0.3$ inch

Figure 9.5: Comparison between infrared and thermocouples measurement and computed backside temperature difference as a function of time for $P = 65$ W

9.1. 65 WATT CASE

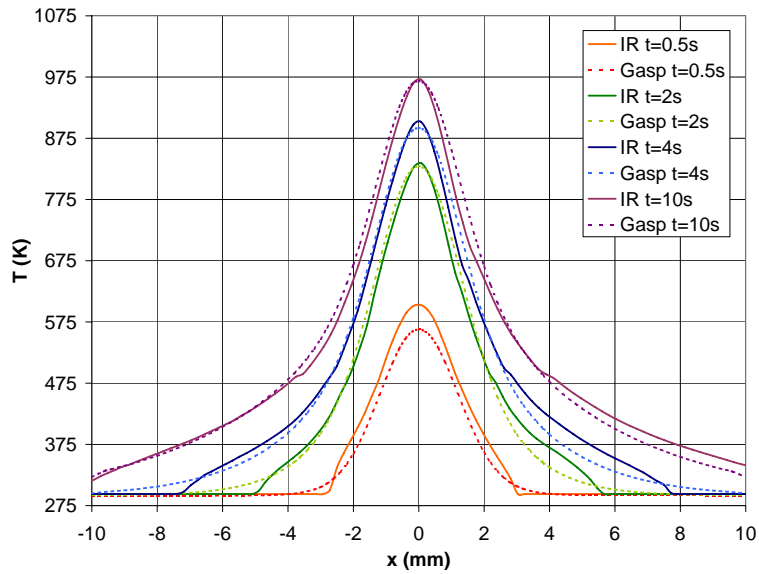


Figure 9.6: Comparison between infrared measurement and computed surface temperature as a function of time for flow-off condition and $P=65$ W

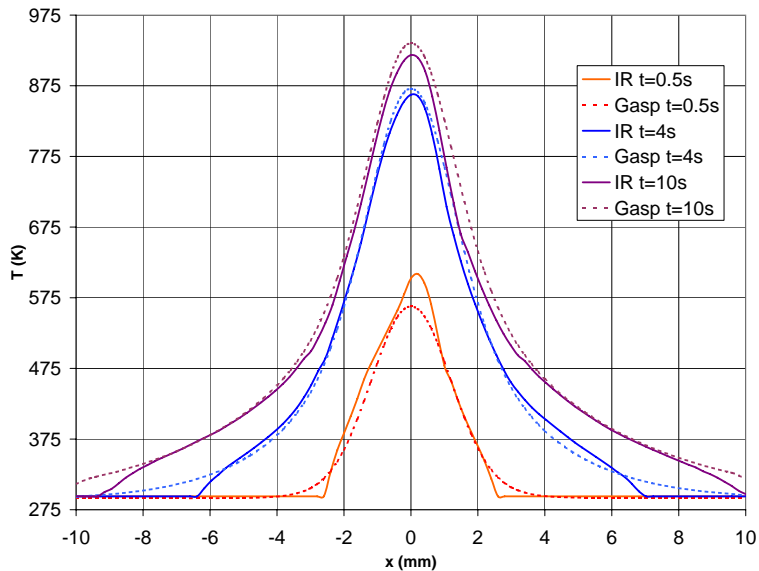


Figure 9.7: Comparison between infrared measurement and computed surface temperature as a function of time for flow-on condition and $P=65$ W

9.1. 65 WATT CASE

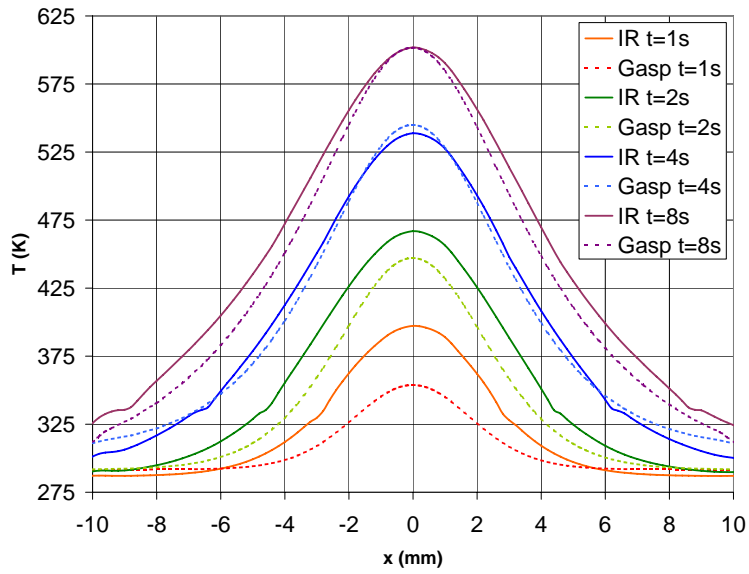


Figure 9.8: Comparison between infrared measurement and computed backside temperature as a function of time for flow-off condition and $P=65$ W

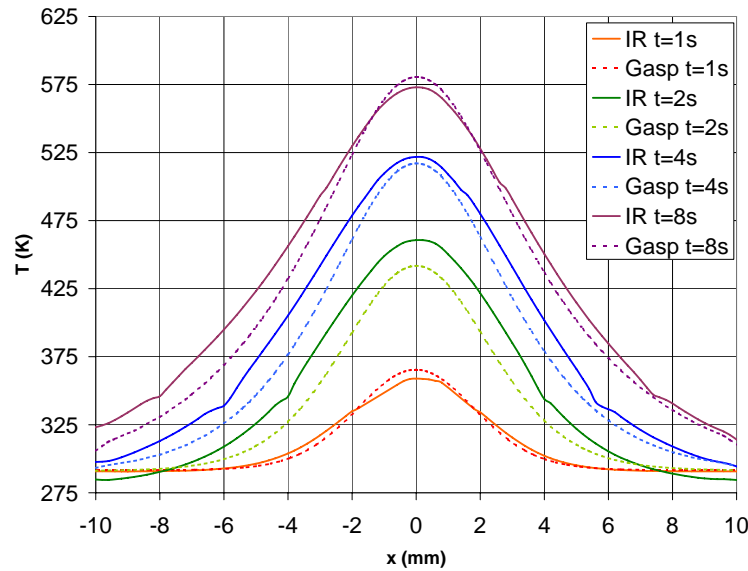


Figure 9.9: Comparison between infrared measurement and computed backside temperature as a function of time for flow-on condition and $P=65$ W

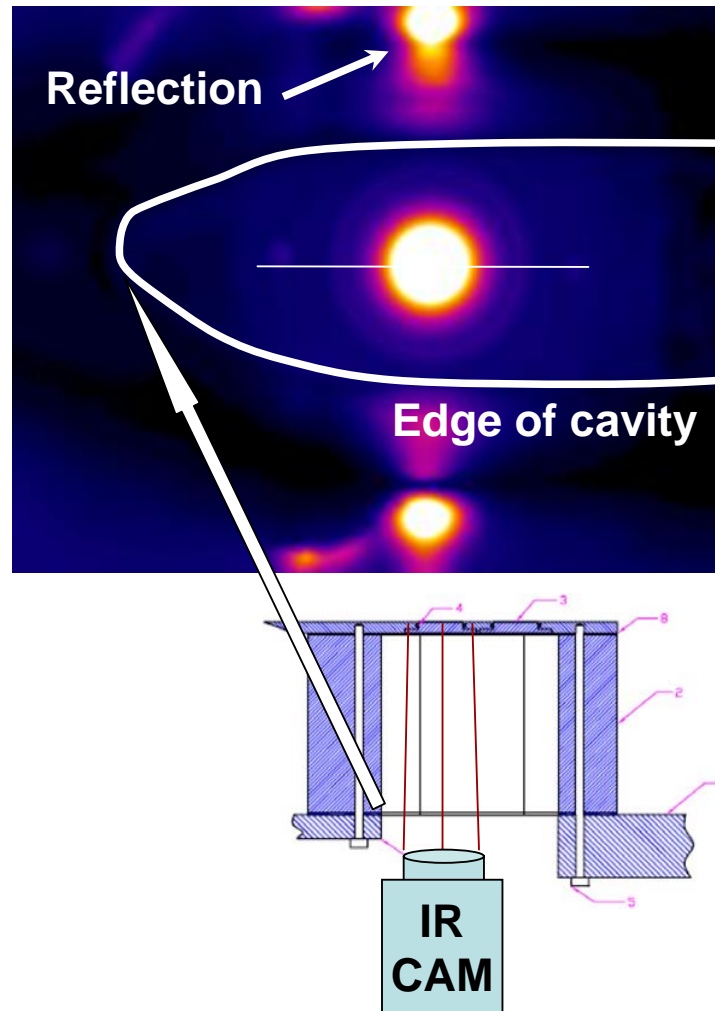
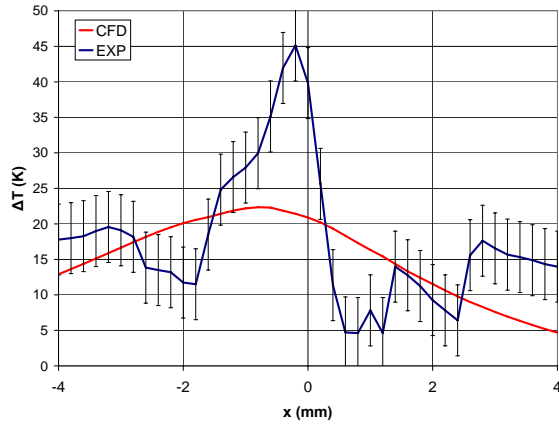
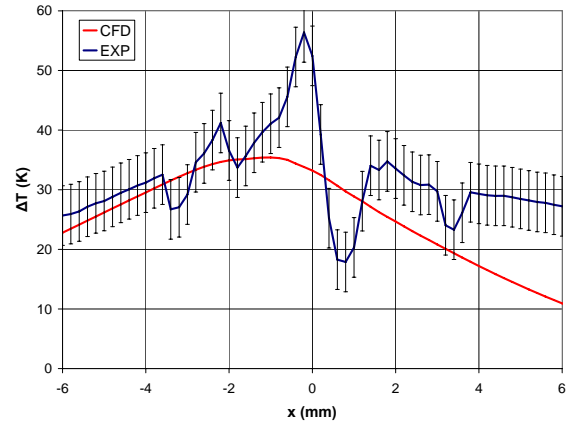


Figure 9.10: Infrared image on the backside: The target is located in a cavity and reflection is seen on the upper and lower part of the image

9.1. 65 WATT CASE



(a) Temperature difference at the surface for $t = 4s$



(b) Temperature difference at the surface for $t = 10s$

Figure 9.11: Comparison of the surface temperature difference between CFD and experiment for $P=65$ W

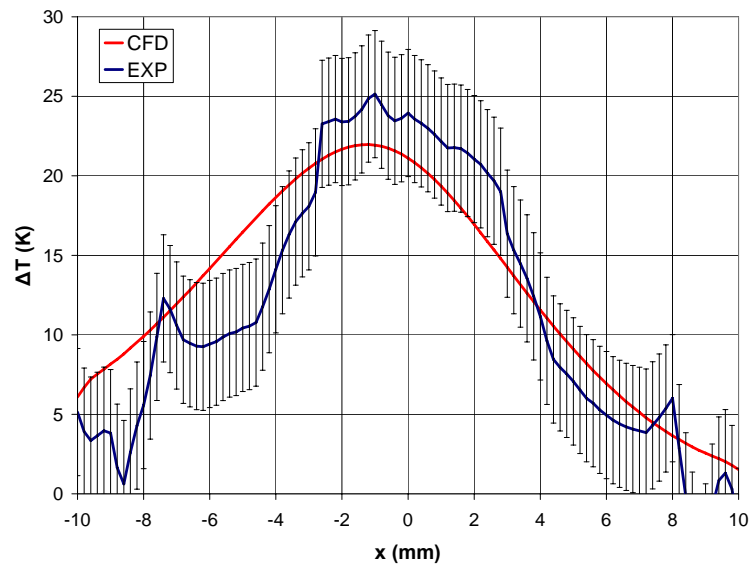


Figure 9.12: Comparison of the backside temperature difference between CFD and experiment for $P=65$ W for $t = 8s$

9.2 81 Watt case

The same comparison process is performed for a power of 81 Watts.

9.2.1 Surface Temperature Contour Plots

Contours of temperature difference on the surface of the target are presented in Fig. 9.13 for a time varying between 3 and 10 seconds. Again, as for the 65 Watt case, the temperature is underpredicted at the center. At $t = 10s$ the measured temperature difference reaches $60K$ compared to $30K$ for the experiment. However, contrary to the 65 Watt case, the experiment reveals a region of strong cooling upstream further away from the center. Upstream of this intense cooling region, good agreement is found between the computation and the experiment. This means that the level of cooling before the perturbation introduced by the strong heating seems to be well modelled. For the 65 Watt case, this couldn't be assessed since no data was available at that location. Downstream, away from the center, good agreement is also seen which leads one to think that the boundary layer relaxes quickly from its heat induced perturbation.

Results on the backside for a time varying between 3 and 8 seconds are shown in Fig. 9.14. As for the 65 Watt case, much better agreement is seen on the backside. For $t = 3$, the lower cooling seen in the experimental results is probably due to the timing error. Overall, good agreement is seen near the center and downstream. Upstream, more cooling is seen in the experimental results which is consistent with the surface temperature data.

9.2.2 Time variation plot

Comparison between infrared and thermocouple measurements and the computed surface temperature as a function of time for the flow-off condition is shown in Fig. 9.15. Measurements corresponding to a distance of 0.1, 0.2 and 0.3 inch from the center are shown. At all the position, the infrared measurements (in red) agree relatively well with the numerical results (in blue). The same thing can't be said about the thermocouple measurements as the agreement gets worse over time. We believe that this phenomenon is due to conduction losses through the thin thermocouple wires and the cement used to fix the wires. Close to the center, a greater temperature gradient exist which should translate into greater conduction losses. As expected, the greatest discrepancy is observed close to the center. The temperature is plotted as a function of time at the center and at distances equal to 0.1, 0.2 and 0.3 inch upstream and downstream. Those positions are chosen since they correspond to the location of the backside thermocouples. Data corresponding to mismatching NUC is removed to make the plots cleaner. Similarly, at the center, for $t < 2s$ the timing is error is important and many different calibrations are used over a small period of time such that the data displays an erratic behavior.

9.2. 81 WATT CASE

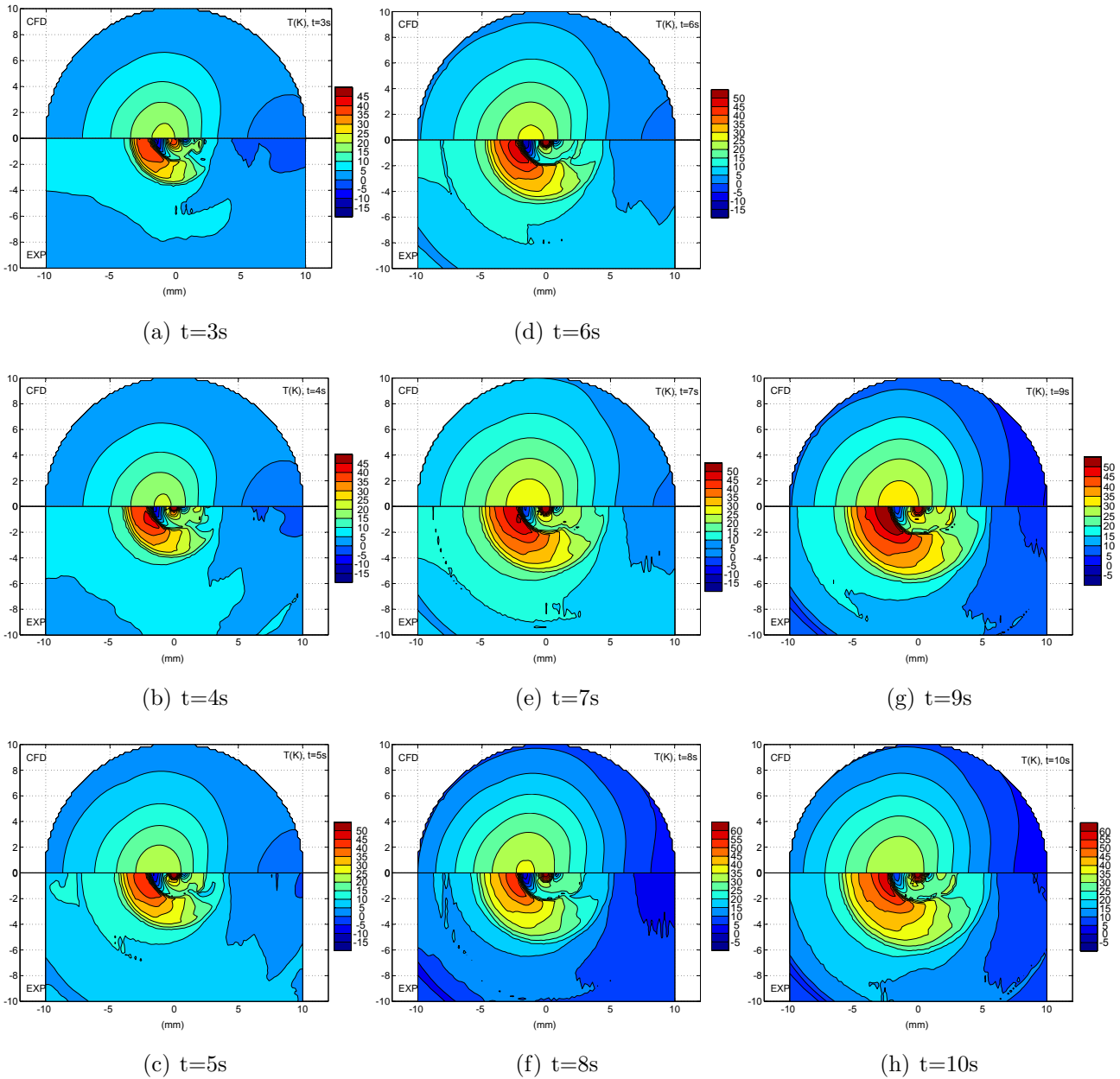


Figure 9.13: Comparison of surface temperature between CFD and experiment for $P=81$ W. Computation on top and experiment on bottom

9.2. 81 WATT CASE

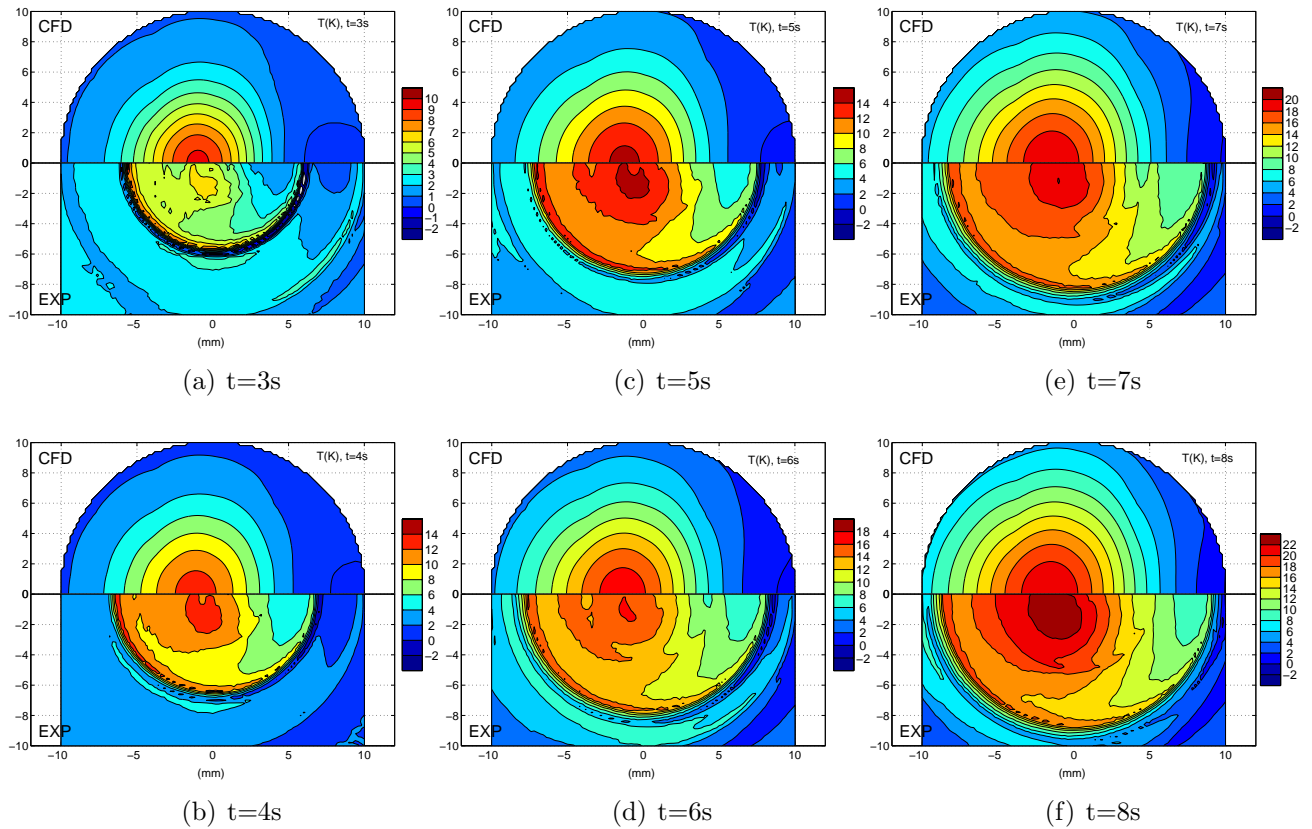


Figure 9.14: Comparison of backside temperature between CFD and experiment for $P=81$ W. Computation on top and experiment on bottom

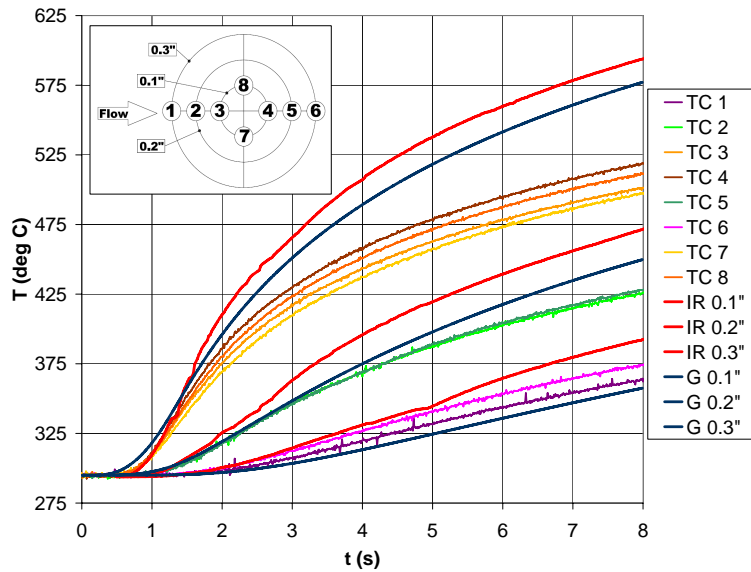


Figure 9.15: Comparison between infrared and thermocouple measurements and computed surface temperature as a function of time for the flow-off condition at $P=81$ W.

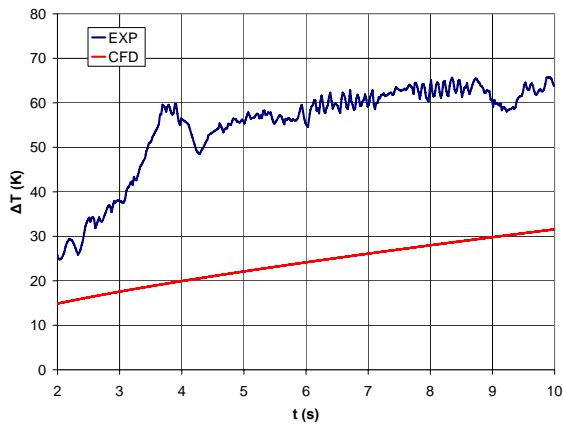
The surface temperature difference is plotted as a function of time in Fig. 9.16. At the center, a sharp increase in the measured temperature is seen between 2 and 3 seconds. This behavior was also noticed for the 65 Watt case. Between 4.5 and 10 seconds, the measured temperature difference rate is similar to the computed rate. At 0.1 inch downstream, reasonable agreement is seen. At 0.1 inch upstream, the temperature difference is underpredicted by $20K$. However, this temperature difference is generated between 0 and 2 seconds such that the rate of change the measured and computed cooling rates are similar. At 0.2 inch upstream and downstream, good agreement is seen for $t < 5s$. For greater values of time, the measured cooling increases.

Fig. 9.5 presents the comparison on the backside. Infrared measurements are smoother on the back compared to the surface. As for the 65 Watt case, very good agreement is seen between the computation in both the thermocouple and infrared camera measurements.

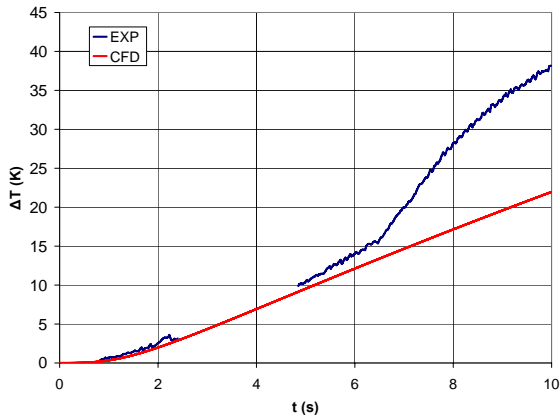
9.2.3 Streamwise Temperature Profiles

The temperature is plotted as a function of the distance from the center on the symmetry plane for different values of time. Figs. 9.18 and 9.19 show the temperature profiles for the flow-off and flow-on conditions on the target surface. Plots displaying the uncertainty bars are shown shown in Figs. F.1 to F.6 of Appendix F for the surface and backside temperature. For both the backside and surface, the temperature is underpredicted by the computation with the exception of $t = 0.5s$ for the flow-off case. However, this difference is

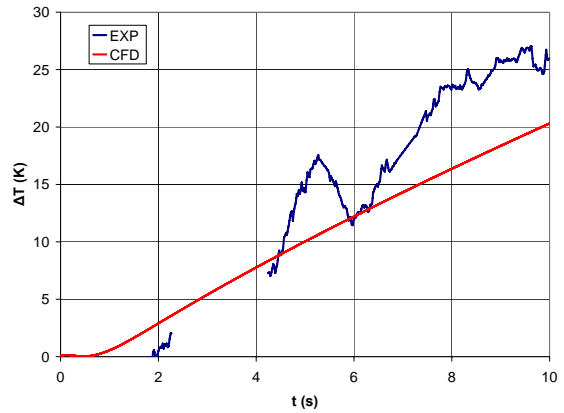
9.2. 81 WATT CASE



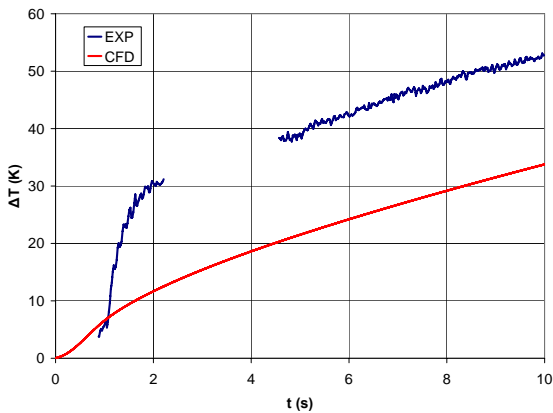
(a) Surface temperature difference at center ($x=0$)



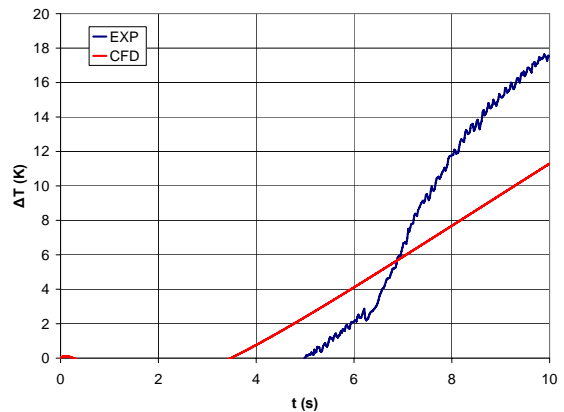
(b) Surface temperature difference at $x=-0.2$ inch



(d) Surface temperature at $x=0.1$ inch



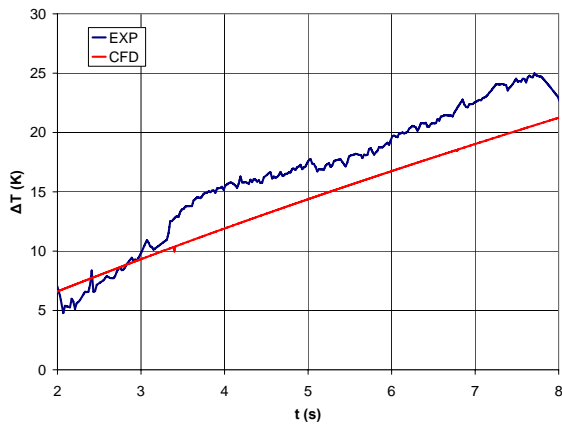
(c) Surface temperature difference at $x=-0.1$ inch



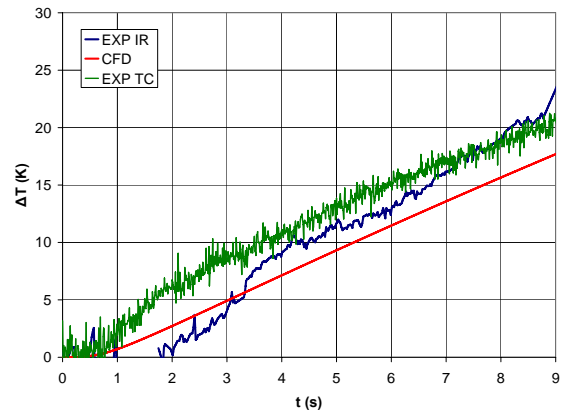
(e) Surface temperature difference at $x=0.2$ inch

Figure 9.16: Comparison between infrared measurement and computed surface temperature difference as a function of time for $P=81$ W

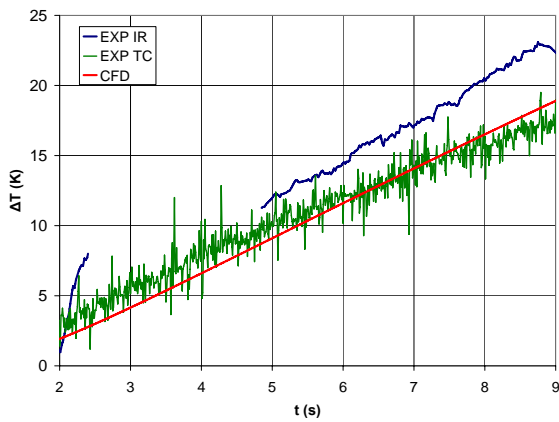
9.2. 81 WATT CASE



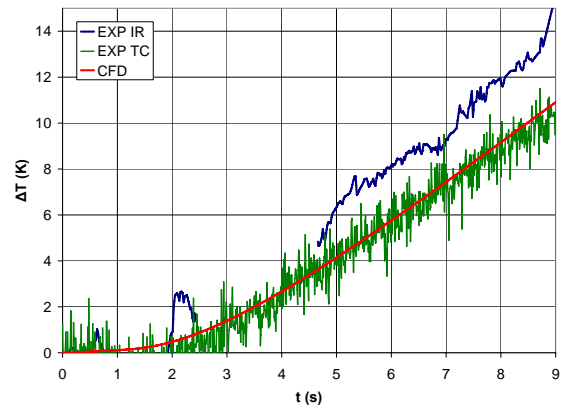
(a) Backside temperature difference at center ($x=0$)



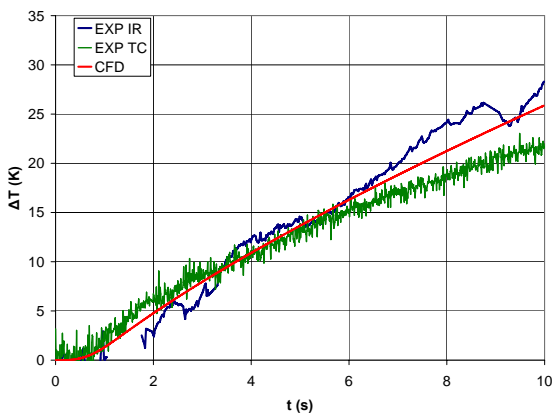
(d) Backside temperature at $x=0.1$ inch



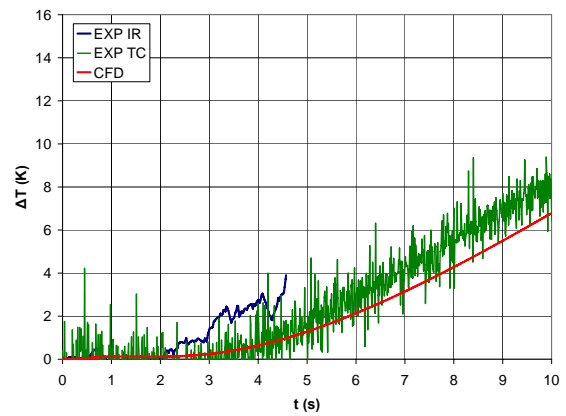
(b) Backside temperature difference at $x=-0.2$ inch



(e) Backside temperature difference at $x=0.2$ inch



(c) Backside temperature difference at $x=-0.1$ inch



(f) Backside temperature difference at $x=0.3$ inch

Figure 9.17: Comparison between infrared and thermocouples measurement and computed backside temperature difference as a function of time for $P=81$ W

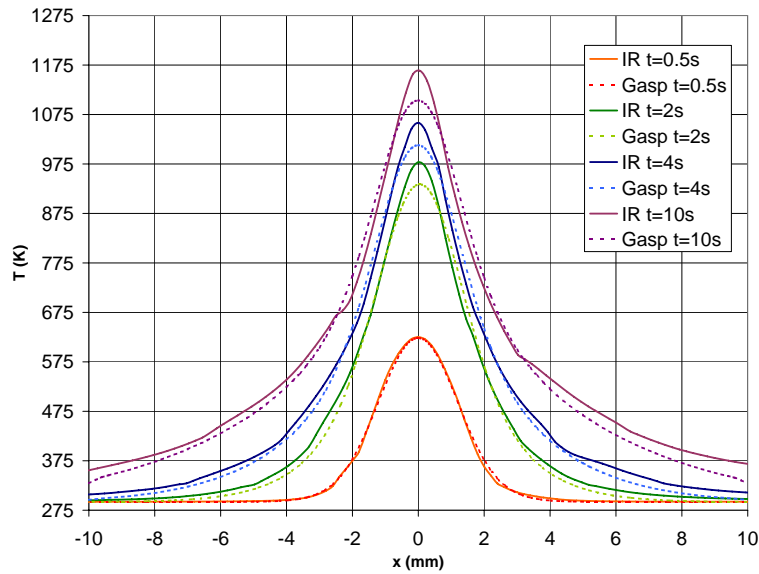


Figure 9.18: Comparison between infrared measurement and computed surface temperature as a function of time for the flow-off condition at $P=81\text{ W}$

contained in the uncertainty margin taking into account the bias error. Here, the laser power is probably greater than what is reported by the manufacturer. The temperature difference of 60 K observed between the computation and the experiment at $t = 10\text{ s}$ corresponds to a difference of 7% in the power level. The dependence of the emissivity on the temperature could also explain the discrepancy between the measurement and experiment. However, since the value of emissivity as a function of temperature for the paint is not known, this remains pure speculation. A raise in emissivity of 10% would lead to an increase in temperature of 30. The difference between the experiment and the computation is less for the flow-on case since the measured temperature decrease due to the flow is greater than the one computed. At $t = 0.5$, significant asymmetry is found in the measured temperature for the flow-on condition contrary to the computation which appears almost perfectly symmetric. With an increase in time, this asymmetry is convected further downstream between $x = 4\text{ mm}$ and $x = 6\text{ mm}$.

The backside temperature is shown in Figs. 9.20 and 9.21 for the flow-off and flow-on conditions. Overall, good agreement is seen for both the flow-on and flow-off conditions. Except for the lower value of time, the measured temperature is greater than the measured one. This situation is consistent with the one observed on the top surface where the measured temperature is also greater. On the backside, the temperature is measured in a cavity which can contribute to increase the emissivity of the surface. (see Fig. 9.10)

The temperature difference profiles are shown in Fig. 9.22 and 9.23, where the uncertainty bars are shown. On the top surface, agreement is acceptable away from the center. On the

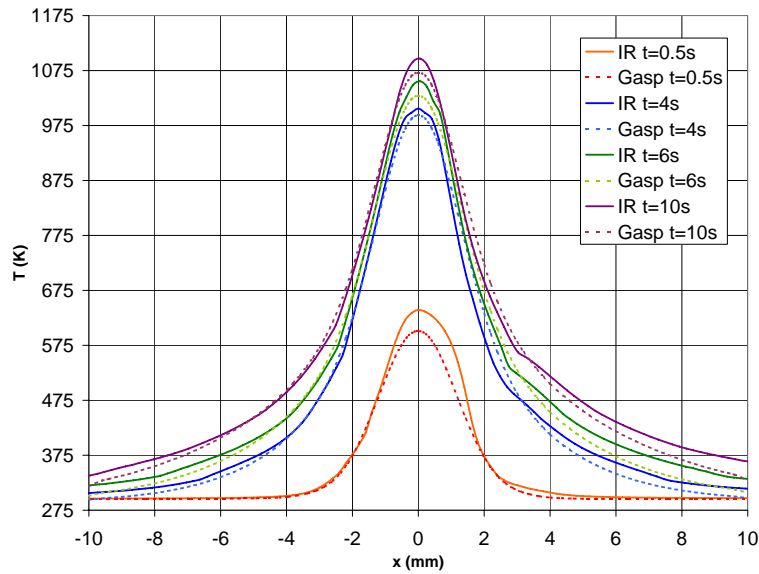


Figure 9.19: Comparison between infrared measurement and computed surface temperature as a function of time for the flow-on condition at $P=81$ W

backside, good agreement is generally found but more cooling is measured upstream

9.3 Discussion

In interpreting the temperature difference results, it is useful to think about the superposition principle for a linear partial differential equation. Hence, we can think of the heat flux as being the superposition of a positive heat flux due to the laser and a mostly negative heat flux due to the flow. When subtracting the flow-on condition from the flow-off condition, the laser heat flux cancels out (for a perfectly repeatable laser) such that one is only left with the heat flux due to the fluid. Strictly speaking, this superposition can't be used to perform a computation since the heat flux of the fluid is actually a function of the wall temperature.

Looking at Fig. 9.22, we notice good agreement away from the center. Close to the center, the measured temperature displays an oscillatory behavior. The interface between the region of cooling and heating isn't probably as sharp as the measurements indicate since heat diffusion should smooth the gradient out unless a strong flow feature such as a vortex is able to maintain it. For instance, one can imagine strong heat extraction dragging the heat aft such that the downstream wall temperature is increased. The oscillation in the temperature distribution at the center should damp out with diffusion inside the solid. This can explain to some extent that a different surface temperature distribution can lead to a similar temperature distribution on the back. Also, we have noticed that for both the 65

9.3. DISCUSSION

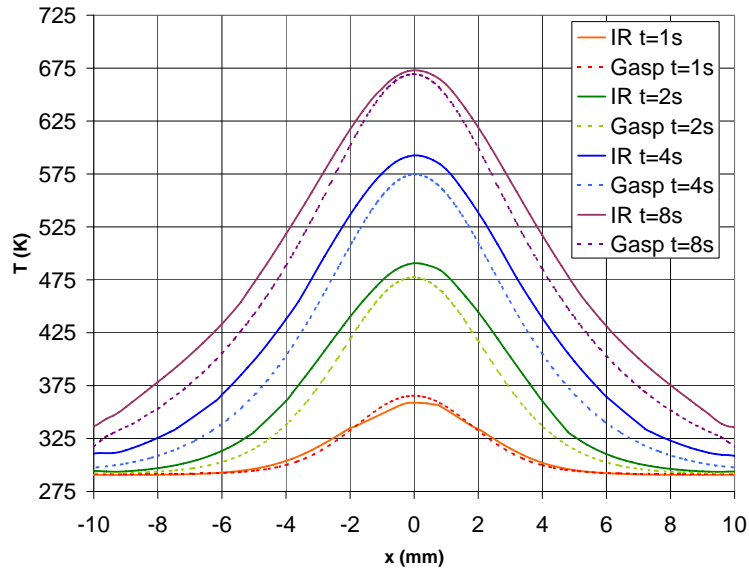


Figure 9.20: Comparison between infrared measurement and computed backside temperature as a function of time for flow-off condition and $P=81$ W

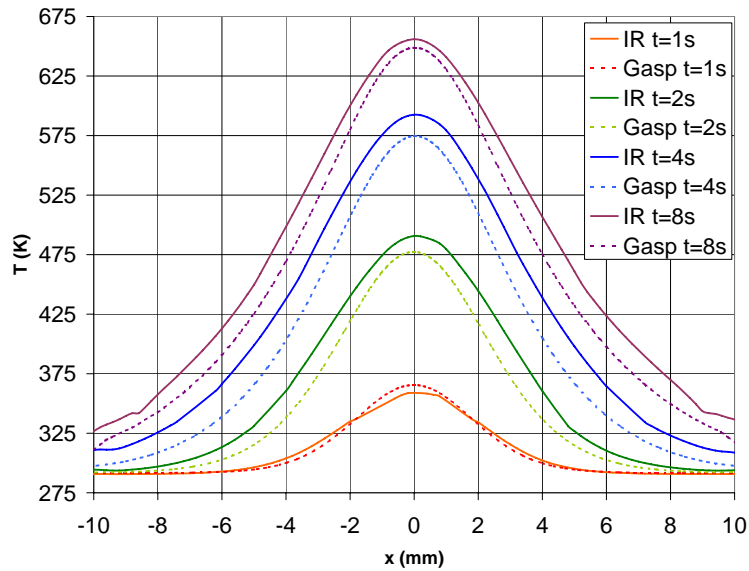
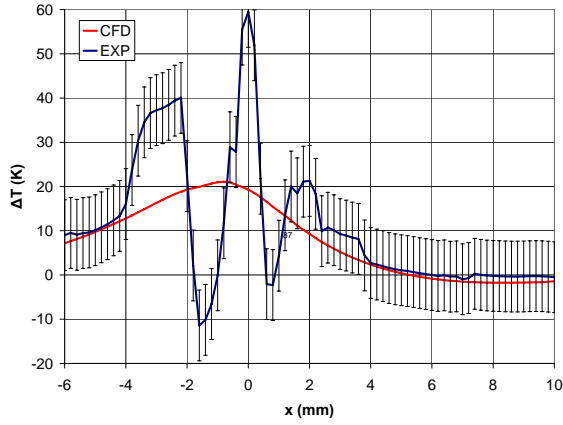
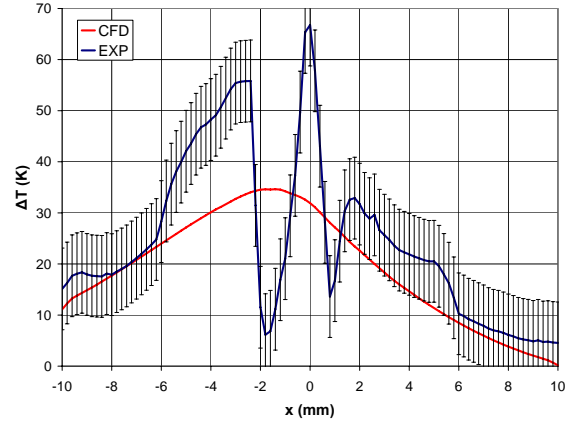


Figure 9.21: Comparison between infrared measurement and computed backside temperature as a function of time for flow-on condition and $P=81$ W

9.3. DISCUSSION



(a) Temperature difference at the surface for $t = 4s$



(b) Temperature difference at the surface for $t = 10s$

Figure 9.22: Comparison of the surface temperature between CFD and experiment for $P=81$ W

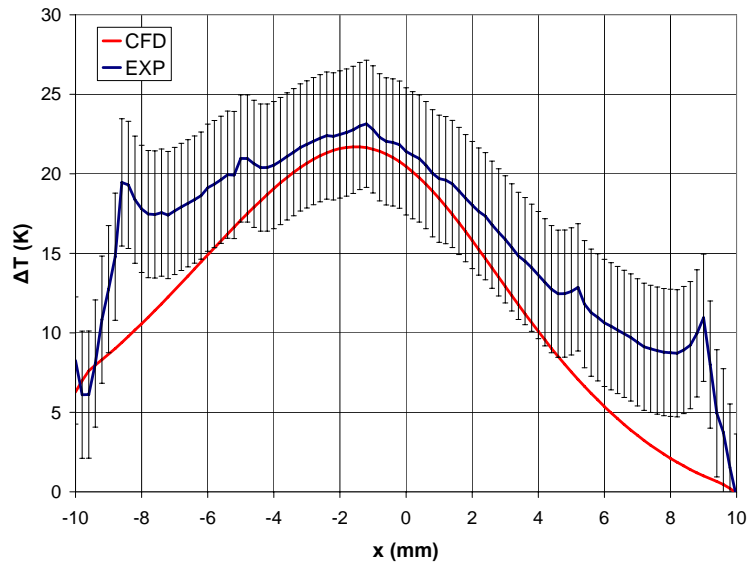


Figure 9.23: Comparison of the backside temperature between CFD and experiment for $P=81$ W $t = 8s$

Watt and the 81 Watt cases the greatest temperature difference arises near the center over a very small area. Moreover, the area of intense cooling is surrounded by an area of heating such that the difference in cooling near the center is not as large as it appears.

Issues with the laser repeatability could explain why the poorer agreement on the surface doesn't translate into a poor agreement on the backside. We have previously shown the good repeatability of the experiment by looking at the backside temperature. One could imagine that a significant temperature difference between two runs could be due to a local fluctuation in the laser power which might not lead to a large temperature difference on the backside as heat diffuses inside the solid. Here, we basically use the same argument as before, but to justify an opposing assertion. For both cases, the same situation is observed, i.e. a good agreement on the backside and a not-so-good agreement on the surface. However, in the first case, this fact is explained by a lack of the numerical model, whereas in the second case it is explained by a lack in the experimental setup and design. This issues might have been clarified by having taken more data on the target surface. However, the excellent repeatability observed on the backside made us confident that the laser repeatability was not an issue.

From the experimental results, a more symmetric temperature distribution was found for the 65 Watt case compared to the 81 Watt case. This was found by looking at both the thermocouple and infrared thermography data which adds to the credibility of the observation. For the 81 Watt case, a region of strong cooling was found upstream of the center, this region was also observed on the backside when looking at both the infrared thermography and the thermocouple results.

The disagreement at the center could be due to the incapacity of the turbulence model to respond to the strong distortion of the boundary layer. As was discussed in Section 3.2.5 the analytical method proposed by Reynolds et. al. to compute the heat transfer coefficient for an arbitrary temperature distribution underpredicts the film coefficient by more than 30% close to a temperature step. Here, a very large step is introduced such that it is possible that the turbulence model can't give a good prediction close to the center. Returning to Section 4.1.1 we have seen that in the turbulence model only the solenoidal part of the dissipation rate is modelled, and the terms due to the fluctuation in viscosity are neglected as well as the compressible term. Since there is a large temperature gradient inside the boundary layer, we can expect large viscosity fluctuation such that the viscosity fluctuation terms in the dissipation rate equation may become important. The same can be said about the density, as a large density gradient exist in the boundary layer. Therefore, the validity of Morkovin's hypothesis which assumes small density fluctuation is questionable for a flow over a laser-heated wall. The assumption of a constant turbulent Prandtl number is also questionable as it implies a similarity between the velocity and thermal fields. For the considered flow, the thermal boundary layer is greatly modified by the heat source such that the use of this similarity is questionable. One can compute a variable turbulent Prandtl number by solving two extra transport equations [64, 6] namely one for the variance of the temperature fluctuation and the other for its dissipation rate. Such a model was

9.3. DISCUSSION

partly implemented in GASP, but was not completed due to time constraints. Future work regarding such a model should be pursued in trying to improve the prediction for laser heated flows. However, this might not provide an effective solution since to our knowledge, all of the two-equation turbulence models available for the computation of the turbulent Prandlt number in a compressible flow are extensions of their incompressible counterparts made possible through Morkovin's hypothesis.

Chapter 10

Conclusions

The contributions made in this research are outlined and recommendations as well as possible research extensions are proposed.

10.1 Contributions

An analytical solution for the heat distribution onto a laser heated target was presented. The solution was extended to allow the modelling a beam moving with an arbitrary trajectory. This solution can be used to analyze the temperature distribution when the beam is oscillating on the target. This situation is found in directed-energy weapons when the laser can't perfectly stay still on the target. Typically, this effect is taken into account by increasing the diameter of the beam in the analysis [32].

Numerical simulations were performed for low-speed flow with a complex wall temperature variation. We have shown that good agreement in the heat transfer coefficient can be found through a RANS simulation. Here, we believe that a RANS analysis is preferable to a traditional boundary layer solution, since the boundary layer equation is parabolic meaning that no upstream influence is allowed. This approximation is not valid near a temperature step, as the step introduces a disturbance similar to the one occurring at the leading edge of a plate where it is well known that the boundary layer approximation doesn't apply. Good agreement with the experiment from Debieve et al. [20] was also found for supersonic boundary layers with a step in wall temperature. We have shown that it is important to accurately reproduce the boundary layer profile at the boundary layer inlet. A methodology to generate the missing turbulence information was developed in Appendix A. Simulations of the flow inside the Virginia Tech supersonic wind tunnel have been performed and are reported in Appendix B. We have shown that a flat plate analysis doesn't lead to the right skin friction coefficient on the wind tunnel wall since the boundary layer is accelerated through a nozzle. By modeling the nozzle and the oblique shock occurring on the test

section floor, very good agreement is obtained compared with the direct measurements of Orr [52].

A new conjugate heat transfer algorithm was validated by predicting the temperature distribution inside a cooled nozzle wall. Good agreement was found, but the solution was shown to be sensitive to the turbulence model. For the cases considered in this study, the cooled nozzle case is the only one sensitive to the turbulence model. We believe that this is due to the acceleration of the flow which reduces the turbulence intensity. For that case, the Spaart-Allmaras model showed the best agreement. The different turbulent models respond differently to this flow expansion. This can be seen in the value of the eddy viscosity which varies from model to model.

An experiment to assess the effect of supersonic flow over a laser heated target was designed and performed. To our knowledge it is the first time such an experiment is performed. Numerical simulations and analytical methods have been used extensively in the design of the experiment. We strongly believe that numerical simulations and experiments are symbiotic and that this work corroborates that assertion.

When comparing the experimental results at 65 Watt to those at 81 Watt a greater asymmetry is found in the 81 Watt case. This was observed on the surface and backside with both the infrared and thermocouples measurement. For the 81 Watt case, a region of increased cooling is seen upstream where a coherent structure clearly appears. More testing would be required to explain why such a difference is seen between the 81 Watt and 65 Watt cases.

The experimental results have been compared with our numerical model. Good agreement is found on the backside and on the surface away from the center. Close to the center the measurements display significantly more cooling than the computation. We believe that the strong perturbation of the boundary layer by the heat source can explain this discrepancy.

10.2 Recommendations and Extensions

Since no previous work has been performed to quantify the effect of a supersonic flowfield on a laser-heated target, we feel that the contributions made herein represent a starting point. We hope that this is only a first, but significant, step in a long journey toward the analysis and complete understanding of supersonic flow over a laser-heated wall.

The developed experimental methodology could be applied to full scale testing at AEDC. If anything, measurements on a larger scale model would be easier as the spatial resolution wouldn't be as much of an issue.

However, since a missile must typically be killed under 4 seconds [42], the time response of the measurement will be important for a typical missile configuration. Using a camera with a larger dynamic range would greatly reduce the uncertainty at shorter times. In the current experiment, many different calibrations needed, to be used in succession such the bias error

doesn't cancel when subtracting temperature measured with a different calibration. This was found to produce erratic data for $t < 2s$.

The computational model can be extended to missile/laser interaction problem since a more complex geometry can be handled. For instance, the temperature due by a laser beam on a rotating missile could be modelled. For that situation, the flow field would surely play a more important role as cooling should significantly increase.

The experimental heat surface heat flux could be obtained from an inverse heat transfer method. Here, the temperature distribution is three-dimensional such that is posed a challenging problem for the inverse method.

This study also showed some weaknesses in the modeling of compressible turbulent flows. We were surprised to notice that for the simplest case imaginable namely a supersonic flow over a flat plate, different turbulence models lead to different boundary layer profiles. The cause of this inconsistency was discovered by Catris and exposed in section 4.2.4. We believe that his proposed modifications should be included in GASP as they seem straightforward and make physical sense. Another problem which probably can't be fixed as easily is the modeling of the dissipation rate of the $\mathcal{TK}\mathcal{E}$. It was shown by Sinha and Candler, that only modeling the solenoidal dissipation rate is adequate for a Mach 4 flow. However, for strongly heated flows, density and viscosity gradients could play an important role in the dissipation of turbulence. Efforts should be made in trying to model the effect of the density and viscosity on the dissipation rate of the $\mathcal{TK}\mathcal{E}$

The modeling of the turbulent heat flux is another area where improvement can be made. In our model the eddy diffusivity for heat is assumed proportional to the eddy viscosity using a fixed Prandtl number value. It would be interesting to see if the agreement near the center can be improved by computing the turbulent Prandtl number by using a two-equation turbulence model for the temperature variance and its dissipation rate. Such a model should soon be implemented in Gasp. We also have an idea for a model that should be better suited for compressible wall bounded flows than the ones currently available in the literature. Using the specific dissipation rate of the variance of the temperature fluctuation contrary to the dissipation rate would make it possible to avoid using damping functions. This would lead to a more robust model for wall-bounded flows.

Bibliography

- [1] *GASP 3.0 User Manual*. AeroSoft, 1997. ISBN 0-9652780-0-x.
- [2] *GASP 4.0 User Manual*. AeroSoft, 2002. ISBN 09652780-5-0.
- [3] L.H. Back, P.F. Massier, and H.L. Gier. Convective heat transfer in a convergent divergent nozzle. *Int. J. Heat Mass Transfer*, Vol. 7:549–568, 1964.
- [4] T. J. Baker. On the relationship between mesh refinement and solution accuracy. *AIAA Paper No. 2005-4875*, June 2005.
- [5] Boeing. Airborne laser (abl). <http://www.boeing.com/defense-space/military/abl/index.html>.
- [6] K.W. Brinckman, D.C. Kenzakowski, and S.M. Dash. Progress in practical scalar fluctuation modeling for high-speed aeropropulsive flows. *AIAA 43rd Aerospace Sciences Meeting, Reno, Nevada*, 10-13 Jan 2005.
- [7] K. Brugger. Exact solution for the temperature rise in a laser-heated slab. *Journal of Applied Physics*, Vol. 43(2):557–583, 1972.
- [8] H.S. Carslaw and J.C. Jeager. *Conduction of Heat in Solids*. Oxford University Press, 1959.
- [9] S. Catris. *Etude de Contraintes et Qualification de Modeles a Viscosite Turbulente*. PhD thesis, Ecole Nationale Superieure de L’Aeronautique et de l’Espace, 1999.
- [10] T. Cebeci and A.M.O. Smith. *Analysis of Turbulent Boundary Layers*. Academic Press, 1974.
- [11] I. Celik. Procedure for estimation and reporting of discretization error in CFD applications. *Journal of Fluids Engineering Editorial Policy Statement on the Control of Numerical Accuracy*.
- [12] I. Celik, J. Li, G. Hu, and C. Shaffer. Limitations of richardson extrapolation and some possible remedies. *Journal of Fluids Engineering*, July 2005.

BIBLIOGRAPHY

- [13] F.J. Chen, M.R. Malik, and I.E. Beckwith. Boundary-layer transition on a cone and flat plate at mach 3.5. *AIAA Journal*, Vol. 7(6):687–693, 1989.
- [14] K.-Y. Chien. Predictions of channel and boundary-layer flows with a low-Reynolds number turbulence model. *AIAA Journal*, 20(1):33–38, 1982.
- [15] H.E. Cline and T.R. Anthony. Heat treating and melting material with a scanning laser. *Journal of Applied Physics*, Vol. 48(9):3895–3900, 1977.
- [16] K.D. Cole. Conjugate heat transfer from a small heated strip. *International Journal of Heat and Mass Transfer*, Vol. 40(No. 11):2709–2719, 1996.
- [17] J.C. Conde, F. Lusquinos, P. Gonzalez, B Leon, and M. Perez-Amor. Temperature distribution in a material heated by laser radiation, modelling and application. *Vacuum, Surface Engineering, Surface Instrumentation and Vacuum Technology*, Vol. 64:359–366, 2002.
- [18] Medtherm Corporation. Measure surface temperature with a response time as little as 1 microsecond. *Bulletin 500*.
- [19] CVI. Optical components and assemblies. <http://www.cvilaser.com>.
- [20] J.F. Debieve, P. Dupont, D.R. Smith, and A.J. Smits. Supersonic turbulent boundary layer subjected to step changes in wall temperature. *AIAA JOURNAL*, Vol. 35, No. 1, Jan 1997.
- [21] J.C. DeLise and M.H.N. Naraghi. Comparative studies of convective heat transfer models for rocket engines. *31st AIAA/ASME Joint Propulsion Conference and Exhibit*, 10-12 Jul 1995.
- [22] D.Plemmons, L. Baxter, and B. Stewart. Development of high-energy laser lethality testing capability for hypersonic targets. AIAA Paper 2005-7649, 2005.
- [23] E. R. G. Eckert. *Heat & Mass Transfer 2nd Edition*. McGraw Hill, 1959.
- [24] ESDU. 67019: Static strength of screwed fasteners. 1988.
- [25] A. Favre, L.S.G. Kovasznay, R. Dumas, J. Gaviglio, and M. Coantic. *La Turbulence en Mecanique des Fluides*. Villars, 1988.
- [26] Matt Ferber. Thermal shock testing of advanced ceramics - subtask 9, final report. *International Energy Agency Implementing Agreement for A Program of Research and Development on High Temperature Materials for Automotive Engines, Final Report*, 2000.
- [27] Matt Ferber and Kristin Breder. Thermal shock testing of advanced ceramics - subtask 9, draft. *International Energy Agency Implementing Agreement for A Program of Research and Development on High Temperature Materials for Automotive Engines, Final Report*, 1999.

BIBLIOGRAPHY

- [28] T. Fergusson. National instruments application note 043, measuring temperature with thermocouples - a tutorial.
- [29] H.H. Fernholz, P.J. Finley, and V. Mikulla. A further compilation of compressible boundary layer data with a survey of turbulence data. Technical Report AGARDograph AG-263, AGARD, 1981.
- [30] P. Giulio. Burning mirrors, stanzio della matematica, 1587-1609. http://web.mit.edu/2.009/www/experiments/deathray/10_ArchimedesResult.html.
- [31] G.C. Holst. *Testing and Evaluation of Infrared Imaging Systems*. JCD Publishing, 1998.
- [32] J. A. Horkovich. Directed energy weapons: Promise and reality. AIAA Paper 2006-3753, 2006.
- [33] P.G. Huang, P. Bradshaw, and T.J. Coakley. Turbulence models for compressible wall-bounded flows. *AIAA Journal* 1994, Vol. 32, No. 4, 1994.
- [34] P.G. Huang, P. Bradshaw, and T.J. Coakley. Skin friction and velocity profile family for compressible turbulent boundary layers. *AIAA Journal*, Vol. 31, No. 9, Sep 1993.
- [35] P.G. Huang, G.N. Coleman, and P. Bradshaw. Compressible turbulent channel flows: Dns results and modelling. *Journal of Fluid Mechanics*, Vol. 305:185–218, 1995.
- [36] R.J. Dunn III. Operational implications of laser weapons. Technical Report Analysis Center Papers, Northrop Grumman, September 2005.
- [37] G.V. Candler K. Sinha. Turbulent dissipation-rate equation for compressible flows. *AIAA Journal*, Vol. 41(No. 6):1017–1021, 2003.
- [38] H. Kaplan. *Practical Applications of Infrared Thermal Sensing and Imaging Equipment*. SPIE Optical Engineering Press, 1999.
- [39] W.M. Kays, M.E. Crawford, and B. Weigand. *Convective Heat and Mass Transfer Fourth Edition*. McGraw-Hill, 2005.
- [40] W. L. Ko and L. Gong. Thermoelastic analysis of hyper-x camera windows suddenly exposed to Mach 7 stagnation aerothermal shock. *NASA/TP-2000-209030*, September 2000.
- [41] W.C. Lee and Y.H. Ju. Conjugate leveque solution for newtonian fluid in a parallel plate channel. *International Journal of Heat and Mass Transfer*, Vol. 29:941–947, 1986.
- [42] S. G. Leonard. Laser options for national missile defense. Master's thesis, AIR COMMAND AND STAFF COLLEGE AIR UNIVERSITY, 1998.

BIBLIOGRAPHY

- [43] Y. Li and A. Ortega. Forced convection from a rectangular heat source in uniform shear flow the conjugate peclet number in the thin plate limit. *The Sixth Intersociety Conference on Thermal and Thermomechanical Phenomena in Electronic Systems*, 1998.
- [44] E. C. Marineau, J. A. Schetz, and R. E. Neel. Turbulent navier-stokes simulations of heat transfer with complex wall temperature variations. *AIAA Paper No. 2006-3087*, June 2006.
- [45] J. Melendez. Infrared cameras: Principles and general presentation. *Euro-Mediterranean Wildland Fire laboratory, D-07-05*.
- [46] M. Morkovin. Effect of compressibility on turbulent flows. *Mecanique de la Turbulence*, pages 369–380, 1962.
- [47] D. Mukerji, J. K. Eaton, and R. J. Moffat. Convective heat transfer near one-dimensional and two-dimensional wall temperature steps. *Journal of Heat Transfer*, Vol. 126:202–209, 2004.
- [48] S. Musikant. *Optical Materials*. Marcel Dekker, 1985.
- [49] A.J. Musker. Explicit expression for the smooth wall velocity distribution in a turbulent boundary layer. *AIAA Journal*, June 1979.
- [50] J.T. Nakos. Uncertainty analysis of steady state incident heat flux measurements in hydrocarbon fuel fires. Technical Report SAND2005-7714, Sandia National Laboratories, 2005.
- [51] NIKON. Nikon-made calcium fluoride. <http://www.nikon.co.jp>.
- [52] M. W. Orr. *Design, Analysis, and Initial Testing of a Fiber-Optic Shear Gage for 3D, High-Temperature Flows*. PhD thesis, Virginia Polytechnic Institute and State University, 2004.
- [53] S. Pokorni. Error analysis of surface temperature measurement by infrared sensor. *Internation Journal of Infrared and Millimeter Waves*, 25(10):1523–1533, 2004.
- [54] E.A. Luke Q. Liu, P. Cinnella, and L. Tang. Coupling heat transfer and fluid flow solvers for multi-disciplinary simulations. *AIAA 42nd Aerospace Sciences Meeting, Reno, Nevada*, 5-8 Jan 2004.
- [55] W. C. Reynolds, W. M. Kays, and S. J. Kline. Heat transfer in the turbulent incompressible boundary layer iii- arbitrary wall temperature and heat flux. *NASA Memorandum 12-3-58W*, 1958.

BIBLIOGRAPHY

- [56] W. C. Reynolds, W.M. Kays, and S.J. Kline. Heat transfer in the turbulent incompressible boundary III- arbitrary wall temperature and heat flux. NASA Memorandum 12-3-58W, 1958.
- [57] W. C. Reynolds, W.M. Kays, and S.J. Kline. Heat transfer in the turbulent incompressible boundary layer I-constant wall temperature. NASA Memorandum 12-1-58W, 1958.
- [58] P.J. Roache. *Verification and Validation in Computational Science and Engineering*. Hermosa, Albuquerque, NM, 1998.
- [59] P. L. Roe. Approximate Riemann solvers, parameter vectors, and difference schemes. *Journal of Computational Physics*, 43:357–372, 1981.
- [60] J.A. Schetz. *Boundary Layer Analysis*. Prentice Hall, 1993.
- [61] F. Schultz-Grunow. A new resistance law for smooth plates. *Luftfahrt-Forsch*, 17:239–246, 1940.
- [62] I.H. Shames and C.L. Dym. *Energy and Finite Element Methods in Structural Mechanics*.
- [63] A.M.O. Smith and T. Cebeci. Solution of the boundary-layer equations for incompressible turbulent flow. *Proceeding of the 1968 Heat Transfer and Fluid Mechanics Institute*, 1968.
- [64] T.P. Sommer, R.M.C. So, and H. S Zhang. Near-wall variable-Prandtl-number turbulence model for compressible flows. *AIAA Journal*, Vol. 31, No. 1, Jan 1993.
- [65] P. R. Spalart and S. R. Allmaras. A one equation turbulence model for aerodynamic flows. *La Recherche Aerospatiale*, 1:5–21, 1994.
- [66] I.J. Spiro and M. Schlessinger. *Infrared Technology Fundamentals*. Marcel Dekker, 1989.
- [67] C.R. Hedlund S.R. Sargent and P.M. Ligrani. An infrared thermography imaging system for convective heat transfer measurements in complex flows. *Meas. Sci. Technol.*, 9:1974–1981, 1998.
- [68] Vecor. Calcium fluoride plane parallel windows. <http://www.vecorus.com>.
- [69] D. C. Wilcox. Reassessment of the scale-determining equation for advanced turbulence models. *AIAA Journal*, 26(11):1299–1310, 1988.
- [70] D. C. Wilcox. *Turbulence Modeling for CFD*. DCW Industries, 2nd edition, 1998.
- [71] W.S. Wong and N. Qin. A numerical study of transonic flow in a wind tunnel over 3D bumps. *AIAA 43rd Aerospace Sciences Meeting, Reno, Nevada*, 10-13 Jan 2005.

BIBLIOGRAPHY

- [72] J. Zhang and E. Morishita. An efficient and accurate way of posing inflow profile boundary conditions. *Transacation of The Japan Society of Aeronautical and Space Science*, Aug 2004.

Appendix A

Generation of Missing Information at the Boundary

When trying to match experimental results using numerical simulations, great care must be taken into accurately reproducing the experimental conditions [72, 71]. For the problem, this translates into making sure that the initial boundary layer profile used for the computation matches that of the experiment. To perform the simulation, the profiles of $\rho, u, v, w, p, k, \omega$ must be specified at the inlet. Measurements for all variables are rarely available. Therefore, they must be assumed or created. In our case, the temperature and u-velocity profile are available. Assuming constant pressure across the boundary layer, the density profile can be computed from the perfect gas law. The considered flow is two-dimensional such that $w = 0$. This means that the profiles of the v-velocity, turbulent kinetic energy (k) and specific dissipation rate (ω) must be generated. Different approaches were considered.

One approach consists of running a flat plate simulation to the measured integral boundary layer parameter [71]. This was used for case A. However, for case B, the incoming boundary layer is developed through a converging-diverging nozzle, the computed and measured u-velocity profiles are dissimilar in the outer region of the boundary layer where adjustment is slower. Another approach consists of using the measured u-velocity profile to compute the turbulence quantities [72]. This was accomplished using the Cebeci-Smith [63] algebraic turbulence model. The approach used is described as follows. For this model, the eddy viscosity is computed differently in the outer and inner layer, such that we have:

$$\mu_t = \begin{cases} \mu_{t_i}, & y \leq y_m \\ \mu_{t_o}, & y > y_m \end{cases} \quad (\text{A.1})$$

where y_m is the smallest value of y for which $\mu_{t_i} = \mu_{t_o}$. In the inner layer, μ_{t_i} is computed as:

$$\mu_{t_i} = \rho l_{mix}^2 \left[\left(\frac{\partial u}{\partial y} \right)^2 + \left(\frac{\partial v}{\partial x} \right)^2 \right]^{\frac{1}{2}} \approx \rho l_{mix}^2 \left| \frac{\partial u}{\partial y} \right| \quad (\text{A.2})$$

where l_{mix} is the mixing length given as:

$$l_{mix} = \kappa y \left[1 - e^{-y^+/A^+} \right] \quad (\text{A.3})$$

whereas in the outer layer we have:

$$\mu_{t_o} = \alpha U_e \delta^* F_{kleb}(y; \delta) \quad (\text{A.4})$$

where F_{kleb} is the Klebanoff intermittency function given as:

$$F_{kleb}(y; \delta) = \left[1 + 5.5 \left(\frac{y}{\delta} \right)^6 \right]^{-1} \quad (\text{A.5})$$

and δ^* the boundary layer displacement thickness:

$$\delta^* = \int_0^\delta \left(1 - \frac{\rho u}{\rho_e U_e} \right) dy \quad (\text{A.6})$$

The closure coefficient are:

$$\kappa = 0.40, \quad \alpha = 0.0168, \quad A^+ = 26 \quad (\text{A.7})$$

The principal Reynolds shear stress is computed from the eddy viscosity:

$$\tau_{xy} = \mu_t \frac{\partial u}{\partial y} \quad (\text{A.8})$$

Outside the viscous sublayer the kinetic energy is readily computed using the structural parameter $a = 0.3$:

$$\tau_{xy} = ak \Rightarrow k = \frac{\mu_t}{a} \frac{\partial u}{\partial y} \quad (\text{A.9})$$

whereas the specific dissipation rate ω is given by:

$$\omega = \frac{\rho k}{\mu_t} \quad (\text{A.10})$$

Inside the viscous sublayer we use the asymptotic analysis of the boundary layer performed by Wilcox [70]:

$$k = C_2 y^n, y \rightarrow 0 \quad (\text{A.11})$$

with $n = 3.23$ and:

$$\omega = \frac{C_1 \nu}{\beta^* y}, y \rightarrow 0 \quad (\text{A.12})$$

where $\beta^* = 9/100$ is a closure coefficient of the Wilcox $k-\omega$ turbulence model and $C_1 = 7.20$. The value of C_2 is found by matching the expression for k valid outside the viscous sublayer

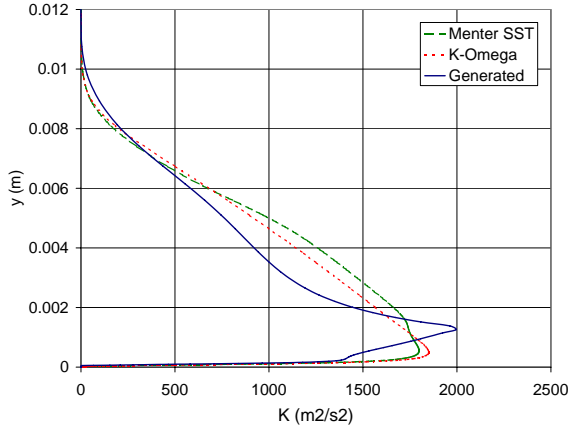


Figure A.1: Generated turbulent kinetic energy compared with computation

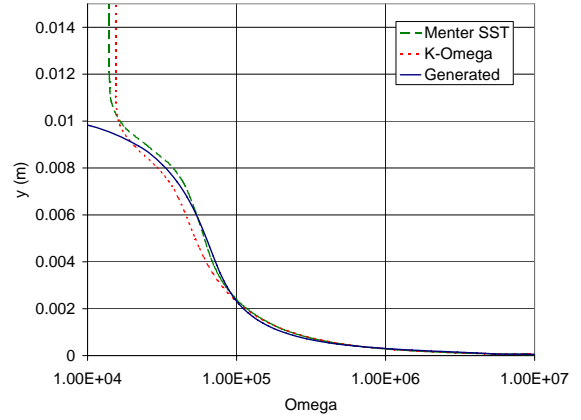


Figure A.2: Generated ω compared with computation

(equation A.9) to that valid inside (equation A.11) at the edge of the viscous sublayer located at $y^+ = 7$. This yields:

$$C_2 = \left(7 \frac{\mu_w}{\rho_w u_\tau}\right)^{-n} \left(\frac{\mu_t}{a}\right) \frac{\partial u}{\partial y} \Big|_{y^+=7} \quad (\text{A.13})$$

The methodology used to generate k and ω was validated by employing a flat plate simulation ran at the same condition as the experiment from Debieve et al. [20]. The values of k and ω generated from the u-velocity profile (obtained from the flat plate simulation) are compared to those obtained directly from the flat plate simulation: Figs. A.1 and A.2 show a good agreement such that we are confident in this approach. Next the v-velocity profile must be generated. An approach based on the work of Zhang and Morishita [72] is used. The missing v-velocity component is found by integrating the Favre-averaged continuity equation:

$$\frac{\partial \rho u}{\partial x} + \frac{\partial \rho v}{\partial y} \quad (\text{A.14})$$

and because the pressure is constant across the boundary layer can be discretized as:

$$v_{i,j+1} = \frac{T_{i,j+1}}{T_{i,j}} v_{i,j} - \frac{T_{i,j+1} h_j}{\Delta x} \left[\frac{u_{i+1,j}}{T_{i+1,j}} - \frac{u_{i,j}}{T_{i,j}} \right] \quad (\text{A.15})$$

Where h_j is grid spacing in the y direction and Δx the spacing between stations i and $i + 1$. However, to compute v , the u-velocity and temperature profiles must be known at station i and $i + 1$. To generate these two profiles, we use the integral momentum equation:

$$\frac{d\theta}{dx} = \frac{C_f}{2} \quad (\text{A.16})$$

Which in return requires knowing the skin friction coefficient and the momentum thickness at station $i+1$. The following analysis is made to get these quantities. Experimental results

and analysis have shown that the compressible boundary layer follows the Law of the Wall and the Law of the Wake when the velocity is transformed according to:

$$u_c = \int \left(\frac{\rho}{\rho_w} \right)^{\frac{1}{2}} du = \int \left(\frac{T_w}{T} \right)^{\frac{1}{2}} du \quad (\text{A.17})$$

Since the pressure is constant across the boundary layer. Starting from the momentum and the energy equation for a two-dimensional boundary layer [60] without pressure gradients, a relation between the temperature and the velocity field can be obtained by acknowledging that the convective terms are negligible close to the wall. This simplification enables the integration of the momentum equation which now states that the total stress is constant across the boundary layer:

$$(\mu + \mu_t) \frac{\partial u}{\partial y} = \tau_w \quad (\text{A.18})$$

This result can be substituted into the energy equation which is integrated twice, yielding Crocco's integral:

$$T = T_w - \frac{Pr_m q_w u}{c_p \tau_w} - \frac{Pr_m u^2}{2c_p} \quad (\text{A.19})$$

where the mixed Prandtl number Pr_m , defined as:

$$Pr_m = c_p \frac{\mu + \mu_t}{k_f + k_t} \quad (\text{A.20})$$

is assumed constant to perform the integration. In practice for a wall-bounded turbulent flow of air $Pr_m \approx Pr_t \approx r \approx 0.9$. Using equation A.19, equation A.17 can be analytically integrated to obtain the Van Driest's transformation:

$$u_c = \sqrt{B} \left[\sin^{-1} \left(\frac{A+u}{D} \right) - \sin^{-1} \left(\frac{A}{D} \right) \right] \quad (\text{A.21})$$

where:

$$A = \frac{q_w}{\tau_w} \quad (\text{A.22})$$

$$B = \frac{2c_p T_w}{pr_t} \quad (\text{A.23})$$

$$D = \sqrt{A^2 + B} \quad (\text{A.24})$$

The inverse transformation is given by:

$$\frac{u}{u_\tau} = \frac{1}{R} \sin \left(\frac{Ru_c}{u_\tau} \right) - H \left[1 - \cos \left(\frac{Ru_c}{u_\tau} \right) \right] \quad (\text{A.25})$$

where:

$$R = \frac{u_\tau}{\sqrt{B}} \quad (\text{A.26})$$

$$H = \frac{A}{u_\tau} \quad (\text{A.27})$$

Contrarily to Van Driest I transformation [60] the previous is valid for non-unity Pr and Pr_t as well as non-adiabatic walls since all these effects are included in Crocco's integral. We use an explicit expression for the law-of-the-wall in the inner region and law-of-the-wake in the outer region which is was found by Musker [49]:

$$u_c^+ = 5.424 \tan^{-1} \left[\frac{2y^+ - 8.15}{16.7} \right] + \log_{10} \left[\frac{(y^+ + 10.6)^{9.6}}{(y^{+2} - 8.15y^+ + 86)^2} \right] - 3.52 + 2.44 \left\{ \Pi \left[6 \left(\frac{y}{\delta} \right)^2 - 4 \left(\frac{y}{\delta} \right)^3 \right] + \left(\frac{y}{\delta} \right)^2 \left(1 - \frac{y}{\delta} \right) \right\} \quad (\text{A.28})$$

where Π is the wake parameter [10] defined as:

$$\Pi = 0.55 \left[1 - \exp \left(-0.24 \sqrt{Re_\theta} - 0.298 Re_\theta \right) \right] \quad (\text{A.29})$$

We now have all the analytical expressions required to compute the velocity and temperature profiles from either δ or θ . When θ (or δ) and $[T_w, T_e, U_e, \rho_e, \rho_w, y_i]$ are known we can compute δ (or θ) and $[u(y_i), T(y_i), C_f, q_w]$ using the following algorithm first developed by Huang et al. [34] and improved by Zhang and Morishita [72].

1. Guess the value of δ (or θ) and u_τ . $\theta = 7/72\delta$ is a reasonable estimate assuming a power law velocity profile with $n = 7$ (see Schetz [60]). u_τ can be estimated from Schoenherr's skin friction correlation [60]
2. Compute q_w using Crocco's integral (equation A.19) evaluated at U_e
3. Compute u_{c_e} using Van Driest transformation (equation A.21) evaluated at U_e
4. Compute $Re_\theta = \frac{\rho_e U_e \theta}{\mu_w}$ and evaluate the wake parameter Π using equation A.29
5. Compute $Re_{\delta_w} = \frac{\rho_w u_{c_e} \delta}{\mu_w}$
6. Compute $\delta^+ = \frac{\rho_w u_\tau \delta}{\mu_w}$ by solving numerically $Re_{\delta_w} = u_{c_e}^+ \delta^+$ where $u_{c_e}^+$ is obtained from equation A.28 evaluated at $y = \delta$
7. Compute $u_\tau = \frac{\delta^+ \mu_w}{\rho_w \delta}$
8. Compute $C_f = 2 \frac{T_e}{T_w} \left(\frac{u_\tau}{U_e} \right)^2$ and $\tau_w = \rho_w u_\tau^2$
9. Compute u_c^+ at each y_i using equation A.28
10. Compute $u_c = u_c^+ u_\tau$ and u at each y_i from u_c using Van Driest inverse transformation (equation A.28)
11. Compute T at each y_i from u using Crocco's integral (equation A.19)
12. Compute a new estimate of δ (or θ) from the u -velocity profile using $\frac{\theta}{\delta} = \int_0^1 \frac{T_e u}{T U_e} \left(1 - \frac{u}{u_e} \right) d\eta$

Steps 2 to 12 are repeated until convergence. This algorithm was implemented using Matlab and convergence is reached within less than 10 iterations. For higher Mach numbers, a scaling of y^+ was done by Zhang and Morishita [72]. This was implemented but wasn't significant for the Mach number considered herein. The following steps are used to compute the v -velocity profile:

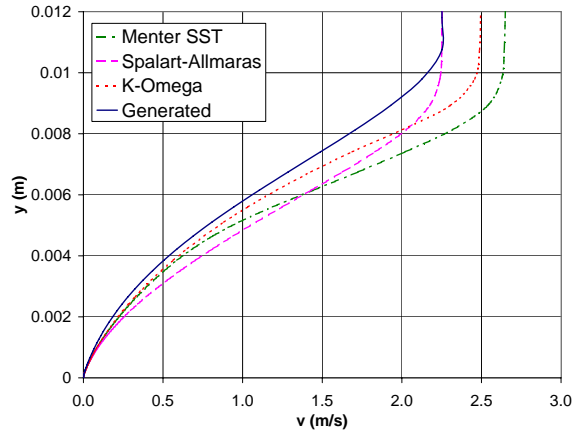


Figure A.3: Generated v-velocity component compared with computation

1. Compute θ_i from the known temperature and u-velocity profile at station i
2. Compute θ_{i+1} for known values of θ_i and C_f using the momentum integral equation (equation A.16)
3. From θ_{i+1} compute $u_{i+1,j}$ and $T_{i+1,j}$ using the previous algorithm
4. Compute $v_{i+1,j}$ explicitly for the discretized Favre-averaged continuity equation (equation A.15)

The generated v-velocity profile is compared against results from a flat plate simulation in Fig. A.3. We notice a difference between the v-velocity profiles among the turbulence models. In the inner layer, the generated v-velocity profile agrees with the one obtained with $k - \omega$, whereas in the outer layer, it reaches the same free stream value as the one obtained using Spalart-Allmaras turbulence model.

Appendix B

Numerical and Experimental Investigation of Mach 4 Flow in the Virginia Tech Supersonic Wind Tunnel

A detailed flow survey is conducted in the Virginia Tech supersonic wind tunnel at Mach 4. Numerical computations of the flow field are performed with and without modelling the nozzle. An overview of the experimental results is given first.

B.1 Experimental Results

A boundary layer survey is performed in the Virginia Tech supersonic wind tunnel at Mach 4 using a Pitot, cone-static and total temperature probes. The Pitot probe had an outer diameter of 1.59 mm and an inner diameter of 1.04 mm , which gives a capture area of 0.85 mm^2 . The cone-static has a 10° half-angle and an outer diameter of 1.59 mm with four small ports arranged around the cone to reduce misalignment effects of the probe with respect to the flow. The uncertainty in pressure measurement is evaluated at 0.06 atm . Total temperature is measured with a rake consisting of three tubes of 1.59 mm outer diameter spaced 6.4 mm apart. Each tube has an inner diameter of 1.04 mm giving a capture area of 0.85 mm^2 . The total temperature probes also has 4 small ports to increase the recovery factor. The ratio of capture to recovery area is 5 to 1 resulting in a recovery factor 0.97. Exposed junction type-E thermocouples with 0.25 mm diameter bead are placed inside the three total temperature probes. The uncertainty on temperature measurement is evaluated at 2 K . The Pitot, cone-static and total temperature probes are fixed to a single assembly inserted through the tunnel floor and mounted to a traversing system as seen in Fig. B.1.

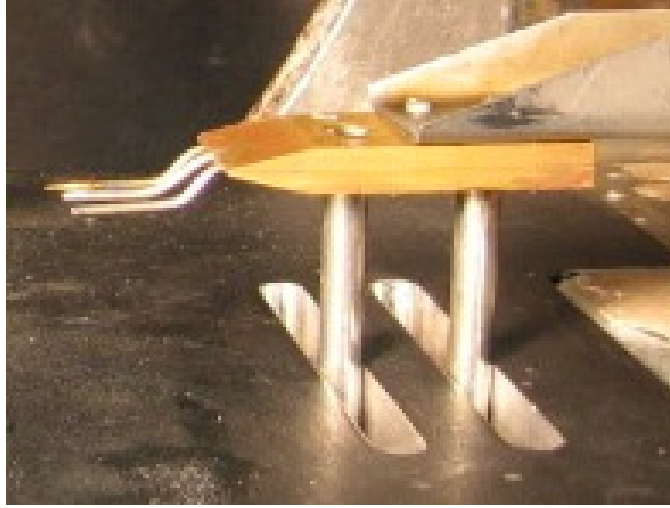


Figure B.1: Pitot, cone-static and total temperature probes mounted on a assembly inserted through the tunnel floor

The measured Mach, Temperature and Velocity profiles are shown in Figs. B.2,B.3 and B.4. The thermal and velocity boundary layer profiles thicknesses are approximately equal to 1.7 cm.

We notice that the edge Mach number is equal to 3.65 which isn't the Nozzle design Mach number. This is due to the presence of an oblique shock starting from the nozzle and test section junction that brings the Mach number from 4 to 3.65. The measured change in Mach number corresponds to a 5° change in direction. The shock is observed on a Schlieren picture as seen in Fig. B.5.

The boundary layer is also visible on the Schlieren image and its thickness agrees with the one determined from the u-velocity profile measurement.

B.2 Computational Results

Our experimental setup doesn't allow to measured the boundary layer properties at less than 1 mm from the wall due to the thickness of the Pitot probe. Also, it is well known that near wall measurements are difficult. Having the right near wall velocity and temperature profiles is essential to predict the correct heat transfer at the wall. For an equilibrium boundary layer, one can extrapolate the velocity profile all the way to the wall when the wall shear is known. Knowing the boundary layer thickness, the velocity profile can also be determined using the algorithm of Appendix A. Then, the temperature profile can be obtained from the temperature profile using Crocco integral.

B.2. COMPUTATIONAL RESULTS

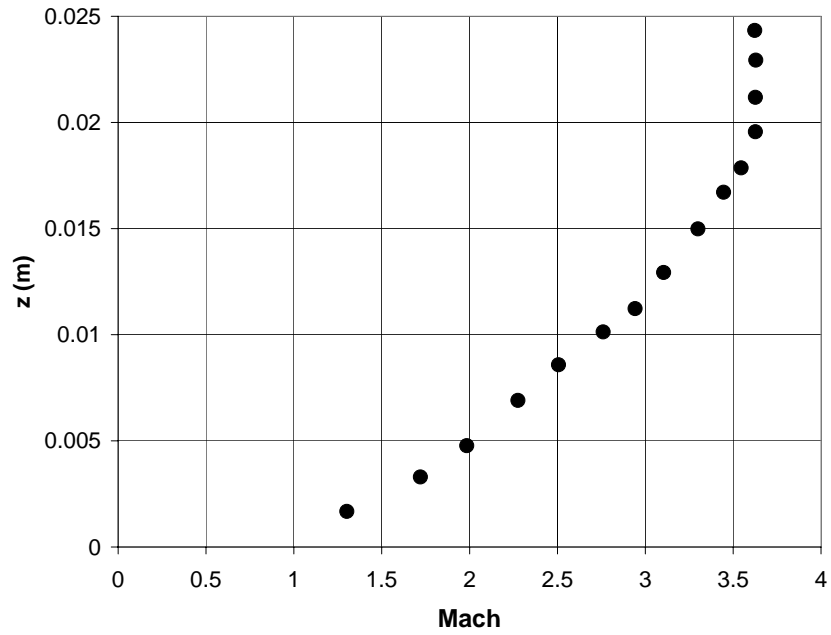


Figure B.2: Measured Mach profile number in VT SST at Mach 4

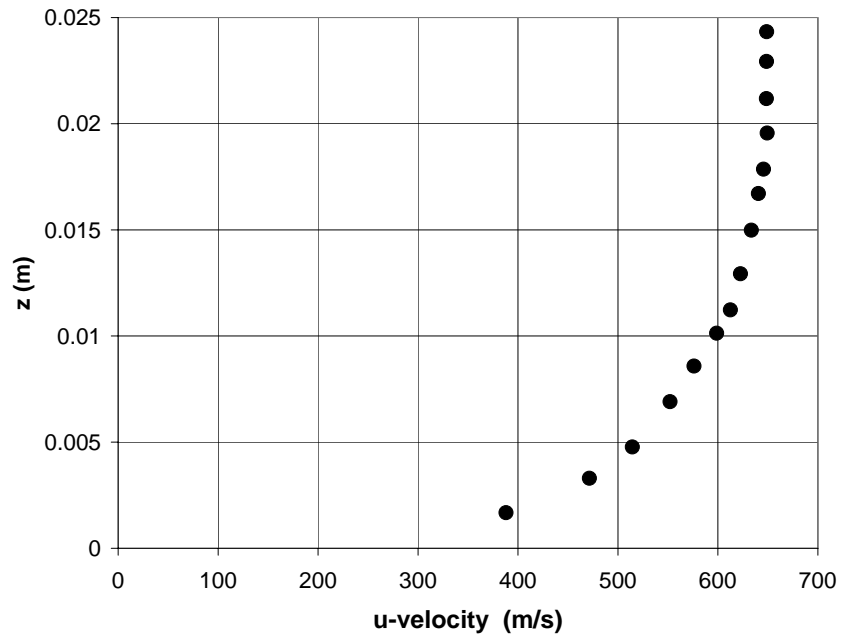


Figure B.3: Measured u-velocity profile in VT SST at Mach 4

B.2. COMPUTATIONAL RESULTS

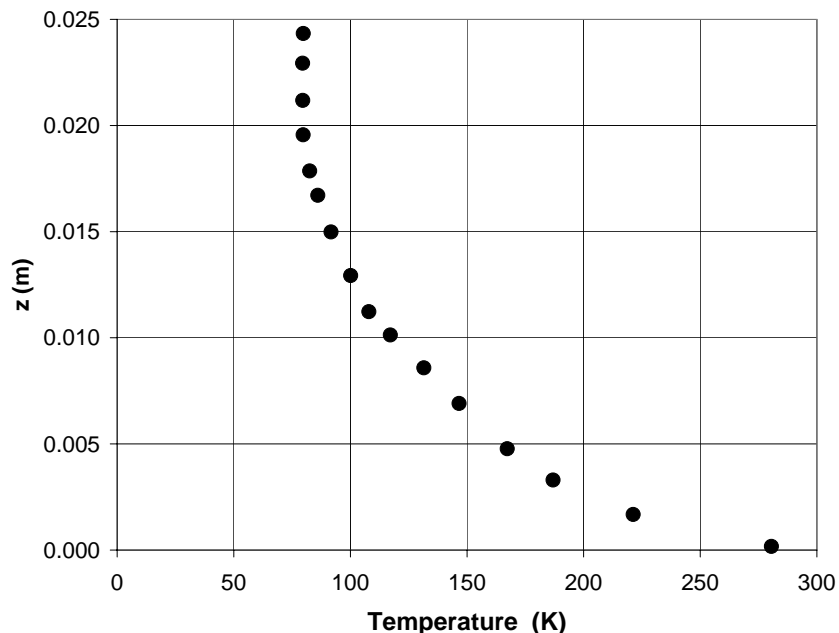


Figure B.4: Measured temperature profile in VT SST at Mach 4

The wall shear in the Virginia Tech supersonic wind tunnel at Mach 4 was directly measured by Orr [52] using both a strain gage and a fiber optics sensor. His results are plotted in Fig. B.6. A value of the axial shear stress of 85 Pa was obtained leading to a skin friction coefficient of $0.0007 \pm 1.25 \times 10^{-4}$.

The objective is to perform a numerical simulation of the flow field in the Virginia Tech supersonic wind tunnel and compare the wall shear to that of Orr.

First, Van Driest II correlation and Gasp CFD code are used to compute the skin friction coefficient in the test section. A flat plate simulation is run up to the measured boundary layer thickness. The numerical results are compared with Van-Driest II correlation in Fig. B.7. Good agreement is found between the two methods but the computed skin friction is about 30% higher than that of Orr.

Our initial intuition in explaining this discrepancy is that the expansion inside the nozzle reduces the vorticity and the level of turbulence in the fluid leading to a lower skin friction. The next step is therefore to make a computation which includes the expansion through the nozzle. Only one half of the nozzle is modeled and a symmetry boundary condition is used on the symmetry plane. A two dimensional model is used as we believe that the effect the side-wall can be neglected near the center of the test section. Two computational models are generated: one without the shock and another with a 5° turn at the nozzle-exit in order to replicate what is was measured and observed in the Schlieren picture. Mach number

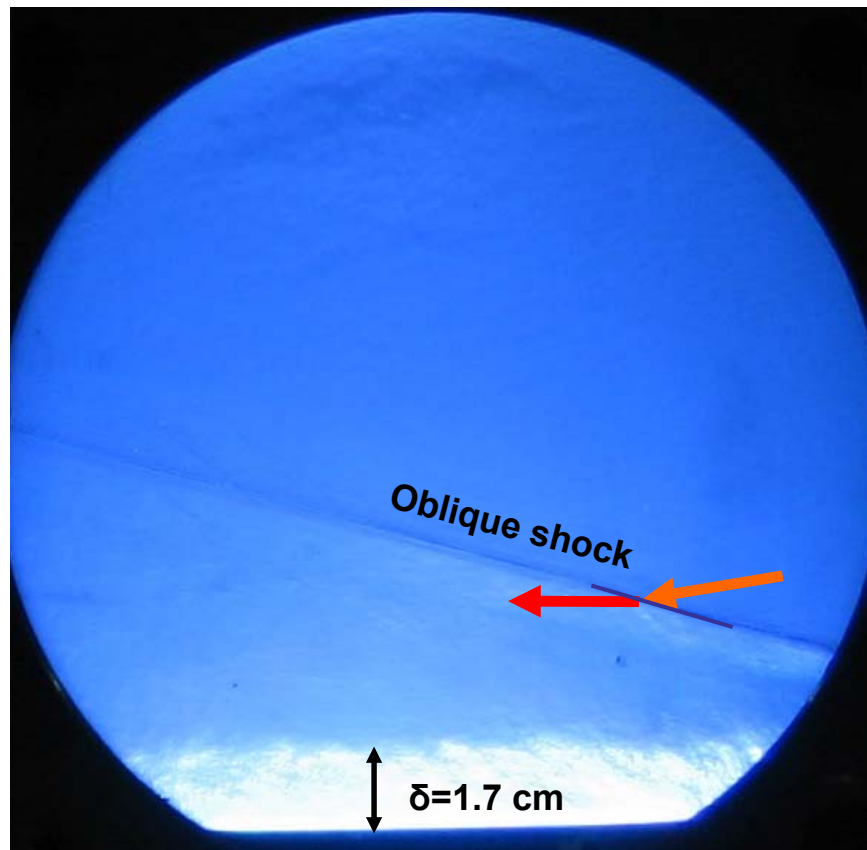


Figure B.5: Schlieren picture showing the oblique shock and the boundary layer thickness

B.2. COMPUTATIONAL RESULTS

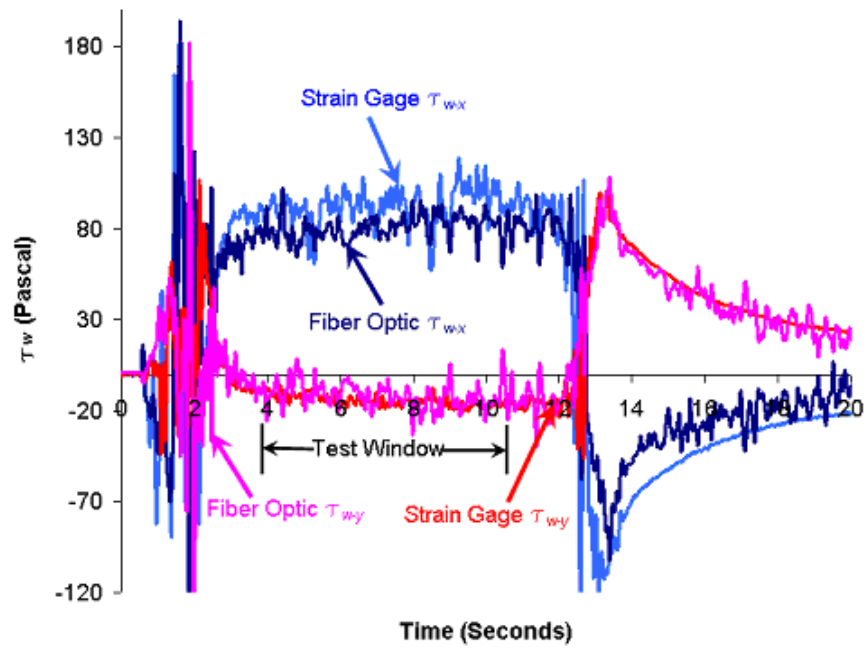


Figure B.6: Shear measurements performed by Orr in VT SST (taken from Orr [52])

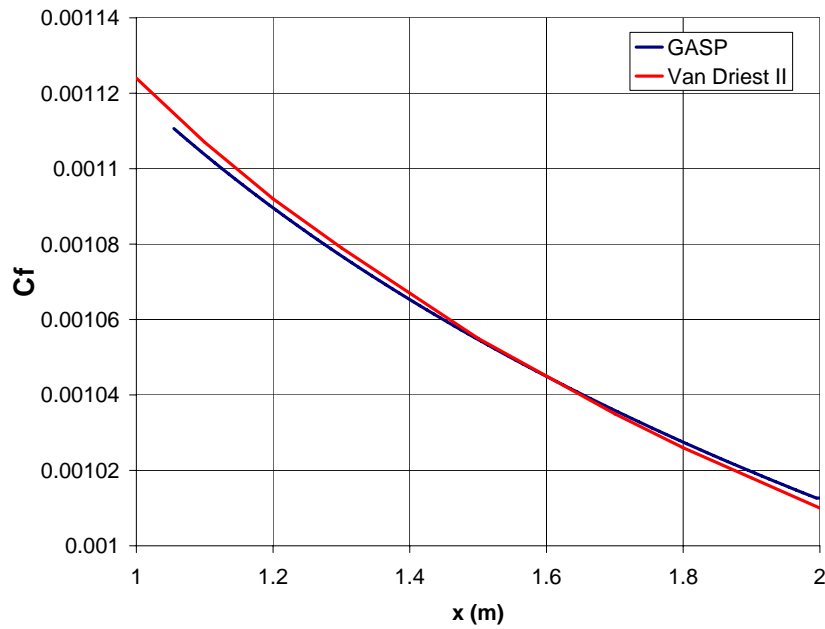


Figure B.7: Skin friction coefficient for a numerical simulation on a flat plate for the conditions measured behind the oblique shock compared to Van Driest II correlation



Figure B.8: Computed Mach number profiles for the VT SST Mach 4 nozzle

contours are seen in Fig. B.8 for the case with the oblique shock.

The skin-friction coefficient for the shock-less case is plotted in Fig. B.9 using both $k - \omega$ and Menter's SST turbulence model. No significant difference is found between the two models. The geometry of the nozzle is also shown. A strong increase in friction is seen at the throat and a strong decrease occurs as the flow expands through the nozzle. Fig. B.10 shows the skin friction coefficient upstream and inside the test section for the shock and no-shock cases. The skin friction coefficient increases sharply through the shock. For the shock case, the computed shear equal to $88 Pa$ which agrees very well with the value measured by Orr ($85 Pa$). This shows that to predict the skin friction on the tunnel floor, one needs to model the expansion of the fluid inside the nozzle as well as the shock. Since heat transfer and skin friction are closely related through Reynolds Analogy, the same features need to be modeled to get a good prediction of the heat transfer rate.

The u-velocity profiles are plotted in Fig. B.11 where the measurements are compared with the flat-plate and nozzle solution with a shock. We notice that near the wall, the measured u-velocity is not as full as the computed solutions. In Fig. B.12, the near wall velocity profiles are compared. As expected, the flat plate has a larger slopes in that region.

B.2. COMPUTATIONAL RESULTS

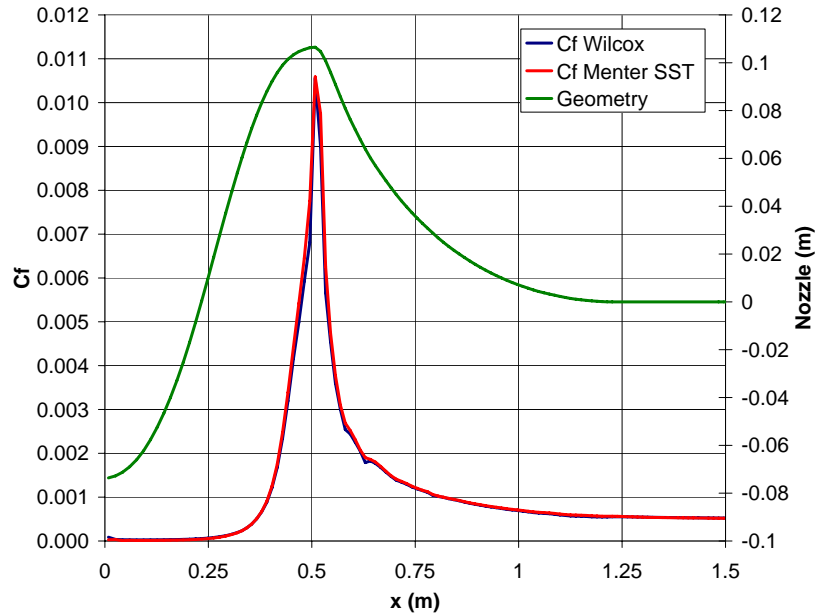


Figure B.9: Computed skin friction coefficient on the floor plate of VT SST at Mach 4 for $k - \omega$ and Menter's SST turbulence models. The geometry of the nozzle is also shown

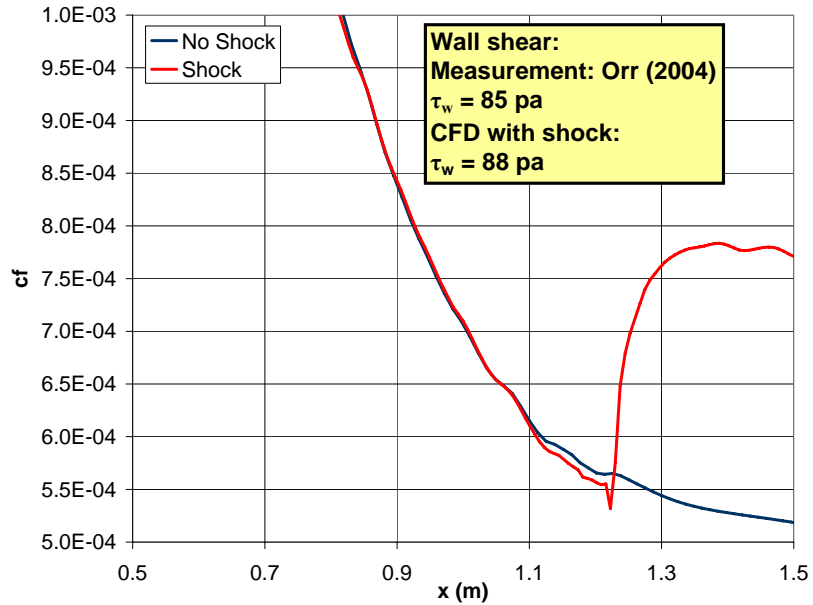


Figure B.10: Computed skin friction coefficient on the floor plate of the VT SST with and without the floor-plate shock

B.2. COMPUTATIONAL RESULTS

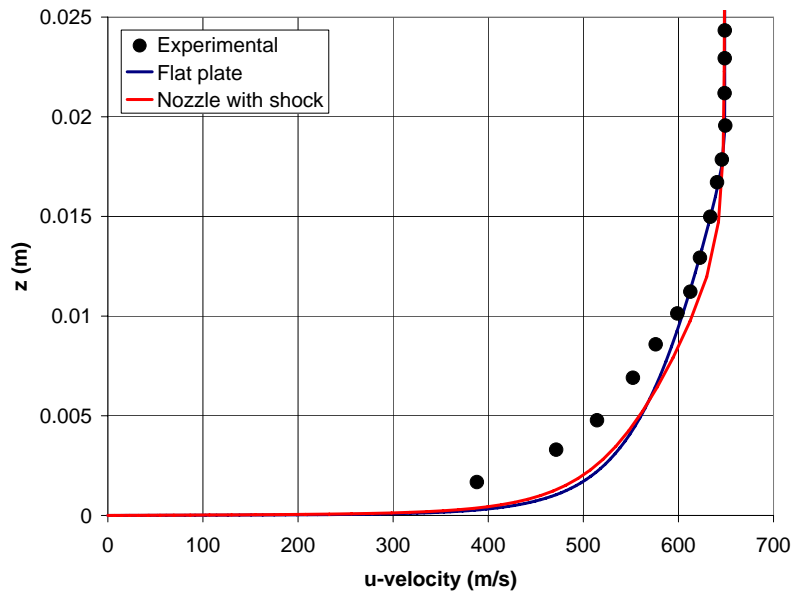


Figure B.11: Comparison of computed u -velocity profiles with measurements

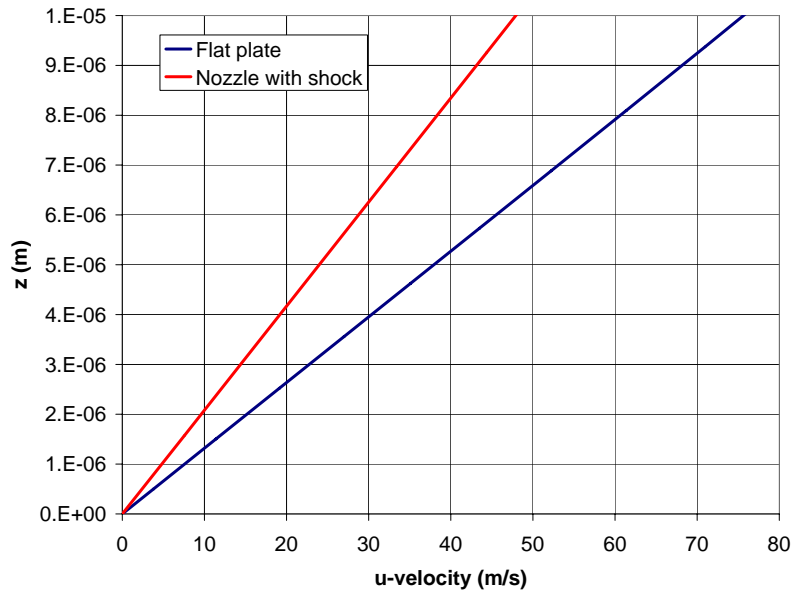


Figure B.12: Linear velocity in laminar sublayer: as expected the flat plate solution has a greater slope

Appendix C

Infrared Camera Model and Dynamic Response

The main advantage of infrared thermography is that it enables noncontact surface temperature measurements not like the embedding of many thermocouples in the object which can modify the internal temperature distribution. The initial plan was to use a borrowed Radiance 1T infrared camera which uses an indium antimonide focal plane array detector sensitive to infrared radiation from 3-5 microns. Eventually an Indigo Merlin Mid-Wave infrared camera was rented. Those two camera are very similar as they both used a cooled InSb detector.

A Mathematical model developed for the Radiance 1T is presented here. This model is useful in assessing the system requirements for the temperature measurement of a laser irradiated target. This model can also be useful for calibration purposes and understanding the parameters influencing the performance of the device. First, the Radiance 1T specifications are found in Table C.1.

The following definitions [45, 38, 31, 66] are helpful in understanding the mathematical model which is presented next.

Irradiance, E : Radiant heat flux per unit area [W/cm^2] reaching the detector

Exitance, M : Total radiant heat flux per unit area [W/cm^2] leaving the target

Radiance, L : Radiant heat flux per unit area per unit solid angle [$W/cm^2/sr$]

Spectral Irradiance, $E(\lambda)$: Radiance per wave length [$W/cm^2/\mu m$]. Spectral irradiance must be integrated with respect to the wave length to compute the irradiance.

Black body : A body for which the emissivity is maximal and the spectral irradiance is given by Plank's law

Table C.1: Infrared Camera Specifications

Detector	Indium antimonide
Format	256 X 256 - 65536 elements
Sensitivity	0.025°C NETD
Dynamic Range	12 bits
25 mm Lens	22° X 22° Field of View - $f/2.3$
50 mm Lens	11° X 11° Field of View - $f/2.3$
100 mm Lens	5.6° X 5.6° Field of View - $f/2.3$
IFOV	0.76 Milliradians
Temperature Range (No filter)	-20°C – 120°C
Temperature Range (ND1 filter)	40°C – 260°C
Temperature Range (ND2 filter)	120°C – 520°C (750°C with a lower integration time)

Grey body : A body for which emissivity e isn't a function of the wave length

Lambertian body : A Body for which $M = L\pi$. Black bodies are Lambertian bodies whereas it constitutes a valid approximation for grey bodies

Digital Number, DN : The output of the analog-to-digital converter (ADC). For a 12 bits ADC there is 4096 (2^{12}) levels

Sensor model : Relates the irradiance that reaches the detector E_D to the digital number of the camera, DN . The relation is usually linear such that $DN = K_D E_D + k_{off}$

Radiometric model : Relates the exitance of the objects to the irradiance at the detector such that M_o is expressed as a function of E_D .

NDX Filter : Neutral density filter of optical density of X. Meaning that the transmissivity t_f is equal to 10^{-X} . Filters must be used when a hot target is visualized to avoid saturation of the detector.

The size of the detector d can be computed from principles of geometrical optics using:

$$d = 2f \tan\left(\frac{\alpha}{2}\right) \quad (\text{C.1})$$

Where f is the focal length of the lens. It is important to note that the previous expression isn't applicable for wide angle lenses. The same value of d was obtained for all three lenses such that equation C.1 is applicable.

The size of a target h_t located at a given distance x_f is given as:

$$h_t = \frac{d(x_t - f)}{f} \quad (\text{C.2})$$

Table C.2: Computed Infrared Camera Specifications

Detector size	9.7 mm	
Distance to get 1 sqin area	4"	Spatial resolution of 0.004"

The previous expression makes it possible to compute the spatial resolution. Among all the available lenses, the $25mm$ is the best choice to get maximum magnification since it has a much smaller minimum focussing distance. The computed specifications for the $25mm$ lens are found in Table C.2. The focussing distance can be increased by using an extender ring. However, such a device will change the calibration of the camera.

By positioning the camera at 4" from the target an area of 1 square inch is covered. For that distance, each pixel of the detector corresponds to square having sides of 4 thousand of an inch. Such a spatial resolution was achieved by Ferber [26] with the same lens and infrared camera combination.

Quantitative measurement requires a relation between the digital number and the temperature of the body such that we must combine the radiometric and the sensor models and the use Planks law to relate the spectral irradiance $M(\lambda, T)$ to the temperature T :

$$M(\lambda, T) = \frac{C_1}{\lambda^5 \exp\left(\frac{C_2}{\lambda T}\right) - 1} \quad (C.3)$$

The complete model has the following form:

$$DN(T) = K_g \int_{\lambda_1}^{\lambda_2} R(\lambda)e(\lambda)t_f(\lambda)M(\lambda, T)d\lambda + K_{offset} \quad (C.4)$$

Where K_g is the gain, $R(\lambda)$ the detector responsivity, $e(\lambda)$ the surface emissivity, $t_f(\lambda)$ the filter transmissivity and K_{offset} the calibration offset. Since the distance between the target and the camera is small and considering that the atmosphere doesn't absorb much between 3 and 5 microns the invariance of radiance can be used such that the body exitance is equal to the radiance incident to the detector.

Using values of the detector responsivity [38] and the temperature ranges provided by the manufacturer for each filters the gain and offset are computed such that curves relating T to DN can be obtained for a given filter by numerical integration of equation C.4. These curves found in Fig. C.1 are useful in selecting a filter suitable for our application.

We notice that adding a filter increases the maximum temperature that can be measured. Reducing the integration time also enables the increase of the maximum temperature as saturation is avoided. However, the sensitivity is reduced. Saturation is achieve when all the electron are released. One electron is release when a photon hits the photodetector (actually, it is around 0.85 electron/photon hitting the detector, 0.85 being the quantum efficiency of the detector). The maximum number of electrons to be released is called the well capacity of

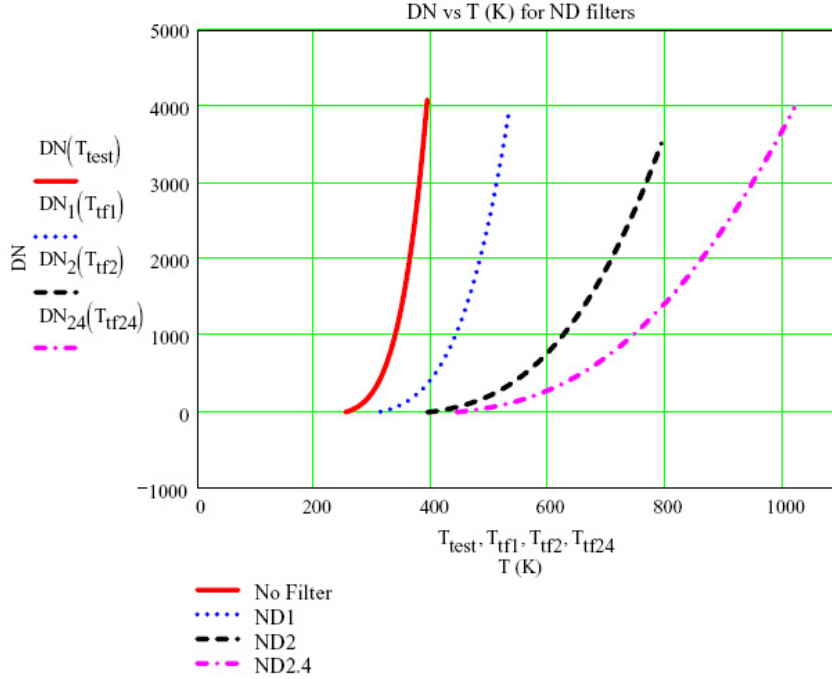


Figure C.1: Calibration curves for different filters

the detector. However, nothing being free, a shorter integration time decreases the sensitivity of the camera. This can be seen in the following way. The noise bandwidth is related to the integration time as:

$$\Delta f = \frac{1}{\Delta t} \quad (\text{C.5})$$

The noise equivalent delta temperature of the detector NEDT is an indication of the sensitivity which is defined as the minimum detectable temperature change (such that a lower NEDT implies a greater sensitivity). The NEDT can be expressed as [31]:

$$NEDT = \frac{4(f/\#)^2 \sqrt{\Delta f}}{\sqrt{A_d} \int_{\lambda_1}^{\lambda_2} D^*(\lambda) e(\lambda) t_f(\lambda) M(\lambda, T) d\lambda} \quad (\text{C.6})$$

where $D^*(\lambda)$ is the detectivity which depends on the detector material and temperature (InSb at 77 K for the Radiance 1T camera) and A_d the area of the detector. Equations C.5 and C.6 show that the NEDT increases when the integration time diminishes such that the sensitivity decreases. The sensitivity also diminishes when a filter is used (low value of $t_f(\lambda)$). It is not clear what is the advantage in using a filter versus reducing the integration time. Obviously, for very high temperature, a filter is required as the camera will still saturate when using the smallest allowable integration time. The NEDT is also a function of temperature which doesn't make sense for a manufacturer to state a value of the NEDT without indicating the temperature. (this is the case for this camera)

A new calibration must be performed when the integration time is changed. Different camera settings must be used to visualize the center of the heated target and the periphery.

Since the laser beam is perpendicular to the surface, the infrared camera can't be aimed perfectly perpendicular to the surface in order to avoid the beam. The incidence angle will be small (around 20° between the surface normal and the camera angle) such that it shouldn't change the irradiance on the detector. Moreover, the image will only be slightly distorted as the horizontal distortion is proportional to $\cos(20^\circ)$.

Appendix D

Window Structural Analysis

The analysis was performed using plate theory for clamped and simply supported boundary condition [40, 62]. The deflection, tangential and radial stresses are shown in Fig. D.1, D.2 and D.3. The transverse shear can be neglected as it is two order of magnitude lower compared to tangential and radial stress.

The deflection and the stresses are greater for the simply supported case. However, it is difficult to mount the window such that rotation at the root is totally eliminated. The window was assumed as being simply supported which is a conservative analysis. A thickness of 8 *mm* provides a sufficient factor of safety.

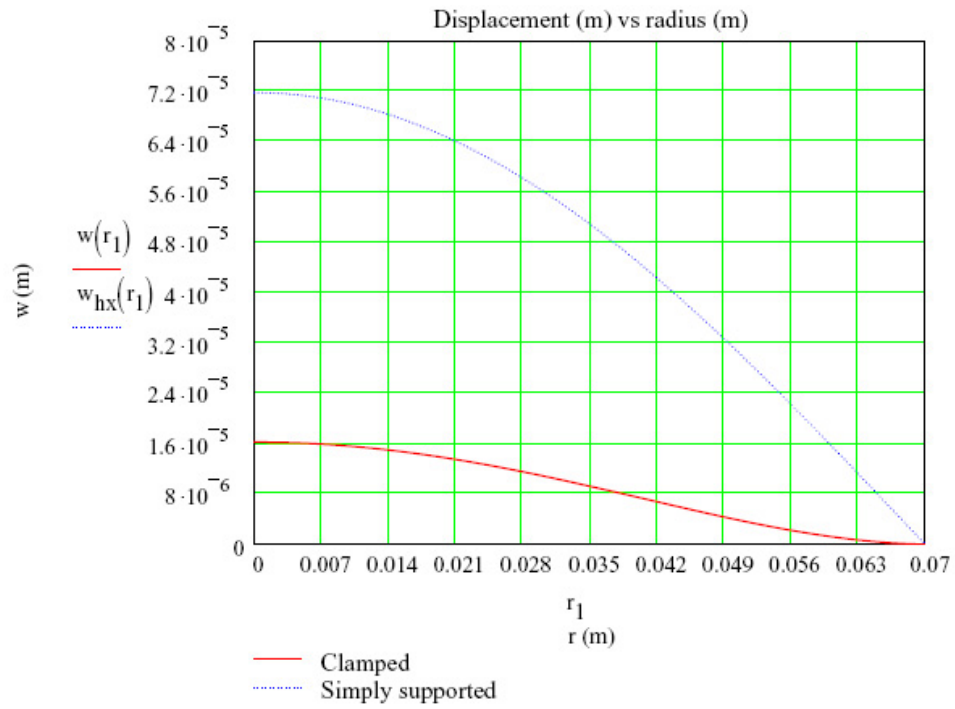


Figure D.1: Window displacement

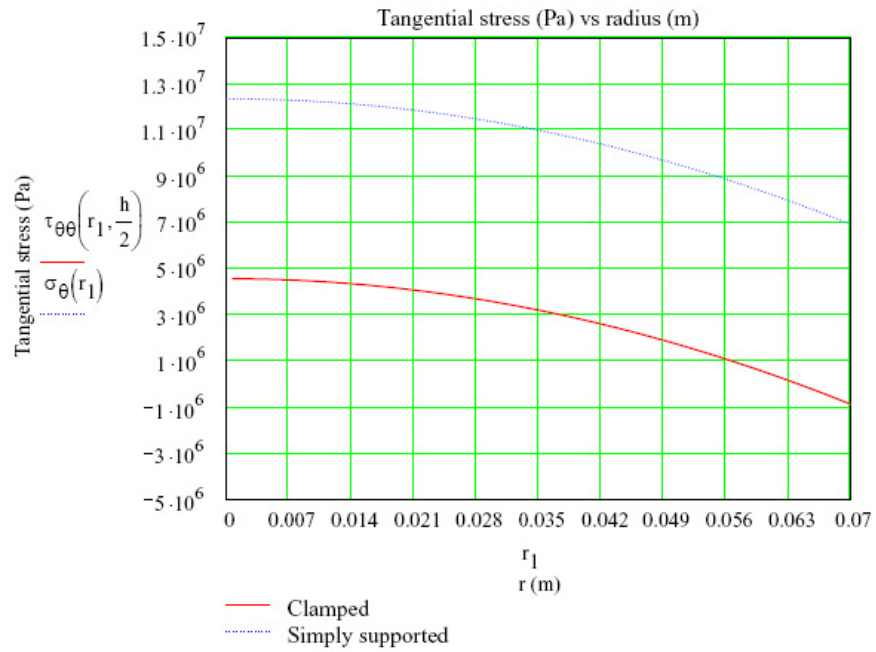


Figure D.2: Window tangential stress

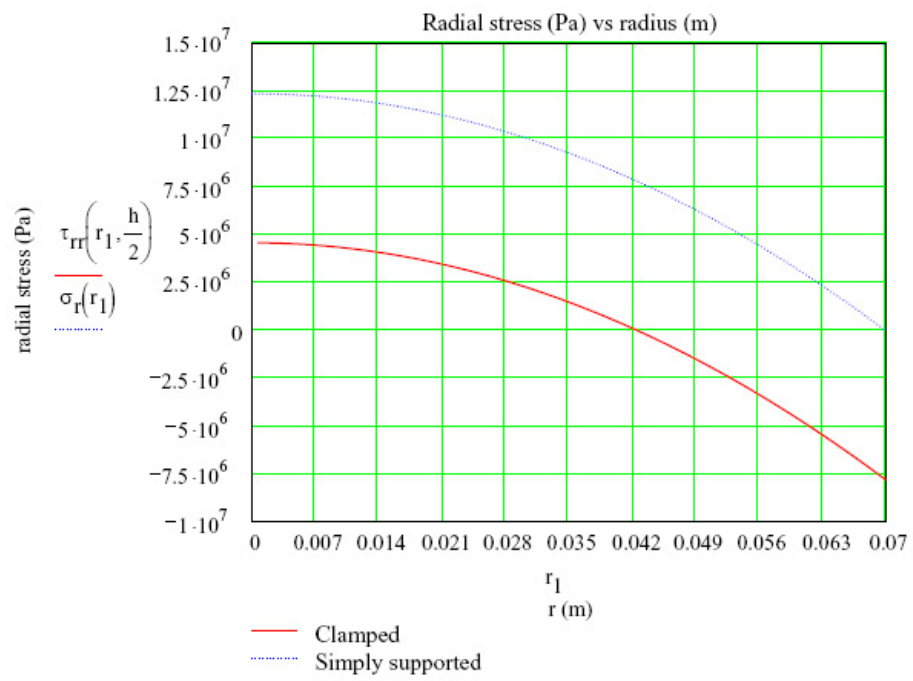
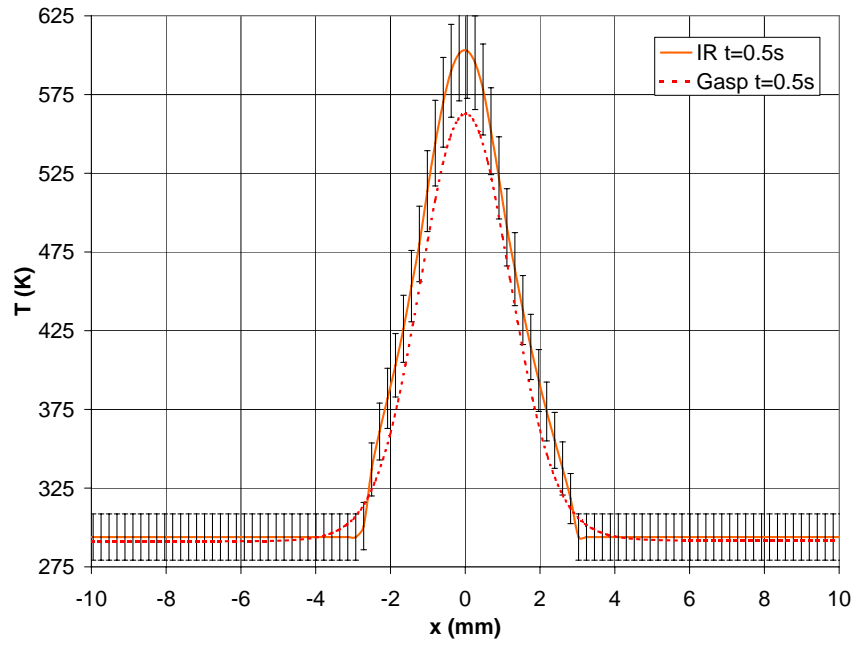


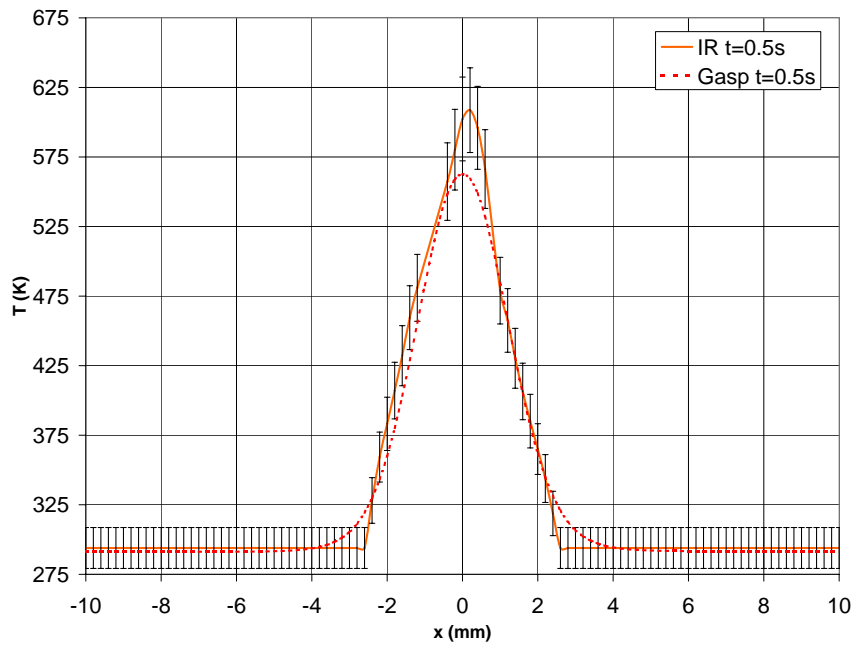
Figure D.3: Window radial stress

Appendix E

Streamwise Temperature Profiles for $P = 65W$

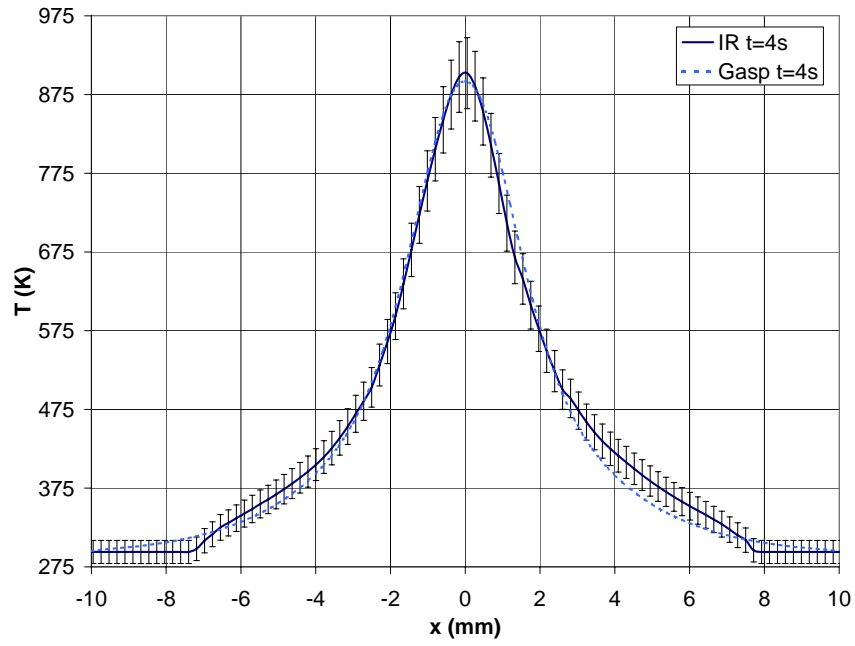


(a) Flow-off

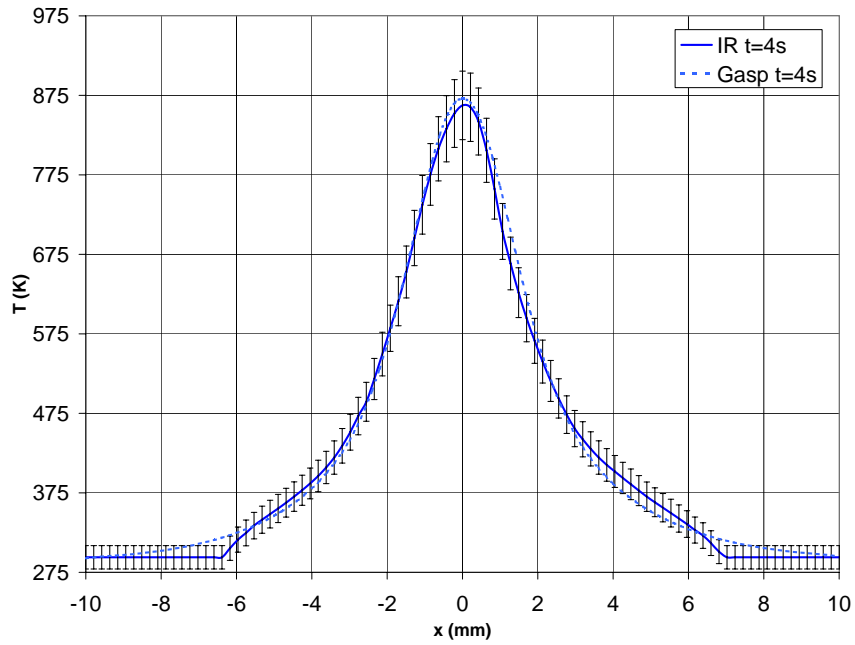


(b) Flow-on

Figure E.1: Comparison of surface temperature between computation and experiment at $t = 0.5$ s for $P = 65$ W

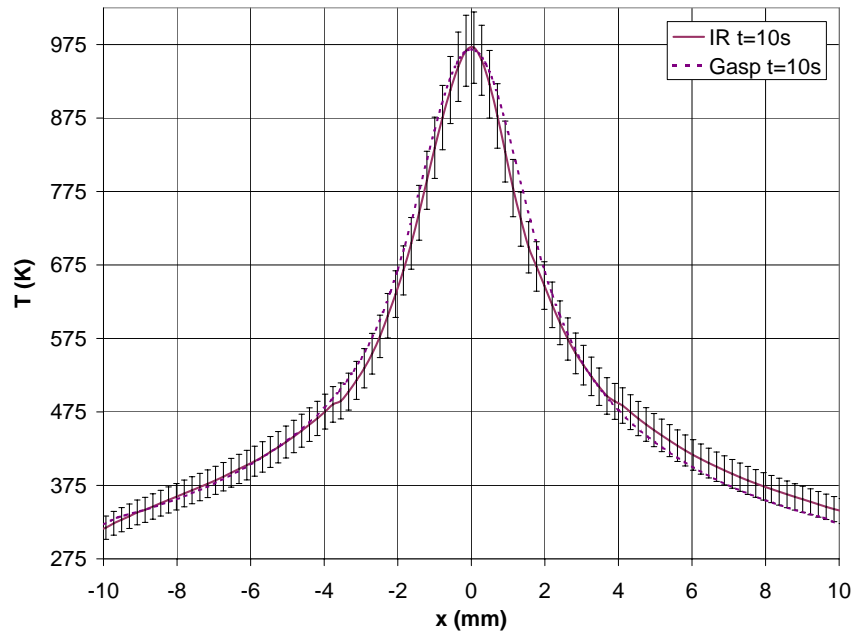


(a) Flow-off

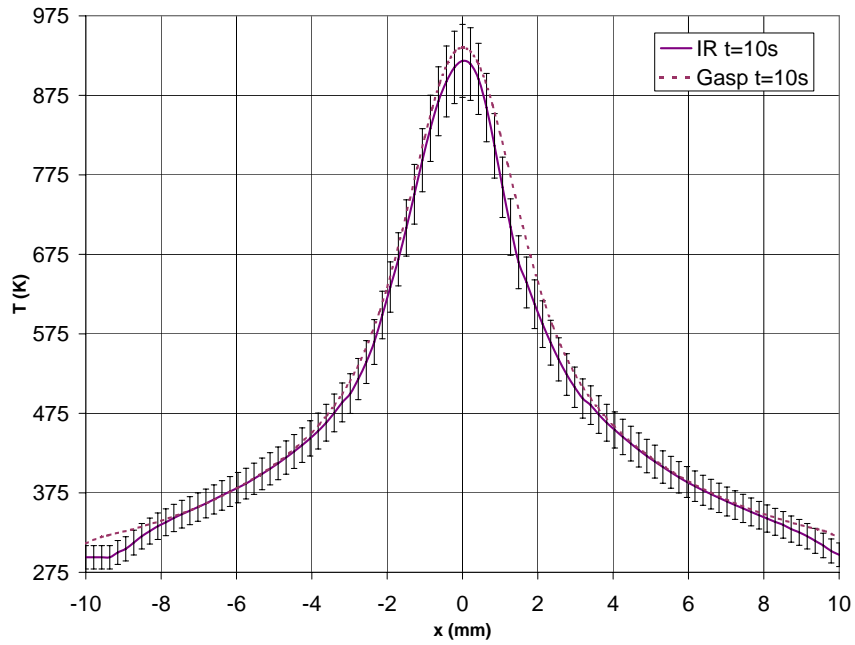


(b) Flow-on

Figure E.2: Comparison of surface temperature between computation and experiment at $t = 4s$ for $P = 65W$

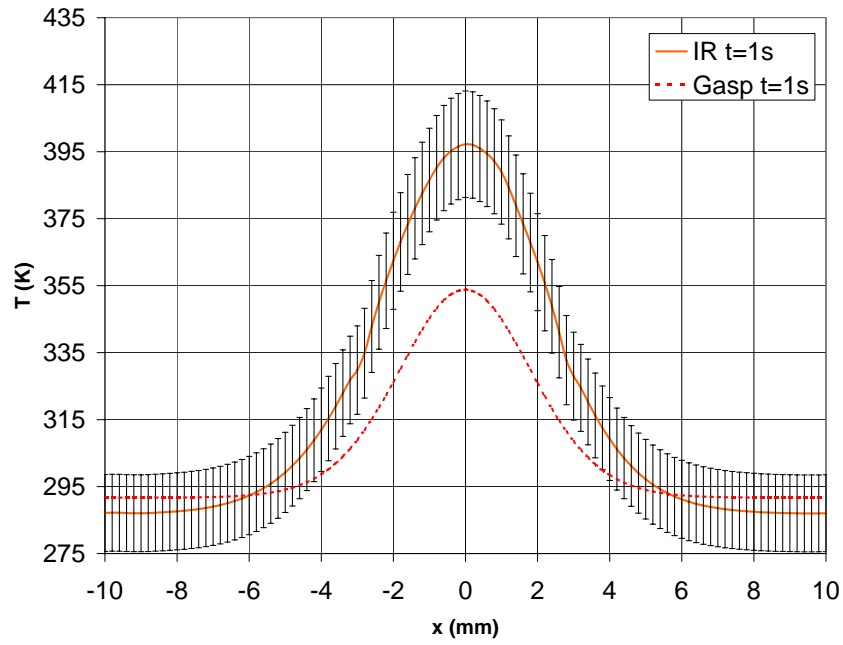


(a) Flow-off

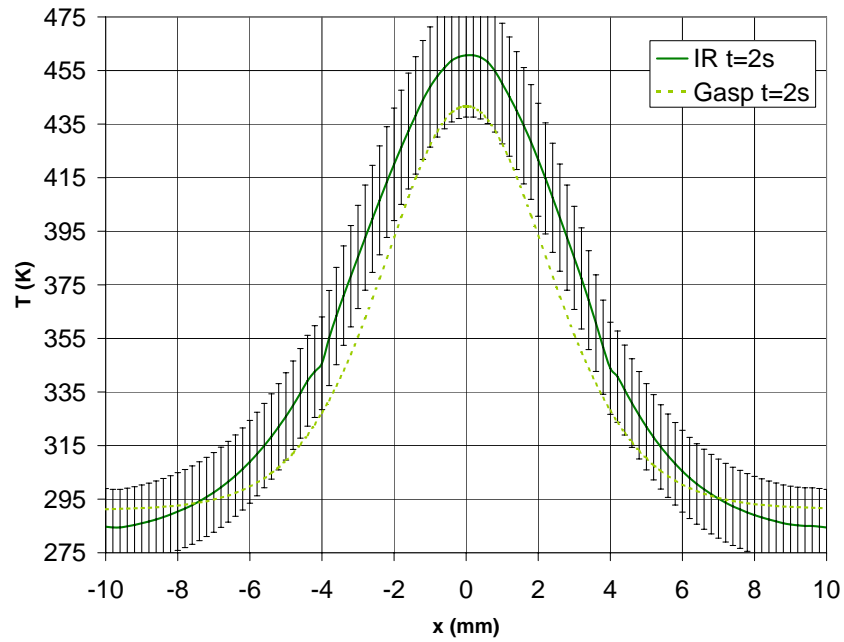


(b) Flow-on

Figure E.3: Comparison of surface temperature between computation and experiment at $t = 10s$ for $P = 65W$

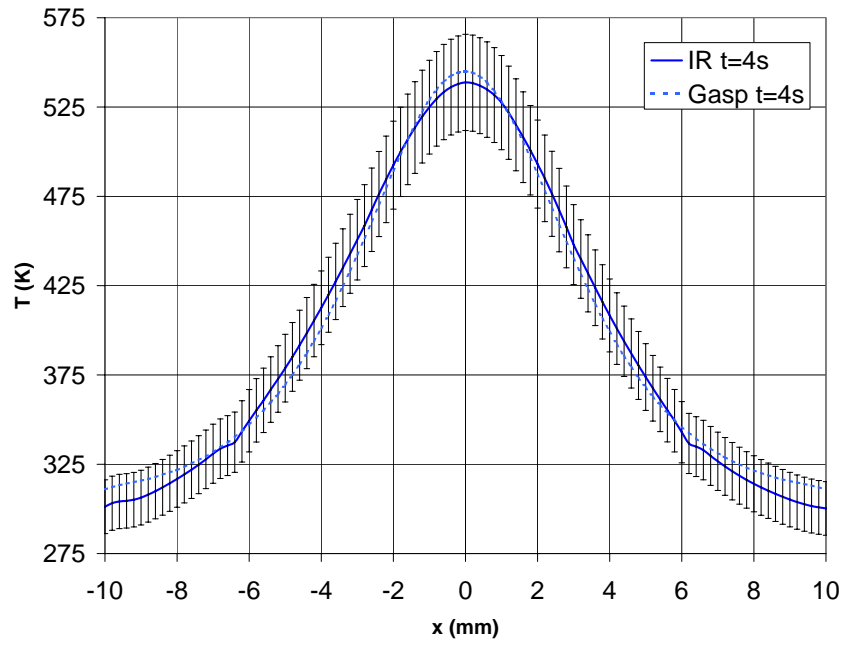


(a) Flow-off

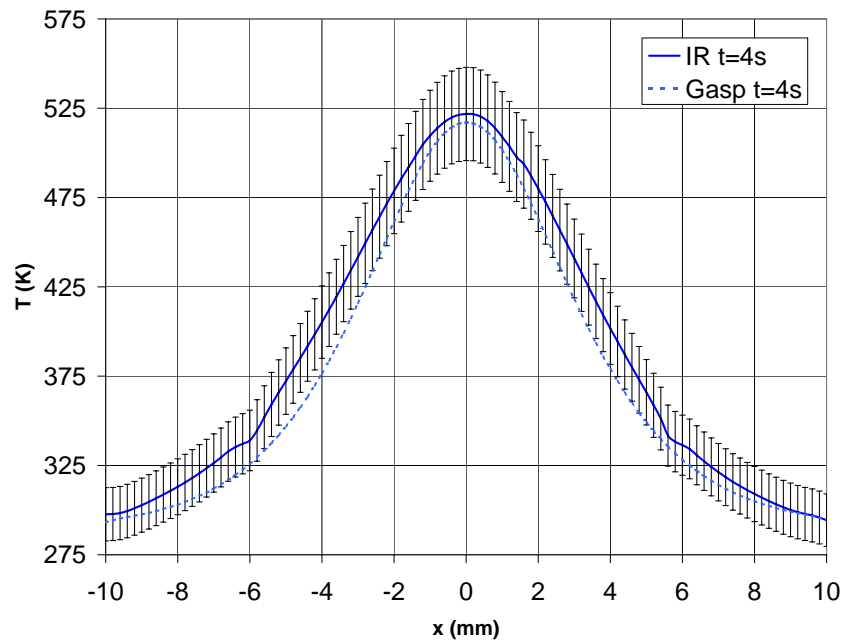


(b) Flow-on

Figure E.4: Comparison of backside temperature between computation and experiment at $t = 1s$ for $P = 65W$

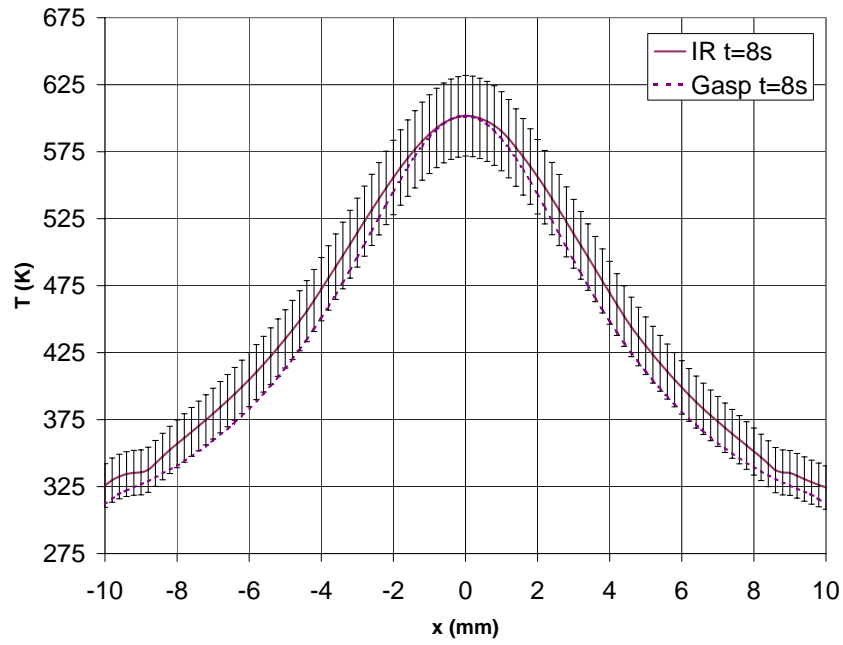


(a) Flow-off

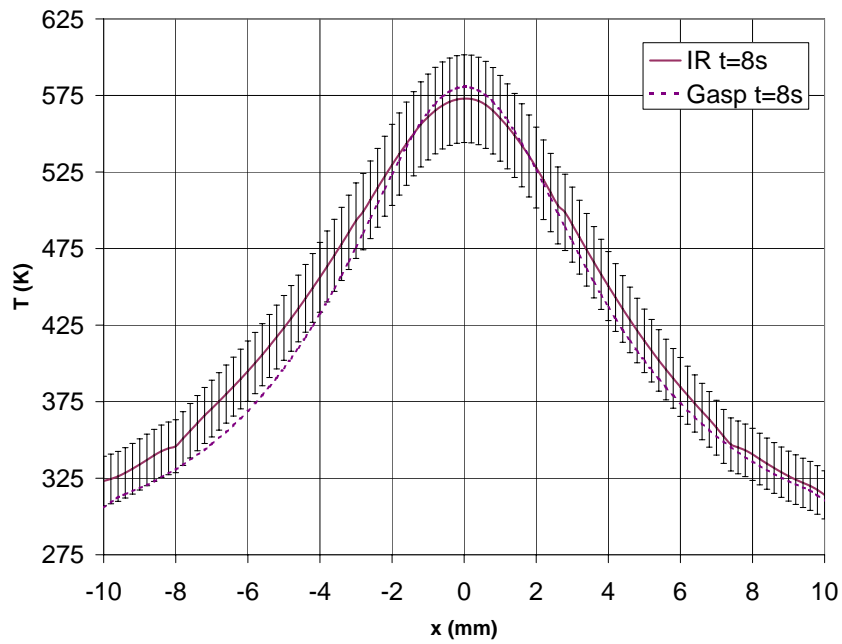


(b) Flow-on

Figure E.5: Comparison of backside temperature between computation and experiment at $t = 4s$ for $P = 65W$



(a) Flow-off

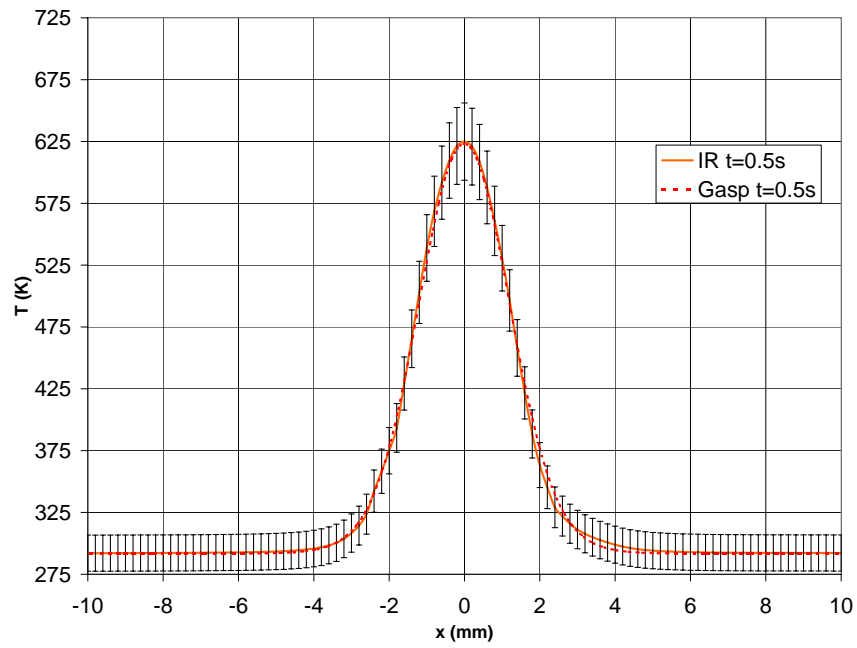


(b) Flow-on

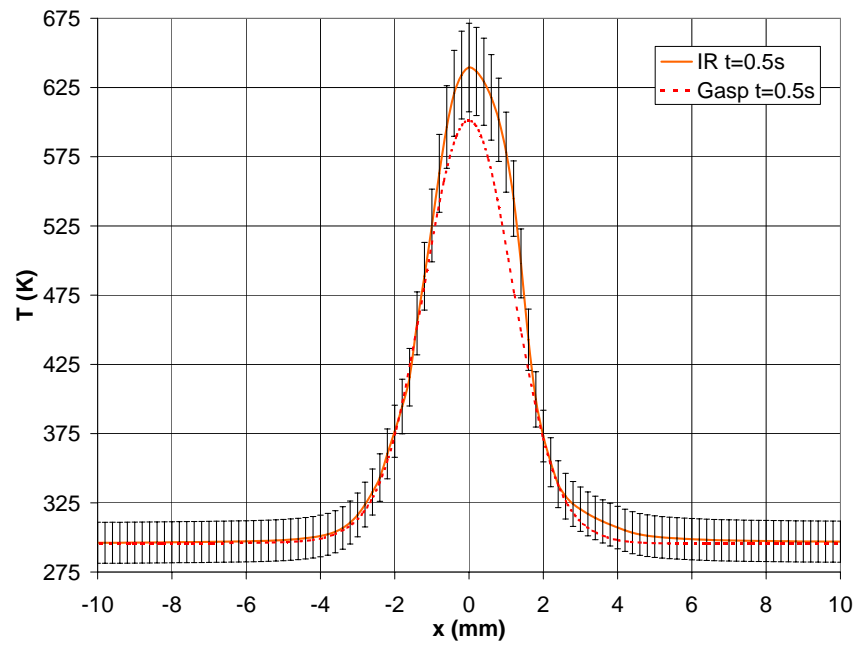
Figure E.6: Comparison of backside temperature between computation and experiment at $t = 8s$ for $P = 65W$

Appendix F

Streamwise Temperature Profiles for $P = 81W$

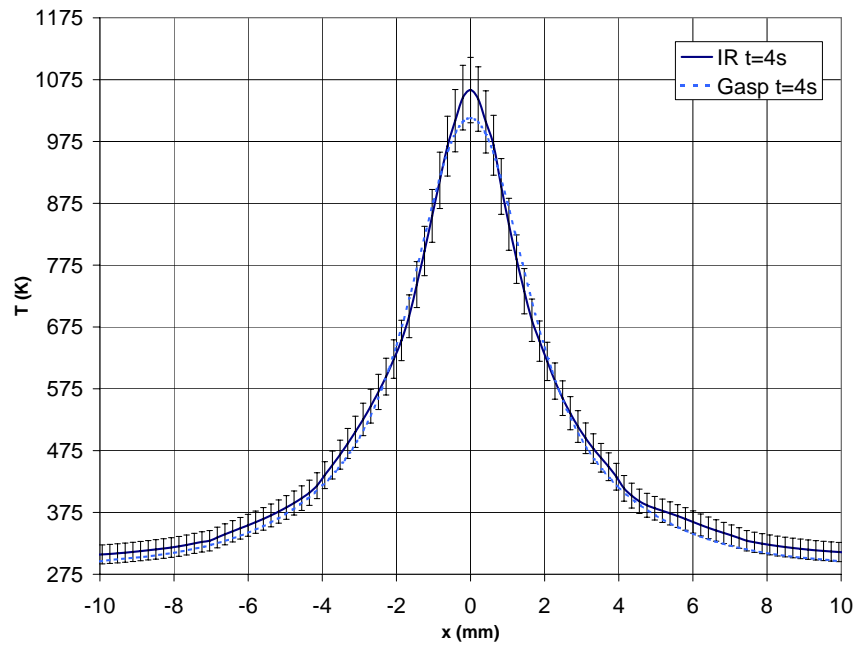


(a) Flow-off

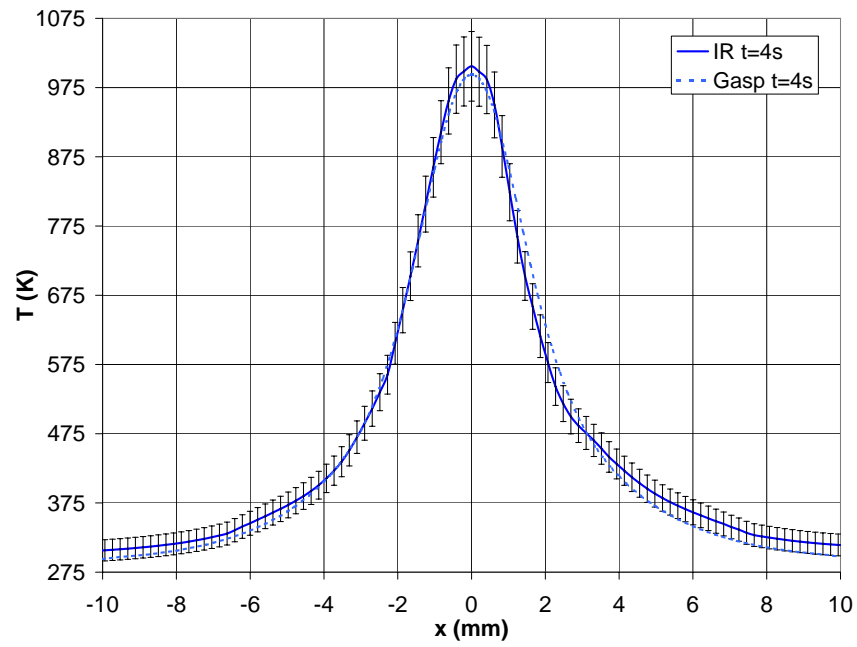


(b) Flow-on

Figure F.1: Comparison of surface temperature between computation and experiment at $t = 0.5$ s for $P = 81$ W

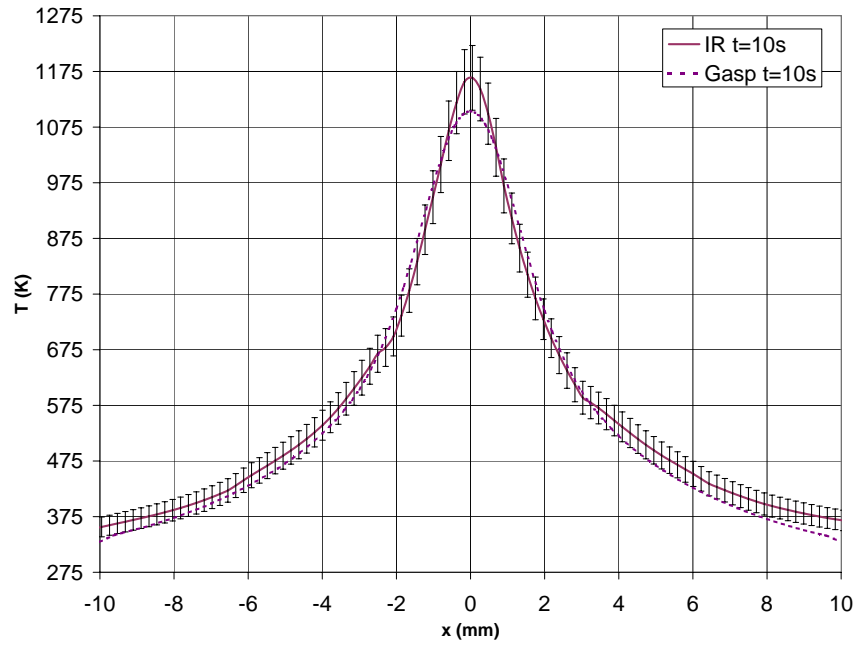


(a) Flow-off

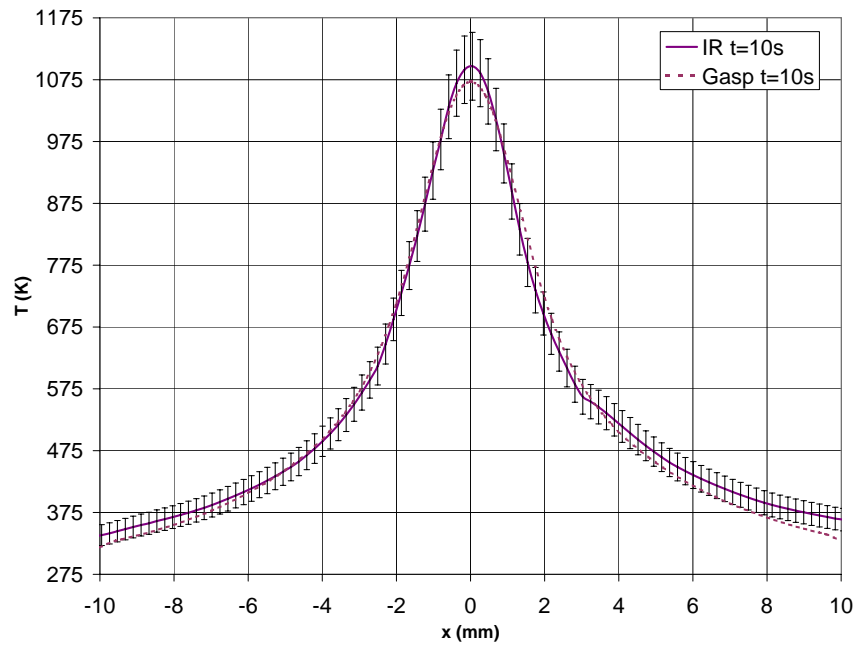


(b) Flow-on

Figure F.2: Comparison of surface temperature between computation and experiment at $t = 4s$ for $P = 81W$

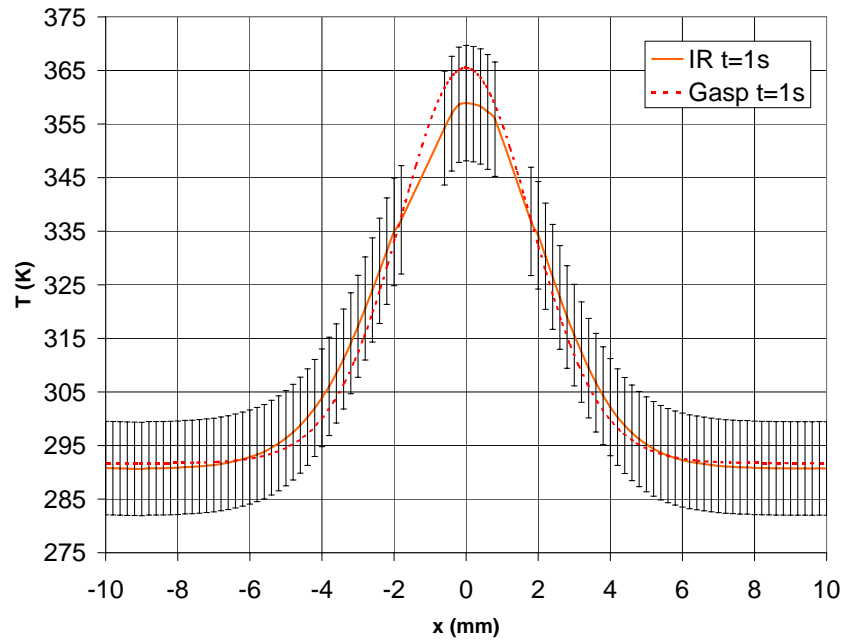


(a) Flow-off

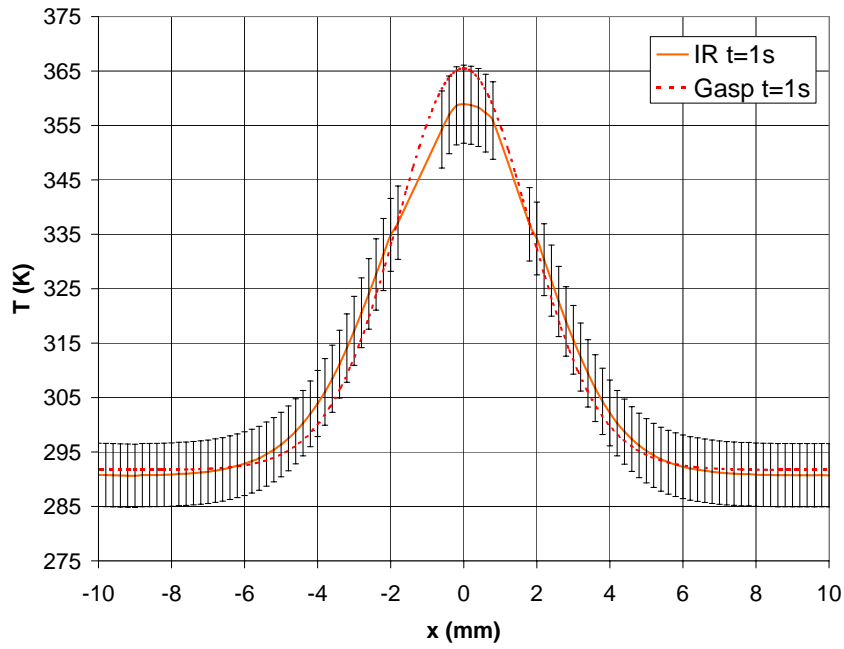


(b) Flow-on

Figure F.3: Comparison of surface temperature between computation and experiment at $t = 10s$ for $P = 81W$

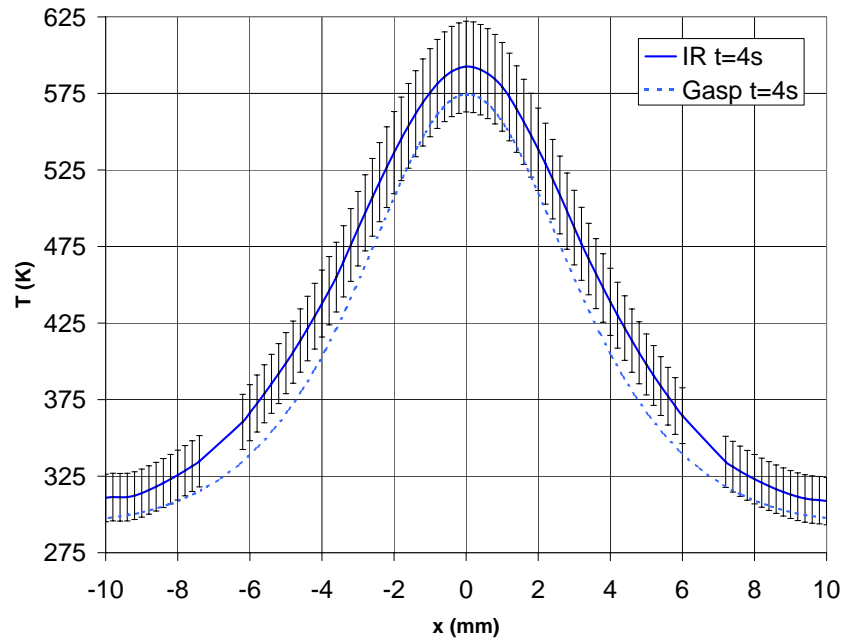


(a) Flow-off

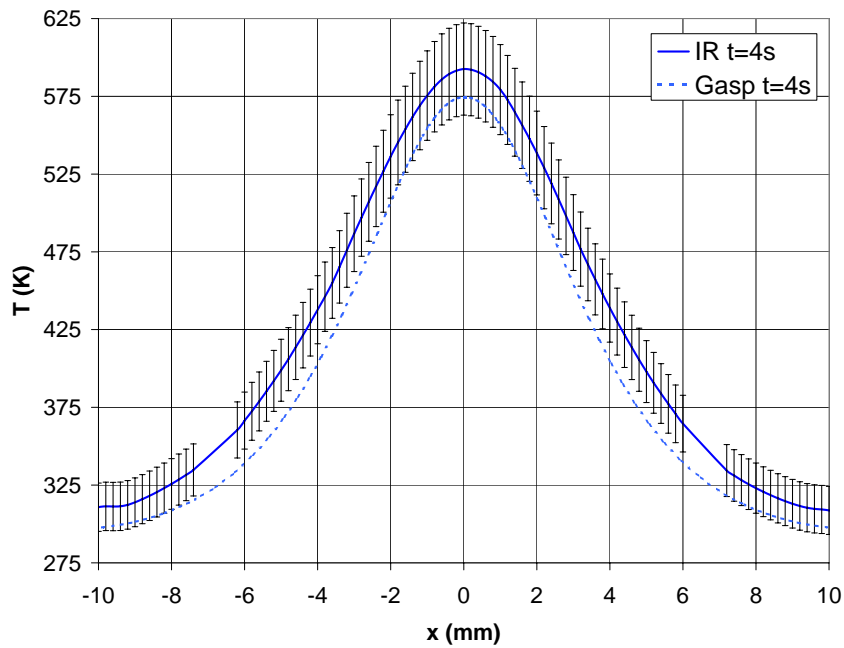


(b) Flow-on

Figure F.4: Comparison of backside temperature between computation and experiment at $t = 1s$ for $P = 81W$

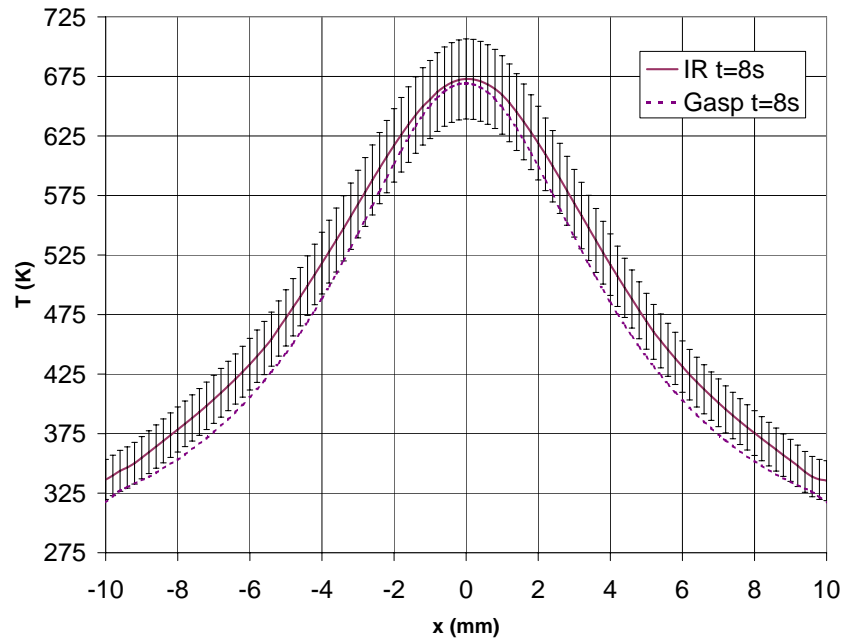


(a) Flow-off

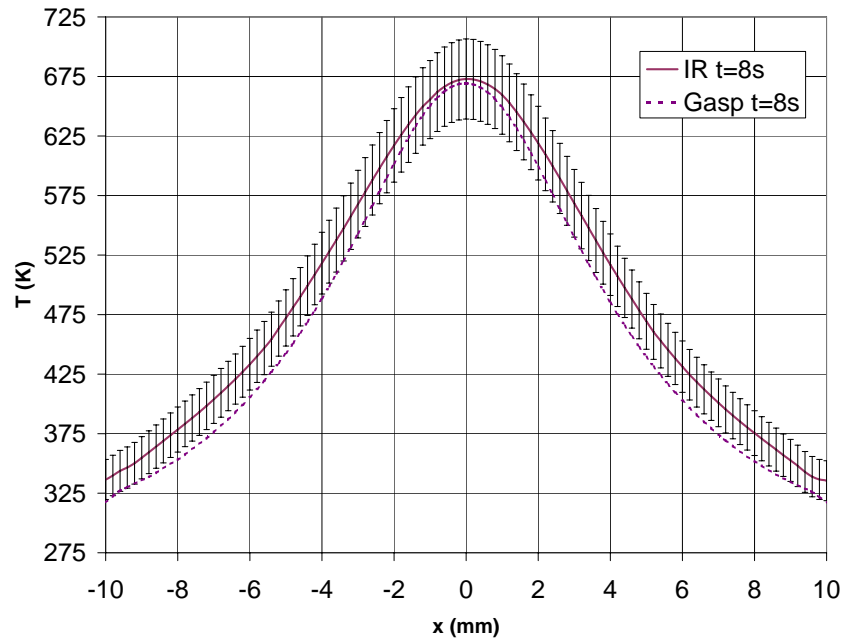


(b) Flow-on

Figure F.5: Comparison of backside temperature between computation and experiment at $t = 4s$ for $P = 81W$



(a) Flow-off



(b) Flow-on

Figure F.6: Comparison of backside temperature between computation and experiment at $t = 8s$ for $P = 81W$

Vita

Eric Marineau was born August 15 1978 in Highland Park Illinois and grew up in Chateauguay Quebec where he enjoyed playing and teaching tennis. He received a bachelor's degree in Mechanical Engineering with a specialty in Aeronautical Engineering and a Master's degree in Aerospace Engineering in 2001 and 2003 respectively from Ecole Polytechnique de Montreal. During his senior year, he developed a Matlab toolbox for the intuitive knowledge of turbomachinery. As a research assistant at Polytechnique, his work focused on the use of virtual reality for aerodynamic design and education, and on the development of a load transfer algorithm for coupling CFD and structural analysis codes in fluid/structure interaction. In 2003-2004, he studied Mathematics at the Universite de Montreal. In 2004, he was awarded the NATEQ and NSERC Ph.D. scholarships and enrolled in the Ph.D. program in Aerospace Engineering at Virginia Tech under the supervision of Dr. Joseph Schetz. After completing of his Ph.D. in May 2007, he is joining Caltech where he accepted a postdoctoral research position working for Dr. Hans Hornung.